ATMOSPHERIC GRAVITY WAVES IN CONSTITUENT DISTRIBUTIONS

By

Dorothy E. Gibson-Wilde, B.Sc. (Hons)

Thesis
submitted for the degree of
DOCTOR OF PHILOSOPHY
at the
UNIVERSITY OF ADELAIDE
(Department of Physics and Mathematical Physics)

December 1996

Dedicated to the memory of my grandfather
John Richard (Jack) Gibbard
2 October 1907 – 30 June 1996

This work contains no material which has been accepted for the award of any other degree or diploma in any university or other tertiary institution and, to the best of my knowledge and belief, contains no material previously published or written by another person, except where due reference has been made in the text.
I give consent to this copy of my thesis, when deposited in the University Library, being available for loan and photocopying.

Signed: dated: ...19/12/96...................

Dorothy E. Gibson-Wilde, B.Sc. (Hons)

Abstract

This thesis has investigated the influence of atmospheric gravity waves on constituents, particularly ozone in the stratosphere and neutral sodium in the mesosphere. The study included theoretical, modeling, and observational approaches. The motivation for the work is presented first as previous studies are reviewed. A theoretical basis for gravity wave studies is then provided, leading into modeling, simulation studies, and data analysis.

A simple linear gravity wave simulation was developed and applied to the mesospheric neutral sodium layer. The simulation is particularly straightforward for the sodium layer due its approximate horizontal homogeneity and long chemical lifetime relative to gravity-wave timescales. This simulation was used to evaluate processing techniques presently applied to experimental sodium resonant lidar data to determine gravity wave characteristics. The processing of simulated data containing gravity wave fluctuations indicated that the stated limits and some results obtained from sodium lidar are unreliable. The use of simulated data provides a convenient framework within which to explore the sensitivity and selectivity of experimental techniques.

Stratospheric ozone was investigated as an important atmospheric constituent whose response to gravity-wave scale motions is complex and previously not well documented. Detailed observations of mesoscale ozone variation were obtained from two novel campaigns. A combination of quasi-simultaneous ozonesonde, radiosonde and ER-2 aircraft data from the 1994 Antarctic Southern Hemisphere Ozone Experiment (ASHOE), was used to provide a high-resolution picture of the vertical and horizontal variation of ozone, winds, and temperature.

A separate campaign consisting of simultaneous observations with an ozone differential absorption lidar (DIAL) and a Rayleigh–Mie Doppler wind lidar from the Observatoire de Haute Provence (OHP), France, provided high resolution information on the time evolution of ozone vertical structure including two ozone "laminae". The presence of a well-defined long-period inertia-gravity wave was detected in lidar horizontal winds at the same time and altitude as the two observed laminae. These observations provided an excellent case study through which to examine mesoscale ozone variability and test theoretical concepts of ozone response to wave fluctuations.

A two-dimensional Lagrangian mesoscale parcel advection model was developed in order to explore some of the features evident in the above observations more fully. In particular, the possible interaction between mesoscale fluctuations and synoptic-scale transport in generating observed ozone features was investigated. The impact of such interactions on the calculated ozone spectra was addressed. Aspects of the observed ozone variability from the case study of dual lidar observations were then re-examined from a modeling perspective.

As a detailed study of theory, modeling, and observations of mesoscale variability of constituents in the stratosphere and mesosphere, this thesis provides a useful coverage of constituent transport processes in the middle atmosphere.

Acknowledgements

Thanks to my husband Andrew Shellshear for his encouragement. My supervisors Bob Vincent and Iain Reid at the University of Adelaide and Steve Eckermann at Computational Physics Inc., Fairfax, Virginia, U.S.A., provided much valuable assistance and advice.

In the Atmos group, thanks to Graham Elford, Andrew Taylor, the late Basil Briggs and the staff Dallas Kirby, Lyn Birchby, Mark Ferraretto, and Mike Shorthose. The students, some finished and financially stable, others not yet... Simon Allen, Karen Berkefeld, Manuel Cervera, Scotty Dullaway, Stephen Grant, Trevor Harris, Bridget Hobbs, Dave Holdsworth, Alireza Kazempour, Sujata Kovalam, David Low, Andrew Mackinnon, Deepak Rajopadhayaya, Brenton Vandepeer, Rupa Vuthaluru, and Jonathon Woithe.

For Macquarie Island ASHOE ozonesonde campaign data analyzed in Chapter 4, thanks go to the Bureau of Meteorology's Jim Easson. The ASHOE ER-2 data was supplied by Julio Bacmeister of the Naval Research Laboratory with permission from the ER-2 team. Roger Atkinson at the Bureau of Meteorology Research Centre, Melbourne, gave useful advice on the ASHOE data set and provided the contour advection calculations discussed in Chapter 5.

Financial support to visit France and obtain the lidar data presented in Chapter 5 was provided by Dr Vincent and a University of Adelaide Overseas Travel Grant.

Thanks to Julio and Steve's group at the Naval Research Laboratory, Washington, and Susan Avery's group at CIRES, Boulder, for an enjoyable and useful visit to the US in September 1995.

During my visit to France, special thanks to Claude Souprayen, Mme Marie-Lise

Chanin, and Alain Hauchecorne. Also, the Lidar and Satellite group students and staff Albert Hertzog, Vanessa, Bechir, Thierry, Florence, Fede, Celine and co. The ozone and wind lidars were supported by Mme Anne Garnier and the excellent staff at the Observatoire de Haute Provence. For information on ozone lidar processing, thanks to Mme Sophie Godin at CNRS, Jussieu who interrupted her maternity leave.

I would like to thank my father, mother, and grandparents for their advice and support. My high school teachers Denise Glasgow, Robert Handicott, and Alan Cooke were a source of inspiration, as was my Honours supervisor Ian Whittingham from James Cook University, Townsville. My friends and interests outside physics have been diverting and have kept me mostly sane: special thanks to Gina, Grant, Aase, Jenny, Chris and Amanda, the Daves from Pimlico, Al, Ev, Michael, Sandrine, Jacqueline, and Guido Coppola and the Monteverdi singers.

An (anti-)acknowledgement goes to Dr David Phillips at DSTO, Adelaide, for his comments that women were incapable of scientific research.

To the wit of Dorothy Parker, the future vision of William Gibson, and the style of Oscar Wilde, or something.

List of Symbols

Alphabetical by symbol with definition or value, as appropriate, and typical unit.

c	speed of light (m s^{-1})
c_G	gravity wave group velocity (m s^{-1})
c_P	specific heat at constant pressure (dry air value 1004.5 J kg^{-1} K^{-1})
c_S	speed of sound ($\approx$ 330 m s^{-1})
c_V	specific heat at constant volume (dry air value 718.0 J kg^{-1} K^{-1})
c_h	gravity wave horizontal phase speed (m s^{-1})
c_z	gravity wave vertical phase speed (m s^{-1})
f	Earth Coriolis parameter or inertial frequency (s^{-1})
$\mathbf{g}$	Earth gravitational acceleration ($\approx$ 9.8 m s^{-2})
γ	ratio of specific heats (dry air value $\frac{c_P}{c_V} \approx 1.4$)
H_ρ	atmospheric density scale height (km)
H	pressure scale height (km)
k	zonal wavenumber ($\frac{2\pi}{\lambda_x}$) (rad km^{-1})
l	meridional wavenumber ($\frac{2\pi}{\lambda_y}$) (rad km^{-1})
λ_x	gravity wave zonal wavelength (km)
λ_z	gravity wave vertical wavelength (km)
m	gravity wave vertical wavenumber ($\frac{2\pi}{\lambda_z}$) (rad km^{-1})
m_a	atmospheric mass (kg)
M_i	molecular mass of constituent i (kg mol^{-1})
n	number density or concentration (molecules cm^{-3})
N_A	Avogadro's number or number of atoms per mole of substance (6.022×10^{26})
N^2	squared Brunt–Väisälä frequency ($\frac{g}{\theta}(\frac{d\theta}{dz})$) (s^{-2})
ω_{obs}	ground-based or observed gravity wave frequency (s^{-1})

$\hat{\omega}$	intrinsic or Lagrangian gravity wave frequency (s^{-1})
$\boldsymbol{\Omega}$	Earth rotation frequency (s^{-1})
p	atmospheric pressure (hPa)
q	volume mixing ratio (ppmv) [see Table 2.1]
R	ideal gas constant ($c_P - c_V$) (dry air value 287.0 J kg^{-1} K^{-1})
ρ	atmospheric density (kg m^{-3})
t	time (s)
T	temperature (K)
T_B	Brunt–Väisälä period (s)
T_{obs}	ground-based gravity wave period (s)
$\hat{T}$	intrinsic gravity wave period (s)
θ	potential temperature ($T\left(\frac{p_0}{p}\right)^{\frac{R}{c_P}}$) (K)
u	zonal (east–west) wind (m s^{-1})
$\mathbf{U}$	vector of wind components (u, v, w)
$\mathbf{U}_h$	vector of horizontal wind components (u, v)
v	meridional (north–south) wind (m s^{-1})
w	vertical wind (m s^{-1})
z	height above Earth's surface (km)

Other Notation

$\frac{da}{dt}$	Lagrangian derivative of nominal parameter a
$\frac{\partial a}{\partial t}$	Eulerian derivative of nominal parameter a
$\bar{a}$	mean of nominal parameter a
a'	perturbation quantity (gravity wave perturbation unless otherwise specified)
$\mathbf{a}$	vector quantity
a_0	surface or initial value of nominal parameter a
a_{obs}	observed quantity (ground-based frame of reference)
$\hat{a}$	intrinsic quantity
r_a	relative fluctuation ($a'/\bar{a}$) of nominal parameter a

List of Abbreviations and Acronyms

ALOHA	Airborne Lidar Observations over Hawaii (experiment)
ASHOE	Antarctic Southern Hemisphere Ozone Experiment
BG90	*Beatty and Gardner* [1990]
CAS	Contour Advection with Surgery
CDS	Contour Dynamics with Surgery
CFC	Chloro-fluoro Carbon
CIRA	Committee on Space Research International Reference Atmosphere
CNRS	Centre Nationale de Recherche Scientifique
COSPAR	Committee on Space Research
DIAL	Differential Absorption Lidar
DU	Dobson Units
EASOE	European Arctic Stratosphere Ozone Experiment
ECC	Electrochemical Cell (ozonesonde)
EDH	Equivalent Displacement Height
EISCAT	European Incoherent Scatter (radar)
ER-2	Experimental Research (aircraft)
FFT	Fast Fourier Transform
GASP	Global Atmospheric Sampling Program
GRAVNET	Saskatoon Radar Network
GV87	*Gardner and Voelz* [1987]
IGW	Inertia-gravity Wave

LT	Local Time
MF	Medium Frequency (radar)
MLT	Mesosphere and Lower Thermosphere
MRM85	*Meek et al.* [1985]
Na	neutral sodium
NLC	Noctilucent Cloud
OHP	Observatoire de Haute Provence, France
POAM	Polar Ozone and Aerosol Measurement
ppmm	parts per million by mass
ppmv	parts per million by volume
PSC	Polar Stratospheric Cloud
PSD	Power Spectral Density
QBO	Quasi-biennial Oscillation
RD	Rayleigh–Mie Doppler (lidar)
RMS	Root Mean Square
SAGE	Stratospheric Aerosol and Gas Experiment
SDDFT	Scale-dependent Diffusive Filtering Theory
SG91	*Senft and Gardner* [1991]
SIDFT	Scale-independent Diffusive Filtering Theory
SPARC	Stratospheric Processes and their Role in Climate
SSL	Sudden or Sporadic Sodium Layer
TOMS	Total Ozone Monitoring Spectrometer
UARS	Upper Atmosphere Research Satellite
UIUC	University of Illinois at Urbana Champaign
UV	Ultra-violet
VG86	*Voelz and Gardner* [1986]
VHF	Very High Frequency (radar)
WMO	World Meteorological Organization

Contents

List of Figures

List of Tables

Chapter 1

Introduction

Art is long and life is short, and success is very far off ...

J. Conrad

1.1 The Earth's Atmosphere

Earth is surrounded by a complex, largely stable atmospheric structure which extends to a distance of approximately 400 km from the planet's surface. The atmosphere is influenced by gravitational and rotational effects, solar radiation, and the presence of reactive *constituents* or chemical components.

Classification of the Earth's atmosphere for scientific study relies primarily on the mean vertical temperature structure (Figure 1.1) [*U.S. Standard Atmosphere*,1976]. The lowest region of the atmosphere, known as the *troposphere*, is a region of typically linear decrease of temperature with height which extends from the surface to ~10 km at polar latitudes and to ~15 km at tropical latitudes. The upper limit of the troposphere, the *tropopause*, forms a boundary with the *stratosphere* (Section 1.4) which extends to ~50 km with a predominantly positive temperature gradient. The increase in temperature in this region is due mainly to the presence of the constituent *ozone*, discussed in Section 1.5. At *mesospheric* heights (Section 1.3) the mean vertical temperature gradient is again negative, with a further transition to temperature increase

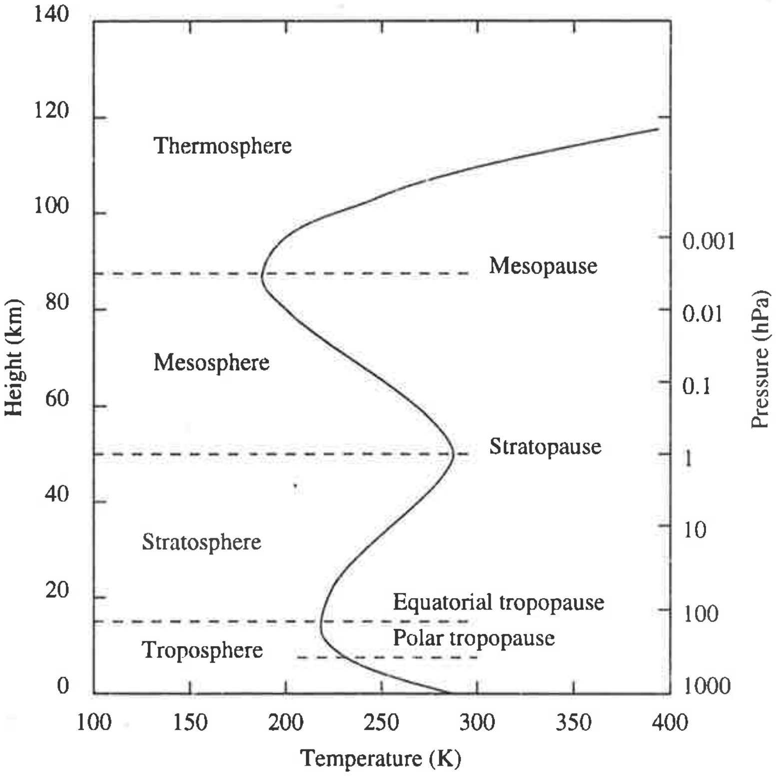

Figure 1.1: Schematic diagram of mean vertical temperature structure based on the *U.S. Standard Atmosphere*, 1976 [after *Andrews et al.*, 1987].

with height occurring at the *mesopause* (90-100 km) and on into the *thermosphere*, where ionization effects and diffusive separation become significant.

The *middle atmosphere*, consisting of the stratosphere and mesosphere (~10-100 km), is the region focussed on in this thesis. Atmospheric observation techniques including *radar* (radio detection and ranging), and *lidar* (light detection and ranging), as well as sonde-, and aircraft-based instrumentation will be used in the following chapters, along with many elements of gravity wave theory, to investigate and model this important region of the Earth's atmosphere. This introductory chapter reviews concepts and previous works which are important in the study of atmospheric gravity waves and their effects on constituent distributions in the middle atmosphere.

1.2 Atmospheric Gravity Waves

Atmospheric gravity waves[1] are wave-induced oscillations of air parcels due to the

---

[1] Gravity waves are also less commonly known as *buoyancy waves* or oceanic *internal waves*.

opposing forces of buoyancy and gravitation, and in some cases planetary rotation. Atmospheric gravity waves arise as simple harmonic solutions of the Navier–Stokes equations which describe the interplay between winds, temperature, pressure, and atmospheric density. Other atmospheric wave motions with specific scales and properties include acoustic waves, atmospheric tides, mixed Rossby-gravity waves, Lamb waves, and other planetary-scale motions, such as Rossby waves and Kelvin waves.

The fluctuations arising from gravity waves are an important part of the so-called *mesoscale*[2] variability of the Earth's atmosphere. In this thesis, mesoscale variability refers to motions with characteristic vertical scales typically ~0.1-10 km and horizontal scales ~1-1000 km, in the absence of a strict definition which has been uniformly applied [*Thunis and Bornstein*,1996]. Motions with smaller vertical scales can be described as *microscale*, commonly ascribed to inertial range three-dimensional turbulence. Motions with horizontal scales >1000 km are referred to as *synoptic* or *planetary-scale.*

Since the initial realization of the importance of atmospheric gravity waves at middle atmospheric mesoscales by *Hines* [1960], a detailed record of gravity wave observations has been compiled and an extensive range of theoretical studies has been accomplished. The study of atmospheric wave motions and long-term cycles has advanced the capability to determine trends and predict elements of the atmospheric circulation. The importance of parameterizing gravity-wave-induced variability over the range of timescales from intra-annual variations through to hourly variations has led to the instigation of gravity wave databases (*e.g.* the Stratospheric Processes and their Role in Climate (SPARC) Gravity Wave Initiative (GWI)) and has prompted detailed observational studies of their seasonal and latitudinal distributions.

The primary physical mechanisms responsible for gravity wave generation are believed to be orographic forcing and tropospheric weather systems, such as frontal systems and intense convection (*e.g.* thunderstorms, squall lines, and cyclones). Progress in the understanding of gravity wave generation has come from simulation and observation of the generation of gravity waves by fronts [*e.g. Griffiths and Reeder*,1996],

---

[2] Mesoscale means literally middle scale.

studies of convective systems [*e.g. Alexander et al.,*1995], and investigations of mountain wave forcing [*Bacmeister and Schoeberl,*1989; *Bacmeister et al.,*1990].

Analysis of observational data has emphasized two general areas of atmospheric gravity wave effects. Many studies, using a variety of measurement techniques, have investigated specific occurrences of quasi-monochromatic wave events [*Reid,*1986; *Cot and Barat,*1986; *Gardner and Voelz,*1987; *Yamamoto et al.,*1987; *Chan et al.,*1991]. The strongly multi-component nature of the gravity wave field, with observations generally indicating the presence of a superposition of waves, has led to extensive study of the gravity wave spectrum, using either vertically, horizontally, or temporally resolved mesoscale data sets. Such studies include measurements using rockets [*Wu and Widdel,*1991; *Thrane et al.,*1994], balloons [*Allen and Vincent,*1995], aircraft [*Bacmeister et al.,*1996], radars [*Murayama et al.,*1992; *Sato and Yamada,*1994], airglow imagers [*Hecht et al.,*1994] and lidars [*Shibata et al.,*1986; *Senft and Gardner,*1991; *Wilson et al.,*1991; *Whiteway and Carswell,*1994].

Characteristic vertical scales of wave motions are ~2-5 km in the lower stratosphere, ~5-15 km in the upper stratosphere, and >15 km in the mesosphere, as determined from spectral studies of radar and rocketsonde measurements [*Smith et al.,*1987; *Murayama et al.,*1992]. These characteristic scales are responsible for the majority of gravity-wave-induced horizontal velocity and temperature variance in the middle atmosphere. The increase of the characteristic vertical scale with height has been interpreted as an indication of a gradual change in the gravity wave field with height, although the exact physical processes involved remain controversial [discussed in Chapter 3]. The theoretical basis for a gravity wave study and further important results will be developed in Chapter 2.

1.3 The Mesosphere (50-100 km)

Early studies of the mesosphere focussed on the partially ionized region (80-100 km) known also as the ionospheric D region. Continued interest in the effect of this region on radio communications and various military applications has resulted in investigations using rockets and ionosondes, as well as remote sensing using medium frequency

(MF) and very high frequency (VHF) radars. These observational techniques yield measurements of atmospheric variables such as temperature, wind velocity, and ionization profiles.

Rocket trail data from early ionospheric experiments indicated significant variability, and were initially interpreted purely in terms of turbulence [*e.g.* *Blamont and de Jager*,1962]. However, the observations were reinterpreted by *Hines* [1960] as strong supporting evidence of the importance of gravity waves. The understanding and appreciation of the role played by gravity waves in the mesosphere has increased significantly since these early studies.

The temperature structure of the mesosphere cannot be explained in terms of radiative equilibrium. Summer temperatures in the upper stratosphere and mesosphere are colder than those in winter. In fact, the coldest region of the Earth's atmosphere is the summer mesopause where temperatures below 100 K have been observed [*Schmidlin*,1992]. The formation of this anomalous temperature structure has been attributed conclusively to gravity wave breaking and the resultant deposition of momentum [*Lindzen*,1981; *Holton*,1982; *Fritts and Lu*,1995]. The gravity-wave-induced changes to the mesospheric momentum budget drive a meridional circulation directed from the summer to winter pole, which is associated with upwelling at the summer pole and subsidence at the winter pole.

The mesosphere has been studied using rocket-based techniques which have provided sporadic high-resolution mesospheric horizontal velocity measurements [*e.g.* *Blix et al.*,1990; *Wu and Widdel*,1991]. Extensive mesospheric observations have been carried out using MF radar and incoherent scatter radar techniques located at mid-latitudes [*Meek et al.*,1985; *Reid*,1986; *Vincent and Fritts*,1987; *Tsuda et al.*,1990], tropical latitudes [*Fukao et al.*,1985; *Vincent and Lesicar*,1991; *Fritts and Isler*,1992], and recently at polar locations [*Vincent*,1994]. These observations have brought to light information on turbulent dissipation [*e.g.* *Hocking*,1987], gravity wave variances [*e.g.* *Tsuda et al.*,1990], tidal oscillations [*Vincent et al.*,1988], as well as planetary-scale wave motions such as the two-day wave [*Harris*,1994]. VHF radars have been used to measure mesospheric winds using reflections from meteor trails [*Cervera and Reid*,1995].

Lidar observations have also revealed gravity wave and tidal structures in the lower mesosphere [*Chanin and Hauchecorne*,1981]. The vertical temperature structure of the entire mesosphere–lower thermosphere (MLT) region has been made accessible recently with the development of increasingly powerful Rayleigh lidars [*Meriwether et al.*,1994; *She et al.*,1995]. Airborne lidar measurements have been carried out to address the spatial limitations inherent in the traditional ground-based lidar observations [*e.g. Qian et al.*,1995]. Observations using resonant lidar techniques, specifically of the mesospheric neutral sodium layer, are the subject of Chapter 3.

Analysis of airglow observations has provided information on the horizontal structure of wave motions in the mesosphere [*e.g. Gavrilov and Shved*,1982]. Recently developed all-sky airglow imagers resolve detailed fluctuations in airglow intensity which enable spectral studies of the gravity wave field [*e.g. Hecht et al.*,1994].

The process of gravity wave breaking at mesospheric heights has been identified as a vital feature in the maintenance of the atmospheric general circulation [*Holton*,1983; *Garcia and Solomon*,1985]. Recent colocated measurements using airglow imaging, MF radar, and sodium resonant lidar observations have revealed important evidence of gravity wave breaking [*Hecht et al.*,1996b].

The synoptic-scale structure of mesospheric velocities, temperatures, and constituents has been observed using satellite-based instruments. The Solar Mesosphere Explorer (SME) obtained temperature measurements in the region 58-90 km [*Clancy and Rusch*,1990]. A range of experiments on board the Upper Atmosphere Research Satellite (UARS) has provided temperature and velocity data at mesospheric heights [*e.g. Manney et al.*,1995a].

Modeling studies of tidal motions in the mesosphere have revealed the complex height, longitude, and latitude dependent structure of this region [*e.g. Forbes and Vial*,1989; *Hagan et al.*,1995]. The interaction between gravity waves and tides has been the subject of recent modeling studies with the aim of reproducing the observed mesospheric variability [*Fritts and Vincent*,1987; *Lu and Fritts*,1993; *Eckermann and Marks*,1996].

Gravity wave variability in the mesosphere has been the subject of previous modeling and simulation studies. Mesoscale modeling has proved a useful tool in the interpretation of gravity wave effects in airglow intensities [*Weinstock*,1978; *Hines and Tarasick*,1987]. *Kirkwood and Collis* [1989] used a monochromatic simulation to investigate the role of gravity waves in the formation of sudden or sporadic sodium layers (SSL) (Section 3.2,2). *Fritts et al.* [1993] and *Jensen and Thomas* [1994] carried out simulations of gravity wave effects on noctilucent clouds (NLCs). *Gardner and Shelton* [1985] modeled gravity-wave variability in mesospheric neutral sodium, which is further described and explored in Chapter 3.

1.4 The Stratosphere (15-50 km)

The stratosphere is the most stable region of the Earth's atmosphere. Many observational techniques have been applied to investigate gravity waves in this region including balloon soundings [*Thompson*,1978; *Cot and Barat*,1986; *Tsuda et al.*,1991; *Allen and Vincent*,1995], rocket studies [*Hamilton*,1991; *Eckermann et al.*,1995], lidar studies [*Shibata et al.*,1986; *Chanin and Hauchecorne*,1987; *Wilson et al.*,1991; *Beatty et al.*,1992; *Whiteway and Carswell*,1994], and aircraft-based instruments [*Lilly and Lester*,1974; *Gage and Nastrom*,1986; *Bacmeister et al.*,1996].

Balloon-borne and radiosonde observations have been the fundamental observational techniques for the lower stratosphere since early this century. Routine radiosonde soundings provide horizontal velocity, humidity, and temperature measurements, which are used in the assimilation of large-scale meteorological information world wide. Recently the high-resolution height-resolved radiosonde measurements of velocities and temperatures have been recognized as providing a unique resource for the study of tropospheric and stratospheric mesoscale dynamics. These measurements have suggested characteristic vertical scales of gravity wave motions in the stratosphere of ~2 km [*Tsuda et al.*,1991; *Allen and Vincent*,1995]. Radiosonde observations are referred to in Chapter 4.

Monitoring of stratospheric density and temperature structure has been carried out at several locations around the world using Rayleigh lidars which measure the density structure of the middle atmosphere, typically over the height range 30-80 km. More recently, the Rayleigh–Mie Doppler (RD) lidar technique has been developed to obtain stratospheric horizontal velocity measurements [*Chanin et al.*,1989; *Garnier and Chanin*,1992]. Both of these techniques provide data with excellent vertical (~100 m) and temporal (~5 min) resolution. The RD lidar technique is discussed further in Chapter 5.

Instrumented aircraft have been used to obtain primarily horizontal profiles of stratospheric velocities and temperatures. These studies have obtained power spectra of horizontal and vertical velocities and potential temperature, and more recently stratospheric chemical constituents such as ozone and nitrous oxide [*e.g. Bacmeister et al.*,1996]. *Lilly and Lester* [1974] used velocity and temperature data from a sequence of vertically separated horizontal aircraft flight paths to develop a two-dimensional picture of the velocity and temperature fields. *Gage and Nastrom* [1986] analyzed a substantial lower stratosphere data set from the Global Atmospheric Sampling Program (GASP). Most recently, *Bacmeister et al.* [1996] carried out an extensive statistical study of power spectra from data acquired by the National Aeronautical and Space Administration (NASA) ER-2 instrumented aircraft. The ER-2 aircraft data are also discussed in Chapter 4.

A key dynamical structure in the polar stratosphere in both hemispheres is the *polar vortex*, which isolates polar air from that of mid-latitudes. The vortex is most strongly defined in the Antarctic spring where planetary wave forcing is absent and polar air masses are effectively isolated above approximately 16 km. The implications of the polar vortex structure in ozone depletion will be discussed in the following section.

Extensive modeling and simulation studies have been carried out to investigate large-scale stratospheric processes. General Circulation Models (GCMs), along with their accompanying assimilation and prediction capabilities, provide frameworks within which to examine long-term trends in important climatic factors such as temperature, and the distributions and abundances of water vapour, methane, and ozone. Currently these GCMs are unable to resolve the scales of gravity wave motions fully, and hence the parameterization of gravity waves has been a major area of research [*Fritts and Lu*,1993; *Hines*,1997a; *Hines*,1997b]. Figure 1.2 illustrates the northern hemisphere meridional distribution of the lower stratospheric constituents potential temperature and ozone mixing ratio.

1.5 Ozone

The presence of trace amounts of ozone in the stratosphere and mesosphere is responsible for much of the heating of the Earth's atmosphere. Ozone absorbs solar ultra-violet (UV) radiation over a broad band of wavelengths [*e.g. Brasseur and Solomon,*1984]. The dual role of ozone in the determination of atmospheric temperatures and the prevention of harmful UV radiation from reaching the Earth's surface makes it one of the most important constituents of the atmosphere.

From the earliest measurements of ozone, there was evidence of latitudinal and seasonal variations in ozone concentration [reviewed by *Craig,*1950]. In particular, the measurement of relatively large ozone concentrations at high latitudes in the northern hemisphere winter [*Dobson,*1930] was not anticipated because of limited knowledge of stratospheric ozone photochemistry and dynamics at the time. The highest concentrations were expected in regions receiving the maximum input of solar radiation, *i.e.* the summer poles. These observations suggested the importance of the interaction between photochemical, radiative, and dynamical effects in the determination of ozone structure which has been the subject of modeling studies [*e.g. Lindzen and Goody,*1965; *Hartmann and Garcia,*1979; *Zhu and Holton,*1986].

Total column ozone measurements have been obtained using ground-based Dobson spectrometers since the 1930s. Umkehr methods were developed to estimate vertical ozone profiles from total column measurements [*e.g. Götz et al.,*1934]. In the last fifteen years, satellite measurements of total column ozone have provided detailed information on the global distribution of stratospheric ozone. The Stratospheric Aerosol and Gas Experiments (SAGE I and SAGE II) [*McCormick et al.,*1989; *McDermid et al.,*1990] and the Microwave Limb Sounder (MLS) instrument on UARS provided ozone measurements with a ~2-5 km height resolution [*Manney et al.,*1995a; *Manney et al.,*1995b]. The recent Polar Ozone and Aerosol Measurement (POAM II) experiment provided ozone mixing ratio measurements from 18-35 km with a height resolution of ~1 km [*Randall et al.,*1995].

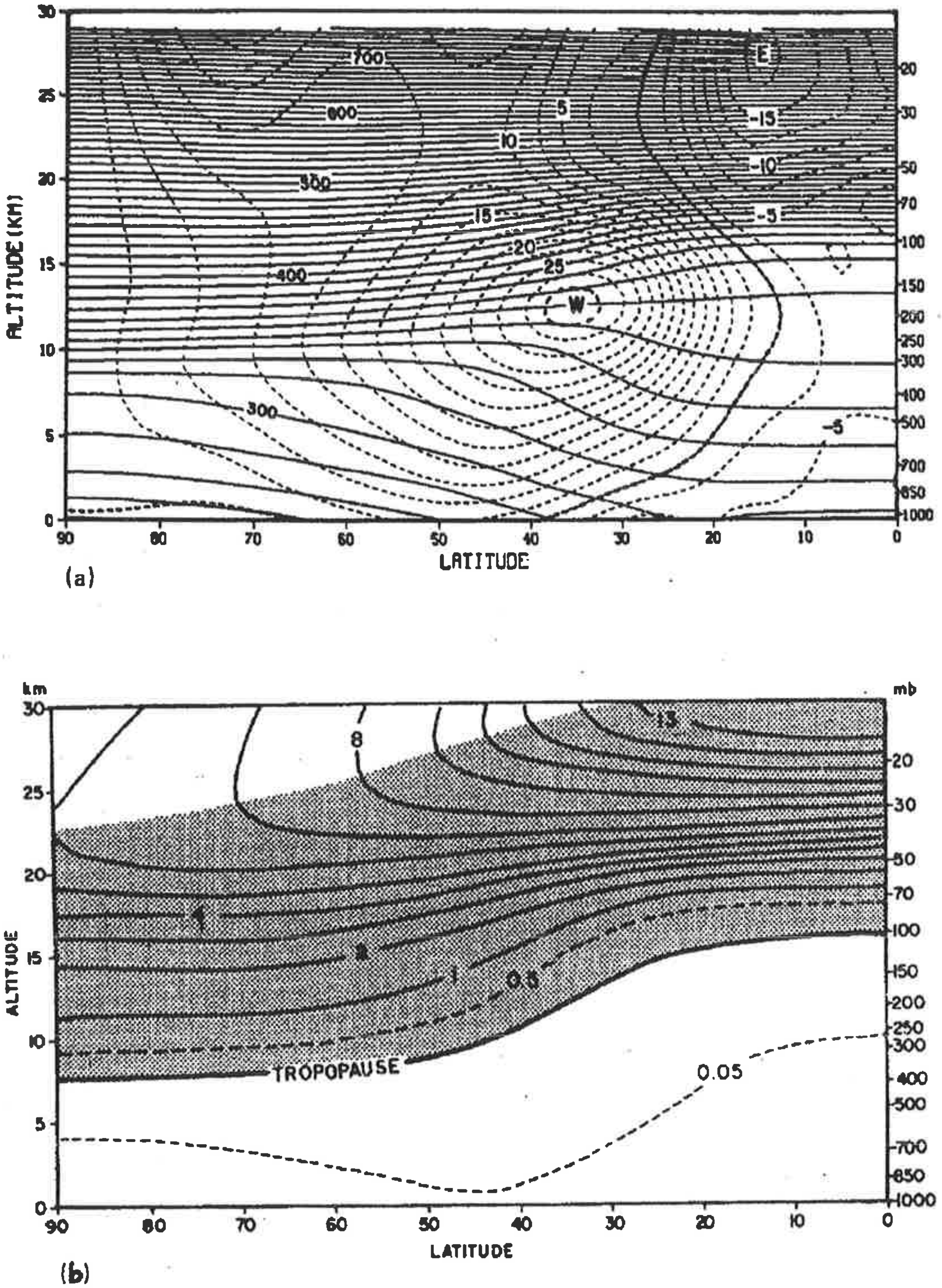

Figure 1.2: Northern hemisphere zonal–annual mean latitude–height contours for: (a) potential temperature (K) as solid line and zonal wind (m s^{-1}) as dashed line, and (b) ozone mixing ratio (10^{-5}K m^2 kg^{-1} s^{-1}) [after *Andrews et al.*, 1987].

Farman et al. [1985] reported total ozone column measurements from a Dobson spectrometer which showed a significant decrease in Antarctic spring total ozone levels. This trend has continued with levels below 100 DU recorded since 1992 [*WMO*,1994]. Since the 1970s the possible contribution of chlorofluorocarbons (CFCs) to ozone photochemical depletion has been recognized [*Molina and Rowland*,1974]. This remains an area of some concern due to the long chemical lifetimes of CFCs at stratospheric levels.

The Antarctic ozone hole develops during the local spring where four important effects combine to deplete ozone efficiently: strong solar radiation input, very low stratospheric temperatures, associated with major formation of polar stratospheric clouds (PSCs), the presence of ozone-destroying substances, and the dynamical isolation of the Antarctic from mid-latitudes due to the polar vortex. The polar vortex isolates air most efficiently above ~16 km so that transfer of air masses between polar and mid-latitudes occurs primarily below 16 km.

Arctic ozone depletion has been identified, particularly since 1995 [*e.g. Donovan et al.*,1995]. The higher temperatures in the Arctic stratosphere are a major contributing factor in the less catastrophic ozone loss that has been observed to-date compared with the Antarctic. The importance of dynamical processes in the maintenance or destruction of the vortex cannot be overestimated in the study of ozone depletion phenomena. For example, studies have identified the quasi-biennial oscillation (QBO) phases of horizontal velocities modulating ozone [*Garcia and Solomon*,1987; *Hess and O'Sullivan*,1995]. Also, the break-up of the Antarctic polar vortex in spring, driven by Rossby wave breaking, leads to the production of filaments of ozone-depleted polar air which are transported away from polar regions toward mid-latitudes [*e.g. Leovy et al.*,1983]. These filaments are believed to be responsible for significant mid-latitude ozone variations and are discussed further in Section 1.5.2 and in Chapters 4-6.

Ozone loss is not restricted to polar regions. Evidence from ozonesondes and satellite sources shows depletion in total ozone measurements at mid-latitudes (30°-60°) in both hemispheres [*WMO*,1994]. The height region where maximum depletion occurs is the lower stratosphere (~12-20 km) [*e.g. Hofmann et al.*,1995]. A role for sulfate aerosols in ozone depletion has been suggested at mid-latitudes, since depletion was not restricted to periods of polar vortex breakdown [*WMO*,1994]. However, the quantification of this issue requires detailed study of the dynamics and transport of ozone. A study of this sort is commenced in Chapter 6.

The influence of equatorially trapped Kelvin waves on stratospheric ozone distribution was investigated using Limb Infrared Monitor of the Stratosphere (LIMS) satellite data [*e.g. Randel*,1990] and Total Ozone Mapping Spectrometer (TOMS) data [*Ziemke and Stanford*,1994]. The tropopause region, particularly in the tropics, has been the subject of extensive recent study of the processes involved in so-called *stratosphere-troposphere exchange*. *Sun and Leovy* [1990] investigated equatorial ozone variability in the upper stratosphere and found modulations due to the *stratospheric semi-annual oscillation* (SSAO) of winds and temperatures.

Total ozone abundances have been the subject of large-scale modeling studies aimed at estimating and predicting long-term ozone variability. Such numerical modeling, commonly in two dimensions, has underestimated the observed downward trends in ozone column abundances by a factor of 1.3-3.0 [*WMO*,1994]. Recent inclusion of parameterization of aerosol input from volcanic eruptions has brought models and observations into closer agreement [*Tie and Brasseur*,1995]. The complexity of mesoscale ozone variability indicated by higher resolution measurements (such as ozonesondes) remains unresolved and unparameterized in large-scale transport models and is one of many possible causes of the continuing disagreement between observational and modeling studies in this area.

The ozone measurement techniques discussed in this section resolve different scales of ozone variability in different configurations, and it is challenging to interpret such measurements and to develop a coherent multi-scale theory which encompasses the observations. A common theme of the analyses carried out in Chapters 4 and 5 of this thesis is the optimal use of available measurement techniques to provide a more detailed and useful description of the ozone distribution. The following two sections provide an introduction to aspects relevant to Chapters 4-6. Figure 1.3 displays a model assimilated mean ozone concentration profile.

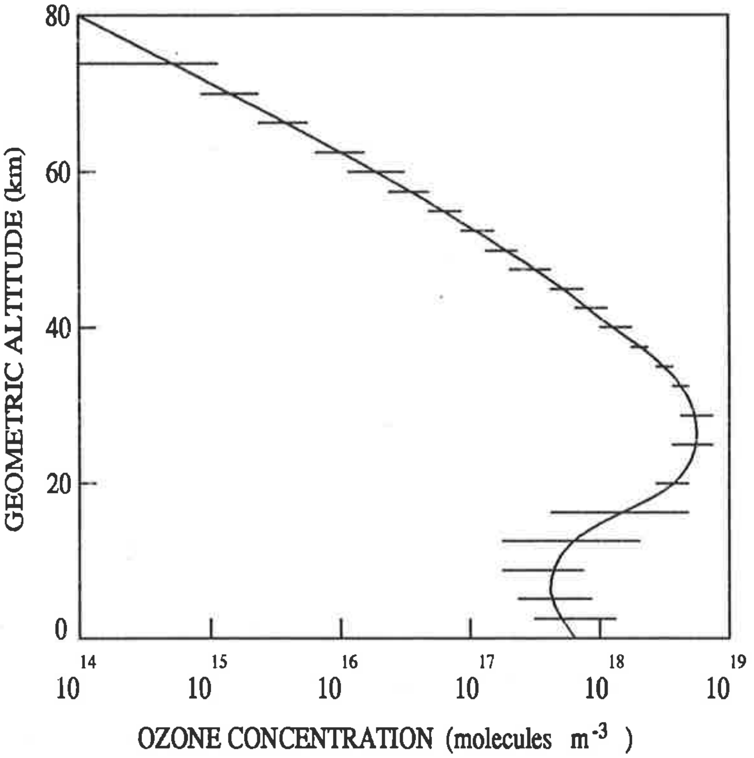

Figure 1.3: Schematic diagram of mid-latitude *U.S. Standard Atmosphere* 1976 ozone concentration profile with horizontal bars indicating the approximate observed standard deviation [after *Andrews et al.*, 1987].

1.5.1 Ozone photochemistry and absorption of radiation

The photochemical processes responsible for the basic structure of the stratospheric ozone layer were put forward by *Chapman* [1930] and are known as the *Chapman mechanism*, and the general vertical distribution of ozone or other constituents which results from these reactions is known as a *Chapman layer.*

The Chapman mechanism consists of four basic ozone photochemical equations [*Wayne*,1988].

$$\mathrm{O_2} + h\nu_2 \rightarrow 2\mathrm{O} \quad (Q_2) \tag{1.1}$$

for $\lambda < 242.4$ nm

$$\mathrm{O_3} + h\nu_3 \rightarrow \mathrm{O} + \mathrm{O_2} \quad (Q_3) \tag{1.2}$$

for $\lambda < 1180$ nm

$$\mathrm{O_2} + \mathrm{O} + \mathrm{M} \rightarrow \mathrm{O_3} + \mathrm{M} \quad (k_{12}) \tag{1.3}$$

$$O_3 + O \rightarrow 2O_2 \quad (k_{13}) \tag{1.4}$$

Here $h\nu$ represents a quantum of energy absorbed, k_{12} and k_{13} are the chemical reaction rate coefficients, and Q_2 and Q_3 represent the number of quanta of incident radiation absorbed by O_2 and O_3 per unit volume and per unit time. Atomic oxygen in the stratosphere can be considered to be in chemical equilibrium [*Brasseur and Solomon*,1984]. Hence, the net rate of production or destruction of ozone (r_3), considering only the above oxygen chemistry, is

$$r_3 = k_{12} n_1 n_2 n_m - k_{13} n_1 n_3 - Q_3, \tag{1.5}$$

where the n_i represent the number densities of the oxygen species present.

Blake and Lindzen [1973] considered a very detailed set of ozone-related chemical equations. Of primary importance is the modification to the rate coefficients k_{12} and k_{13} due to HO_x, NO_x and ClO_x. The basic form of this set of reactions is given by *Wayne* [1988], where X represents one of H, N and Cl.

$$X + O_3 \rightarrow XO + O_2 \tag{1.6}$$

$$XO + O \rightarrow X + O_2 \tag{1.7}$$

This pair of reactions is equivalent to reaction (1.4) in the Chapman mechanism and will clearly have an important effect on the rate of ozone destruction. The net action of H, N and Cl in the above equations is one of catalytic destruction of ozone. The *National Research Council (U.S.)* [1982] indicates a value of about 10000 for the chain length indicating number of times H, N and Cl act as catalysts for the reactions. These chemical reactions indicate that the presence of increased amounts of H, N and Cl in the atmosphere accelerates the rate of ozone depletion.

Also, it has been necessary to consider the chemistry of the ozone destruction more carefully given recent information relating to PSCs. The ozone destruction rate is much increased as the temperature falls below a threshold value for PSC formation, where ozone destroying chemical species are present. The clouds have been classified according to their chemical composition as type I (consisting primarily of nitric acid trihydrate) and type II (consisting of mainly water ice). PSCs have extremely important implications for the processes involved in ozone destruction, since the surfaces of the clouds provide sites on which ozone-destroying heterogeneous gas-phase chemical reactions occur at an accelerated rate. The formation locations and persistence of the clouds are both heavily influenced by the localized effects of gravity wave fluctuations in temperature through the temperature dependence of ice-crystal formation [*Meilinger et al.*,1995; *Murphy and Gary*,1995; *Bacmeister and Eckermann*,1997].

1.5.2 Ozone laminae and large-scale structure

Ozone laminae are large positive or negative ozone values that are confined to narrow, vertically localized layers, and are most commonly observed at mid-latitude and polar locations. The laminae have been ascribed to the dynamical *filamentation* of the ozone distribution by large-scale advection, and so are often referred to as *filaments*. The earliest study of ozone laminae by *Dobson* [1973] addressed some qualitative features of vertical ozone profiles.

A more recent series of studies, mainly based on northern hemisphere data sets, has made use of extensive databases of height-resolved ground-based ozone measurements including ozonesondes and ozone lidar to investigate more fully the occurrence of laminar features [*Reid and Vaughan*,1991; *Reid et al.*,1993]. *Reid et al.* [1993] found laminae occurred most commonly in the lower stratosphere in the height range 12-18 km, with 14 km the height at which laminae most frequently occur, almost independent of latitude. The strongest and most prevalent laminae were observed at polar locations.

The dominant process of lamina formation is believed to be the breakdown of the polar vortex (discussed in Section 1.4). Rossby wave effects act to perturb the large-scale structure of the vortex and to disrupt the so-called *vortex wall* [*Leovy et al.*,1983; *Norton*,1994]. This results in a region in the vicinity of the vortex wall known as the surf zone, where meridional mixing of ozone-rich and ozone-poor air masses can occur [*e.g. Tuck*,1989]. The probable effect of meridional transport on total ozone column amounts at mid-latitudes has yet to be fully studied. However, ozone-depleted air originating in the polar vortex has been identified at mid-latitude locations and there is evidence of depletion of ozone column amounts at mid-latitudes [*WMO*,1994].

Complex structures of atmospheric constituents and temperature have been examined using ER-2 aircraft data [*e.g. Tuck*,1989] and satellite observations [*e.g. Manney et al.*,1995b]. Large-scale transport modeling techniques, such as contour advection with surgery (CAS) [*Waugh and Plumb*,1994] and contour dynamics with surgery (CDS) [*Norton*,1994], have been used extensively to chart the evolution of material in and around the polar vortex. Such observations and modeling have provided evidence that tongues or filaments of ozone-rich air may be conservatively transported over large distances. The process of differential transport results in horizontal elongation of the air masses. It is these features of estimated large horizontal extent (~100 km) but very narrow (~1-2 km) vertical extent, with ozone concentrations typically 2-5 times background values, which are observed in vertical profile measurements by ozonesondes and lidar [*e.g. Reid et al.*,1993; *Orsolini et al.*,1995]. Transport modeling techniques are applied in Chapter 6 to investigate the mesoscale structure of stratospheric ozone.

1.6 Thesis Overview

Having introduced the major topics to be developed further in the course of the thesis, it is appropriate to provide an overview of the structure of the material. The thesis can be viewed as consisting of three major segments: a presentation of the major theoretical concepts [Chapter 2], a mesospheric gravity wave simulation and comparison of observational techniques [Chapter 3], and an extensive observational and modeling study of gravity wave effects on the stratospheric ozone distribution at Macquarie Island, Australia, and at the Observatoire de Haute Provence, France [Chapters 4-6]. Alternatively, the thesis can be approached as chapters addressing primarily theory and modeling [Chapters 2, 3, and 6] and those focussing on observations and data analysis [Chapters 4 and 5].

Chapter 2

Theory

This chapter provides a theoretical basis of gravity wave study for the thesis as a whole. A general set of equations is developed first and gravity wave characteristics are discussed. Specific results used in later applications are introduced and reference is made to their continuation in subsequent chapters.

Section 2.1 introduces the Navier–Stokes equations, describing the fundamental fluid dynamics of the Earth's atmosphere. *Tracer transport* — the study of atmospheric constituents which can be used to trace the movement of air parcels — is then discussed in Section 2.2.

These equations are solved in Section 2.3 using an approach which separates the *mean flow* processes from the *wave* or *perturbation* processes. In this way the mesoscale structure of the atmosphere can be isolated and studied separately from the large-scale dynamical processes. This mean–perturbation approach is fundamental to the extraction of gravity wave information and spectral parameters from observations.

Section 2.4 discusses the properties and characteristics of atmospheric gravity waves and develops key concepts which are vital in analyzing observations in terms of gravity waves, specifically monochromatic waves. Section 2.5 moves away from a purely monochromatic perspective on gravity wave motions to describe theories behind the observed spectrum of gravity waves. A spectral approach to gravity wave theory is important since the majority of observations of gravity wave activity suggest the presence of a broad range of wave scales, and the parameterization of gravity waves in order to incorporate their effects in large-scale models must reflect the complexity of the observed wave spectrum.

2.1 The Navier–Stokes Equations

The three fundamental conservation laws of mass, energy, and momentum are first introduced in a fluid dynamics context leading into a general formulation of the Navier–Stokes equations. The equations are developed for a non-hydrostatic, compressible, and temperature-varying atmosphere in order to obtain their solutions in a general form. These equations are fundamental to any atmospheric wave study.

It is often appropriate to simplify the Navier–Stokes equations by applying assumptions or approximations relevant for specific atmospheric regions or scales. Some examples of these simplifications, such as incompressibility and hydrostatic balance, are discussed in the following sections.

2.1.1 Conservation of mass and the continuity equation

The total mass of the atmosphere is a conserved quantity. For a given air parcel defining a region of the atmosphere which is stationary relative to a ground-based observer, the flux of mass m_a into or out of the parcel must be equal to the mass transport by total wind motions $\mathbf{U} = (\mathbf{u}, \mathbf{v}, \mathbf{w})$.

$$\frac{\partial m_a}{\partial t} = -\mathbf{U} \cdot \nabla m_a \tag{2.1}$$

Here ∂ denotes a derivative evaluated relative to the ground-based frame of reference, $\nabla = (\frac{\partial}{\partial x}, \frac{\partial}{\partial y}, \frac{\partial}{\partial z})$ is the gradient operator and x, y, and z are the zonal (east–west), meridional (north–south), and vertical directions.

The fundamental expression of the conservation of mass is conveniently applied to atmospheric dynamical variables by expressing (2.1) in terms of atmospheric density ρ, so that for a parcel of constant volume,

$$\frac{\partial \rho}{\partial t} + \rho \nabla \cdot \mathbf{U} + \mathbf{U} \cdot \nabla \rho = 0. \tag{2.2}$$

This equation is known as the ***continuity equation*** for a ground-based frame of reference. A ground-based reference frame will be used extensively in this thesis when examining lidar and sonde[1] data in Chapters 4 and 5.

The Lagrangian frame of reference, following the motion of a parcel of air, is well suited to visualization and description of atmospheric transport and leads naturally into the concept of parcel displacement which will be fully developed in Chapter 6. To express the continuity equation in terms of the Lagrangian frame, it is necessary to transform the ground-based derivative $\frac{\partial}{\partial t}$ into the so-called Lagrangian derivative $\frac{d}{dt}$ through

$$\frac{\partial}{\partial t} = \frac{d}{dt} + \mathbf{U} \cdot \nabla. \tag{2.3}$$

The continuity equation in a Lagrangian frame of reference is then

$$\frac{1}{\rho}\frac{d\rho}{dt} + \nabla \cdot \mathbf{U} = 0. \tag{2.4}$$

The concept of conservation of mass as applied to the atmosphere will be developed explicitly in Section 2.2 for atmospheric minor constituents.

2.1.1.1 Incompressible atmosphere

The approximation of an incompressible atmosphere neglecting density variation is relevant where gravity wave solutions, rather than acoustic or compressibility wave solutions, are sought. From the continuity equation (2.4) it is clear that an incompressible atmosphere results in a zero wind divergence wave field. For an incompressible atmosphere the continuity equation is then simply [*e.g. Holton,*1979]

$$\nabla \cdot \mathbf{U} = 0. \tag{2.5}$$

The assumption of an incompressible atmosphere is very widely applied in gravity wave studies where vertical displacements are sufficiently small that incompressibility is a relevant approximation. This chapter formulates and solves the Navier–Stokes equations without the assumption of an incompressible atmosphere.

---

[1] The analysis techniques typically applied to sonde data (*e.g.* hodograph analysis and Stokes parameter analysis) assume a profile as a function of height only.

2.1.2 Energy balance and the heat equation

The first law of thermodynamics states that for a system, here applied to an air parcel [*Gossard and Hooke*,1975],

$$\Delta E = \Delta H - \Delta W. \tag{2.6}$$

The (infinitessimal) change in internal energy of the parcel (ΔE) is related to its temperature, and the work done on or done by the parcel (ΔW) is determined by pressure and/or volume changes occurring in the parcel. The form of the heat term (ΔH) depends on properties of the parcel's motion.

For atmospheric thermodynamical processes it is usual to make use of the heat equation [*Sears and Salinger*,1975]

$$\Delta H = c_P \Delta T - \frac{V}{m_a}\Delta p, \tag{2.7}$$

where $\frac{V}{m_a}$ is the specific volume of the parcel, T is the temperature, and p is the pressure. Then using the *ideal gas law*

$$p = \rho R T, \tag{2.8}$$

where R is the ideal gas constant, (2.7) gives

$$\Delta H = c_P \Delta T - \frac{RT}{p}\Delta p. \tag{2.9}$$

From this general form of the heat equation two specific cases can be considered which are relevant for different timescales of atmospheric motions: *isothermal* and *adiabatic transport* of air parcels ($\Delta T = 0$ and $\Delta H = 0$, respectively).

2.1.2.1 Isothermal heat equation

A parcel moving sufficiently slowly, *e.g.* undergoing planetary-scale wave motions, can be considered to be transported *isothermally* or as if in contact with a background heat reservoir. For these large-scale motions it is then relevant to use the *isothermal heat equation* [*Lindzen and Goody*,1965; *Gossard and Hooke*,1975].

$$\frac{1}{\rho}\frac{\partial \rho}{\partial z} = \frac{1}{p}\frac{\partial p}{\partial z} \tag{2.10}$$

2.1.2.2 Adiabatic heat equation

For motions with dynamical timescales short relative to radiative transfer and thermal conduction timescales, *e.g.* gravity wave motions, a parcel is transported from its equilibrium position with insufficient time to adjust to background temperature and must be considered to be transported adiabatically [*Hines*,1960; *Zhu and Holton*,1986]. In this case the heat term is zero (ΔH=0), so that [*Gossard and Hooke*,1975]

$$\Delta E = -\Delta W. \tag{2.11}$$

Expressing the internal energy and work done in terms of atmospheric variables yields

$$c_V \frac{\Delta p}{p} = c_P \frac{\Delta \rho}{\rho}, \tag{2.12}$$

or

$$\frac{\partial p}{\partial z} = \frac{1}{c_S^2}\frac{\partial \rho}{\partial z}. \tag{2.13}$$

This defines the *adiabatic heat equation* relevant for gravity wave motions.

By making use of the ideal gas equation (2.8) and neglecting terms proportional to c_S^{-2}, it is then possible to relate temperature and density variations through

$$\rho \frac{\partial T}{\partial z} = -T \frac{\partial \rho}{\partial z}. \tag{2.14}$$

The above direct relation between density and temperature variations leads to a simplification of the Navier–Stokes equations which is applied later in (2.39).

2.1.3 Conservation of momentum and the momentum equations

The conservation of momentum as applied to the Earth's atmosphere can be expressed as a balance between a rotational or Coriolis term, a pressure gradient term, a gravitational term and a frictional term [*e.g. Holton,*1979]. In terms of 3-D vectors representing the zonal, meridional, and vertical directions,

$$\frac{d\mathbf{U}}{dt} - 2\mathbf{\Omega} \times \mathbf{U} + \frac{1}{\rho}\nabla\mathbf{p} + \mathbf{g} + \frac{\mathbf{F}}{m_a} = 0, \tag{2.15}$$

where $\mathbf{\Omega}$ is the angular velocity vector of the Earth, $\nabla\mathbf{p} = (\frac{\partial p}{\partial x}, \frac{\partial p}{\partial y}, \frac{\partial p}{\partial z})$ is the pressure gradient, and $\mathbf{g} = (0, 0, -g)$ is the gravitational acceleration.[2] $\mathbf{F} = (F_x, F_y, F_z)$ is a total drag term which may be used to parameterize atmospheric processes such as friction, diffusion, and ion drag.

Simplifying (2.15), separating the zonal, meridional, and the vertical components of the motion, and neglecting drag terms gives the three momentum equations:

Zonal momentum equation

$$\frac{du}{dt} - fv + \frac{1}{\rho}\frac{\partial p}{\partial x} = 0, \tag{2.16}$$

Meridional momentum equation

$$\frac{dv}{dt} + fu + \frac{1}{\rho}\frac{\partial p}{\partial y} = 0, \tag{2.17}$$

Vertical momentum equation

$$\frac{dw}{dt} + g + \frac{1}{\rho}\frac{\partial p}{\partial z} = 0. \tag{2.18}$$

Here, f is the *Coriolis parameter*, also known as *inertial frequency*, defined as

$$f = \frac{2\pi}{12\ \mathrm{hr}}\sin(\phi), \tag{2.19}$$

where ϕ is the latitude.

---

[2] Gravitational acceleration is a weakly varying function of height.

2.1.3.1 Hydrostatic approximation

In applications where vertical motions are negligible ($\frac{dw}{dt} \approx 0$) it is valid to apply the *hydrostatic approximation* in (2.18), which yields

$$\frac{\partial p}{\partial z} = -\rho g. \tag{2.20}$$

Equation (2.20) is known as the ***hydrostatic equation*** and describes a balance between pressure gradient and gravitational terms in the vertical momentum equation. This is a common approximation applied in general large-scale flow problems in fluid mechanics. The hydrostatic approximation is also widely used in large-scale modeling of the atmosphere.

2.1.3.2 Zonal mean motion

Although the magnitude of the zonal winds driving the large-scale structure of the Earth's atmosphere makes these winds a vital component of the circulation, they often exhibit a largely uniform structure around a latitude circle. The differential effect of the Earth's rotation and solar radiation between the tropics and the poles leads to particular interest in latitudinal or meridional variation of wind velocities, temperatures, and — most importantly for this work — the constituent ozone. For some applications, such as the mesoscale Lagrangian model developed in Chapter 6, it is convenient to make use of zonal mean motions in order to focus on meridional structure.

2.2 Tracer Transport

The continuity equation (2.4) refers to the mass of a parcel of air as a whole, including all atmospheric constituents present. For a trace constituent transported by dynamical processes, as will be a primary area of interest in this thesis, a *tracer continuity equation* can be developed. The case of *conservative* or *quasi-conservative* tracers, which are subject to purely dynamical processes, will be addressed first.

Table 2.1: Summary of quantities used to express measurements of trace constituents after *Andrews et al.* [1987]. The subscripts i and a denote tracer and atmosphere, respectively.

Quantity	Calculation	Symbol	Unit
Concentration or Number density	molecules/volume	n	molecules cm^{-3}
Partial pressure	pq	pp	dimensionless
Volume mixing ratio	n/n_a	q	ppmv
Mass mixing ratio	$q(M_i/M_a)$	q^*	ppmm, kg kg^{-1}

2.2.1 Conservative or quasi-conservative tracers

By analogy with the atmospheric continuity equation (2.4), a tracer continuity equation is introduced here which is valid for conservative or quasi-conservative[3] tracers. Examples of quasi-conservative tracers of interest in atmospheric science include ozone in the lower stratosphere, neutral sodium in the mesosphere, chlorofluorocarbons, and long-lived radioisotopes from nuclear testing.

For such quasi-conservative tracers the mixing ratio q is conserved during Lagrangian transport [*Lindzen and Goody*,1965; *Waugh and Plumb*,1994]. Table 2.1 describes the various representations of tracer content in the atmosphere. In this thesis q denotes *volume mixing ratio*[4] throughout, as obtained from ozonesonde measurements.

The conservation of constituent mixing ratio in the Lagrangian frame can be expressed as [*Andrews et al.*,1987]

$$\frac{dq}{dt} = 0. \tag{2.21}$$

This result can be adapted for an Eulerian frame through (2.3) giving

$$\frac{\partial q}{\partial t} + \mathbf{U} \cdot \nabla q = 0. \tag{2.22}$$

The second term can be expanded to give

$$\frac{\partial q}{\partial t} + u\frac{\partial q}{\partial x} + v\frac{\partial q}{\partial y} + w\frac{\partial q}{\partial z} = 0. \tag{2.23}$$

---

[3] Tracers which have long chemical or diffusive lifetimes relative to dynamical timescales in a given region of the atmosphere [*e.g. Andrews et al.*,1987].

[4] The volume of tracer per unit volume of atmosphere, which is often expressed in parts per million by volume (ppmv).

The importance of the horizontal and vertical structure of the tracer in determining the tracer variability is already clear in (2.23). For mesospheric neutral sodium, investigated in Chapter 3, the horizontal tracer gradients $\frac{\partial q}{\partial x}$ and $\frac{\partial q}{\partial y}$ are assumed negligible, so that transport of sodium is modeled as a vertical advection process through

$$\frac{\partial q}{\partial t} + w\frac{\partial q}{\partial z} = 0. \tag{2.24}$$

For stratospheric ozone [Chapters 4-6], strong meridional variations have been observed, particularly in polar regions, so that the above simplification is not automatically justified. However, there is no measurement technique currently able to observe simultaneously the horizontal and vertical ozone structure at a sufficiently high resolution to characterize each of the terms in (2.23). Hence it is often assumed that horizontal transport is negligible in the analysis of purely vertically resolved data [e.g. *Teitelbaum et al.*,1994]. The structure in both the horizontal and vertical ozone field leads to a more complex problem in understanding ozone transport and will be the theme of Chapter 4.

Measurements such as mesospheric neutral sodium profiles [Chapter 3] and lidar ozone profiles [Chapter 5] are available only in terms of number density or concentration rather than mixing ratio. Table 2.1 presents the major measures of constituent composition. The number density n of a constituent is related to the volume mixing ratio through

$$n = q\rho\frac{N_A}{M_a}, \tag{2.25}$$

where N_A is the number of molecules of substance per mole[5] and M_a is the molecular mass of the atmosphere. Number density is not conserved during Lagrangian transport. The tracer continuity equation in number density terms is [*e.g. Chiu and Ching*,1978]

$$\frac{\partial n}{\partial t} + \nabla \cdot n\ \mathbf{U} = 0. \tag{2.26}$$

---

[5] Avogadro's number, N_A=6.022×10^{26}.

This equation is the starting point for the analysis of *Chiu and Ching* [1978] and *Gardner and Shelton* [1985] as discussed in Chapters 3 and 6 and Appendix A.

A conservative tracer on a large scale (*e.g.* global scale modeling and interpretation of satellite measurements) is often investigated in terms of a Lagrangian modeling scheme [*e.g.* *Waugh and Plumb*,1994; *Norton*,1994]. These techniques initialize a grid of large-scale time-resolved mean winds and potential temperatures, either directly from observations or through an assimilation of satellite and/or ground-based measurements, and a tracer distribution. Tracer parcels are defined, typically with dimensions of the order of the satellite measurement resolution (*e.g.* 2° latitude by 5° longitude [*Manney et al.*,1995a]), and are then transported by the mean winds. The distribution of the advected parcels is often presented in terms of tracer distribution on potential temperature surfaces.

The process of Lagrangian parcel advection, making use of the conservation of mixing ratio and potential temperature is useful in generalized transport studies on a variety of different scales. In Chapter 6 the concept of direct Lagrangian transport is developed in a mesoscale context.

2.2.2 Non-conservative tracers

A non-conservative tracer is subject to radiative or photochemical processes, or to latent heat release, in addition to the dynamical processes implied by (2.21). Examples of non-conservative tracers include ozone in the upper stratosphere (above $\sim$25 km) and the mesosphere, and water vapour in the troposphere.

In regions where a constituent is not conserved, either diffusion or chemical reactions are occurring, and hence changing the local mixing ratio. It is important to determine the relative timescales of any dynamical, chemical, and diffusive processes acting in order to determine whether the tracer can be treated as conservative. The following segments discuss diffusive and chemical processes and their role in tracer variation, in addition to the advective dynamical processes already discussed.

2.2.2.1 Diffusive processes

A diffusion process is implicated where there are localized sources or sinks of a constituent. Relevant examples are pollutants and volcanic aerosols released in the troposphere and meteor ablation in the mesosphere. Diffusion results in a net change in mixing ratio over both space and time, as opposed to the wave-like or advective transport where a parcel of air retains its local mixing ratio.

The signature of a diffusive process is a time rate in change of constituent content proportional to a spatial rate of change. Hence the action of a diffusive process is typically parameterized in terms of a diffusion coefficient, discussed in Appendix A, and for a two- or three-dimensional process in terms of a *diffusion tensor* [*Andrews et al.*,1987]. The parameterization of gravity wave effects in terms of Rayleigh friction is an example of approximating a physically advective process as a simpler diffusion process.

In summary, diffusive transport of constituents describes a very important set of atmospheric processes which act to change the local parcel mixing ratio. Different physical processes, such as eddies, turbulence, and breaking waves may be described using similar diffusion-type terms. These processes are microscale motions and are not discussed in detail in this thesis. Hence in focussing on the mesoscale features of the atmosphere, the diffusive effects are sub-gridscale, resulting in an implied parameterization of these microscale motions.

2.2.2.2 Chemical and photochemical processes

Chemical or photochemical reactions drive important sources and sinks for many atmospheric constituents such as ozone, water vapour, nitrous oxide, neutral sodium and CFCs. Of primary interest in this work are neutral sodium and stratospheric ozone. To characterize the effect of chemistry-related terms, other important variables are implicated, such as atmospheric temperature and solar radiation.

It is possible to consider height regions where ozone acts as a purely dynamical, conservative tracer (below ~25 km), a transition region where both dynamical and photochemical effects determine ozone variations (25-35 km), and a predominantly photochemically driven region at upper heights. So far in this chapter predictions have been developed which are based on dynamics only, without photochemical terms. In the upper stratosphere, where both photochemical and dynamical effects are important, ozone perturbations are dependent not only on transport but also the radiative heating structure of the atmosphere and the complex feedback between ozone and temperature [*e.g. Zhu and Holton*,1986].

The inclusion of ozone photochemical terms in the Navier–Stokes equations was undertaken by *Lindzen and Goody* [1965] to examine planetary wave effects, and more recently by *Zhu and Holton* [1986] to investigate the photochemical damping of inertia-gravity waves and by *Randel* [1990] to investigate the ozone response to Kelvin waves. The photochemistry of ozone is parameterized in terms of two coefficients representing the destruction of ozone by photochemical processes and the temperature dependence of the reaction rates. Below ~25 km, ozone and temperature are in phase or anti-phase, as predicted by a dynamics-only model [Chapter 4]. Above 25 km the phase between ozone and temperature perturbations increases as a result of the interaction of photochemistry and dynamics, such that they are in quadrature at about 30 km [*Randel*,1990]. The work presented in Chapters 4-6 concentrates on the dynamically controlled region of the stratospheric ozone layer below ~25 km.

2.3 A Wave Solution

To solve the differential equations (2.4), (2.13), (2.16), (2.17), (2.18), and (2.21) describing the relationships between the atmospheric state variables, we first examine the form of the equations. It is clear that the momentum equations are of the form

$$\frac{df_1}{dt} \propto \frac{df_2}{d\mathbf{r}}. \tag{2.27}$$

This differential equation is of the form of a wave equation and hence a wave solution is sought, but the exact form of the solution is not prescribed. The form of solution used here follows most closely the development presented in *Walterscheid and Hocking* [1991].[6]

---

[6] Other common choices are *Gossard and Hooke* [1975] and *Holton* [1979].

The state variables $S(x, y, z, t)$ are represented as the sum of a mean, time invariant, component $\bar{S}(x, y, z)$ which exactly satisfies the Navier–Stokes equations, and a wave-induced, time-varying perturbation $S'(x, y, z, t)$. For each state variable a mean–perturbation solution is assumed.

$$S(x, y, z, t) = \bar{S}(x, y, z) + S'(x, y, z, t) \tag{2.28}$$

The form of wave solution chosen here is

$$S'(x, y, z, t) = S_0 \exp(\frac{z}{2H_\rho}) \exp[i(kx + ly + mz - \hat{\omega}t)], \tag{2.29}$$

where k, l, and m are the zonal, meridional, and vertical wavenumbers, respectively, and $\hat{\omega}$ is the intrinsic wave frequency. An exponential growth of gravity wave amplitudes with height in (2.29) is implicated by the exponential decrease of atmospheric density with height

$$\rho(z) = \rho_0 \exp(-\frac{z}{H_\rho}). \tag{2.30}$$

(2.30) defines the atmospheric *density scale height* H_ρ.

The temporal and spatial derivatives can then be evaluated using (2.29) as

$$\frac{dS'}{dt} = -i\hat{\omega}S', \tag{2.31}$$

$$\frac{\partial S'}{\partial x} = ikS', \tag{2.32}$$

$$\frac{\partial S'}{\partial y} = ilS', \tag{2.33}$$

$$\frac{\partial S'}{\partial z} = i(m - \frac{i}{2H_\rho})S'. \tag{2.34}$$

There are two major considerations in the solution of the Navier–Stokes equations; the scales of motion that are to be studied, which determine any approximations to be applied and the wave solution chosen, and the initial conditions of the system. In the simplest approach, initial conditions of mean state variables are chosen such that they satisfy the Navier–Stokes equations exactly, and hence initial wave perturbations are zero.

The Navier–Stokes equations with frictional terms included are non-linear since the frictional terms depend on wind velocities also. By setting the frictional terms to zero, the form of the Navier–Stokes equations is simplified and it is possible to use the expression (2.29) in the Navier–Stokes equations. In the notation of *Marks and Eckermann* [1995][7] where $(\hat{u}, \hat{v}, \hat{w}) = \frac{1}{\sqrt{\rho_0}}(u', v', w')$ and $(\hat{p}, \hat{\rho}, \hat{q}) = \sqrt{\rho_0}(p', \rho', q')$, the expressions (2.16), (2.17), (2.18), (2.4), (2.13), and (2.21) become,

$$-i\hat{\omega}\hat{u} - f\hat{v} + ik\hat{p} = 0, \tag{2.35}$$

$$-i\hat{\omega}\hat{v} + f\hat{u} + il\hat{p} = 0, \tag{2.36}$$

$$-i\hat{\omega}\hat{w} + g\hat{\rho} + i(m - \frac{i}{2H_\rho})\hat{p} = 0, \tag{2.37}$$

$$ik\hat{u} + il\hat{v} - i\hat{\omega}\hat{\rho} + i(m - \frac{i}{2H_\rho})\hat{w} = 0, \tag{2.38}$$

$$i\hat{\omega}\hat{\rho} + \hat{w}\frac{N^2}{g} = 0, \tag{2.39}$$

$$-i\hat{\omega}\hat{q} + \hat{w}\bar{q}_z = 0. \tag{2.40}$$

(2.39) introduces the *Brunt–Väisälä frequency* N, also known as the *static stability*, defined as

$$N^2 = \frac{g}{\bar{\theta}}\frac{\partial\bar{\theta}}{\partial z} = \frac{g}{\bar{T}}\left(\frac{\partial\bar{T}}{\partial z} + \frac{g}{c_P}\right), \tag{2.41}$$

where θ is the *potential temperature* defined as

$$\theta = T\left(\frac{p_0}{p}\right)^{\frac{R}{c_P}}. \tag{2.42}$$

(2.35)-(2.39) describe gravity wave perturbations in a rotating, non-hydrostatic, and compressible atmospheric flow. (2.40) describes the gravity wave response of a horizontally stratified tracer.

---

[7] These equations are very similar to *Walterscheid and Hocking* [1991] (36)-(40).

2.4 Linear Gravity Wave Characteristics

In this section, important characteristics and properties of gravity waves will be developed, as well as features which are useful in the identification and analysis of gravity wave signatures in observational data. The so-called *dispersion relation* which describes the relationship between the horizontal and vertical scales and the temporal scale of the gravity wave perturbation, and the *polarization relations*, relating fluctuations between the background atmospheric density, wind velocity components, pressure, temperature, and the mixing ratios of constituents present are obtained. The linearized gravity wave equations imply wave perturbations of small amplitude. Nonlinear effects introduce non-stationarity and changes in wave shape. These issues are addressed in Chapter 6.

2.4.1 Dispersion relation and polarization relations

The gravity wave dispersion relation describes the evolution of the horizontal, vertical, and temporal scales. It is possible to define a full dispersion relation which is valid for the full range of gravity wave scales:

$$m^2 = \frac{(N^2 - \hat{\omega}^2)}{(\hat{\omega}^2 - f^2)}(k^2 + l^2) - \frac{1}{4H_\rho^2} + \frac{\hat{\omega}^2}{c_S^2}. \tag{2.43}$$

Solving the Navier–Stokes equations (2.35)-(2.40) results in the following polarization relations.

$$\hat{u} = \hat{p}\left(\frac{\hat{\omega}k + ilf}{(\hat{\omega}^2 - f^2)}\right) \tag{2.44}$$

$$\hat{v} = \hat{p}\left(\frac{\hat{\omega}l - ikf}{(\hat{\omega}^2 - f^2)}\right) \tag{2.45}$$

$$\hat{w} = \frac{-\hat{p}\hat{\omega}(m - \frac{i}{2H_\rho})}{(N^2 - \hat{\omega}^2)} \tag{2.46}$$

$$\hat{\rho} = \frac{-i\hat{p}N^2(m - \frac{i}{2H_\rho})}{g(N^2 - \hat{\omega}^2)} \tag{2.47}$$

$$\hat{q} = \frac{-i\bar{q}_z\hat{w}}{\hat{\omega}} \tag{2.48}$$

Having stated these relationships, it is most useful then to examine the physical implications of the above equations. Firstly, the right-hand side of the dispersion relation (2.43) consists of three terms. The term $\frac{1}{4H_\rho^2}$ becomes important in environments where $\hat{\omega} \rightarrow N$ and $m \rightarrow 0$, and can otherwise be neglected. Similarly the term in the dispersion relation proportional to c_S^{-2} can be neglected where low-frequency internal or inertia-gravity wave solutions are sought [*Marks and Eckermann,*1995].

2.4.2 Internal and inertia-gravity waves

The dispersion relation and polarization relations allow a number of forms of solution which define various subclasses of atmospheric waves. These subclasses of waves are distinguished by their frequencies. This work examines mainly *internal* gravity waves which can exist in the range of frequencies between the inertial frequency (2.19) and the Brunt–Väisälä frequency (2.41). Such waves are not strongly affected by forces due to the rotation of the Earth.

The term *inertia-gravity* wave refers to waves with horizontal scales large enough to be affected by the Earth's rotation. These waves have intrinsic frequencies in the range $\sim f$–$10f$ and have recently been recognized as having particularly important implications in the stratosphere [*Danielsen et al.,*1991; *Hines,*1995; *O'Sullivan and Dunkerton,*1995]. An example of an inertia-gravity wave observed in horizontal velocity data at mid-latitudes is presented in Chapter 5.

2.4.3 Energy transfer and phase progression

One of the quirks of a gravity wave is that the vertical phase velocity and the group velocity are opposite in sign. To see this, it is first noted that that the vertical phase velocity c_z is given by,

$$c_z = \frac{\hat{\omega}}{m}, \tag{2.49}$$

whereas the vertical group velocity $(c_G)_z$ of the wave is

$$(c_G)_z = \frac{\partial \hat{\omega}}{\partial m}. \tag{2.50}$$

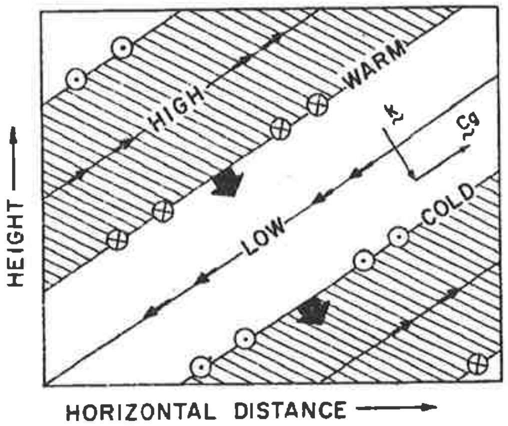

Figure 2.1: Vertical section in a plane containing the horizontal wave vector **k** showing the phase relationships between velocity and temperature fluctuations in an upward-propagating inertia-gravity wave with $m < 0$ and $\omega > 0$ in the northern hemisphere ($f > 0$). The thin sloping lines denote the surfaces of constant phase (perpendicular to the wave vector) and thick arrows show the direction of phase propagation. The wave vector and group velocity are also shown [after *Andrews et al.*, 1987].

This leads to the counter-intuitive result that the surfaces of constant phase are sloping downwards, whereas the surfaces of constant energy are sloping upwards. Hence a time-resolved vertical measurement of a gravity wave perturbation where the downward phase propagation of a peak is visible in the vertical profile, indicates that energy, related to the group velocity, is propagating or being transferred upward. Figure 2.1 shows a schematic view of gravity wave motion.

The importance of gravity waves in the vertical transport of horizontal momentum has been recognized for some time [*Vincent and Reid*,1983]. Hence the proportion of upward and downward propagating waves has been of considerable interest. *Allen and Vincent* [1995] found that a majority of evidence from a mid-latitude location indicated a predominantly upward transfer of energy and momentum throughout the troposphere and lower stratosphere.

2.5 Gravity Wave Spectral Theory

So far this chapter has developed dynamical theory describing monochromatic gravity waves. However, the concept of monochromatic gravity waves in the atmosphere is seldom justified fully by observational evidence. An atmospheric observation (*e.g.* vertical structure of horizontal winds) contains fluctuations on a range of scales, occasionally with a strong monochromatic component. This structure has been interpreted as a consequence of a superposition of gravity waves present in the atmosphere [*Eckermann and Hocking*,1989].

The concept of a superposition of waves lends itself to Fourier spectral analysis and more recently wavelet analysis which is able to isolate individual wave events [*Sato and Yamada*,1994; *Bacmeister et al.*,1996]. Extensive examination of power spectra of atmospheric observations has led to so-called "spectral theories" and "spectral models" [*e.g. Dewan and Good*,1986; *Smith et al.*,1987; *Weinstock*,1990; *Hines*,1991*b*; *Gardner*,1994; *Zhu*,1994; *Gardner*,1996*b*] which invoke different physical processes responsible for the observed spectra.

Some basic properties of the vertical wavenumber spectrum which are common to each of the spectral models are the large-wavenumber spectral slope $-q$ and the so-called characteristic wavenumber m_* which are illustrated in Figure 2.2. The modified Desaubies form of vertical wavenumber spectrum $F_a(m)$ has been suggested for atmospheric relative density, relative temperature, and horizontal velocity spectra based on observations [*e.g. Fritts and VanZandt*,1993]

$$F_a(m) = E_0 \frac{\mu^s}{1 + \mu^{(s+q)}}, \tag{2.51}$$

where E_0 is a normalization factor, $\mu = m/m_*$, and the spectral indices s and q are equal to 1 and 3, respectively, in the model.

Experimental studies of the frequency spectrum of atmospheric density variations $G_a(\omega)$ suggest that it also follows a power law decay of the form [*e.g. Fritts and VanZandt*,1993].

$$G_a(\omega) \propto \omega^{-p}, \tag{2.52}$$

where typical values of p are 1.7-2. The two-dimensional vertical wavenumber and frequency spectrum is then expressed as

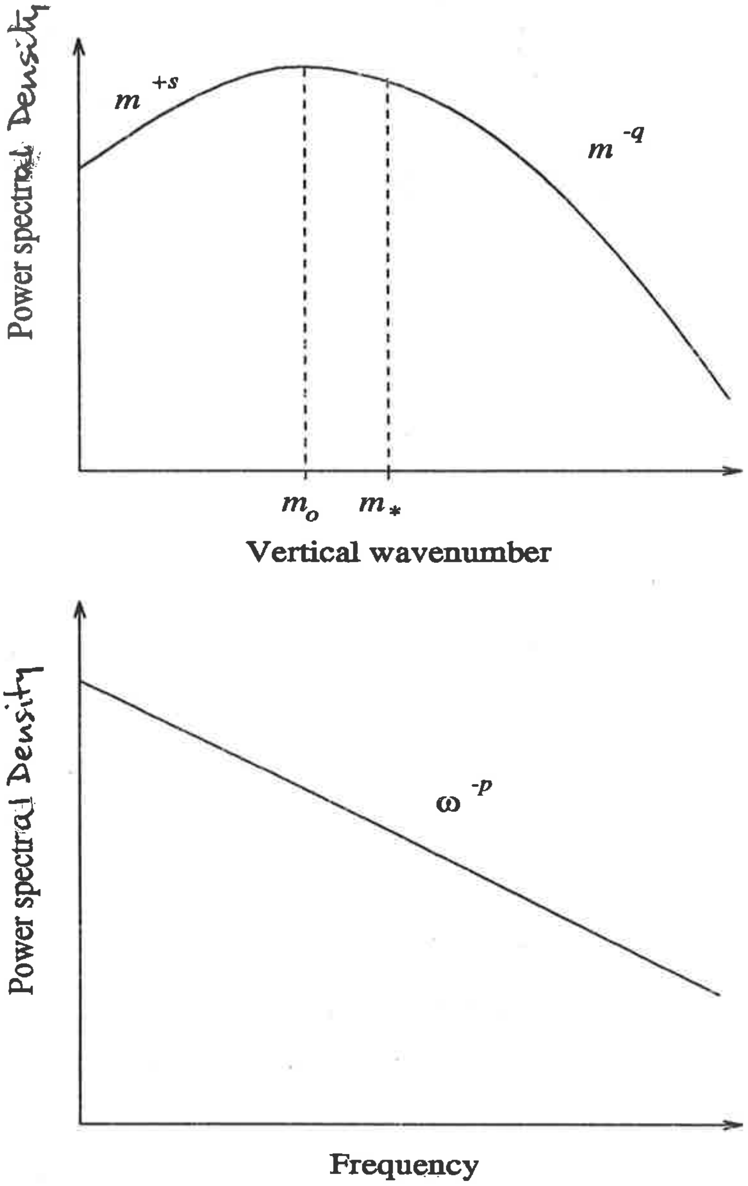

Figure 2.2: Schematic diagram of Desaubies vertical wavenumber spectrum (upper panel) and model frequency spectrum (lower panel). Note axes are logarithmic scales.

Table 2.2: Summary of gravity wave spectral theories

Spectral theory	Paper reference	'Source'	'Sink'
Saturation and instability	*Dewan and Good* [1986] *Smith et al.* [1987]	amplification	linear instability
Radiative damping	*Zhu* [1994]	amplification upward transport	radiative damping and off-resonant wave-wave interaction
Doppler spread	*Hines* [1991b]	empirical forcing	Doppler spreading
Nonlinear interactions	*Weinstock* [1990]	unspecified	off-resonant wave-wave interaction
Diffusive filtering	*Gardner* [1994]	unspecified	diffusive filtering

$$H_a(m,\omega) \propto F_a(m)G_a(\omega), \tag{2.53}$$

where *separability* has been assumed (see also Section 5.4.3).

The following sections will discuss the different theories proposed at time of writing to describe the observed gravity wave spectrum. A major reason that there is as yet no conclusive explanation for the physical processes giving rise to the observed spectral shape is the somewhat contradictory observational record. The atmosphere can be observed using different experimental techniques [Chapter 1]. In particular, the height ranges, height and time resolution, and data processing used will strongly affect measured spectra [*Mitchell et al.*,1990; *Lintelmann and Gardner*,1994; *Eckermann*,1995; *Gibson-Wilde et al.*,1996]. Hence, intercomparison between techniques and sites is difficult and specific spectral quantities are "clouded". The consequences of the application of different measurement techniques are further addressed in Chapter 3. This is particularly important in obtaining a physically real model of the gravity wave spectrum.

The *Zhu* [1994] idea of a gravity wave spectrum resulting from so-called spectral source and sink processes provides a convenient means of summarizing the spectral theories. Table 2.2 presents a summary of the spectral theories. Each of these theories will be discussed as well as their application in different models, where applicable.

2.5.1 Saturation or linear instability theories

The basic mechanism postulated for the observed spectral shape in this theory is the *saturation* of atmospheric gravity waves. Through this process, gravity waves, which have increased exponentially in amplitude with height, experience convective or dynamical instabilities. At these critical levels the observed horizontal phase velocity of the gravity wave $c_{h\mathrm{obs}}$ becomes equal to the local total horizontal velocity $U_h + U'$, so that [*e.g. Dewan and Good,*1986]

$$U' = |c_{h\mathrm{obs}} - U_h| = \frac{N}{m}. \tag{2.54}$$

Since the horizontal and vertical phase speeds are inversely proportional to the horizontal and vertical wavenumbers, waves with large wavenumbers are supposedly filtered out at lower heights so that the spectrum of waves present is gradually eroded. This results in an evolution of spectral shape with height so that at higher altitudes the majority of the wavenumber components have saturated spectral magnitudes (Figure 2.3). This saturation process was first devised for oceanic gravity wave spectra and a so-called Desaubies shaped universal spectrum was suggested [*Desaubies,*1976].

There has been an evolution of wave models from the above theoretical basis. Initially a *universal* or height invariant saturated spectrum was suggested in a direct analogy with ocean wave spectra [*VanZandt,*1982]. Atmospheric observations indicated a variation in spectral shape and magnitude with height leading *Dewan and Good* [1986] and *Smith et al.* [1987] to put forward a height varying spectrum (Figure 2.3).

2.5.2 Summary of other spectral theories

The *Weinstock* [1990] scale-dependent[8] off-resonant wave–wave interaction theory retained the idea from saturation theory that waves disperse, or saturate. A diffusion term was parameterized to represent the effects of relatively small-scale waves acting to break down the large-scale motions — hence the scale dependence of the theory.

---

[8] Idea of scale-dependence is important in spectral studies of a gravity wave field with reference to *Weinstock* [1990] and to the diffusive filtering theory. A scale-dependent diffusion process, also described as nonlocal, such as *Weinstock* [1990], occurs where the scales being diffused are larger than those of the process on which diffusion is acting. For a scale-independent process, all scales are subject to diffusion due to motions on all other scales.

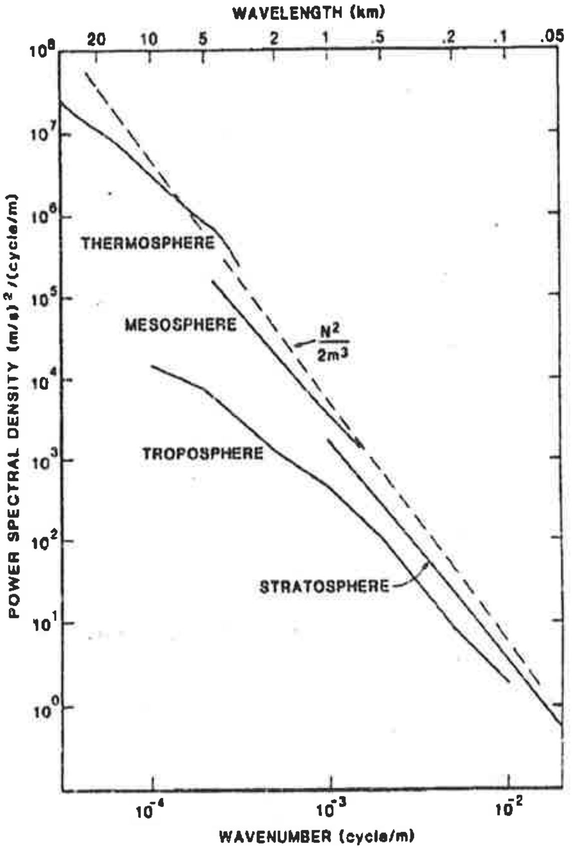

Figure 2.3: Observed variation of the power spectrum of horizontal velocity versus vertical wavenumber as a function of altitude [after *Smith et al.*, 1987].

Zhu [1994] extended the off-resonant wave–wave interaction theory and corrected the expression for $F(m)$ stated by *Weinstock* [1990] (Section 3.5). The significant new feature of the *Zhu* [1994] spectral theory was the introduction of radiative damping as a spectral sink.

The strongly monochromatic treatment of the saturation theories and the dependence on their assumption that $\delta m \propto m$ led *Hines* [1991*a*] to criticize the saturation explanation for the observed form of the gravity wave spectrum. As an alternative, *Hines* [1991*b*] proposed that waves from a source spectrum driven in the lower atmosphere propagate through a wave field where Doppler shifting of wave components by wave-perturbed winds results in a "spread" of associated vertical wavenumbers. This effect is expected to be most important for large-m (small λ_z) waves which make up the so-called *tail spectrum* ($m \gg m_*$).

The Doppler spread theory, resulting from the so-called advective non-linearity, can be contrasted with the Weinstock non-linear wave–wave interaction theory; the Hines non-linear wave-field interaction acts to refract waves, whereas the non-linear wave–wave interaction acts to diffuse the gravity wave spectrum.

The primary motivation for the *Gardner* [1994] development of *scale-dependent diffusive filtering theory* was the evidence from lidar observations that the observed quasi-monochromatic gravity wave vertical wavelengths and periods were grouped in a well-defined distribution [see *e.g. Gardner and Voelz*,1987]. It is noted here, and discussed further in Chapter 3, that this distribution is at odds with observations from other techniques such as MF radar, airglow observations, and rocket data.

2.5.3 Discussion of spectral theories

Observational evidence from a variety of techniques has provided support for a so-called Desaubies-shaped vertical wavenumber spectrum and ω^{-p} frequency spectrum. However, comparison between gravity wave spectra obtained using different techniques and at different sites indicates significant variability of specific gravity wave spectral parameters.

It is clear from the above review that controversy surrounds the mechanism(s) responsible for the observed gravity wave spectra. Each of the theories is able to provide an explanation for spectral shapes and indices, however none is without significant 'parameterization'. Hence the spectral theories do not provide a full theoretical basis, but are invoked in models along with some empirical features.

The spectral properties of gravity waves in the atmosphere and their parameterization are still a major area of research. This section has surveyed the current observational and theoretical viewpoints. A Desaubies form of spectral shape has been used as a basis for the simulations presented in Chapter 3. Through simulations based on an assumed spectral shape, it has been possible to examine the reliability of experimental determinations of gravity wave spectral parameters. The aim of such simulations has been to investigate some of the disagreements and uncertainties in observations of the gravity wave spectrum due to the sensitivity and selectivity of measurement and analysis techniques.

Chapter 3

Gravity Waves in the Mesospheric Sodium Layer

3.1 Introduction

This chapter presents an evaluation of the extraction of gravity wave information from resonant lidar measurements of neutral sodium (Na) abundances in the mesosphere. The fundamental elements of gravity wave theory, as developed in Chapter 2, are used as a basis for numerical simulations of gravity wave activity in the Na layer. This simulation and results from the MF radar and Rayleigh lidar techniques are used to test both monochromatic and spectral determinations of the gravity wave field.

Segments of this work have been published in *Gibson-Wilde et al.* [1996] which is included as Appendix A. The published paper fully describes two simulations, monochromatic and spectral, of linear gravity wave activity in the mesospheric sodium layer. These simulations can be tailored to investigate various atmospheric regions, constituents, scales, and conditions. This chapter complements and extends the work presented in Appendix A.

The investigation of gravity wave activity in the middle atmosphere has relied primarily on experimental studies, as discussed in the introduction. From these studies various spectral theories, and hence models, have been developed which attempt to explain observed features of the wave spectrum (Section 2.5). At the time of writing, several models are able to generate the basic features measured in experimental studies, each based on a different assumed physical process responsible for the observed gravity wave spectrum [*e.g. Smith et al.*,1987; *Weinstock*,1990; *Hines*,1991*b*; *Gardner*,1994; *Zhu*,1994]. Simulation studies provide a third tool for the investigation of gravity wave effects in the atmosphere, in addition to experimental and purely theoretical approaches. The advantages of making use of a simulation include providing test-bed data for experimental analysis techniques, and the realization of theoretical concepts and predictions which cannot otherwise be investigated analytically.

Sodium layer observations and chemistry are introduced in Section 3.2. The phenomenon of sporadic sodium layers is then reviewed with emphasis on the possible role of gravity waves in the formation of sporadic layering events (Section 3.3). The application of a gravity wave simulation to the mesospheric Na layer is developed and the results are summarized, with further information referred to in Appendix A. This application was chosen both as a relatively simple example to demonstrate the gravity wave simulation technique, and to investigate some anomalous results in atmospheric physics.

3.2 The Mesospheric Sodium Layer

Following a survey of mesospheric observations in Section 1.3, this chapter concentrates on direct observations of Na in the mesosphere. The resonant scattering lidar technique is the only direct Na measurement. This technique was pioneered in the 1970s with the advent of sufficiently high-power lasers [*e.g. Rowlett et al.*,1978] and is well suited to other mesospheric metal measurements; such as iron, calcium, lithium, and magnesium.

Lidar observations indicate an approximately Gaussian background Na number density vertical profile, with the centroid at ~90 km and half-width half-maximum of ~3 km [*e.g. Gardner and Shelton*,1985]. Hence the range of heights over which Na number density can be measured effectively is typically 80-100 km.

Superimposed on this approximately stationary layer are fluctuations with observed vertical scales and timescales often consistent with gravity wave variations (*e.g.* Figure

3.1). The high temporal and spatial resolution of lidar measurements is ideally suited to the investigation of gravity wave processes. This height–time resolution makes it the only technique presently able to explore the vertical structure of the mesosphere in such detail.

The Na lidar technique consists of a lidar system tuned to the sodium D2 resonance line (589/589.6 nm). Systems are (or have been) operated by groups in Brazil [*Clemesha et al.*,1980; *Batista et al.*,1989; *Clemesha et al.*,1996], France [*Juramy et al.*,1981; *Chanin and Hauchecorne*,1981; *Tarrago and Chanin*,1982], Germany [*von Zahn and Hansen*,1988], Japan [*Shibata et al.*,1986], and the United States [*Rowlett et al.*,1978; *Gardner and Voelz*,1987; etc.]. Multiple lasers were used by *Beatty et al.* [1992] to provide simultaneous observations of the stratosphere, from Rayleigh scatter, and the mesosphere, from Na resonant scatter (discussed in Section 3.6).

Throughout this chapter the Na lidar systems in the United States operated by the University of Illinois at Urbana–Champaign (UIUC) at Urbana, Illinois and elsewhere are used as a reference. These systems have been thoroughly documented [*e.g. Voelz and Gardner*,1986 (VG86); *Gardner and Voelz*,1987 (GV87); *Beatty and Gardner*,1990 (BG90); *Senft and Gardner*,1991 (SG91); *Beatty et al.*,1992; *Collins et al.*,1994]. The lidar systems used by VG86 and GV87 at Urbana and by *Collins et al.* [1994] in Antarctica are examples of an earlier zenith-pointing system with height resolution 37.5 m and time resolution 1-10 min. An example of a sequence of Na lidar profiles measured using the UIUC system is reproduced in Figure 3.1.

3.2.1 Chemistry of the Na layer

The mesospheric Na layer first came to light as a result of airglow studies of the night sky [*Slipher*,1929] which revealed a strong emitted spectral component corresponding to the Na D2 resonance line. The Na found at mesospheric heights results from meteor input of high Na content minerals directly into the mesosphere [reviewed in *Swider*,1992]. The chemical composition of so-called 'stony' or predominantly metallic meteors entering the Earth's atmosphere indicated that sodium is the

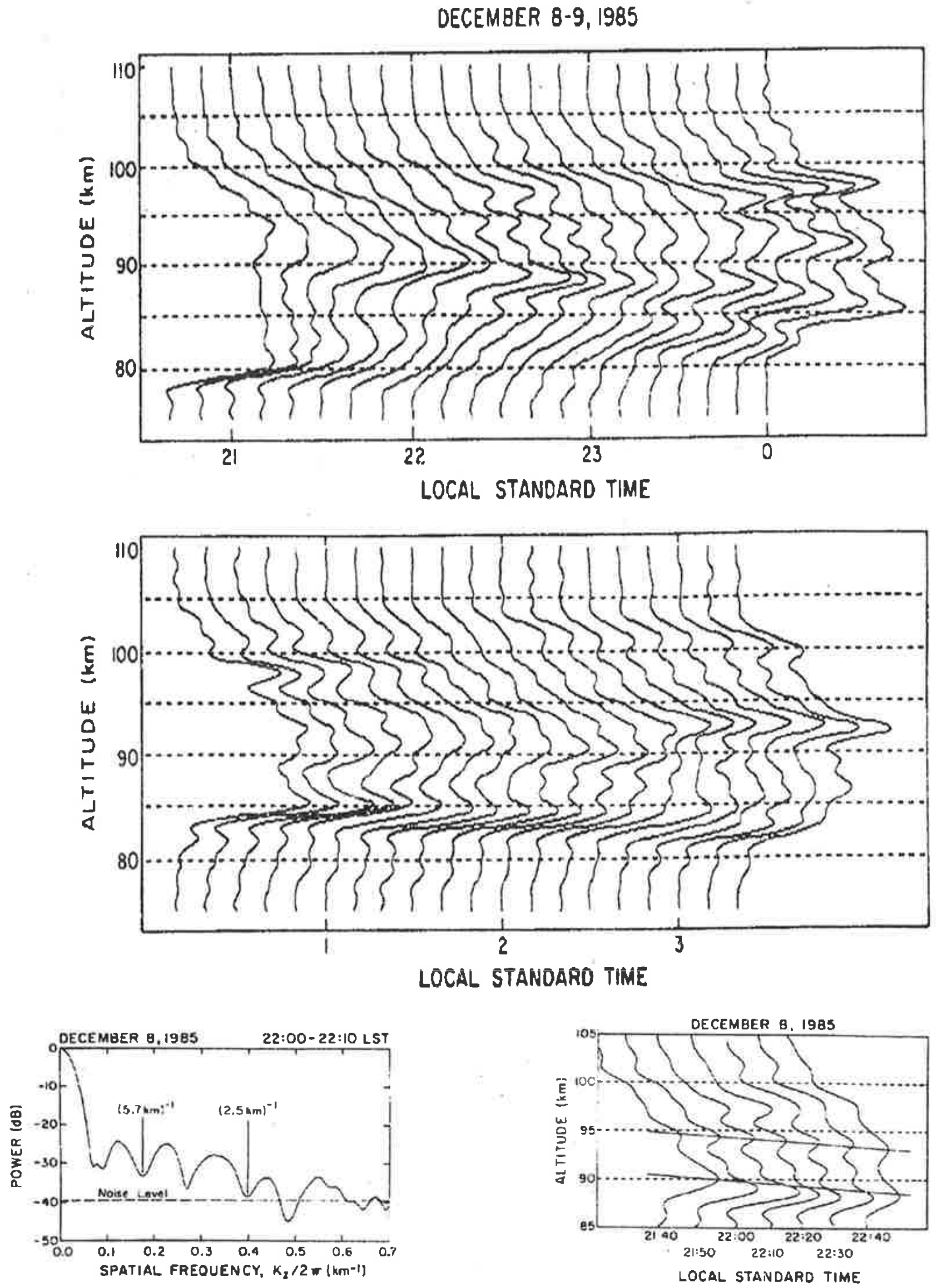

Figure 3.1: (a) and (b) mesospheric neutral sodium number density profiles measured on the night of 8-9 December 1985. For comparison purposes the profiles have been normalized so that each has the same column abundance. Power spectral density (lower left panel) and expanded sequence of profiles exhibiting a quasi-monochromatic wave feature (lower right panel) [after *Gardner and Voelz*, 1987].

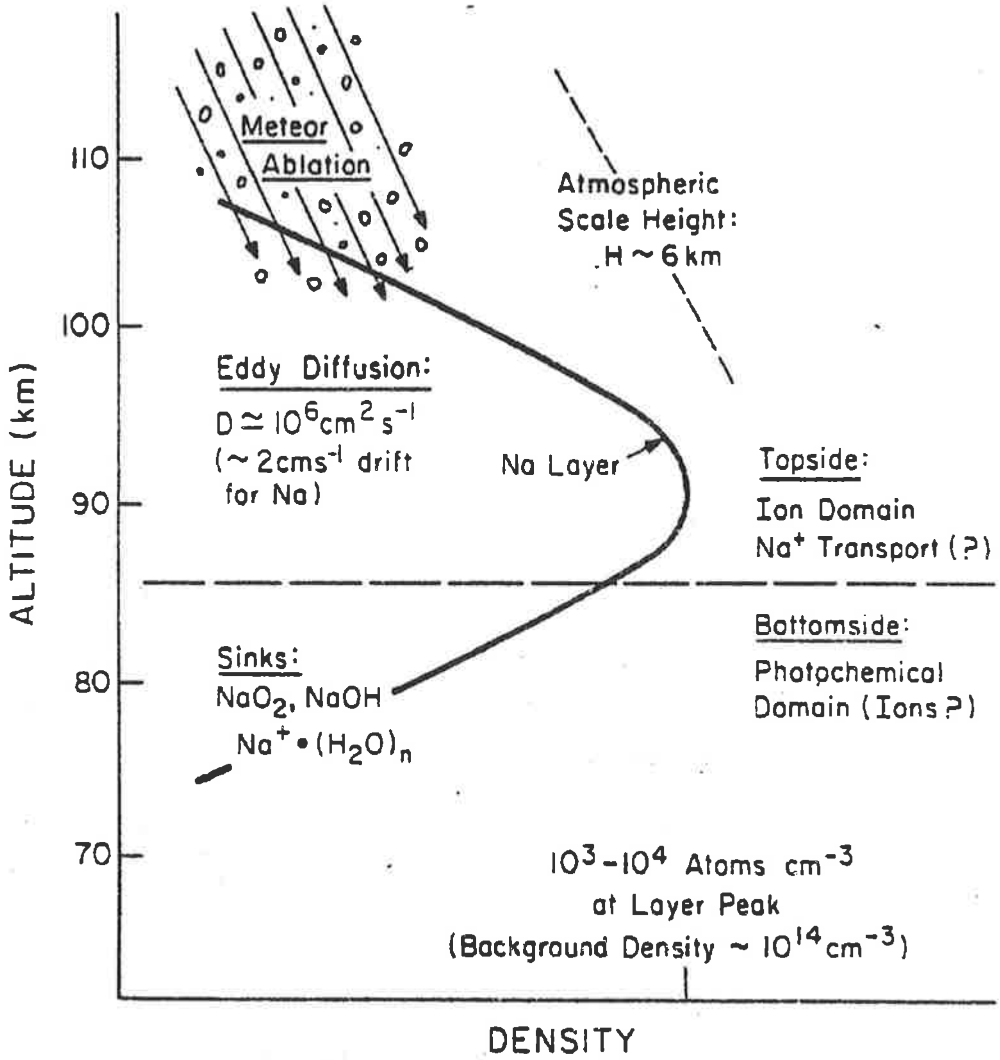

Figure 3.2: Schematic diagram summarizing the principal processes involved in the formation of the mesospheric Na layer [after *Voelz and Gardner*, 1986].

most commonly occurring of the alkali metals, lending weight to the meteoric explanation [*Swider*,1992]. Figure 3.2 provides a schematic diagram showing the major processes involved in the formation of the mesospheric Na layer structure.

Thomas et al. [1983] presented a model based on an influx of Na at the upper levels of the Na layer due to meteor ablation[1] and loss on the lower side of the layer due to chemical destruction. For mesoscale studies (maximum timescales of the order of tens

---

[1] whereby incoming particles burn up or evaporate in the Earth's atmosphere

of hours) the dynamical timescales are assumed sufficiently short relative to the chemical and meteoric input timescales to approximate a stationary background Na layer of Gaussian or skewed Gaussian form [*Thomas et al.,*1983; *Helmer and Plane,*1993]. In the case of mesospheric Na, the chemical timescale is determined from laboratory-measured chemical reaction rates [*e.g. Helmer and Plane,*1993].

In contrast, the meteoric input timescales are not straightforward to determine and are certainly subject to temporal, seasonal, and latitudinal variation. Profiles obtained from lidar imaging of the Na layer are typically 'normalized' in column abundance to the mean value over a night of observations (*e.g.* Figure 3.1). The Na content often changes during the observation period, at times quite intermittently [*e.g. Gardner and Shelton,*1985]. This feature of lidar profiles is distinct from the sudden sodium layer events (Section 3.2.2) and has been studied inadequately to-date.

Other mesospheric neutral metallic layers, such as iron, calcium, and lithium, have also been investigated using lidar techniques [*e.g. Granier et al.,*1985]. The mesospheric calcium layer is of a similar form to the Na layer, although the number density of atmospheric calcium is much smaller than that of Na. Hence calcium lidar measurements are subject to larger experimental errors and are less suitable for mesoscale dynamical studies. Basic characteristics of the mesospheric metal layers are similar [*Granier et al.,*1985, Figure 2]. The modeling approach developed in this chapter to simulate wave perturbations measured by the Na and Rayleigh lidar techniques is also applicable to other tracer-like metallic layers imaged using lidar techniques.

3.2.2 Sudden or sporadic Na layers

Sudden or sporadic sodium layers (SSLs) are vertically localized enhancements in Na abundance which have been observed using the Na lidar technique. An example observation of a SSL at Urbana, Illinois is reproduced here in Figure 3.3 [*Senft et al.,*1989]. These layers were first reported by *Clemesha et al.* [1978] in Brazil (23°S, 46°W) and have since been reported at Urbana, Illinois [*Gardner et al.,*1993], Arecibo, Puerto Rico (18°N, 67°W) [*Beatty et al.,*1989], at tropical latitudes during the ALOHA-90 campaign [*e.g. Kane et al.,*1991], and at polar latitudes [*Hansen and von Zahn,*1990].

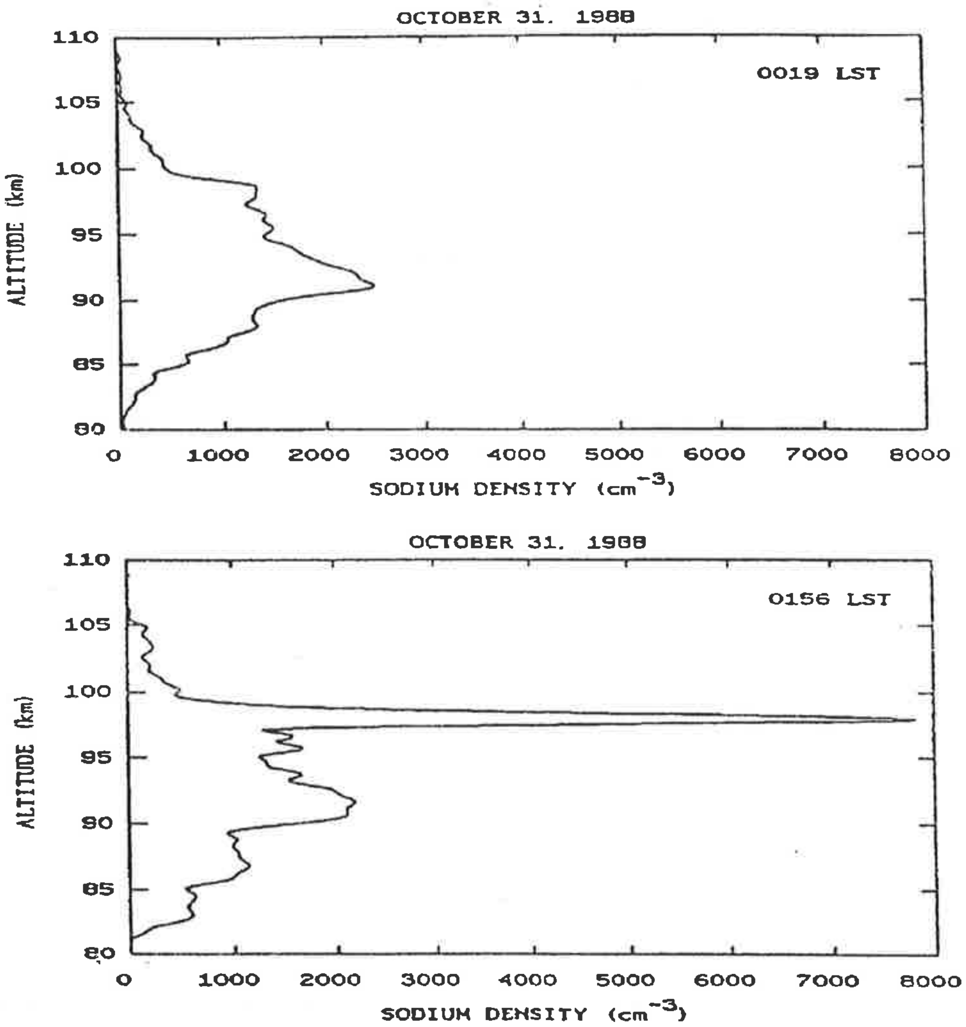

Figure 3.3: Neutral sodium number density profiles measured at Urbana on 31 October 1988 at 0019 LST, before the SSLs appeared (upper panel), and at 0156 LST, the time when the sporadic layer reached its maximum number density (lower panel) [after *Senft et al.*, 1989].

The SSLs are observed most commonly in the height range 93-105 km [*Rajasekhar and Plane*,1993] with maximum Na number densities up to 10 times normal peak levels. These SSLs are somewhat analagous to ozone laminae, discussed extensively in Chapters 4-6, and ionospheric sporadic E layers (E_s). Like both these other phenomena, SSLs are typically only a few kilometres thick and occur "sporadically", superimposed on a relatively stationary background vertical distribution. The possible connection between E_s and SSLs has been investigated at Arecibo using measurements from incoherent scatter radar and lidar [*Beatty et al.*,1989] and at polar latitudes using the European Incoherent Scatter (EISCAT) radar and colocated lidar [*von Zahn and Hansen*,1988].

Meteor ablation at the heights of observation of the SSLs has been proposed as a mechanism of sporadic layer formation [*Clemesha et al.*,1978]. The timescales of SSL formation (~1 min) suggest that these features are more immediately linked to meteor ablation than the typical broad Na layer which is itself formed over time from the net effects of ablated meteoric material. The meteor ablation explanation has been disputed recently by *Clemesha et al.* [1996] as a result of new observational evidence of a distortion of the background Na layer shape accompanying SSL observations.

The chemical basis for SSLs is believed to be a process known as dissociative attachment [*e.g. Rajasekhar and Plane*,1993], whereby an ionized compound, acting as a chemical reservoir, undergoes the reaction

$$\mathrm{NaX} + e^- \rightarrow \mathrm{Na} + \mathrm{X}^-. \tag{3.1}$$

This process is suggested in SSL formation since an E_s layer is not always accompanied by a SSL [*von Zahn and Hansen*,1988]. However, the variation in composition of metallic meteors is such that although Na is the most abundant of the alkali metals, the most abundant metals present are iron, silicon and magnesium which may cause E_s in the absence of a SSL event [*Swider*,1992].

Gardner et al. [1993] have reported simultaneous observations of an E_s, a SSL, and sporadic iron (Fe) and calcium (Ca) layers. If gravity waves are important in formation and destruction of the sporadic layers it may be expected that similar variations would be observed in the different sporadic events. Identical variations would not be expected since the magnitudes and phases of the number density perturbations for each mesospheric layer depend on the vertical concentration gradients of the background profiles through the tracer continuity equation (2.24). The densities and ablation properties of the different meteoric metals lead to different vertical structure and heights of occurrence of the metallic layers [*e.g. Granier et al.*,1985].

The observations of *Gardner et al.* [1993] do not indicate whether the simultaneously observed sporadic layers contain corresponding variations. The importance of temperature variations and wind shears in the formation of sporadic layers was indicated by *Gardner et al.* [1995]. Using a simulation approach similar to that developed in the following sections, it would be possible to predict magnitude and phase relations between number density perturbations in mesospheric Na, Ca, Fe, etc. for known temperature perturbations and background constituent distributions.

Rajasekhar and Plane [1993] suggested that upward transport of Na by gravity waves may form a reservoir of $NaHCO_3$ which then undergoes dissociative attachment due to auroral electrons. The SSL is then theoretically formed in the overlap region where both $NaHCO_3$ and auroral electrons coexist.

Cox et al. [1993] considered a background Na layer from a steady state model [*Helmer and Plane*,1993] with a superimposed SSL driven by diffusion and chemistry. *Cox et al.* [1993] determined that a minimum source strength or deposition rate of approximately 3 Na atoms cm^{-3} s^{-1} was necessary to produce a typical SSL at 95 km. The time period necessary for a model SSL to develop was between 70 min and 21 hr, dependent on the type of diffusion assumed and whether chemical removal was included in the model.

It is clear from the Na lidar simulation and from published experimental lidar results that gravity-wave-scale perturbations can result in rapid Na transport. *Kirkwood and Collis* [1989] made use of a simple model to indicate that gravity wave variations in vertical velocity could bring about a localized SSL-like layer from an initially Gaussian background Na profile. For an SSL event identified in Na lidar data and an ionosonde profile [*von Zahn and Hansen*,1988], *Kirkwood and Collis* [1989] examined EISCAT radar data and found evidence for strong vertical ion drifts associated with probable strong neutral winds. They showed that an initially broad Na layer could be deformed into a narrow band by the action of strong vertical winds.

Kirkwood and Collis [1989] also emphasized that the observation period (12 August) corresponds to the Perseid meteor shower and hence that sporadic meteor ablation is the likely source of material for the observed E_s and SSL. However, *von Zahn et al.* [1987] indicated that the narrow extent of layers is not consistent with the process of meteor ablation. Hence, *Kirkwood and Collis* [1989] conclude that meteors ablate, depositing material over a wide range of heights as observed, and a strong vertical velocity associated with a gravity wave acts to accumulate the meteoric material into the narrow layers observed.

Hence the suggestion that gravity wave transport of constituents forms a reservoir for chemical reactions which form Na remains a plausible explanation [*Rajasekhar and Plane*,1993]. It is clear that dynamics alone cannot produce such large localized Na concentrations. The addition of material through meteor ablation or chemical reaction must also play a role. A simultaneous observation with Na lidar and a meteor radar could provide a test of the link between meteor ablation and SSL occurrence.

3.3 Monochromatic Gravity Wave Studies from Na Lidar

Monochromatic gravity waves, or clearly-defined combinations of wave components that can be identified in the power spectrum of the Na profiles, have been considered by *Rowlett et al.* [1978], GV87, BG90, *Collins et al.* [1994], and *Collins et al.* [1996]. These papers analyzed sequences of Na lidar profiles exhibiting so-called monochromatic wave signatures and hence determined gravity wave characteristics for different latitudes and seasons.

How are monochromatic wave events defined? Using a simulation it is possible to produce a true monochromatic wave. However, Na lidar observations of so-called monochromatic events most commonly indicate a dominant scale accompanied by fluctuations on a range of other scales which are partially removed, or selected, by filtering (*e.g.* Figure 3.1). In this thesis the term *quasi-monochromatic* refers to observations which indicate that dominant gravity wave scales are present (equivalent to GV87 monochromatic waves) as distinguished from true *monochromatic* fluctuations consisting of exactly one wavelength and frequency component.

The reliability of the determinations of basic gravity wave parameters from Na lidar profiles is investigated here. To test the limits of the Na lidar processing procedure, a simulation of monochromatic wave fluctuations in a modeled Na layer was developed. The so-called GV87 technique was then used to extract vertical wavelengths and observed vertical phase velocities. These two gravity wave parameters were considered first since they are measured directly from the lidar profiles. Values of horizontal wavelength, observed period, and wave amplitude are derived from these measurements.

This simplified simulation produces monochromatic wave perturbations in the mesospheric Na layer according to the expression [*Chiu and Ching*,1978]

$$r_{\mathrm{Na}}(z,t) = \frac{-r_\rho(z,t)}{\gamma - 1}\left(1 + \gamma H \frac{\bar{n}_{\mathrm{Naz}}(z)}{\bar{n}_{\mathrm{Na}}(z)}\right), \tag{3.2}$$

where $r_{\mathrm{Na}}(z,t)$ is the relative Na density perturbation, $r_\rho(z,t)$ is the relative atmospheric density perturbation, $\bar{n}_{\mathrm{Naz}}(z)$ is the vertical derivative of the background Na number density profile, and γ is the ratio of specific heats [see also Chapter 6].

In the simulation the background wind was assumed to be zero ($\mathbf{U}=0$) which is equivalent to the GV87 assumption that $\omega_{\mathrm{obs}} = \hat{\omega}$. Although this is an oversimplification of mesospheric conditions, it is used in this simulation since it is an assumption of the GV87 technique. The effect of background winds has been investigated by *Lintelmann and Gardner* [1994]. Recent Na lidar wind and temperature measurements [*Collins et al.*,1996] remove the necessity for this assumption.

In the following sections the processes involved in extracting quasi-monochromatic gravity wave parameters from Na lidar data are presented and evaluated.

3.3.1 Data processing — the GV87 technique

Rowlett et al. [1978] developed a method by which quasi-monochromatic gravity wave parameters could be extracted from Na lidar data. This technique was further defined and documented by *Gardner and Shelton* [1985], VG86 and GV87 and is here referred to as the GV87 technique.

The GV87 technique is based on the identification of coherent wave-like features in a sequence of lidar profiles. From such an observation, a manual analysis is carried out in order to estimate a vertical wavelength from the separation of observed peaks and vertical phase speed from the rate of vertical movement of peaks visible in the

Wave parameter	Symbol	Source of measurement
Vertical wavenumber	m	position of notched peak
Wave amplitude	A	depth of notch
Amplitude growth factor	β	peak separation

Table 3.1: Gravity wave parameters determined from the vertical wavenumber power spectrum in the GV87 technique.

successive profiles. A power spectrum in vertical wavenumber is calculated for each of the successive profiles and hence an average power spectrum.

A characteristic *double-peaked* or *notched* signature is sought, indicating a wave component present in the layer which undergoes a phase change at the layer peak [*e.g.* GV87; Appendix A]. This information is used to determine gravity wave parameters from the power spectrum (Table 3.1). These processing techniques and the methods of extraction of each of these parameters are examined in detail in the following sections.

3.3.1.1 Zeropadding

Zeropadding consists of including extra zero values to extend the effective lengths of *signal-domain*[2] data arrays in order to increase the resolution in the Fourier domain. In adding extra zeroes to an array, the effect is analagous to applying a box window to a longer data set, resulting in superimposed short-period fluctuations in the power spectrum. Zeropadding of data is a commonly used procedure in Fourier analysis based signal processing and has been applied, if not explicitly, by the UIUC group [*e.g.* GV87].

Increasing the effective resolution of power spectra calculated in the GV87 technique is definitely advantageous in the process of identifying the presence of quasi-monochromatic wave features. Figure 3.4 displays power spectra, calculated with and without zeropadding, applied to the simulated vertical profiles of Na number density before Fourier transformation (gravity wave parameters $\hat{\omega}$=0.0008 cyc s^{-1}, λ_z=2 km and 3 km, amplitude 3%). The zeropadded case included 530 data values zeropadded to a 2056 element array. The increase in wavenumber resolution is clear; however, it must be noted that the parameters determined from the peak separation β and notch

---

[2] This term may refer to either the time domain in the case of a Fourier analysis applied to time-series data or the spatial domain in the case of spatially varying data.

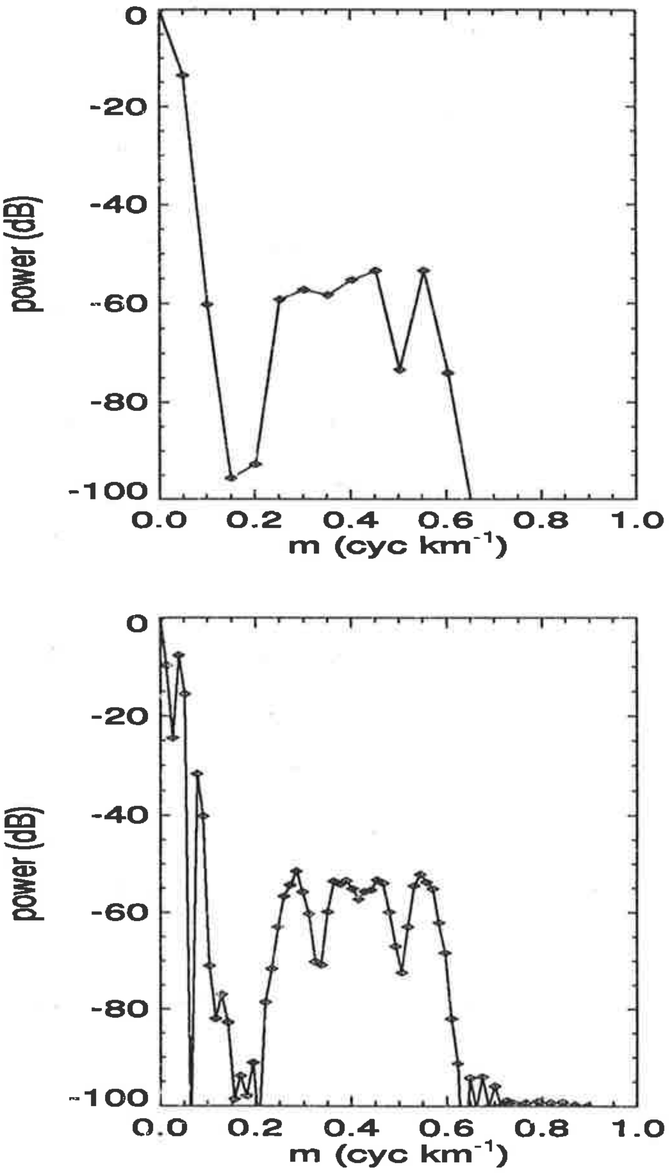

Figure 3.4: Power spectra calculated without (upper panel) and with (lower panel) zeropadding applied to the vertical profiles of neutral sodium number density before Fourier transformation.

depth A are certainly affected by the zeropadding process.

The advantage of the zeropadding has been to define clearly the positions of the two notched peaks associated with the 2 km (m = 0.50 cyc km^{-1}) and 3 km (m = 0.33 cyc km^{-1}) waves (Figure 3.4). The disadvantage is that the zeropadding results in extra fluctuations superimposed on the power spectrum due to the convolution of the box window.

3.3.1.2 Vertical phase velocity

The vertical phase velocity is, in principle, simple to determine from lidar measurements for a sequence of profiles exhibiting coherent wave motions [*e.g.* Chapter 5; *Gibson-Wilde et al.*,1997]. However, to measure a vertical phase velocity using the GV87 technique requires that a wave motion remains coherent over ≥10 min of lidar profiles, which sets limits on the wave parameters that can be extracted.

Several effects are important. Firstly, a superposition of waves may complicate both the profiles and (consequently) the power spectrum, leading to a quasi-monochromatic profile. Secondly, *Lintelmann and Gardner* [1994] found that Doppler shifting of atmospheric gravity waves by background winds, a height-dependent effect, may result in a change in apparent propagation direction.

Thirdly, the timescales of the wave-packets or events are a consideration since there is evidence that diffusion has a major impact on waves of short vertical wavelength in the mesosphere [*Fukao et al.*,1985; *Gardner*,1994; *Marks and Eckermann*,1995]. This last point has important consequences with respect to lidar measurements, since small vertical wavelength waves may be present for very short timescales making it difficult to identify them correctly using the GV87 technique. This difficulty is more severe for radar and other lower resolution techniques where information on these scales is lost. The reliability of determinations of vertical phase velocity is discussed further in Appendix A.

3.3.1.3 Vertical wavelength

The vertical wavelength λ_z is determined by a cross-check between the peak separations of wave-like features visible in successive profiles and the position of the notched peak in the vertical wavenumber power spectrum. Both these methods depend on the wavelength remaining constant throughout the height range of observations.

The value of λ_z is dependent on the mean horizontal wind through the relation

$$m = \frac{2\pi}{\lambda_z} = \frac{N}{\mid c_{hobs} - \mathbf{U}_h(z) \mid}. \tag{3.3}$$

In conditions of zero or constant background horizontal wind and constant N, the value of m remains constant with height. Under such conditions the determination of λ_z using the GV87 technique is well justified. However, as will be further discussed in Chapter 6, vertical variations of both $\mathbf{U}_h$ and N^2 are important in the variation of vertical wavelength with height. Also, the mesosphere is a primary region of gravity wave breaking as has been determined from mesospheric wind measurements [Chapter 1], suggesting that identification of wave events with constant vertical wavelength occurring throughout the mesospheric Na layer is often a poor representation of the real atmosphere. This identification of probable wave breaking is not restricted to lidar studies of the region. The discussion of the Saskatoon (52°N, 107°W) GRAVNET MF radar in the following section examines this issue of wave coherence over large horizontal scales.

Typical values of vertical wavelength calculated from the observed profiles are 1-15 km [*e.g.* GV87; *Beatty et al.*,1992; *Collins et al.*,1994]. The identification of large vertical wavelength (>10 km) waves from power spectra is clouded by the presence of the background Na layer spectral shape. This concept is illustrated in Figure 3.5 where spectra corresponding to three different large vertical wavelength gravity waves (10, 12, and 15 km) are overplotted. The gravity wave peaks are not well-resolved in the power spectrum since the power spectral signatures of the waves and the background layer cannot be resolved adequately.

This result limits the reliability of the extraction of gravity waves of large vertical wavelength from Na lidar data. This uncertainty is increased when the vertical extent of the sodium layer is typically 20 km so that the 'Nyquist' vertical wavelength of the layer is effectively 10 km. Hence the conclusion from such an analysis must be that 10 km is an upper limit to the determination of gravity wave vertical wavelengths from Na lidar data.

3.3.1.4 Wave amplitude and amplitude growth factor

Amplitude growth factor (β) values are determined from the peak separation of the notched gravity wave spectral signature. GV87 assume a scale height (H_ρ) of 6 km and an RMS width (σ_0) of the Na layer of 4 km. The following equation is used to calculate β from a measured value of peak separation (δm) in the power spectral density (PSD)

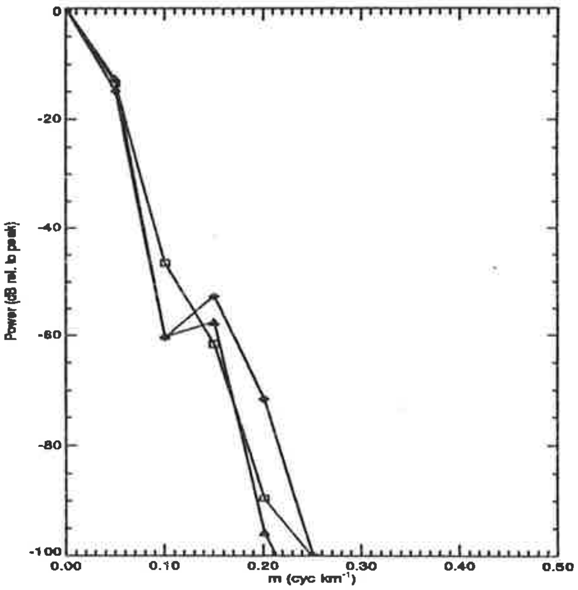

Figure 3.5: Power spectra of simulated Na lidar observations of single waves with vertical wavenumbers 0.1 cyc km^{-1} (diamond), 0.083 cyc km^{-1} (triangle), and 0.067 cyc km^{-1} (square).

[VG86; GV87]:

$$\delta m = 2(\frac{1}{\sigma_0^2} - [\frac{1}{2H_\rho} - \frac{1}{\beta}]^2)^{\frac{1}{2}}. \tag{3.4}$$

This method of determining β is dependent on the wavenumber resolution of the PSD. The widest possible peak separation corresponds to the σ_0 term dominating the expression for δm so that the value is about 0.5 cyc km^{-1}. For typical values of β measured for the mesosphere by GV87 the value of δm ranges between <0.1-0.5 cyc km^{-1}. Since the effect of β is negligible in the simulated Na layer and σ_0 is significantly smaller than $2H_\rho$, it is reasonable to expect the peak separation to be very close to 0.5 cyc km^{-1} for all simulated gravity wave PSDs. However, since the mean Na profile is a skewed Gaussian, rather than a perfect Gaussian, the measured value of δm is approximately 0.7 cyc km^{-1}.

3.4 Comparison of Na Lidar and MF Radar Measurements

Moving beyond the specific measurements obtained with Na lidar and the processing techniques used to extract quasi-monochromatic wave parameters, this section examines the physics of the gravity wave field which has been inferred from Na lidar measurements and its relation to other experimental techniques. Different experimental techniques impose different sensitivities and selectivities on the measurement of atmospheric motions. Factors such as height and time resolution of an instrument will significantly affect information extracted from a measurement technique.

GV87 comment that "lidar studies of gravity waves .. concentrated almost entirely on individual events" and "lidar profiles tend to have a (quasi)monochromatic appearance". These comments indicate significant differences between radar and Na lidar techniques since radar techniques detected quasi-monochromatic features only about 25% of the time [*Reid,*1986]. Although, as pointed out by GV87, the selection criteria as imposed by the experimental setup are significantly different for the two techniques (see later discussion).

The issue of determining unbiased measurements of gravity wave parameters is a controversial one. This section investigates the disagreement between Na lidar and MF radar determinations of gravity wave parameters by assessing the affect of the assumption of zero background winds in the Na lidar measurements. A comparison is developed between the Na lidar [GV87; BG90] determinations of quasi-monochromatic gravity wave parameters and those obtained using the GRAVNET MF radar [*Reid,*1986; *Manson,*1990].

The GRAVNET MF radar consisted of an equilateral triangular arrangement of three spaced-antenna receiving systems with an antenna spacing of 40 km [*Reid,*1986]. Wave propagation direction, mean background wind, and intrinsic horizontal phase speeds were measured by comparing received signals from the three locations using standard spaced antenna analysis techniques. The wave events identified by the system exhibited coherency between the three received signals.

Of the (about) 55 gravity wave events identified by *Meek et al.* [1985] only about

15 have parameters observable by the Na lidar system (*i.e.* with vertical wavelengths from ~1-10 km). Further comparison between GRAVNET radar and Na lidar data is developed in the following section.

3.4.1 The $\lambda - T$ relations

For gravity wave motions it is possible to express the vertical phase speed c_z as the ratio of vertical wavelength λ_z to intrinsic wave period $\hat{T}$ [see also Chapter 2]. This is done by rearranging the definition of vertical phase speed, (2.49), to give

$$c_z = \frac{\lambda_z}{\hat{T}}, \tag{3.5}$$

and similarly for the horizontal phase speed c_h

$$c_h = \frac{\lambda_h}{\hat{T}}. \tag{3.6}$$

However, observed rather than intrinsic quantities are available from ground-based lidar and radar measurements. For this reason GV87 assume that $\hat{\omega} = \omega_{\text{obs}}$, so that the observed quantities $c_{z\text{obs}}$, $c_{h\text{obs}}$, and T_{obs} are equal to the intrinsic quantities c_z, c_h, and $\hat{T}$ respectively. The relationships (3.5) and (3.6) were then used by GV87 to represent relationships between observed or apparent, rather than intrinsic, quantities.

Under this assumption (3.5) was used by GV87 to calculate the observed wave period

$$T_{\text{obs}} = \frac{\lambda_z}{c_{z\text{obs}}}. \tag{3.7}$$

From this value, a horizontal wavelength (λ_h) was calculated from a simplified dispersion relation

$$\lambda_h = \frac{\lambda_z^2}{c_{z\text{obs}} T_B}, \tag{3.8}$$

where T_B is the Brunt–Väisälä period, approximately equal to 100π s in GV87, and it is assumed that $c_z = c_{z\text{obs}}$. In fact, the true value of λ_h, taking into account the background horizontal velocity $\mathbf{U}_h$, will be

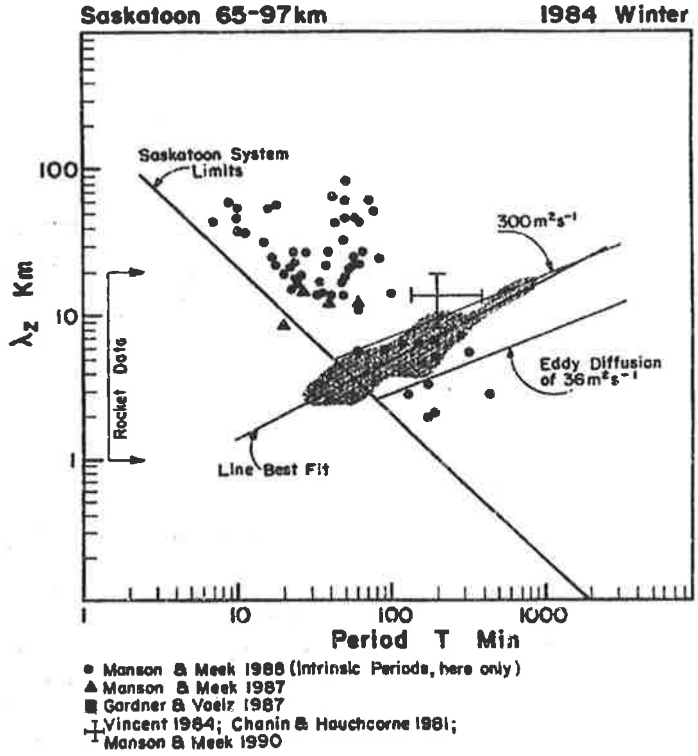

Figure 3.6: Collation of measurements of vertical scales and observed periods for the 60-110 km height range for various locations and observing techniques [after *Manson*, 1990].

$$\lambda_h = T_{\mathrm{obs}}\left(\frac{\lambda_z N}{2\pi} + \mathbf{U}_h\right), \tag{3.9}$$

which for typical middle atmosphere horizontal wind speeds [*e.g. COSPAR*,1986] will be significantly different from the value calculated assuming the intrinsic and observed wave periods are equal, as in (3.8).

These measured λ_z and estimated T_{obs} values were used by GV87 to calculate power-law relationships between the gravity wave parameters from lines of best fit to measured distributions [GV87]. A power-law relation between λ_h and $\hat{T}$ was obtained from a collation of radar and airglow observational results [*Reid*,1986; *Manson*,1990]. Two examples of collations are reproduced here in Figure 3.6 (λ_z–T_{obs}) and Figure 3.7 (λ_h–T_{obs}). *Reid* [1986] and *Manson* [1990] compared the relationship between λ_h and $\hat{T}$, a so-called $\lambda - T$ relation, obtained from lidar measurements with similar measurements from optical (airglow and noctilucent cloud imaging) and radar measurements. Strong grouping is apparent in the lidar data, which is not apparent in the other

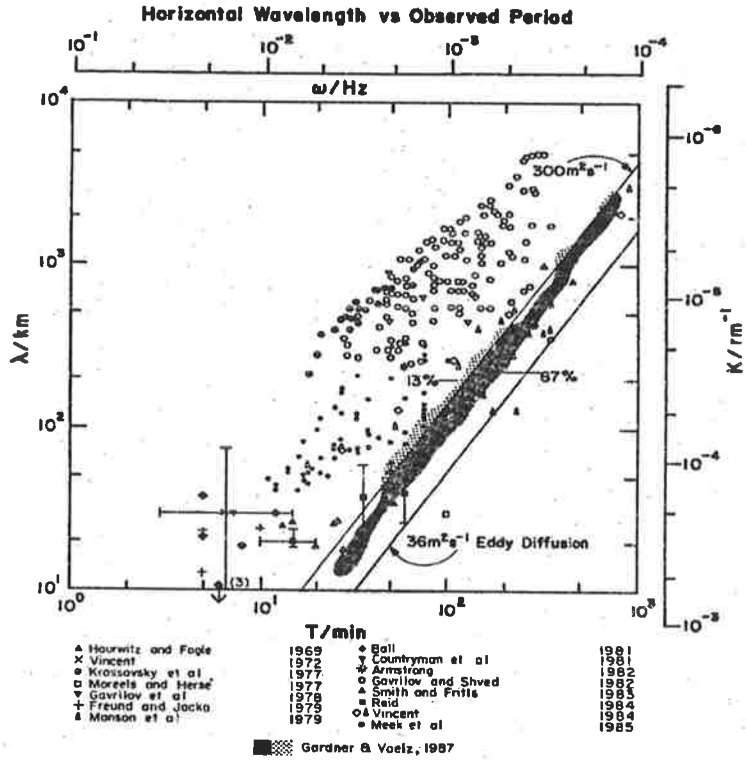

Figure 3.7: Collation of measurements of horizontal scales and observed periods for the 60-110 km height range for various locations and observing techniques [after *Manson*, 1990].

measurement techniques (Figure 3.7). These conflicting results were interpreted by GV87 as evidence that the Na lidar technique was observing a more exact picture of the atmosphere and (by implication) that other observational techniques were biased [*e.g. Hines*,1993]. The contrasting results of the lidar technique and other techniques, particularly radar wind measurement, have led to much speculation as to the true relation between λ and $\hat{T}$.

The different results displayed in *Manson* [1990] are certainly due, at least in part, to the specific observational techniques, as summarized in the following table.

Observation technique	Gravity wave parameter measured	Assumption
Airglow	$\lambda_h,\ c_h$	height 'integrated'
Na lidar	$\lambda_z,\ c_{z\text{obs}} \rightarrow T_{\text{obs}}$	zero mean wind assumed
MF radar	$\lambda_h,\ c_{h\text{obs}},\ \mathbf{U} \rightarrow \hat{T}$	mean wind measured

For the lidar and radar measurement techniques it is particularly important to note two points:

1. The assumption of $T_{\mathrm{obs}} = \hat{T}$ in (3.8) implies that mesospheric winds are uniformly zero when in fact values vary [*e.g. COSPAR*,1986].

2. The relationship between λ_h and $\hat{T}$ is even more susceptible to background wind effects through the calculation of λ_h based on assumption 1 (compare (3.8) and (3.9)).

Can the difference between Na lidar and MF radar results (and by implication airglow etc.), as presented in *Manson* [1990], be explained by the neglect in GV87 of background wind effects? With background wind data from, for example, the Illinois MF radar in order to obtain mesospheric winds simultaneous with the lidar measurements it would be possible to calculate the intrinsic quantities λ_z and $\hat{T}$. This could provide a direct answer.

In the absence of such a direct calculation, data from the GRAVNET radar system, compatible with radar data as presented in *Meek et al.* [1985] (MRM85), were made available [Iain Reid, private communication]. These data were used to perform an analysis of horizontal wind effects on the relation between observed and intrinsic wave periods. The GRAVNET radar measured T_{obs}, $c_{h\mathrm{obs}}$, $\mathbf{U}_h$, λ_h, and λ_z from which the intrinsic period was calculated as $\hat{T} = \lambda_h/(c_{h\mathrm{obs}} - \mathbf{U}_h)$.

The four plots shown in Figure 3.8 display GRAVNET MF radar data (diamond symbols) along with lines of best fit determined by MRM85 from GRAVNET data and GV87 from Na lidar data. Panel (a) shows two lines of best fit:

$$\text{GRAVNET radar [MRM85]} \quad \lambda_h = 9\ (T_{\mathrm{obs}})^{0.68}, \tag{3.10}$$

$$\text{Na lidar [GV87]} \quad \lambda_h = 0.093\ (T_{\mathrm{obs}})^{1.52}. \tag{3.11}$$

Hence panel (a) indicates the differing $\lambda_h - T$ relations obtained experimentally by lidar and radar techniques.

Panel (b) indicates three Na lidar lines of best fit:

$$\text{Na lidar [GV87]} \quad \lambda_z = C_0\ (T_{\mathrm{obs}})^{0.55}, \tag{3.12}$$

where C_0=0.2, 0.4, and 0.6. The bold line in panel (b) is a calculated line of best

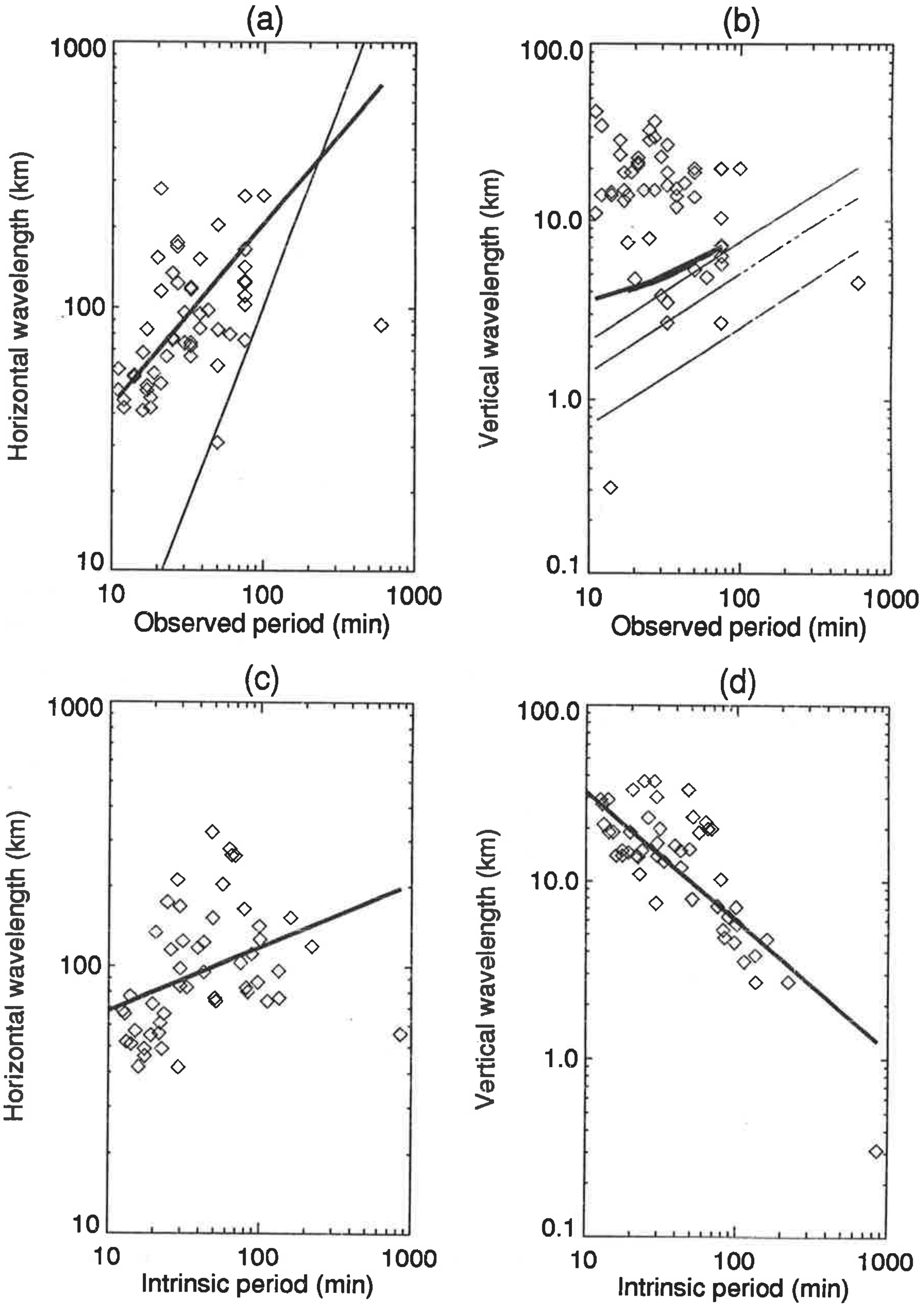

Figure 3.8: Comparison of GV87 results with the results of MRM85. Throughout, GV87 lines of best fit are indicated by thin lines, MRM85 GRAVNET data lines of best fit by bold lines, and GRAVNET data points by diamond symbols. (a) Horizontal wavelength plotted against observed period, (b) vertical wavelength plotted against observed period, (c) horizontal wavelength plotted against intrinsic period, and (d) vertical wavelength plotted against intrinsic period. Further details in text.

fit from the GRAVNET radar data fitted only for waves with λ_z between 1-10 km. The sparseness of GRAVNET data for smaller vertical wavelength waves limits the reliability of the bold line. However, panel (b) suggests that the Na lidar-determined line of best fit may represent a fit to a selected subset of waves; the lidar and radar lines of best fit being similar for waves with vertical scales 1-10 km.

Panels (c) and (d) display only GRAVNET data and associated lines of best fit from MRM85:

$$\text{(c)} \quad \lambda_h = 39(\hat{T})^{0.24}, \tag{3.13}$$

$$\text{(d)} \quad \lambda_z = 172(\hat{T})^{-0.73}. \tag{3.14}$$

Figure 3.8 indicates that the line of best fit to the GRAVNET data calculated using observed periods exhibits a positive slope (panel (b)), whereas the best-fit slope is negative using intrinsic periods (panel (d)). The processing of the GRAVNET data displayed in Figure 3.8 thus suggests that background wind effects, in the case of the Saskatoon data, changed the slope of the $\lambda_z - T$ curves from positive (T_{obs}) to negative ($\hat{T}$).

It is clear that the transformation between observed and intrinsic frequency or period is a highly time and height dependent effect. The observed and intrinsic periods measured by MRM85 during the GRAVNET campaign differ by up to ~100 min [Table of values, Iain Reid, private communication].

In conclusion, direct measurements of gravity wave horizontal wavelengths obtained from radar and airglow measurements are more reliable than any horizontal scale determination from the lidar technique unless background winds are used to determine intrinsic wave periods.

3.5 Spectral Gravity Wave Studies

The current picture of atmospheric gravity wave activity as a field or superposition of waves has led to an emphasis on studying spectral characteristics rather than identifying individual wave events. Recent works such as *Senft and Gardner* [1991] (SG91) and *Collins et al.* [1996] have concentrated on the power spectra of gravity wave perturbations in the atmospheric Na layer. These studies have found good agreement between spectral parameters determined from Na lidar data and spectral models.

However, it is important to note that Na lidar studies of gravity wave spectra agree most closely with the spectral model of *Weinstock* [1990] which has since been shown to be in error by a factor of four [*Zhu*,1994] (Section 2.5.2). Other spectral models, commonly the saturation models as discussed in Section 2.5.1, were found to provide strong agreement with radiosonde and radar determinations of gravity wave spectral magnitudes [*e.g. Allen and Vincent*,1995]. The above indicates that spectra calculated from Na lidar measurements have, on average, larger spectral magnitudes than those calculated using other techniques.

In order to try to explain the disagreement between the Na lidar technique and other mesospheric measurement techniques, a spectrum of waves was simulated. This collection of waves then 'perturbed' a simulated Na layer and the SG91 technique for extracting gravity wave atmospheric density spectra from the spectra of Na lidar profile measurements was applied to these simulated data.

3.5.1 Removal of background Na layer

In gravity wave spectral studies it is usual to extract a mean component of the motion, representing large-scale structure, leaving a perturbation component which contains mesoscale and microscale motions [see also Chapter 2]. These perturbations are then filtered to obtain spectra of mesoscale fluctuations. In time-resolved experimental studies, such as radar or lidar, the mean component is typically calculated as a time average, whereas single-shot measurements from rockets or sondes are detrended or low-pass filtered to calculate a background. These analysis techniques are equivalent, provided that a sufficiently long time-average is used and that long timescale motions have correspondingly long spatial scales.

A velocity or constituent profile may contain fluctuations on a range of temporal and spatial scales. In Chapter 5 two commonly-used techniques for extracting gravity wave (mesoscale) spectra with reference to a time and height resolved data set are examined. The background obtained from a low-pass filtered high resolution profile is compared with that obtained from a time-average of a sequence of lidar profiles. It is cautioned that long-period inertia-gravity waves (large temporal scales) with vertical scales of order 2-3 km have been observed in the troposphere and stratosphere and are treated differently by the two techniques for removing background (mean) motions.

A time-averaged profile of the RD lidar data set presented in Chapter 5 indicates the presence of a long-period wave which is then extracted to produce a spectrum of motions with timescales less than 6.5 hr. In contrast, a gravity wave spectrum of atmospheric motions calculated by extracting the low-pass filtered vertical profile, such as is used in sonde observations [discussed in Chapter 4], will include any long-period, quasi-stationary waves present, resulting in a stronger peak in gravity wave energy associated with incomplete removal of waves present over long timescales. This effect is similar to the problem of using a time-averaged profile over too short a time interval as discussed in Appendix A.

The individual spectra calculated from single-shot measurements may therefore be biased by motions with vertical scales well-resolved by the measurement technique (*i.e.* not low-pass vertical scale filtered) but associated with long timescales, such as inertia-gravity waves. If these waves are rarely present, spectra of monthly or seasonal variation of gravity wave activity will be unaffected as a single profile containing a long-period wave will be statistically insignificant. However, at a location where long-period waves are common, due perhaps to orographic forcing [*e.g. Langford et al.,*1996], the contribution to spectra of single-shot measurements may be very important.

3.5.2 Rayleigh/Na lidar comparison

Lidars can be configured to obtain density profiles through Rayleigh scattering in the stratosphere as well as the Na resonant scattering in the mesosphere [*e.g. Beatty et al.,*1992]. By making use of this technique it is possible to obtain detailed measurements of gravity wave fluctuations in the height ranges ~30-65 km and ~80-100 km. The height resolution of measurements in these two regions is ~100 m which gives excellent possibilities for gravity wave measurements; either quasi-monochromatic or spectral studies.

The difficulty with such measurements is that Rayleigh lidar directly provides total atmospheric density profiles whereas the Na lidar directly measures Na number density. To interpret these two types of measurement in a cohesive fashion it is necessary to convert the Na number density measurements to atmospheric density profiles, using, for example, the procedure discussed in SG91. In other words, the density measurements determined using the Na lidar technique in the mesospheric region are subject to the uncertainties associated with the determination of the background Na layer, as discussed previously.

A set of 150 simulations was carried out to evaluate the effect of the background Na layer shape on determinations of the gravity wave spectral indices. The generating gravity wave spectral indices were q=3, m_*=0.067 cyc km^{-1} and p=2 [defined in Chapter 2] with each of the 150 sets associated with different random wave phases. Figure 3.9 shows the resulting histograms relating parameters calculated from a direct density spectrum, as would be measured by a 'perfect' Rayleigh lidar in the mesosphere, to the parameters extracted through the SG91 technique.

3.6 Discussion of Lidar Processing

The treatment of lidar data in terms of quasi-monochromatic wave events [GV87] and the spectral processing technique [SG91] are in some respects inconsistent. Firstly, the SG91 technique requires the removal of the background Na layer from lidar profiles in order to produce a 'gravity wave only' spectrum. The uncertainty involved in determining a background layer profile in order to extract mesoscale fluctuations is discussed fully in Appendix A. In contrast to the SG91 technique, the GV87 technique supposes that the background layer signature is independent of the double-peaked signature and no background is subtracted before a spectrum is calculated. However, even in the case of a quasi-monochromatic wave event, particularly for large vertical wavelengths, it can be argued that the double-peaked wave signature may be contaminated by the spectral response of the background layer. This primarily effects the parameters A and β.

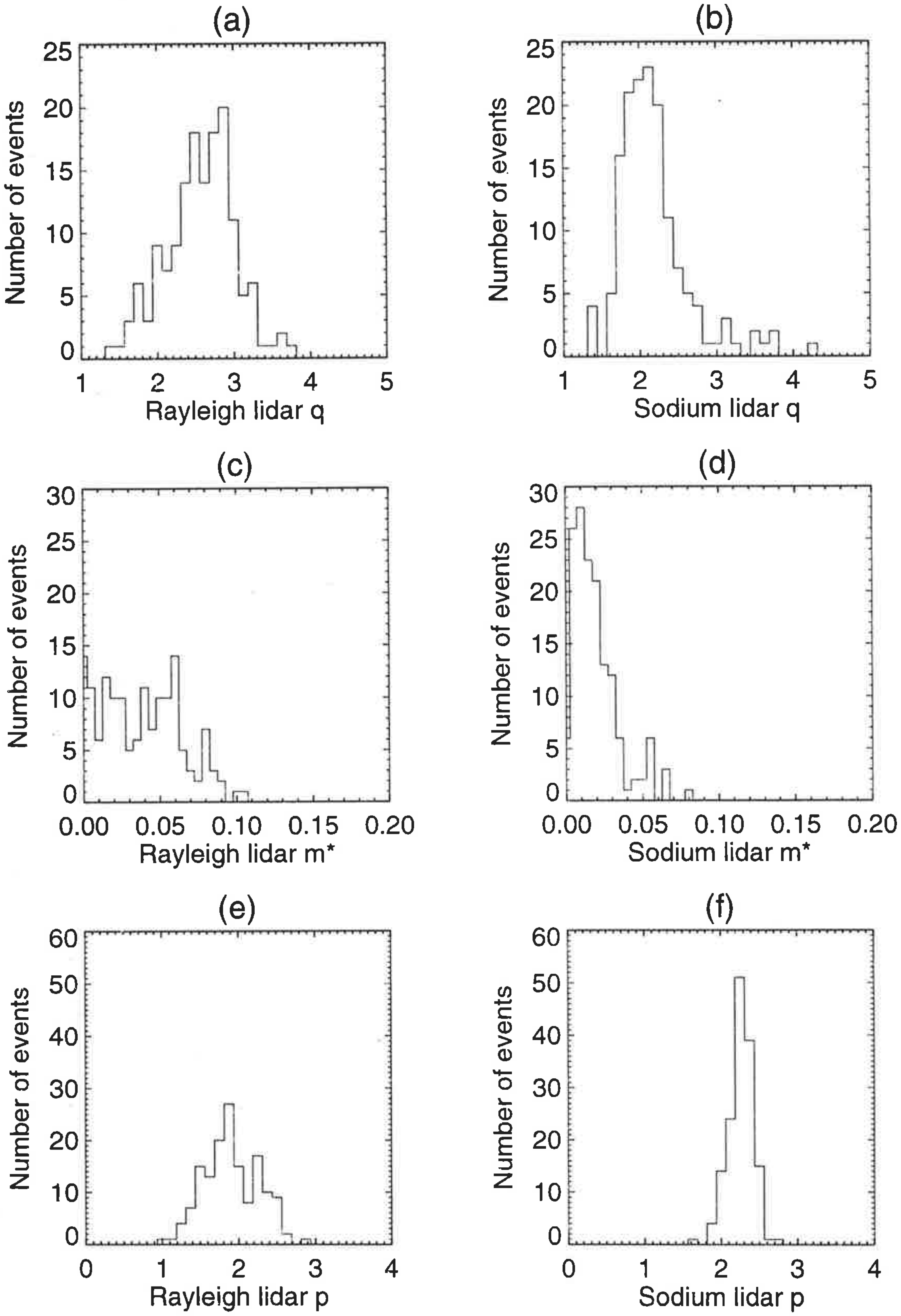

Figure 3.9: Histograms of input (Rayleigh lidar-like) and extracted (Na lidar-like) spectral parameters from 150 simulations of 2-hour observations of Na lidar-like data sets. (a) Input q. (b) Extracted q. (c) Input m_*. (d) Extracted m_*. (e) Input p. (f) Extracted p.

Secondly, the decision must be made as to which processing technique to perform – is a single wave or a spectrum of waves a better representation of the atmosphere in a given case? How should we treat a system consisting of, for example, a random superposition of waves, gradually one wave dominating (due to background winds, filtering effects, tropospheric forcing, etc.) and then the wave field returning to an incoherent state as the dominant wave breaks down?

The characteristic m^{-3} spectral shape [Chapter 2] is obtained very commonly from long-term monthly or seasonal averages [*e.g. Tsuda et al.*,1991; *Allen and Vincent*,1995]. Since lidar data have very high temporal resolution, ~2-5 min, power spectra which were obtained from only two hours of lidar profiles were presented in SG91. Although these certainly do not represent long-term averages in the same sense as monthly or seasonal averages, they represent averages over many samples.

The atmosphere exhibits wave packets or events. This is evidenced very clearly by airglow imagers [*Hecht et al.*,1994] where a night of observations may exhibit periods without any evidence of wave activity interspersed with periods of strong, coherent wave activity [*e.g.* Buckland Park campaign, 1995]. Nights of continuous lidar observations, as presented by GV87 for the mesosphere and BG90 also for the stratosphere, indicate an intermittent wave field. This variation of wave activity during the course of typical observations is a key point in trying to evaluate the contribution of gravity wave motions to the atmospheric circulation.

In using a traditional FFT-based monochromatic wave analysis of Na lidar (here referred to as the GV87 technique), some wave events remain undetected or may be incorrectly detected unless a wave persists unchanged throughout the observation period. GV87 solely treated cases where a coherent wave event was noticeably present in Na lidar profiles for a defined minimum time period. Of 171 identified Na lidar quasi-monochromatic wave events [GV87] only 109 could be analyzed to determine phase velocities and observed periods, implying that even some quasi-monochromatic data sets cannot be analyzed using the GV87 technique.

A SG91-type spectral analysis technique has the advantage that it can be applied to all data sets, however information on spatial and temporal localization of specific wave events is lost. In contrast, a GV87-type analysis technique is only sensitive to any strong, coherent wave components present. The previous discussion leads to the interest in wavelet analysis and other higher-order analysis techniques which are well suited to investigating processes made up of fluctuations on different temporal and spatial scales [*Sato and Yamada*,1994; *Bacmeister et al.*,1996].

3.7 Chapter Summary

A simple, linear model of Na number density response to background atmospheric density fluctuations has been used to generate gravity wave perturbations due to both monochromatic and spectral wave fields. The simulation has indicated some previously overlooked limitations in the processing of Na lidar data.

For quasi-monochromatic wave events it was found that:

- The vertical extent of the mesospheric Na layer imposes an upper limit of 10 km (not 17 km as previously stated [GV87]) on the vertical wavelengths of individual gravity waves able to be identified using the GV87 technique.
- The process of identifying notched gravity wave peaks in the power spectrum is liable to misinterpretation in the presence of more than one strong wave component, as is typically the case.
- The calculation of wave amplitudes and amplitude growth factors is very sensitive to the signal processing methods applied in the calculation of the power spectra.

For gravity wave spectra it was concluded that:

- The removal of the background Na layer through calculation of an average over 2 hr [SG91] is not a good estimate of the true "background" structure of the Na layer since long-period waves were typically removed as part of the background structure.
- Consequently the inferred vertical wavenumber power spectra of gravity wave motions were distorted.

- The characteristic wavelength for gravity wave motions in the mesosphere was generally overestimated.
- The extracted frequency spectra agreed well with the generating parameters.

Chapter 4

Ozone Variability at Macquarie Island

4.1 Introduction

This chapter analyzes electrochemical cell (ECC) ozonesonde, Väisälä radiosonde, and ER-2 aircraft measurements from the 1994 Antarctic Southern Hemisphere Ozone Experiment (ASHOE). The ozonesondes and radiosondes were released from Macquarie Island (54.5°S, 159.0°E) at an elevation of 7 m by the Australian Bureau of Meteorology. The ER-2 aircraft carried out flights in the region south of Christchurch, New Zealand (43.3°S, 172.4°E) towards the Antarctic polar vortex which passed within the vicinity of Macquarie Island on both the southern and northern legs of the flight path (Figure 4.1). The related sonde and aircraft data sets allow a more thorough examination of the structure of stratospheric ozone than is possible from a single data source.

Analysis of northern hemisphere mid-latitude and polar ozonesonde measurements of ozone mixing ratio and potential temperature by *Teitelbaum et al.* [1994] and *Moustaoui* [1995] indicated that in cases exhibiting quasi-monochromatic wave variability there was evidence of similar wave-like activity in the ozone mixing ratio and temperature fields in the dynamically-controlled region of the stratosphere. However, a disagreement in the statistically determined magnitudes of measured and expected ozone

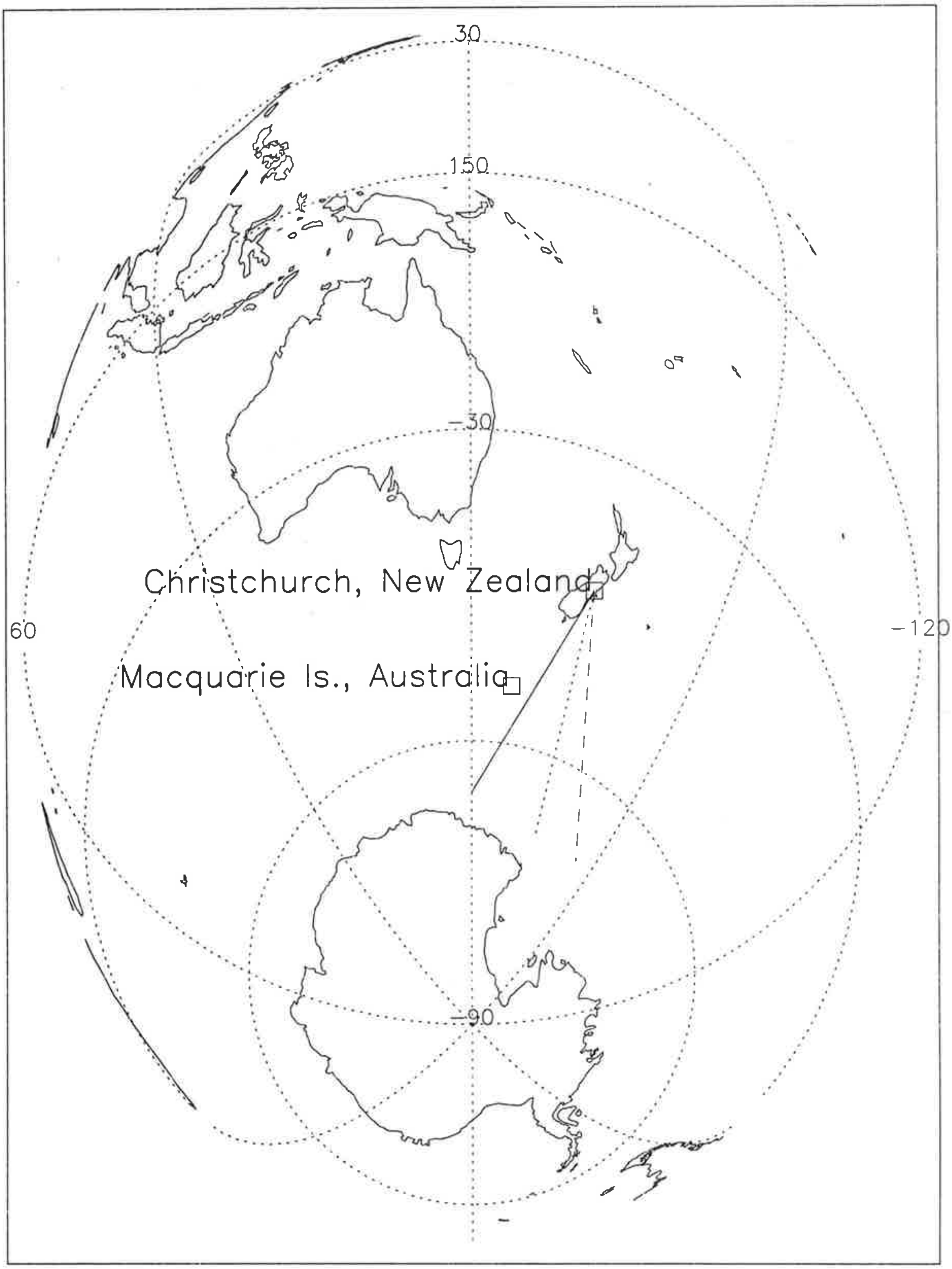

Figure 4.1: Diagram showing three ER-2 flight paths and position of Macquarie Island. Flight paths are shown for 1 June 1994 (solid line), 13 October 1994 (dashed line), and a typical south–north flight (dotted line).

mixing ratio variances of a factor of ~5 has been noted previously by *Ehhalt et al.* [1983] based on ozonesonde data from Hohenpeissenberg, Germany (48°N, 11°E). Such an inconsistency suggests caution in any purely wave-based explanation of ozone variances and the importance of large-scale transport processes in addition to mesoscale advective processes in driving the observed ozone fluctuations [*e.g. Holton,*1987; *Reid et al.,*1993; *Mitchell et al.,*1996].

Radiosonde measurements of horizontal velocity and temperature profiles from Macquarie Island have been analyzed extensively for information on gravity wave activity [*Allen and Vincent,*1995]. The resulting detailed gravity-wave climatology for Macquarie Island based on the period April 1993 to March 1995 indicated important wave activity at the site with the largest velocity variances measured during April–May [*Allen and Vincent,*1995; *Allen,*1996]. Recent ray-tracing experiments have indicated that extratropical jet–front systems were a major source of inertia-gravity waves at this location [*Guest et al.,*1996].

Ozonesonde measurements have been used previously to examine the change in ozone profile associated with the Antarctic ozone hole [*e.g. Hofmann et al.,*1989; *Johnson et al.,*1992; *Hofmann et al.,*1995]. Seasonal trends in mean ozone profiles [*London and Liu,*1992], and total integrated column ozone amounts [*e.g. Hofmann et al.,*1995] have also been investigated using ozonesonde profile ozone measurements. Ozonesonde profiles also provide the detailed height resolution (typically ~50 m) necessary to study smaller vertical scale ozone fluctuations [*Reid and Vaughan,*1991; *Teitelbaum et al.,*1994].

Ozone mixing ratio and potential temperature measurements from the ER-2 aircraft during the ASHOE campaign were of extremely high temporal resolution (1 Hz) along mainly horizontal flight paths. The identification of gravity wave activity from ER-2 aircraft measurements has been discussed in *Chan et al.* [1991], *Danielsen et al.* [1991], and *Pfister et al.* [1993]. Here, ER-2 aircraft data are used to estimate the large-scale horizontal gradients of ozone and potential temperature at the height of the aircraft flight path during the Macquarie Island ozonesonde flights.

The overall aim of this chapter is to examine the database of Macquarie Island sonde data, and aircraft measurements where available, in order to characterize the physical processes involved in producing the observed fluctuations in ozone and temperature. Using simultaneously released high resolution radiosondes and ozonesondes, yielding measurements of horizontal velocity, temperature, and ozone mixing ratio, a detailed study of gravity wave motions and ozone response is possible. In particular, the importance of vertical transport and horizontal advection in the formation of the structures will be examined.

Section 4.2 discusses the analysis performed on the Macquarie Island ozonesonde and radiosonde data sets including the identification of quasi-monochromatic wave activity in individual sonde profiles, an examination of longer-term variability during the ASHOE campaign, and some examples of ozone lamination. Section 4.3 discusses the application of a basic vertical transport model to estimate the contribution of gravity-wave vertical advection to the observed ozone perturbations. In Section 4.4, data from the NASA ER-2 aircraft are used to estimate meridional ozone gradients, and hence meridional quasi-horizontal advection terms [see also Appendix D].

4.2 Ozonesonde and Radiosonde Analysis

The Macquarie Island data set analyzed here consists of simultaneously released Väisälä radiosonde and ECC ozonesonde measurements [*Komhyr,*1969]. Typically two sonde flights per week were carried out during the ASHOE campaign when ER-2 aircraft missions occurred in the area from March to October 1994.

The ozonesonde measurements provide a vertical 'snapshot' of the atmosphere from the surface up to 30-35 km including measurements of pressure, temperature, and ozone mixing ratio, partial pressure, and concentration. The radiosondes at Macquarie Island had a typical burst height of 25 km providing pressure, zonal and meridional velocities, and temperature [*Allen,*1996]. Due to differences in the ascent speeds and paths of the radiosonde and ozonesonde, the data are not simultaneous at every height. The data from the two devices were interpolated using a cubic spline fit to provide ozonesonde and radiosonde data at equispaced heights. The dual sonde measurements of temperature provided a qualitative check that the two sonde paths were similar.

By removing the mean ozone and temperature profile it is possible to extract

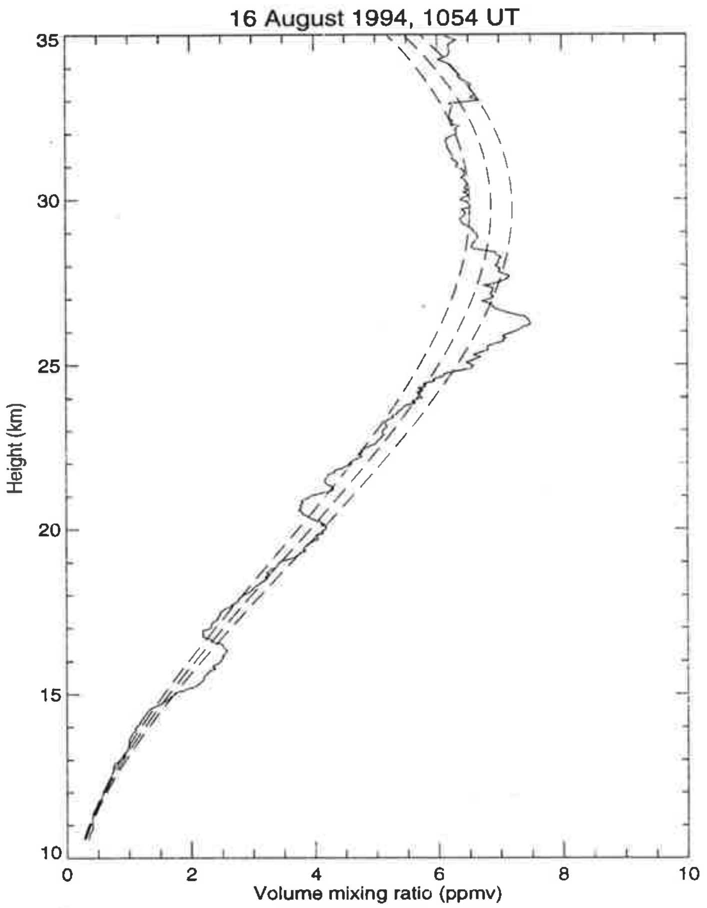

Figure 4.2: Ozonesonde ozone volume mixing ratio profile from Macquarie Island on 16 August 1994 at 1054 UT. A least-squares cubic polynomial fit to the mean profile and 5% nominal error margin either side of the mean profile are overplotted as dashed lines.

mesoscale perturbations. Figure 4.2 shows the ozone mixing ratio profile from a sonde launched at Macquarie Island at 1054 UT on 16 August 1994. A cubic polynomial fitted mean ozone volume mixing ratio and temperature profile has been used throughout this analysis for the extraction of mesoscale perturbations from ozone and temperature measurements. This approach is consistent with the analysis of radiosonde temperature and velocity data carried out by *Allen and Vincent* [1995] and *Vincent et al.* [1996]. In contrast, *Teitelbaum et al.* [1994] made use of a low-pass filter to obtain an estimated mean ozone mixing ratio profile.

The relative fluctuations calculated for the upper and lower segments of the ozone measurement are affected by the process of removing the background profile. In the following analysis, calculations of relative fluctuations are displayed for the stratosphere only.

The 11 months of available ozonesonde data at Macquarie Island were suitable for an analysis of monthly and intra-seasonal stratospheric ozone variability. Figure 4.3 shows the individual cubic polynomial fitted mean ozone mixing ratio profiles as well as seasonal mean ozone profiles for autumn (March–May), winter (June–August), spring (September–November), and all three seasons approximating an annual mean profile. Very few successful sonde launches were carried out in the summer months at the beginning of the ASHOE campaign. The variation in the mean ozone mixing ratio vertical profile between seasons is not pronounced. However, there is strong variation between mean ozone profiles calculated for the winter measurements which may be attributed to the variability in the position of the polar vortex wall relative to Macquarie Island [*Tuck*,1989].

The monthly RMS relative ozone mixing ratio perturbations were calculated over the height range 15-30 km for the 37 ozonesonde launches which provided reliable data. Where more than one valid data set was available during a month (every month except January), error bars indicate the standard deviation. 'Predicted' values of RMS relative ozone mixing ratio perturbations were calculated from temperature perturbations using the basic dynamical model (4.3) (Section 4.3).

Figure 4.4(a) illustrates the huge discrepancy between the measured and predicted RMS relative mixing ratio values. It is noted that the measured RMS variations are at a minimum in September – a month where the Antarctic polar vortex effectively isolates mid-latitude air masses from polar air intrusions. Figure 4.4(b) indicates a tendency for measured ozone perturbations to be larger than those predicted based on temperature perturbations by a ratio of 5-10. There is some indication of a monthly variation with a maximum ratio of ~12 in July (mid-winter) and a minimum ratio of ~5 in spring.

The relation between the variances of ozone mixing ratio and temperature fluctuations is well illustrated in a more physical sense by the equivalent displacement height (EDH) approach of *Röth and Ehhalt* [1987]. The EDH ($\Delta_q(z)$) is a measure of tracer variation which is weighted by the mean vertical gradient of the tracer profile $\frac{d\bar{q}(z)}{dz}$. It is defined as [*Ehhalt et al.*,1983]

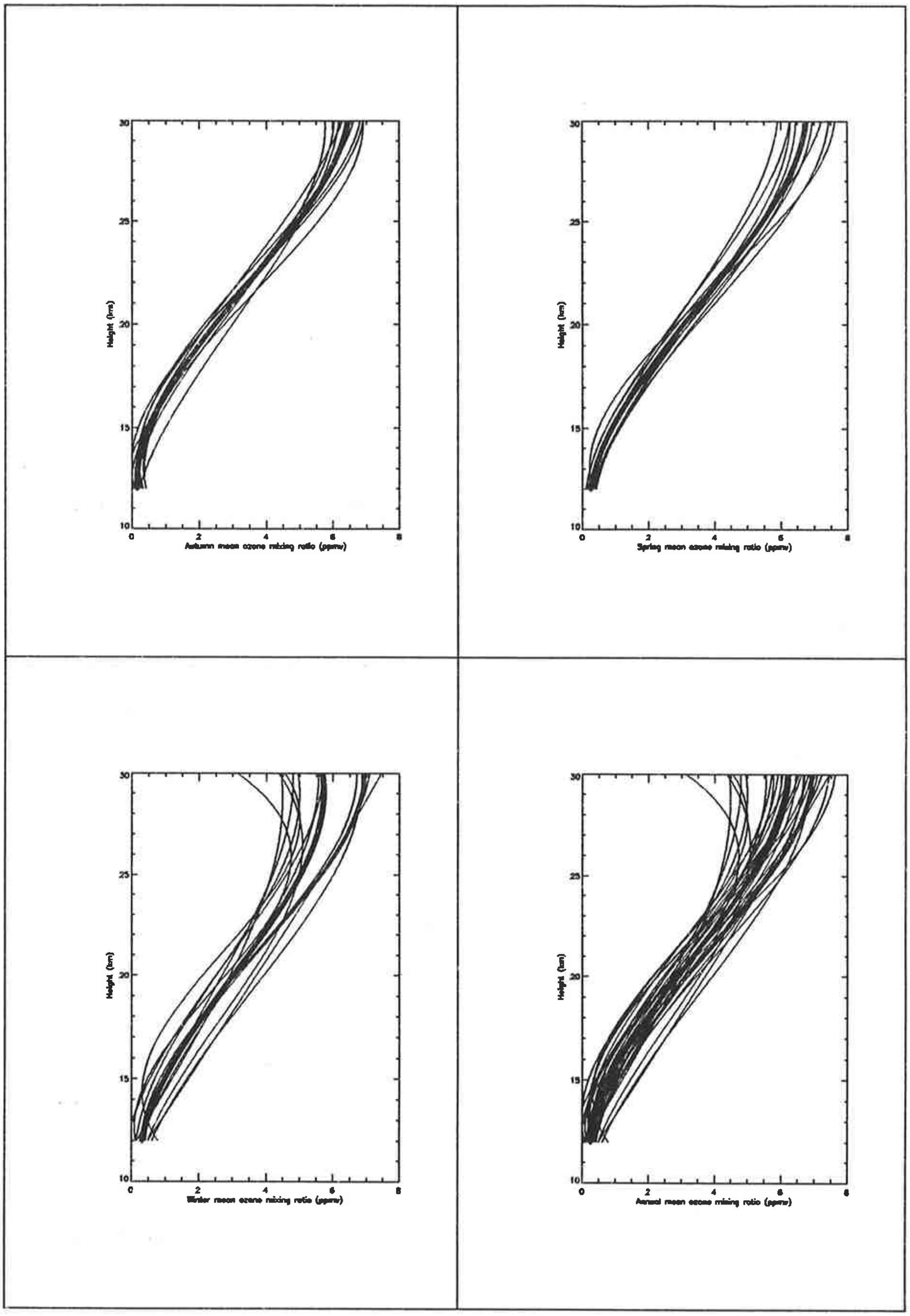

Figure 4.3: Seasonal and annual mean ozone volume mixing ratio profiles at Macquarie Island.

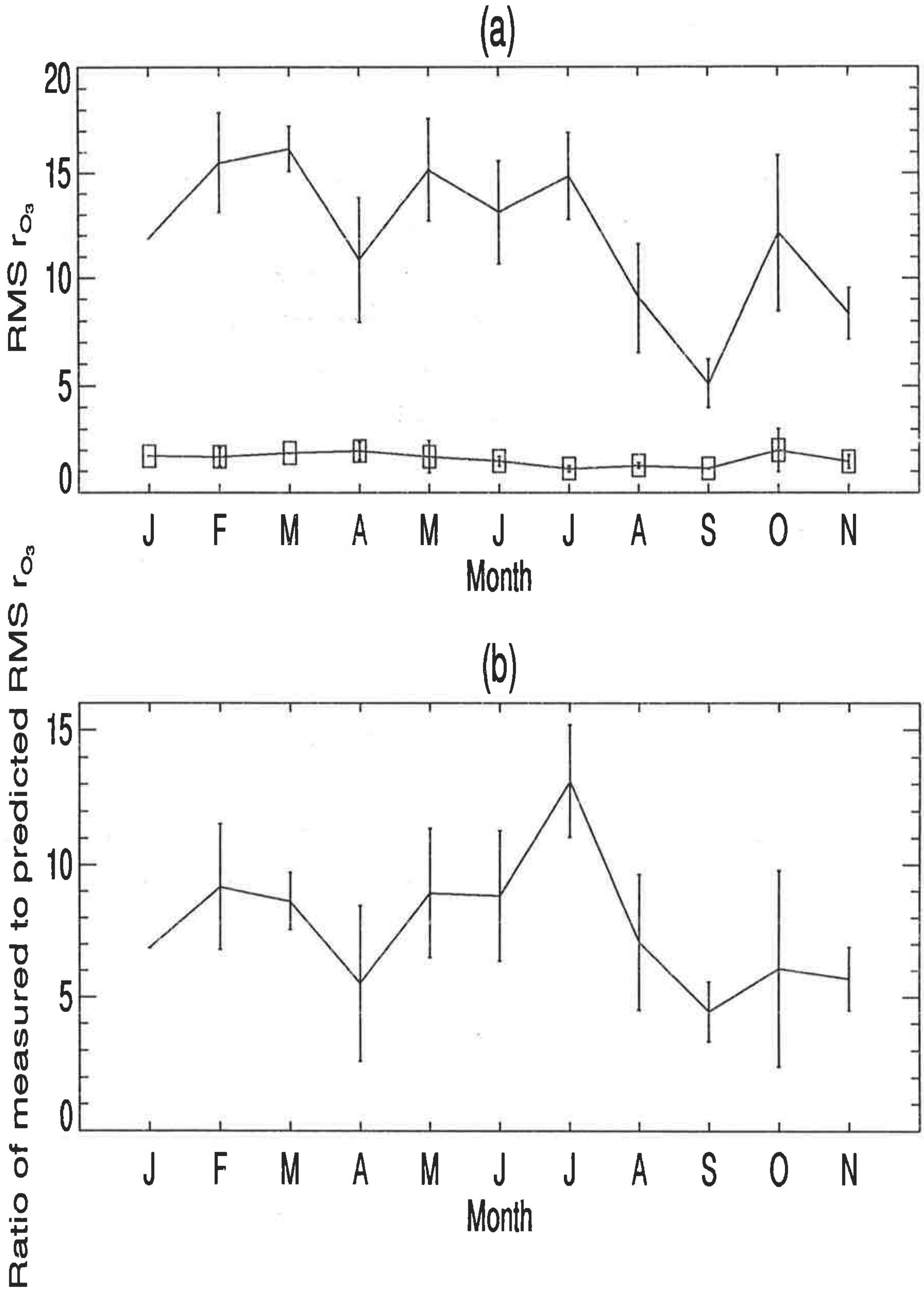

Figure 4.4: (a) Monthly variation of measured (no symbol) and predicted (square) RMS relative ozone mixing ratio perturbations. (b) Monthly variation of the ratio of measured to predicted RMS relative ozone mixing ratio perturbations. RMS values are calculated between 15-30 km and error bars on both plots indicate a standard deviation.

$$\Delta_q(z) = \frac{\sigma_q(z)}{\frac{d\bar{q}(z)}{dz}}, \tag{4.1}$$

where $\sigma_q(z)$ is the tracer mixing ratio standard deviation.

The EDH was developed as a measure of the mean vertical displacement undergone by a parcel. This approach was based on the observation that a variety of stratospheric trace gases exhibited a strong dependence between tracer variance and mixing ratio vertical gradient [*Ehhalt et al.*,1983]. As emphasized by ***Röth and Ehhalt*** [1987], the variations included in the calculation of $\sigma_q(z)$ are not necessarily due to vertical motions only. A tracer with strongly stratified vertical variation, such as potential temperature θ, is relatively insensitive to horizontal parcel displacements; hence the EDH of θ provides an approximate measure of mean vertical displacements.

Figure 4.5 compares the EDH values of ozone mixing ratio and potential temperature calculated for the nine autumn data sets from 21 March to 24 May 1994. The limited extent of presently available ozonesonde observations at Macquarie Island, compared with the extensive Hohenpeissenberg database [*Röth and Ehhalt,*1987], means that this study could only provide an indication of EDH values. However, the values of EDH for ozone of ~0.5 km and for potential temperature of ~0.1 km calculated for the height region of 15-25 km at Macquarie Island are in qualitative agreement with the northern hemisphere mid-latitude values obtained by *Röth and Ehhalt* [1987] of ozone EDH ~0.5-1.0 km and potential temperature EDH ~0.2-0.5 km.

4.2.1 Ozone laminae

Four examples of ozone laminae observed at Macquarie Island are presented in Figures 4.6(a). Ozone laminae were clearly apparent in 18 of the 32 data sets included in this analysis. The first laminar event identified occurred in April (Figure 4.6 upper left). The temperature profiles corresponding to the ozone laminar events (Figures 4.6(b)) indicate that the strong observed ozone features at Macquarie Island are not associated with major temperature perturbations, contrary to the suggestion of temperature lamination by *Mitchell et al.* [1996].

There is a clear tendency for maximal occurrence of laminar events in the heights

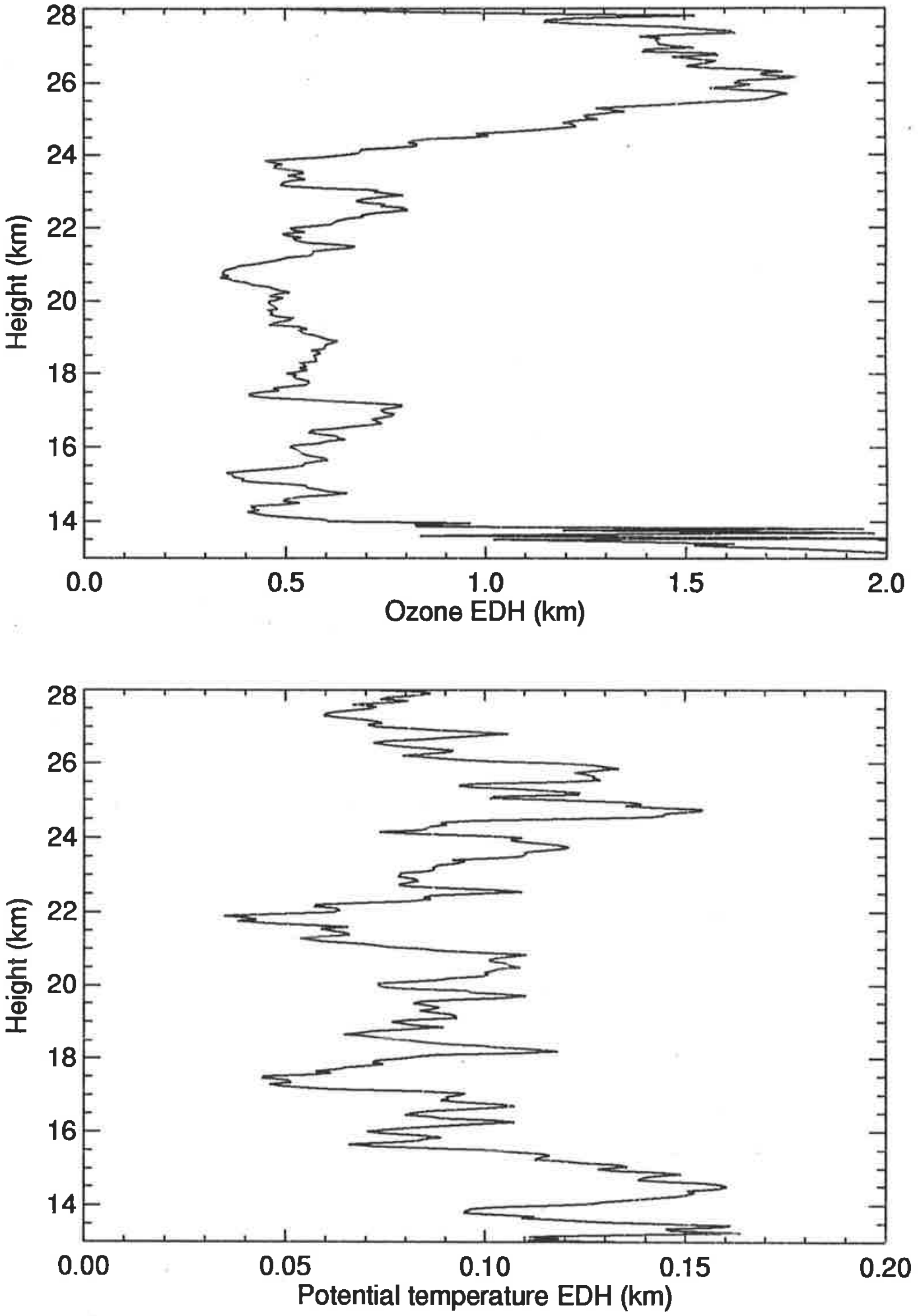

Figure 4.5: Autumn 1994 ozone mixing ratio (upper panel) and potential temperature (lower panel) EDH profiles at Macquarie Island.

12-18 km (Figures 4.6(a)). The observations discussed in Chapter 5 and from other northern hemisphere locations also indicated laminae occurring most commonly at these lower stratospheric levels [*Reid and Vaughan,*1991; *Reid et al.,*1993].

The presence of laminae at Macquarie Island in over half the ozone profiles obtained during the observation period indicates that the dynamical and/or chemical processes responsible for the vertically localized ozone enhancements are not restricted to the period corresponding to the breakdown of the Antarctic winter–spring vortex. In fact, there is evidence of lamination in profiles from April to November 1994. If the lamination of ozone is due primarily to the quasi-horizontal advection of air parcels over large horizontal distances (~1000 km), these results suggest that large-scale processes must be sporadically active in all seasons and further that the height range 14-15 km is a preferred level for large-scale transport.

4.3 Basic Dynamical Model

From the tracer continuity equation and gravity-wave polarization relations [Chapter 2], it is possible to express the predicted relation between ozone mixing ratio and potential temperature perturbations as [*e.g. Teitelbaum et al.,*1994],

$$r_{O_3} = \frac{d\bar{O}_3}{dz}\frac{g}{\bar{O}_3 N^2} r_\theta, \tag{4.2}$$

where r_{O_3} is the relative ozone mixing ratio perturbation, r_θ is the relative potential temperature perturbation, $\bar{O}_3$ is the mean ozone mixing ratio, and horizontal gradients of $\bar{O}_3$ and $\bar{\theta}$ have been neglected. Relative temperature and relative potential temperature perturbations are approximately equal ($r_\theta \approx r_T$) for gravity wave motions, since the relative pressure perturbations are negligible, so that (4.2) becomes

$$r_{O_3} = \frac{d\bar{O}_3}{dz}\frac{g}{\bar{O}_3 N^2} r_T. \tag{4.3}$$

This so-called basic dynamical model suggests that ozone and temperature perturbations should be in-phase at heights below the peak of the mean ozone mixing ratio profile (~25 km), where there is a positive gradient in the mean ozone mixing ratio,

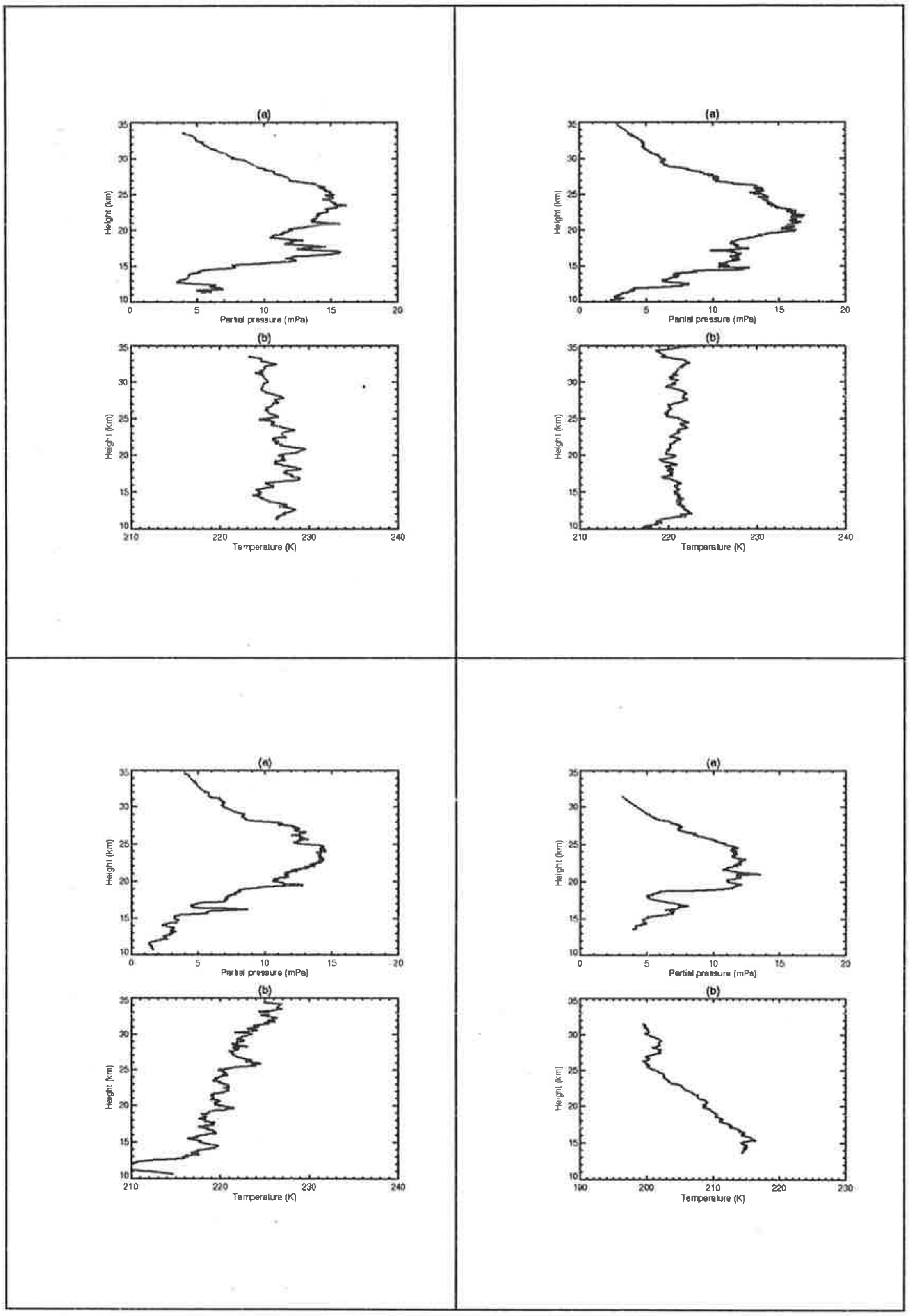

Figure 4.6: (a) Ozone partial pressure and (b) temperature profiles for laminar events of 24 April, 5 May, 24 May, and 6 June, 1994.

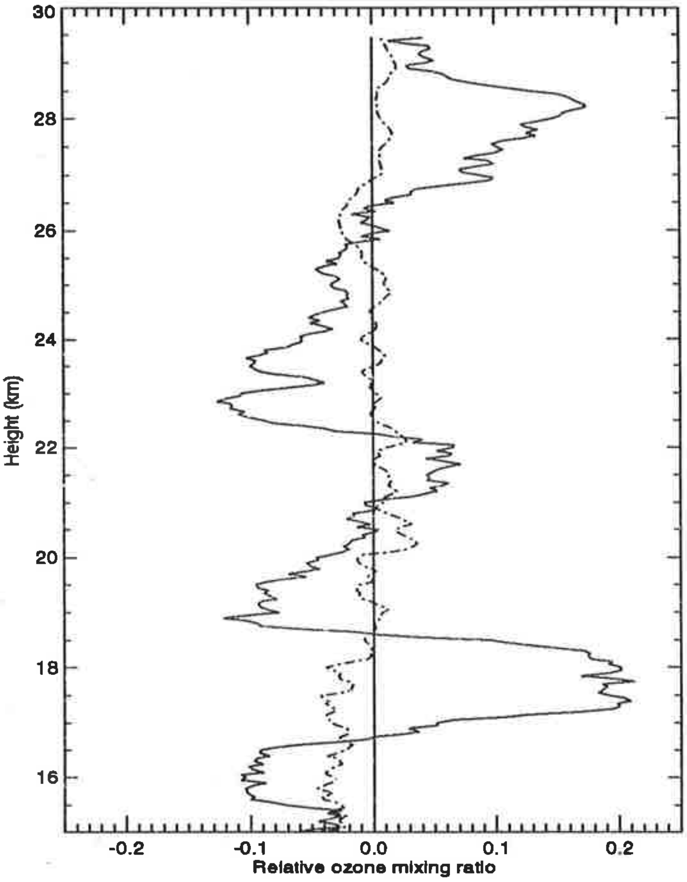

Figure 4.7: Measured (solid line) and predicted (dotted-dashed line) relative ozone mixing ratio perturbations at 1054 UT on 16 August 1994.

and in anti-phase above the peak where the mean ozone mixing ratio gradient is negative. Hence a phase change in ozone perturbations is expected at the layer peak [see also Chapter 3 and Appendix A]. This basic model is only valid at heights where the dynamical timescales are much shorter than the photochemical timescales, *i.e.* below ~25 km. Above these heights it is necessary to include parameterized photochemistry terms as discussed in Section 1.5.1 [*Lindzen and Goody,*1965; *Zhu and Holton,*1986].

The basic dynamical model (4.3) was applied to *predict* relative ozone mixing ratio perturbations using $\frac{d\bar{O}_3}{dz}$ calculated from the mean fitted ozone mixing ratio profile and r_T calculated from the ozonesonde data. Figures 4.7 and 4.8 show examples of comparisons between measured and predicted r_{O_3} using the basic dynamical model. Figure 4.7 shows a case from 16 August where there was significant disagreement between the measured and predicted r_{O_3} values. Figure 4.8 illustrates an ozonesonde

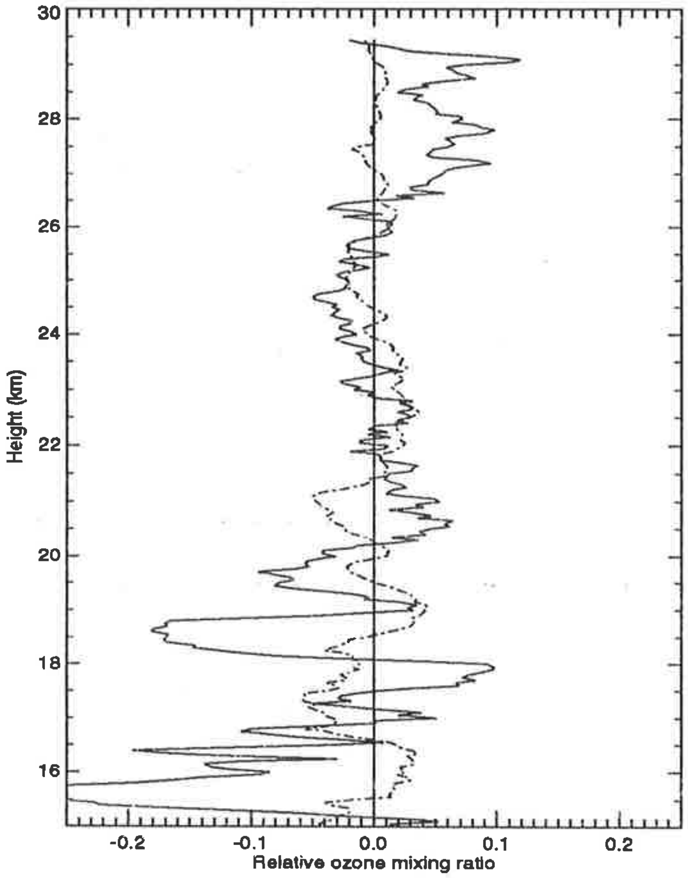

Figure 4.8: Measured (solid line) and predicted (dotted-dashed line) relative ozone mixing ratio perturbations at 0443 UT on 16 September 1994.

observation from 16 September where there was some phase agreement between perturbations in the measured and predicted r_{O_3} profiles below 20 km, suggesting that a similar wave-like structure was present in both ozone and temperature. However, the measured peak values of r_{O_3} of 10-20% (solid line) contrasted sharply with the predicted maximum relative perturbations of approximately 5% based on the basic dynamical model (dotted-dashed line).

A vertical scale of ~1.5-2 km was evident in Figures 4.7 and 4.8 in the measured r_{O_3} fluctuations which is consistent with typical stratospheric gravity wave vertical wavelengths [*Tsuda et al.*,1991]. However, it is emphasized that the lack of agreement between the apparent wave-like fluctuations in the measured r_{O_3} and those calculated from r_T in Figure 4.7 suggests caution in the interpretation of these features in terms of quasi-monochromatic gravity waves.

In general for the Macquarie Island data set, phase agreement between measured and predicted ozone profiles (example Figure 4.8) was evident in about 15 of the 32 valid data sets. However, the magnitudes of the perturbations extracted from ozone were significantly larger than were expected based on the relative temperature perturbations. It is possible to make a qualitative comparison with the results of *Teitelbaum et al.* [1994] who displayed measured and calculated relative ozone fluctuations from individual sonde profiles. The measured ozone fluctuations in *Teitelbaum et al.* [1994] at many heights were larger by a factor of 2-5 than those calculated from the relative temperature profile.

From the above examination of the relation between ozone and temperature variations it is clear that wave-like mesoscale variations are present in some data sets; but that the magnitudes predicted from the temperature perturbations, based on vertical transport alone, are typically much smaller than the observed ozone perturbations. The disagreement in some cases is as large as a factor of 10.

The ozonesonde measurements were used as a stand-alone data set in this section to estimate the relationship between ozone and temperature variations, and hence the importance of gravity-wave-induced vertical transport. Although radiosonde measurements of mean and perturbation horizontal velocities are available, information on the mean horizontal structure of ozone is absent from such measurements. With the additional coordinated ER-2 aircraft data available during ASHOE, an indication of the horizontal ozone structure present during the ozonesonde flights will be obtained in the following sections.

4.4 Ozonesonde, Radiosonde, and ER-2 Aircraft Analysis

Following the initial analysis of the ozone and temperature information from the Macquarie Island sonde ascents, this section extends the analysis to include ER-2 aircraft measurements where available. Firstly, due to the coordinated but non-simultaneous nature of the sonde and aircraft measurements, a comparison is made between the

Date	Sonde (UT)		Approx. time ER-2	Approx. ER-2	Direction
	Release	~18 km	near M.I. (UT)	height at M.I.	of ER-2
(yymmdd)	time	time	south	(km)	
940413	2305	2405	2115	18.7	S/N (1°)
940524	1100	1200	2213	18.3	S/N (1.5°)
940601	1433	1533	2050	18.7	SW/NE (20°)
940603	1143	1243	2155	19.0	S/N (7°)
940730	2302	2402	2155	19.0	S/N (0.5°)
940806	2302	2402	2040	18.6	S/N (0.5°)
941010	0949	1049	2245	18.1	S/N (0.5°)
941013	2359	2459	2245	18.3	SE/NW (15°)
941016	2149	2249	2245	18.2	S/N (3°)

Table 4.1: Macquarie Island (M.I.) ER-2/sonde data set comparison. Ozonesonde release times and the time the sonde reached the ER-2 flight level (~18 km) are shown. The estimated time of closest approach of the ER-2 to M.I. and the height of the aircraft at this time for the southern leg of the flight path is shown. The estimated time of closest approach on the return northern leg was 4 hr 12 min later.

potential temperature–ozone surfaces (θ,O_3) from the ozonesonde and the ER-2 aircraft in order to determine whether the two measurement techniques sampled similar air parcels. As discussed in Chapter 2, θ and O_3 are usually good lower stratospheric tracers which can be used to label air parcels.

4.4.1 Potential temperature–ozone surfaces

This analysis makes use of the horizontal ozone and temperature trajectories (with a correction for the relatively small vertical drift of the aircraft) available from the ER-2 and the quasi-vertical trajectories of the ozonesonde measured on the nine dates listed in Table 4.1.

These nine ozonesonde flights were successfully launched on ER-2 flight days with reliable data from both the radiosonde and the ozonesonde. The height and time of the ER-2 at the point of estimated closest approach to Macquarie Island is shown in Table 4.1. From the radiosonde data it was determined that the background winds were predominantly eastward and hence the drift of the ozonesonde was toward the ER-2 flight path. An estimated horizontal displacement of the sondes during the ~1 hr ascent to 18 km was 50-100 km to the east. Figure 4.1 indicates the approximate positions of three selected ER-2 flight paths and Macquarie Island.

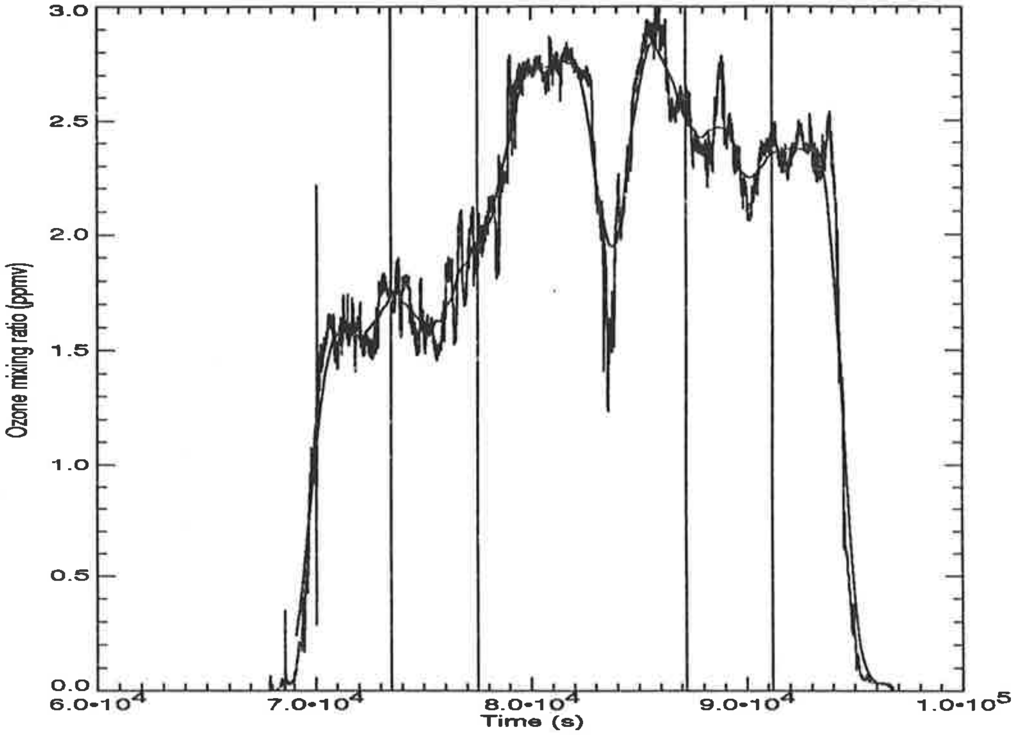

Figure 4.9: Ozone volume mixing ratio measured during ASHOE from the ER-2 aircraft during a quasi-horizontal flight path on 1 June 1994. The aircraft enters the polar vortex at ~80000 s and reverses direction at ~84000 s. The vertical lines mark the region where the aircraft is in the vicinity of Macquarie Island. A smoothed fit has been overplotted which was calculated as a running mean over 300 km flight path segments.

An example of an ozone mixing ratio measurement from a complete ER-2 aircraft quasi-horizontal flight path is shown in Figure 4.9 for the 1 June 1994 flight which approached closest to Macquarie Island. This measurement starts with the aircraft take-off at Christchurch, New Zealand. The aircraft flight path south intersects a region of high ozone content before entering the polar vortex region and reversing direction for the return flight (see caption of Figure 4.9).

For the ensuing analysis it was important to ensure that similar air parcels were sampled by the aircraft and the sonde. For the ozonesonde and ER-2 flights which took place on the same day, (θ,O_3) maps of both ER-2 and sonde data were used to investigate the validity of performing comparisons between the two data sets. Figure 4.10 shows two examples of (θ,O_3) maps where agreement between the sonde and the aircraft is satisfactory. Crosses mark the estimated positions of closest approach of the sonde and ER-2 (*i.e.* the ER-2 at the latitude of Macquarie Island and the sonde at the height of the ER-2 flight path at this position). Of the nine data sets listed in Table 4.1, seven data sets show similar (θ,O_3) maps for the ER-2 and sonde data. It is these seven data sets which have been used in the following comparisons [further examples in Appendix D].

4.4.2 Estimation of meridional ozone gradients

The ASHOE ER-2 aircraft data were used to estimate the mean meridional ozone mixing ratio gradient $\bar{O}_{3MER}^{ER2}$. The ER-2 data set comprised some days with highly variable ozone amounts and others with relatively smooth meridional ozone gradients. Hence, the length of the horizontal trajectory used in the calculation of $\bar{O}_{3MER}^{ER2}$ is an important consideration. The value of the meridional gradient was estimated for several different trajectory lengths in order to investigate the robustness and the variability of the calculated $\bar{O}_{3MER}^{ER2}$.

In the figures included here, four different time intervals were chosen for the calculation of $\bar{O}_{3MER}^{ER2}$: 500 s, 1000 s, 2000 s, and 4000 s. These represent horizontal flight path segments of approximately 100 km, 200 km, 400 km, and 800 km, respectively; assuming an average aircraft speed of 200 m s^{-1}.

The two ER-2 flight paths on 1 June and 13 October, 1994 contain significant longitudinal variation, as well as latitudinal variation (Table 4.1). The value of $\bar{O}_{3PATH}$ measured in these cases represents the combination of zonal and meridional components, *i.e.*

$$\bar{O}_{3PATH} = \frac{1}{PATH}\left(\delta(zonal)\bar{O}_{3ZON} + \delta(meridional)\bar{O}_{3MER}\right). \qquad (4.4)$$

where $\delta(zonal)$ and $\delta(meridional)$ are the distances travelled in the zonal and meridional directions, respectively. Equation (4.4) expresses the gradient measured along the ER-2 flight path in terms of the equivalent movement of the parcel of air along the zonal and meridional directions independently. It is assumed that $\bar{O}_{3ZON}$ and $\bar{O}_{3MER}$ remain constant over the horizontal flight paths.

From data sets with both latitudinal and longitudinal drift, it would be possible to

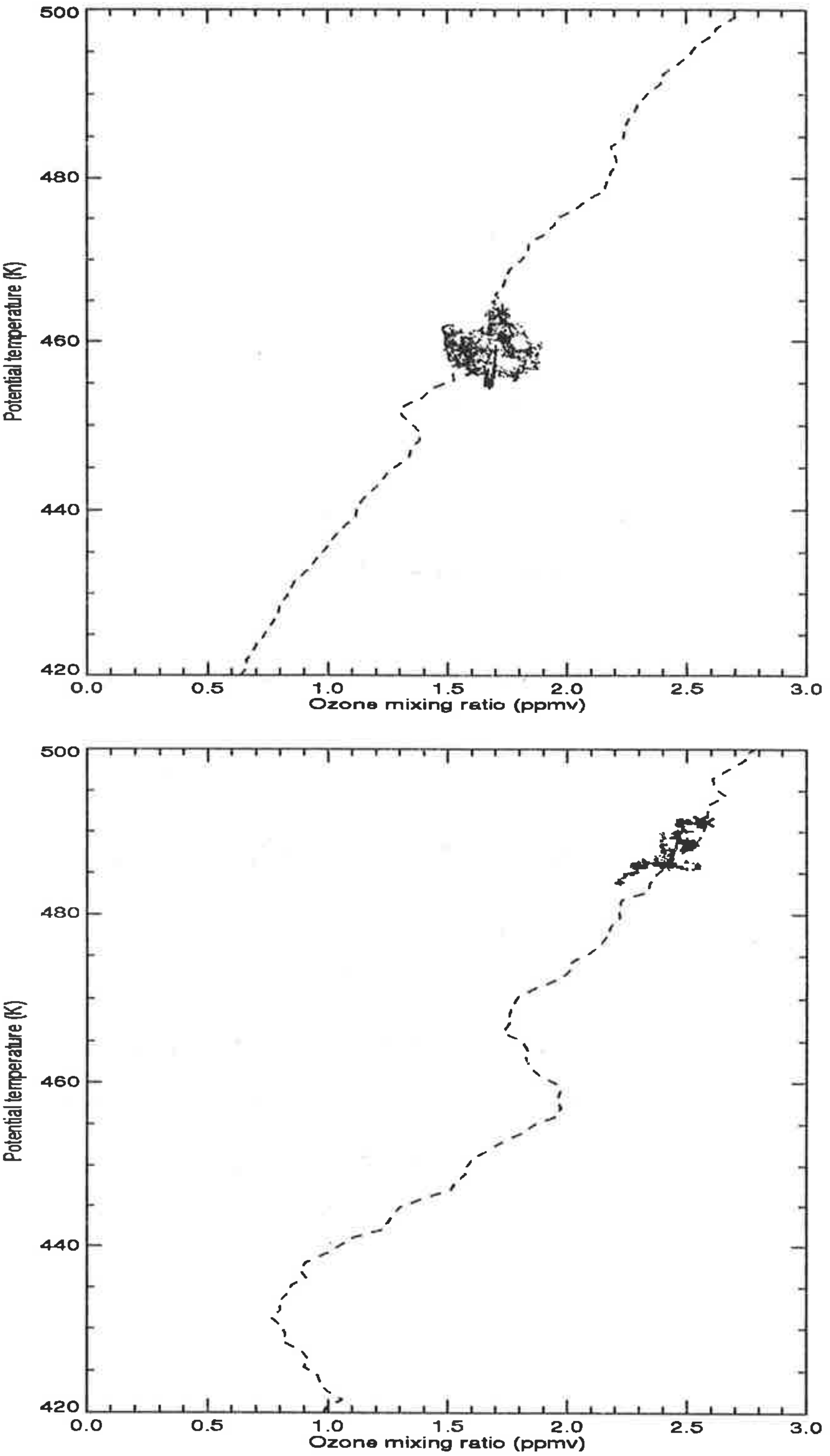

Figure 4.10: Plots of potential temperature–ozone volume mixing ratio for 1 June 1994 (upper panel) and 16 October 1994 (lower panel). The dashed line indicates the ozonesonde measurement and the dotted region indicates the ER-2 values measured in the vicinity of Macquarie Island. The two crosses indicate the values of (θ,O_3) at the estimated positions of the ER-2 aircraft's closest approach to Macquarie Island on the southern and northern flight segments.

examine qualitatively the importance of zonal and meridional mean ozone gradients. Such a comparison requires the use of two closely spaced ER-2 data sets, one of which has a flight approximately due south, the other SE or SW. It is necessary to assume that the meridional gradient of ozone is approximately constant over periods of roughly two days. This is a difficult assumption to justify given the synoptic-scale changes that may occur over this timescale and hence the ASHOE data set was not used for this type of calculation. However, it may be possible to make use of satellite data to investigate the reliability of such an approach or to measure the relative magnitudes of zonal and meridional gradients directly.

Figure 4.11 shows comparisons between the values of $\bar{O}_{3MER}$ obtained directly from the ER-2 data and the values necessary to bring about the fluctuations observed in the ozone profiles. The major limitation on this estimate of $\bar{O}_{3MER}$ is the assumption of negligible $\bar{O}_{3ZON}$. It was found that the values of $\bar{O}_{3MER}$ estimated from the ER-2 aircraft data were ~0.005 ppmv km^{-1}.

4.4.3 Estimation of gravity wave quasi-horizontal advection

Quasi-horizontal advection takes place due to both synoptic-scale motions and gravity-wave horizontal wind perturbations. In this section, the role of gravity-wave-induced horizontal transport is investigated. The relative importance of gravity-wave-induced horizontal motions and mean horizontal motions will be discussed qualitatively.

The response of ozone (O_3) and potential temperature (θ) to gravity wave vertical and horizontal advection can be expressed as [*Teitelbaum et al.*,1994]

$$r_{O_3} = \frac{O_3'}{\bar{O}_3} = \frac{-i}{\hat{\omega}\bar{O}_3}\left(\bar{O}_{3z}w' + \bar{O}_{3x}U'\right), \tag{4.5}$$

$$r_\theta = \frac{\theta'}{\bar{\theta}} = \frac{-i}{\hat{\omega}\bar{\theta}}\left(\bar{\theta}_z w' + \bar{\theta}_x U'\right), \tag{4.6}$$

where U' is the total horizontal wind perturbation and $\bar{O}_{3x}$ and $\bar{\theta}_x$ are the total mean horizontal ozone and potential temperature gradients, respectively.

From (4.6) it is possible to obtain an expression for the vertical wind perturbation w' by assuming that $\bar{\theta}_x$ is negligible (*i.e.* $\bar{\theta}(x,z) \approx \bar{\theta}(x)$) and the motion is adiabatic.

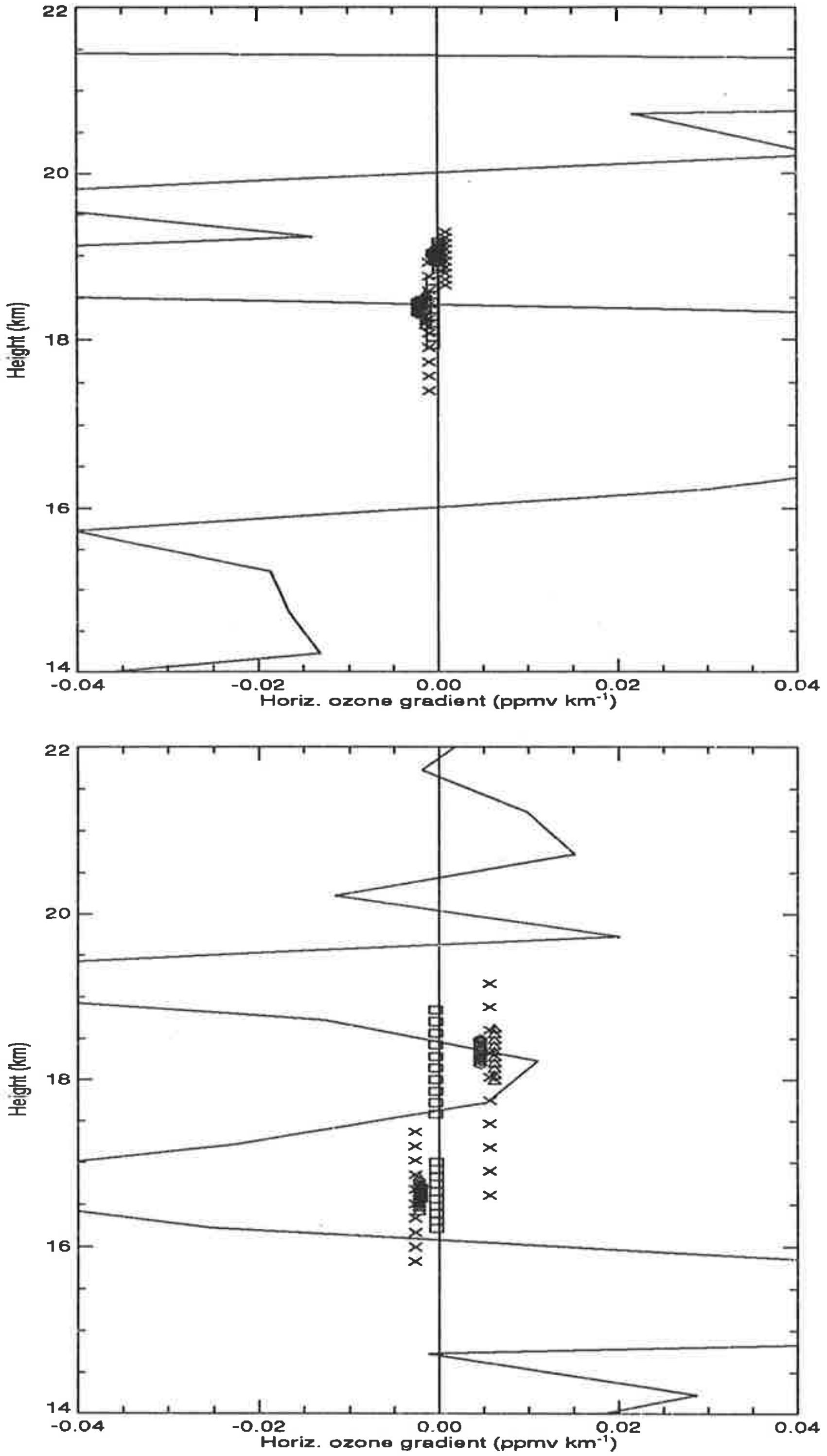

Figure 4.11: Plots of estimated mean meridional ozone mixing ratio gradients for 1 June 1994 (upper panel) and 16 October 1994 (lower panel). The bold line indicates the value of mean meridional ozone mixing ratio gradient calculated from sonde data. Symbols represent gradients calculated over different ER-2 aircraft horizontal flight path lengths: cross - 800 km, square - 400 km, triangle - 200 km, diamond - 100 km.

$$w' = i\hat{\omega}\frac{\bar{\theta}}{\bar{\theta}_z}r_\theta \tag{4.7}$$

The assumption of $\bar{\theta}_x \approx 0$ is supported by the ASHOE ER-2 measurements.

Combining (4.5) and (4.7), it is possible to obtain an expression for the ozone response in terms of the potential temperature and horizontal wind variations

$$r_{O_3} = \frac{\bar{O}_{3z}\bar{\theta}}{\bar{O}_3\bar{\theta}_z}r_\theta - \frac{i}{\hat{\omega}\bar{O}_3}\bar{O}_{3x}U', \tag{4.8}$$

where the first term is due to vertical displacement (equivalent to the basic dynamical model (4.3)) and the second term is due to horizontal displacement by gravity waves.

In the case of the ER-2 data, it is only possible to obtain a mean meridional ozone mixing ratio gradient $\bar{O}_{3MER}$, since most of the flight trajectories are approximately along lines of longitude. For this reason it is necessary to assume that the zonal mean ozone gradient $\bar{O}_{3ZON}$ is negligible compared with the meridional gradient, and hence that $\bar{O}_{3x} \approx \bar{O}_{3MER}$ (from Section 4.4.2).

The ozonesonde and radiosonde data provide information on $O_3(z)$, $\theta(z)$, $u(z)$ and $v(z)$. From the $u(z)$ and $v(z)$ information it was possible to calculate a value of the intrinsic frequency $\hat{\omega}$ using a hodograph analysis and Stokes parameters [Appendix C]. The calculated values of $\hat{\omega}$ are presented in Table 4.2. The most commonly occurring $\hat{\omega}$ value of ~0.0004 rad s^{-1} corresponds to a wave period of ~4 hr. Using this value of $\hat{\omega}$, an estimate of $\bar{O}_{3MER}$ was calculated directly using (4.9).

Equation (4.8) was used as a predictive measure of the expected magnitude of r_{O_3} and also as a predictive equation for the calculation of $\bar{O}_{3MER}$. Initially this approach was used to compare the values of $\bar{O}_{3MER}$ as estimated from sonde data with those calculated directly from the ER-2 data. Values of $\bar{O}_{3MER}$ necessary to explain the fluctuations observed in the ozonesonde data were calculated from

$$\bar{O}_{3MER} = \frac{-\hat{\omega}\bar{O}_3}{v'_{90}}\left(r_{O_3} - \frac{\bar{O}_{3z}\bar{\theta}}{\bar{O}_3\bar{\theta}_z}r_\theta\right), \tag{4.9}$$

where $v'_{90} = iv'$ is the meridional velocity component rotated through 90° in the complex plane. The comparison was carried out at two heights (from the southward and northward legs of the ER-2 flight path) on the five flights for which agreement was found between the (θ,O_3) maps for the sonde and ER-2.

The contribution of the term representing gravity-wave-induced meridional transport of ozone will be greatest where the gravity wave meridional displacement η' is large relative to the mean wind displacement $\bar{\eta}$.

$$\eta' = \int v'dt = \frac{iv'}{\hat{\omega}} \leftrightarrow \bar{\eta} = \int \bar{v}dt \tag{4.10}$$

Thus long-period inertia-gravity waves which are associated with large (~250-1000 km) horizontal scales in both the zonal and meridional directions are expected to induce important meridional displacements. The effects of an inertia-gravity wave identified in Rayleigh–Mie Doppler wind lidar data are discussed in Chapter 5.

The estimation of gravity wave horizontal advection performed in this section was severely limited by the assumption of monochromatic wave activity in (4.8) and (4.9). The relation between velocity and ozone fluctuations will be further explored in Chapter 5 where a quasi-monochromatic IGW signature was well defined in velocity components, lending weight to a single component wave analysis.

The value of $\bar{O}_{3MER}$ necessary for gravity-wave-induced meridional and vertical transport to completely describe the structures observed in the sonde profiles was calculated for seven ozonesonde and radiosonde ascents. For the same observation days, values of $\bar{O}_{3MER}$ were calculated from ER-2 aircraft data. In Figure 4.11, the flight of 16 October 1994 (lower panel) indicates agreement between the measured and predicted $\bar{O}_{3MER}$ values. On this date there is agreement between the time of closest approach of the aircraft and the launch of the sondes at Macquarie Island (Table 4.1), and there is also strong agreement in (θ, O_3) surfaces (Figure 4.10). Data sets from 13 April, 24 May, 1 June, 3 June, and 10 October, 1994 show measured $\bar{O}_{3MER}$ values less than was required to produce the observed ozone fluctuations [see Appendix D]. Hence, the vertical and meridional transport by gravity wave motions was sufficient to drive the observed fluctuations in only two of the seven ER-2/sonde data sets.

The relative importance of meridional ozone transport by gravity waves and that by mean meridional motions can be estimated by examining the relative values of the mean and perturbation components of the meridional wind. Table 4.2 lists the

ER2 flight (yymmdd)	$\hat{\omega}$ (rad s^{-1})	$\bar{v}$ (m s^{-1})	v_{RMS} (%)
940413	0.00045	12.7	33
940524	0.00040	5.6	37.9
940603	0.00018	21.4	28.7
940806	0.00014	9.5	16.6
941010	0.00110	4.1	66.9 (19.5-21 km)
941013	0.00040	4.3	63.3
941016	0.00017	2.4	75.6 (17.5-21 km)

Table 4.2: Intrinsic frequency, mean meridional wind ($\bar{v}$), and RMS relative meridional wind perturbations (v_{RMS}) from radiosonde measurements for the ER-2/sonde comparison.

values of mean and RMS relative meridional winds for the ER-2/sonde comparison days. Note that the values of v_{RMS} are not a direct measure of the importance of the gravity-wave transport relative to the mean motions. They are examined here as an indication of the contribution made by gravity wave motions.

In these cases, the contribution of the estimated gravity wave meridional velocity perturbations is very significant in comparison with the mean meridional velocities, which are relatively light. These values of v_{RMS} indicate the importance of gravity-wave-scale variations as a means of transporting ozone in the meridional direction.

4.5 Chapter Summary

This chapter investigated the roles of vertical and horizontal advection in the formation of observed ozone structures through an analysis of high-resolution ozonesonde, radiosonde, and ER-2 aircraft measurements at the mid-latitude southern hemisphere site of Macquarie Island. Observations suggested that similar mesoscale variations are present in ozone and temperature data in roughly half the data sets. From an initial analysis, assuming only gravity wave vertical transport of ozone, it was clear that vertical transport alone could not account for the amplitude of the fluctuations measured in ozone mixing ratio profiles. However phase agreement between ozone and temperature fluctuations was evident in approximately half of the ozonesonde data sets acquired at Macquarie Island. A basic dynamical model appeared to provide only a qualitative representation of the relation between ozone and temperature variations. Large differences were found between measured ozone perturbations from the ozonesonde data and ozone perturbations calculated from radiosonde temperature data in some data sets, in agreement with the results of previous authors.

The process of extracting the background ozone layer in order to calculate ozone perturbations is very important. Some of the discrepancy between measured and calculated ozone must be due to this process. The magnitudes of calculated temperature and ozone perturbations are more sensitive to this process than the phase relationships.

Ozone laminae were observed most commonly in the Macquarie Island data set in the height range 12-18 km. Occasional multiple laminar events were observed. In a majority of cases the temperature information did not provide strong support for direct wave-induced vertical transport as a means of producing the laminae.

The presence of ozone laminae in vertical ozone profiles causes variations which are not visible in the temperature profile. Although *Reid and Vaughan* [1991] have defined a lamina as a layer of height up to ~2 km with an ozone partial pressure change of more than 2 mPa, it is possible that smaller ozone changes may also be associated with filamentary structures. For this reason, the estimation of expected gravity wave activity based on the temperature perturbations, with care taken in removing the background signatures in the two profiles, can provide an indication of the relative contributions of gravity waves and large-scale transport in the ozone perturbations. These aspects of ozone structure will be examined in more detail in Chapters 5 and 6.

The results of *Ehhalt et al.* [1983] and *Röth and Ehhalt* [1987], as well as those presented in Section 4.2, indicate the disagreement between EDH values of temperature and ozone. The small gradients of temperature along quasi-horizontal isentropic surfaces, as compared with ozone gradients, such as measured by the ER-2 aircraft [*e.g. Danielsen et al.*,1991] suggest that an important contribution to the larger ozone EDH is provided by large-scale quasi-horizontal advection.

The data set analyzed in this chapter has provided a novel framework for the investigation of horizontal and vertical structure in wind velocities and tracers. It serves as a proof-of-concept study characterizing quasi-simultaneously both the large-scale horizontal gradients of stratospheric tracers and their vertical gradients. The use of aircraft data rather than satellite observations has the advantage of highlighting mesoscale horizontal ozone structure; however vertically resolved satellite observations are able to provide estimated horizontal ozone gradients at a range of heights.

The following chapter continues the investigation of the mesoscale variability of stratospheric ozone through an analysis of DIAL ozone lidar measurements. The lidar measurements of ozone have the advantage over the sonde measurements discussed so far in monitoring the time-varying structure of the ozone vertical profile. However, the height resolution of the ozonesonde data remains superior to that of the DIAL technique at present.

Chapter 5

Dual Stratospheric Lidar Measurements

Montons, montons, jusqu'au sommet.

This chapter presents a case study of observations, analyses, and interpretation of ozone and wind velocity measurements obtained using lidar techniques at the Observatoire de Haute Provence (OHP), France (44°N, 6°E). The observatory is located in a region of hilly terrain at an altitude of ~170 m. This case study consists of dual time-resolved lidar ozone and velocity measurements in the stratosphere which, to the author's knowledge, are the first such measurements performed. The time-resolved ozone and wind velocity measurements have allowed new perspectives on the timescales and variability of mesoscale processes. Sections of this work have been submitted as *Gibson-Wilde et al.* [1997] which is included as Appendix B.

5.1 Lidar Systems

The data presented in this chapter were obtained at the lidar facility at OHP in collaboration with the Lidar Group of the Service d'Aeronomie du CNRS, France. Simultaneous time- and height-resolved data sets were obtained in the lower stratosphere (12-30 km) using two separate lidar systems; an ozone DIAL system and a Rayleigh–Mie Doppler (RD) wind lidar. An overview of the two lidar systems is presented in

	Ozone DIAL	RD lidar
Beam direction	vertical	vertical, off zenith 40° N/E
Wavelengths	λ absorbed=308 nm λ reference=355 nm	λ=532 nm
PRF	50 Hz	30 Hz
Height resolution	600 m	115 m
Time resolution	30 min	30 min
Height range	12 - 30 km	12 - 45 km
Major error sources	water vapour and aerosol contamination	aerosol contamination

Table 5.1: DIAL ozone and RD lidar capabilities utilized at OHP in October 1995.

the next two sections.

5.1.1 Stratospheric ozone DIAL system

The stratospheric ozone DIAL system is operated as part of the international Network for Detection of Stratospheric Change (NDSC) for long-term monitoring of total ozone and mean ozone vertical structure. For this purpose, the DIAL system performs typically two hours of continuous ozone profile acquisition per night, which is the minimum required to obtain a statistically reliable average profile and hence a total ozone column amount through integration. The monitoring of ozone trends provides a very valuable resource in understanding long-term ozone depletion [*WMO*,1994; *Lacoste*,1994].

The DIAL technique for the measurement of vertical profiles of ozone concentration consists of two independent lasers; one laser tuned to a wavelength which is absorbed by stratospheric ozone (308 nm) and the second laser tuned to a reference wavelength which is not absorbed by ozone (355 nm). The data acquisition steps between the absorbed and reference signals. The DIAL system at OHP operated with 6 channels; two channels optimized for upper stratospheric measurements[1] not used here, two for the lower stratosphere (12-30 km), and two Raman channels for atmospheric density measurement (discussed in Section 5.2.2).

Ozone profiles were obtained from averages over 10,000 laser shots which were each of 20 ms duration giving a sample each 200 s (3 min 20 s). Uncorrected noise levels and mean ozone profiles were calculated as averages over each three samples (600 s).

---

[1] 30-50 km

A statistically reliable average nightly ozone profile in the upper stratosphere required 420,000 shots or approximately two hours acquisition time. Lower stratospheric measurements of average ozone profiles required only one hour of data acquisition due to stronger signal returns at the lower observation levels.

The relatively fast and reliable data acquisition in the lower stratosphere indicated the possibility of obtaining time-resolved ozone concentration measurements in that region. The number of laser shots used in calculating an ozone profile is a compromise between ozone variability and statistical error. For this case study, a statistical error of 10% was accepted, based on calculation of ozone profiles from a shortened data acquisition time, and hence a time-resolved sequence of ozone profiles from a full night of lidar observations was obtained.

DIAL ozone profiles have been processed most commonly with non-equispaced data levels due to the reduced signal-to-noise levels in the upper stratosphere [*McDermid et al.*,1990]. The received signal requires averaging over a larger height interval to obtain a constant statistical significance over the full height range [*McDermid*,1993; *Lacoste*,1994].

However, measurement of small-scale features in ozone profiles required a uniform and better height resolution than is generally attempted for the ozone trend measurements. Also, the time resolved behaviour of the ozone profile was of interest, and so a processing technique was developed to provide a data set suitable for the investigation of time-varying ozone features.

Sources of error for the DIAL technique include instrumental noise, receiver saturation, sky background noise, temperature dependence of ozone absorption cross-sections, aerosol contamination, and the estimated backscatter and extinction coefficients [*Godin*,1984; *Lacoste*,1994].

The algorithm for the extraction of ozone from photon counts consists of four steps: desaturation, calculation of a background signal, differentiation to obtain the slopes of the received signal from the two wavelengths, and the calculation of an error term [*Godin*,1984]. The process of desaturation corrects the received signal according to an assumed form of saturated response of the receiver [*Lacoste*,1994]. The sky background is calculated in a region of very low ozone content with few photon counts expected

(60-75 km).

DIAL ozone lidar measurements with a time resolution of 30 min were obtained at OHP using an adapted processing method. The technique consisted of first correcting the data by desaturating the signal, as described in *Lacoste* [1994], and then removing the background signal in the form of a parabolic fit. This form of background fit was chosen as it gave consistently low error statistics for the short duration profiles [discussed in *Lacoste,*1994 p. 39]. The calculation of the signal slopes is sensitive to the form of the background signal removed and the height range over which the slopes are calculated. Due to shorter integration times, the reliability of the fitted slopes was investigated for each profile in turn. The parabolic fit technique was found to give consistent and compatible slope calculations between successive profiles for both the absorbed and unabsorbed wavelength signals.

5.1.2 Rayleigh–Mie Doppler Wind Lidar

The Rayleigh–Mie Doppler (RD) wind lidar technique was used to obtain time-resolved high resolution vertical profiles of wind velocity in the stratosphere (typically 15-50 km). The technique monitors winds in a region of the atmosphere which has been investigated sporadically using radiosondes, falling spheres, and satellite observations [see Chapter 1]. Lidar wind observations provide a unique time-resolved source of information on stratospheric dynamics.

The technique is based on a conventional zenith-pointing Rayleigh lidar at a wavelength of 532 nm with the additional capability of two laser-pointing directions at 40° off-zenith in the north and east directions. Apart from this, the RD lidar system was operated in its default operation mode as described elsewhere [*Chanin et al.,*1989; *Garnier and Chanin,*1992].

The horizontal velocity components were obtained under an assumption of zero vertical winds using a process analagous to the Doppler Beam Swinging (DBS) radar technique [*e.g. Vincent and Reid,*1983]. The radial wind speed v_R is calculated from a Fabry–Perot interferometer measurement of the wavelength change ($\delta\lambda$) in the laser emission line (λ) through [*Chanin et al.,*1989]

$$v_R = \frac{c\delta\lambda}{2\lambda}. \tag{5.1}$$

For a predetermined beam pointing angle θ of 40° off zenith for the 1995 measurements at OHP, the horizontal velocity components were given by,

$$v_H = \frac{v_R}{\sin\theta}. \tag{5.2}$$

5.2 Observations

The observations presented in this case study were obtained at OHP between 2230 LT on 23 October and 0500 LT on 24 October, 1995. The DIAL ozone lidar and RD wind lidar, located approximately 10 m apart within the same building, were run simultaneously during the observation period. Measurements of lower stratospheric ozone concentration and Raman channel atmospheric density measurements from the DIAL system and zonal and meridional wind velocity from the RD lidar system are discussed in this case study.

Lidar data processing may involve both temporal and spatial averaging of the received signal. Profiles of wind velocities and ozone concentration which were simultaneous in time and had the same temporal resolution were required for this case study. A common time resolution of 30 min was chosen as the minimum necessary to obtain ozone concentration profiles with statistically significant measurable mesoscale variation. The height resolution of 115 m available from the wind lidar, with stronger signal returns, was significantly better than the resolution of 600 m available from the DIAL ozone lidar for the same temporal resolution.

Figure 5.1 presents the sequence of ozone concentration profiles in two consecutive plots. The ozone concentration measurements are displayed at a height resolution of 600 m and the estimated measurement error is 10% in the lower stratosphere.

A correction was applied to the RD lidar zonal velocity measurements based on radiosonde data from 2300 LT on 23 October 1995, from Nîmes, 100 km west of OHP. It was noted that the RD lidar zonal velocities showed a height-independent eastward bias of 8.42 m s^{-1} due to optical misalignment [Claude Souprayen, private

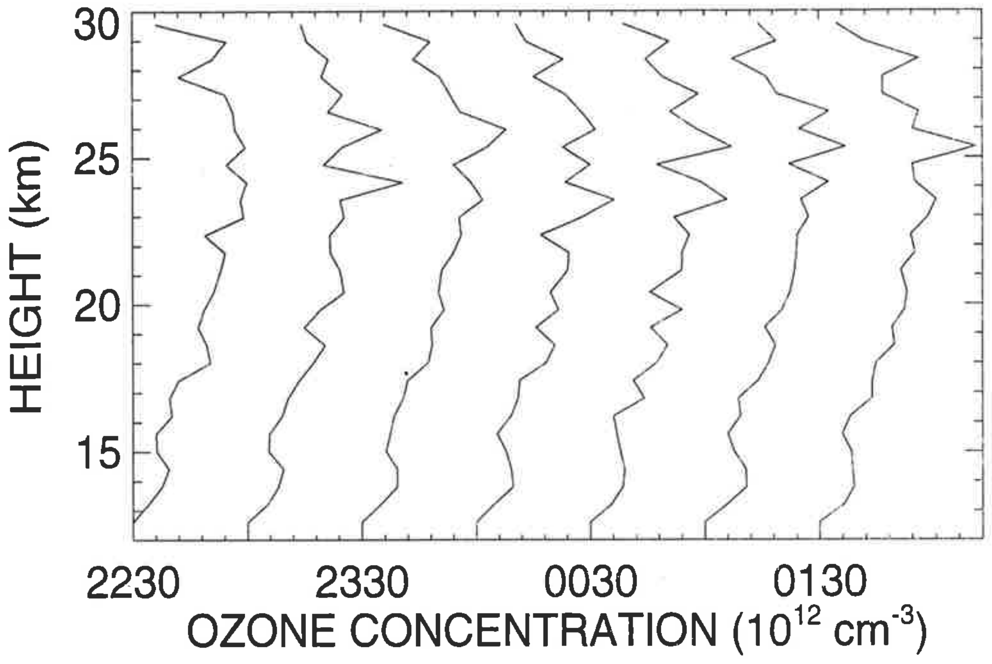

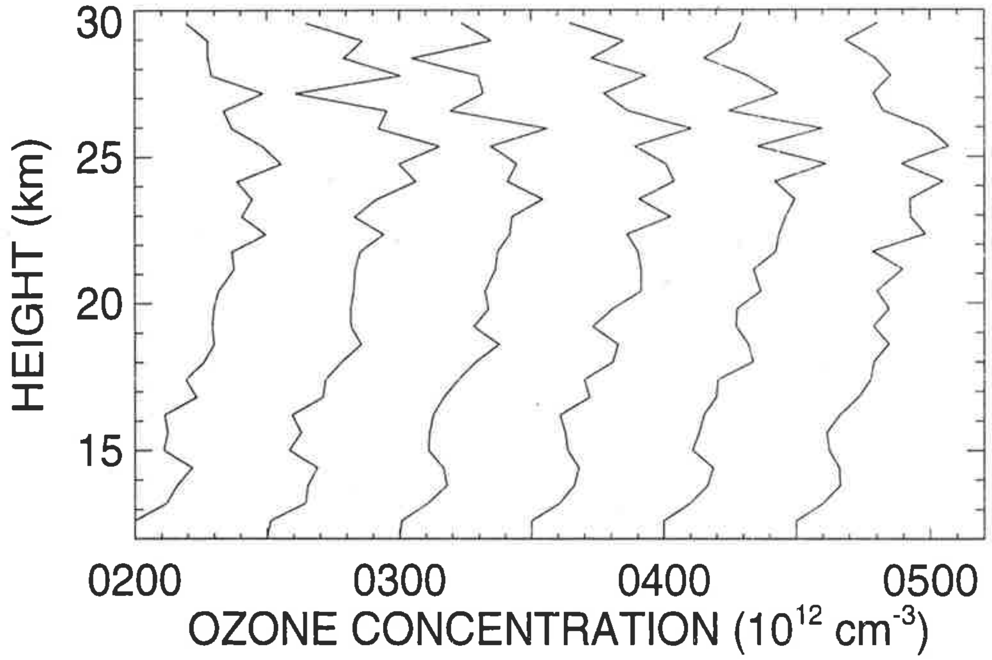

Figure 5.1: Sequence of DIAL ozone concentration profiles from 2230 LT on 23 October to 0500 LT on 24 October, 1995. Successive profiles are labeled with the starting time of the 30 min observation periods and are offset by 5 concentration units.

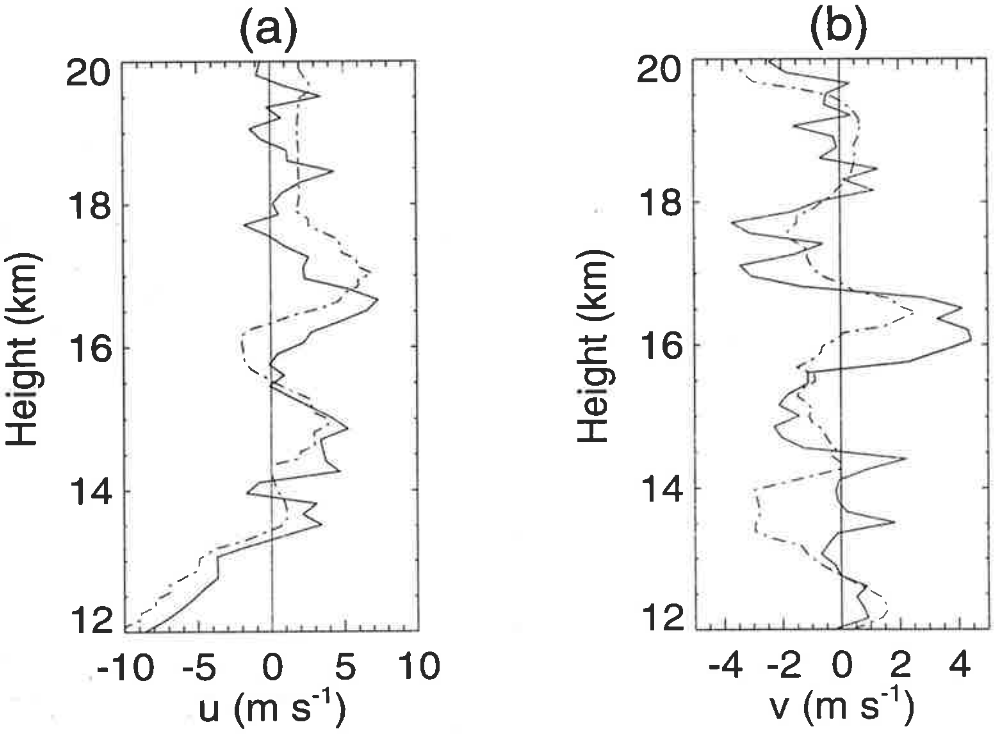

Figure 5.2: Comparison of corrected (a) zonal, and (b) meridional wind velocities measured with the RD lidar between 2230-0500 LT (solid line) and Nîmes radiosonde at 2300 LT (dashed-dotted line).

communication]. The corrected lidar wind velocity profiles and Nîmes radiosonde profiles are shown in Figure 5.2. Comparison between the zonal velocity profiles from the two zonally separated sites indicates a stable wave-like velocity structure with a vertical scale of ~2 km which is further investigated in Section 5.4.

The corrected zonal and meridional wind velocity profiles in Figure 5.3 are displayed at a height resolution of 150 m, spline-interpolated from the raw 115 m resolution for consistency with the DIAL measurements. The RD lidar data are processed typically with a time resolution of 5 min [Claude Souprayen, private communication]. The 30 min profiles presented here have an estimated associated error of less than 5%. The accuracy of the wind data is higher than that of the ozone concentration data.

Figure 5.4 displays the average profile of ozone concentration calculated over the 6.5 hour observation period. The strong fluctuations evident in this average profile must result from dynamical activity on timescales greater than approximately 7 hours. The two local maxima in ozone concentration in Figure 5.4 at approximately 14 km

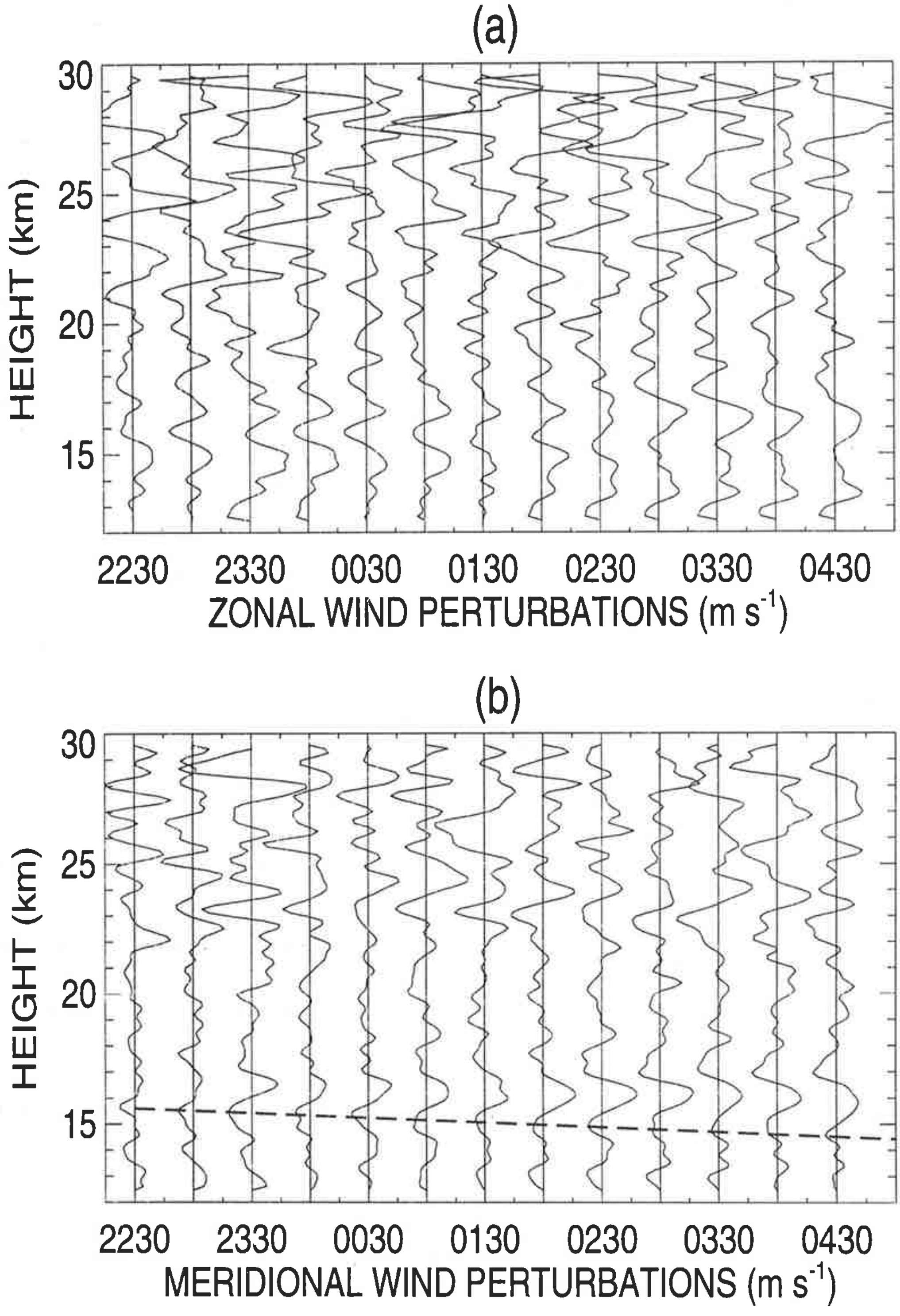

Figure 5.3: RD lidar profiles of (a) zonal, and (b) meridional velocity measured between 2230 LT on 23 October and 0500 LT on 24 October, 1995. Successive profiles are labeled with the starting time of the 30 min observation periods and are offset by 10 m s^{-1}. The dashed line indicates the estimated downward phase progression from which a vertical phase velocity was estimated (see text).

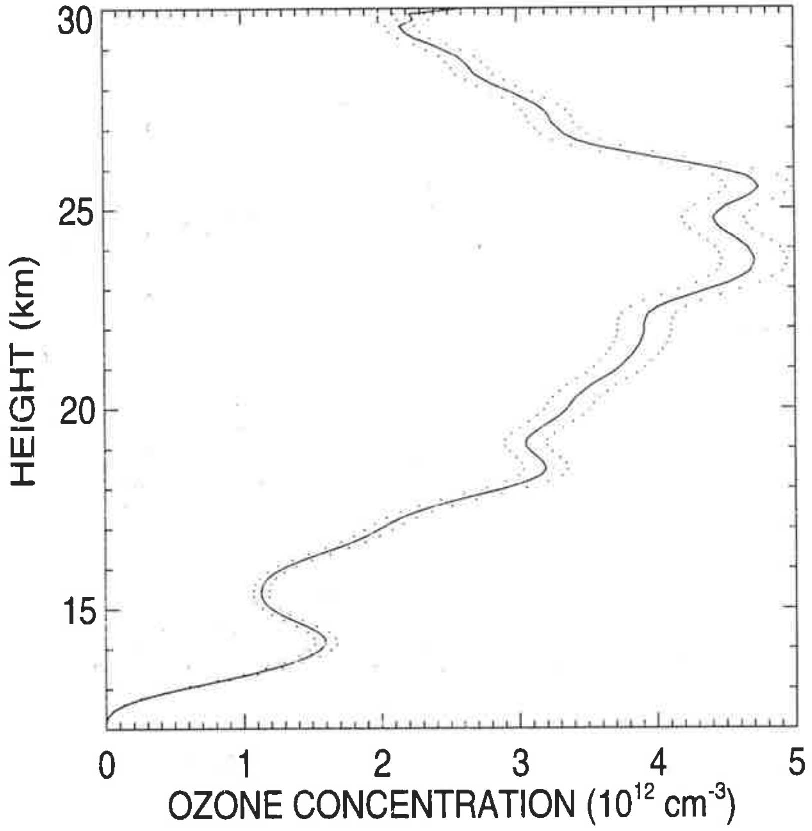

Figure 5.4: Average vertical profile of ozone concentration from DIAL lidar. A 5% error estimate is indicated by the dotted line.

and 18 km are examples of ozone laminae and will be discussed fully in Section 5.3.

Figure 5.5 displays 6.5 hr average zonal and meridional wind velocity profiles. These long term averaged wind profiles have an associated error of 1%. Long-lived wave-like features are evident in both of the velocity components. The wind field will be analyzed in detail in Section 5.4.

5.2.1 Ozonesonde and DIAL ozone lidar observations

An ECC ozonesonde was launched at 1200 LT on 24 October, 1995 from OHP. Figure 5.6 displays the vertical profiles of the conserved quantities of potential temperature and ozone mixing ratio recorded by the sonde. It is important to note that the laminae clearly defined in the ozone concentration profiles in Figures 5.4 and 5.7 are less evident in the ozonesonde mixing ratio profile due to the density weighting, as discussed in

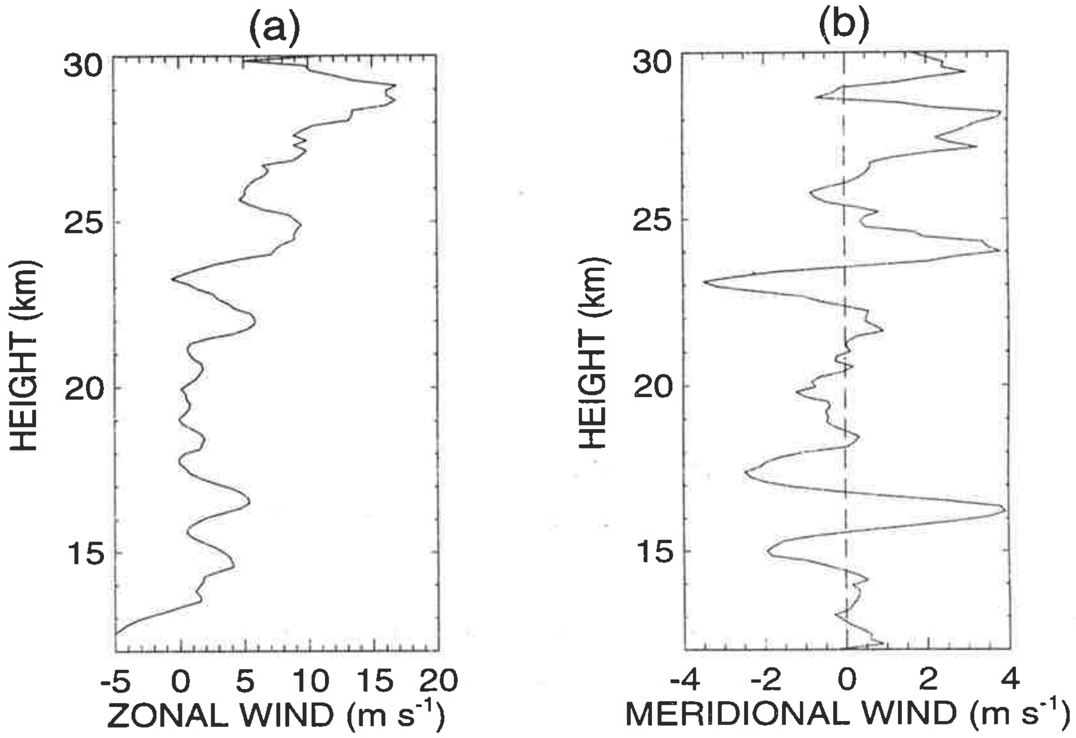

Figure 5.5: Average vertical profiles of (a) zonal, and (b) meridional wind velocity from RD lidar.

the next section.

The final lidar profile in the night sequence 23-24 October 1995 was complete at 0500 LT. In Figure 5.7, the average lidar ozone concentration profile is overlaid with the ozonesonde ozone concentration profile to see if there is evidence of similar mesoscale structures. The comparison between the ozonesonde and lidar measurements of the ozone concentration profile can only be qualitative due to the 7 hour time difference between the measurements. Also, there is evidence that the ozonesonde pump may have been faulty leading to underestimation of ozone concentration above approximately 20 km, as discussed by *Johnson et al.* [1992]. This suspected underestimation by the sonde is supported by the low peak ozone concentration of approximately 3.5×10^{12} cm^{-3} in the ozonesonde measurement compared with average October values from lidar ozone profiles at OHP of $4.0-4.5 \times 10^{12}$ cm^{-3} [*Godin*,1984]. However, the height range 12-20 km where the laminae occur shows agreement between the lidar and sonde measured ozone concentration profiles.

The ozone column content between the heights of 10 and 30 km calculated from

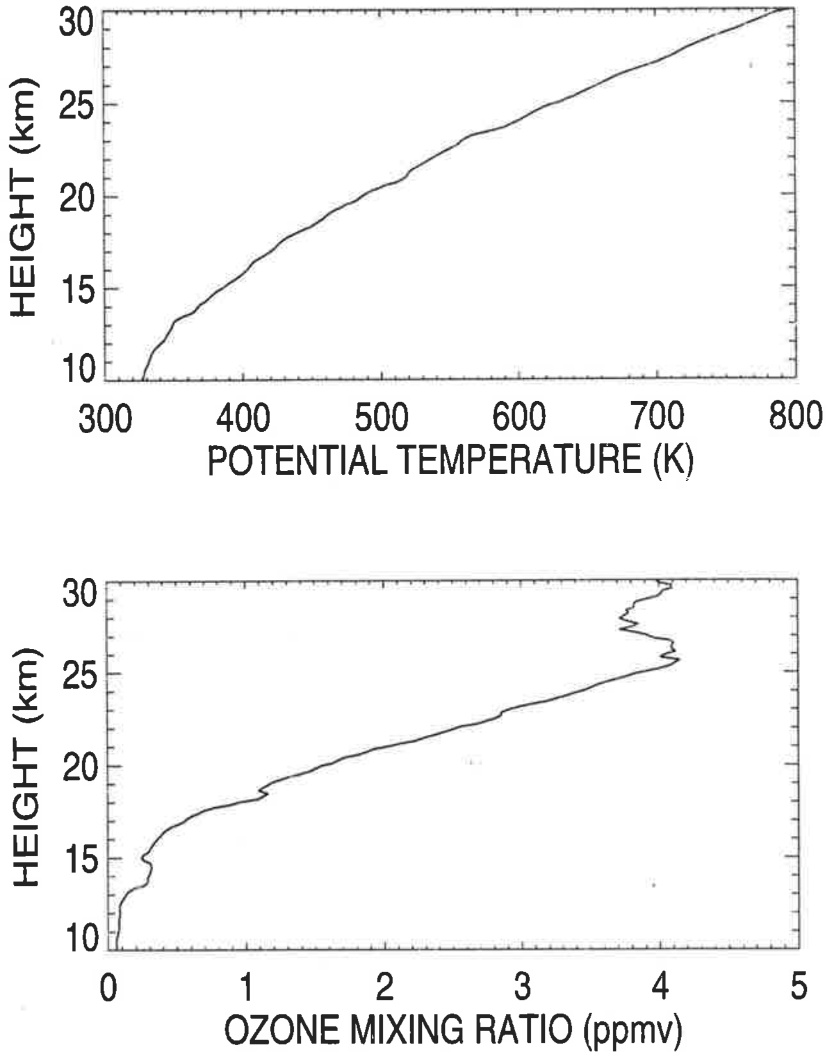

Figure 5.6: Ozonesonde measured ozone volume mixing ratio (lower panel) and calculated potential temperature profiles (upper panel).

the ozonesonde measurement was 169 DU, whereas 203 DU was calculated from the lidar average profile. The climatological average total ozone content, determined from long-term averages, was approximately 295 DU.

The DIAL lidar-measured RMS relative atmospheric density fluctuations of 0.46% compare well with the ozonesonde-measured RMS relative temperature fluctuations of 0.39%, both calculated over the height range 10-30 km. This comparison is limited by the temporal separation of the measurements and the drift of the sonde with

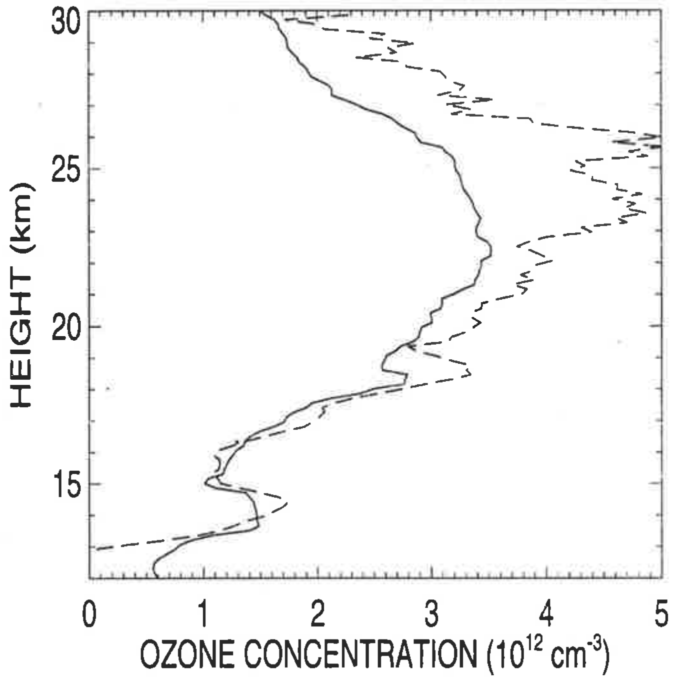

Figure 5.7: Comparison of ozonesonde measured ozone concentration (solid line) and lidar measured ozone concentration (dashed line) profiles.

mean winds. *Beatty and Gardner* [1990] calculated average RMS temperature perturbations of 1.2% in the stratopause region (≈ 50 km) at Arecibo Observatory (18°N, 67°W) using a Rayleigh/Na lidar. Values of RMS temperature perturbations of ~0.5-1.5% have been measured in the upper troposphere and stratosphere from radiosonde observations [*Tsuda et al.*,1989; *Allen and Vincent*,1995; *Eckermann*,1995].

5.2.2 Conversion to relative mixing ratio

It has already been emphasized that mixing ratio is a conserved quantity under Lagrangian transport and is hence a more useful measure of tracer abundance than concentration [Chapter 2]. The DIAL technique directly measures ozone concentration. However, two Raman channels of the DIAL ozone lidar system provide measurements of atmospheric density. These measurements provide a method for the calculation of relative mixing ratio perturbations r_q from the relative concentration perturbations r_n through the relation

$$r_q = \frac{q'}{\bar{q}} = (r_n - r_\rho)/(1 + r_\rho). \tag{5.3}$$

Absolute mixing ratio q can then be calculated by assuming a model density profile, as is typically the case for Rayleigh density/temperature lidar observations, by rearranging (2.25).

$$q = \frac{nM}{\rho N_A} \tag{5.4}$$

The calculation of absolute q was not performed for the case study due to the primary interest in mesoscale perturbations.

The accuracy in an estimation of relative mixing ratio is significantly poorer than that of direct concentration measurements. The relative error associated with the calculation of relative mixing ratio can be estimated as

$$E_q = E_n + 2E_\rho, \tag{5.5}$$

where E_q, E_n, and E_ρ are relative errors in the relative mixing ratio, concentration, and density measurements, respectively. The estimated error for the time-resolved relative mixing ratio profiles is approximately 15% for this case study.

Figure 5.8 presents relative mixing ratio perturbations, calculated using (5.3), for four consecutive DIAL profiles. Note that the perturbation at 14 km is strongly defined in the relative mixing ratio profiles, but that the 18 km feature has been de-emphasized through the dependence of relative mixing ratio on the difference between relative concentration and relative density fluctuations. This observation indicates that lamination events identified in concentration profiles at higher levels, in the vicinity of 20 km, are enhanced by the increase in magnitude of relative density variations with height.

This calculation is presented here as an indication of a useful approach for calculating ozone mixing ratios from lidar measurements. The case study data were not optimized for the calculation of mixing ratio. It is suggested that the use of a reliable, low error density measurement in association with a DIAL ozone system provides an optimal method of observation of tracer variability.

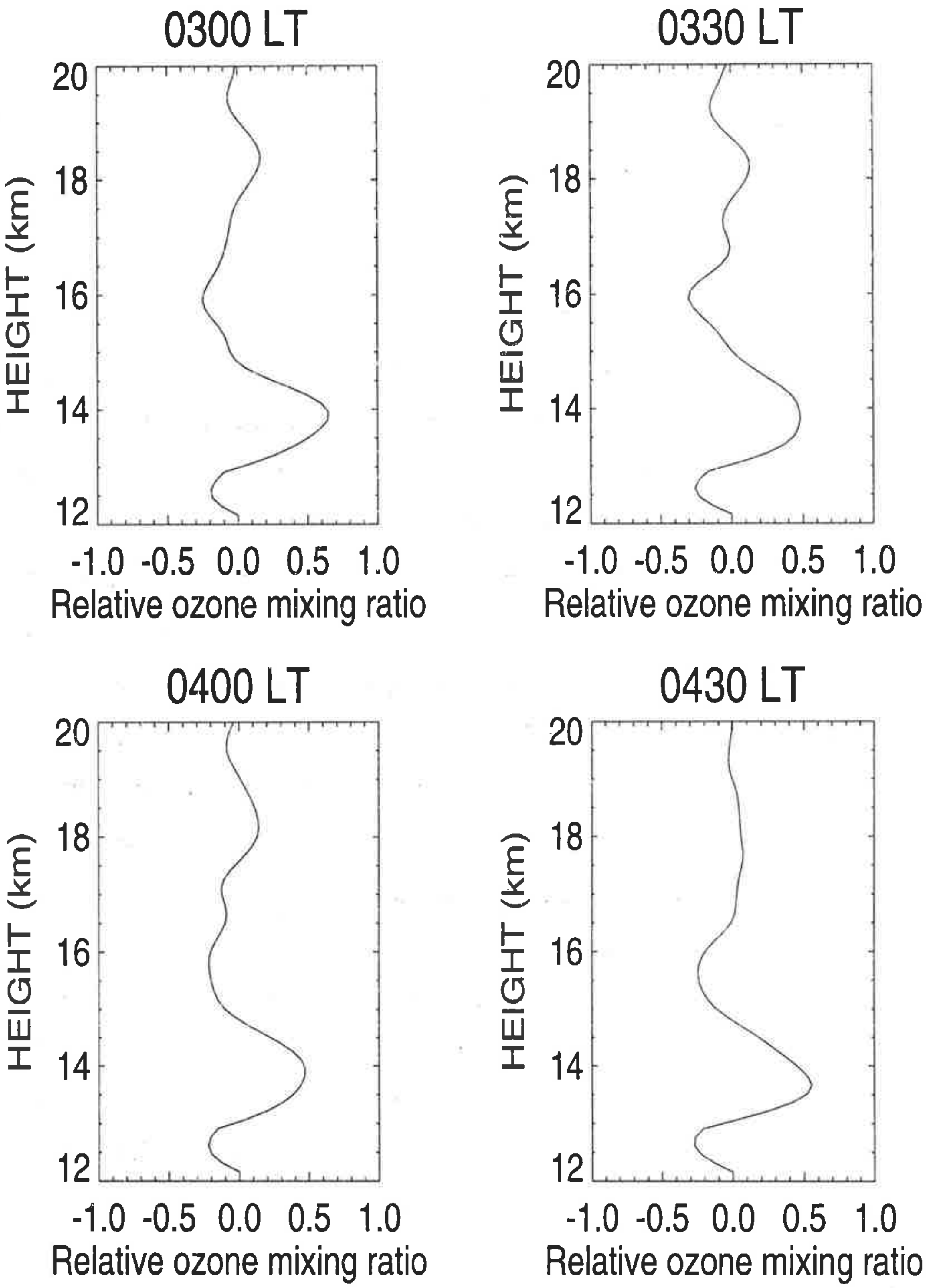

Figure 5.8: Relative ozone mixing ratio perturbations calculated for 30 min average ozone profiles commencing at 0300, 0330, 0400, and 0430 LT, respectively.

5.3 Ozone Laminae Observed at OHP

The concept of lamination in ozone profiles was introduced in Section 1.5.2. Ozone laminae were identified using the definition of *Reid and Vaughan* [1991] which requires positive or negative ozone fluctuations of 2 mPa limited to layers less than 2.5 km in vertical extent. In concentration terms, suitable for comparison with lidar measurements, this limit corresponds to approximately $7\text{x}10^{11}$molecules cm^{-3} at a lower stratospheric temperature of 210 K as measured by ozonesonde (Figure 5.6).

Two ozone laminae which exceed the estimated error margin are illustrated in Figure 5.4. A major lamina occurs at approximately 14 km and a minor lamina also occurs at 18 km. *Reid and Vaughan* [1991] found that a majority of laminae in their mid-latitude ozonesonde data were within the height range 12-18 km. In fact ozone laminae were found to be most prevalent at 14-15 km [*e.g. Reid and Vaughan*,1991].

The two laminae observed in this case study are also evident in Figure 5.1 and the 14 km feature remains well-defined throughout the observation period. This study provides the first observation of time evolution of stratospheric laminar events, to the author's knowledge. The examination of successive ozone profiles indicates that shorter period variations are superimposed on the persistent laminar events.

These complex structures in ozone profiles may be attributed to several different physical mechanisms. The approximate stationarity of the laminae observed in the 6.5 hr average profile suggests longer-timescale generation processes, such as an inertia-gravity wave, differential large-scale advection at the 14 km and 18 km heights, or a synoptic-scale tropospheric event. In the next section, RD lidar velocity measurements and the results of a contour advection with surgery (CAS) determination of large-scale structure will be drawn upon to investigate the dynamical situation at OHP during the case study to try to determine the physical processes responsible for the observed mesoscale ozone structure.

Figure 5.7 presents a comparison of the 6.5 hr mean ozone lidar concentration profile with an ozone concentration profile from an ozonesonde launched at 1200 LT on 24 October 1995 (*i.e.* 7 hr after the final lidar profile). The ozonesonde profile confirms the lidar observation of the laminae. From the lidar observations the estimated minimum lifetime for the two laminae is 6.5 hr. A maximum lifetime of approximately 14 hr is estimated for the 14 km laminar feature based on the occurrence of the lamina in the lidar and ozonesonde profiles. There is evidence that the 18 km lamina is much less prominent in the ozonesonde profile (Figure 5.7), indicating that it may have a different forcing mechanism. Throughout the sequence of lidar profiles, the 18 km feature is heavily affected by superimposed wave-like fluctuations.

The ozone laminar structure presented here can be compared with the southern hemisphere observations analyzed in Chapter 4. In both sets of observations laminae occur in the region 12-18 km and very commonly at 14-15 km.

5.4 Analysis of Mesoscale Dynamical Processes

Stratospheric mesoscale dynamical processes, particularly gravity waves, have been observed and studied extensively in horizontal velocity and temperature data. Below ~25 km, ozone is not photochemically active, in the absence of ozone depletion conditions, and can be considered as a conservative dynamical tracer [*Andrews et al.,*1987; *Zhu and Holton,*1986]. In this region, *Teitelbaum et al.* [1994] showed that ozone fluctuations may be linked to gravity-wave-induced potential temperature fluctuations. *Ehhalt et al.* [1983] found that long-term average variances of ozone abundance were significantly larger than those expected, based on potential temperature variances, which indicated that gravity waves do not explain all of these features. In addition, isentropic trajectory models indicate that quasi-horizontal flow in and out of the vortex can explain many laminar structures in ozone profiles [*e.g. Newman and Schoeberl,*1995; *Orsolini et al.,*1995].

Moustaoui [1995] extended the work of *Teitelbaum et al.* [1994] to examine supposed gravity wave fluctuations observed in ozonesonde profiles of ozone and temperature from the EASOE 1994 campaign. A strong emphasis was placed on identifying simultaneous quasi-monochromatic wave features in ozone and temperature and investigating the phase relationship between fluctuations in ozone and temperature. In Chapter 4, Macquarie Island ozonesonde data were examined for evidence of such correlation between temperature and ozone mesoscale structure. This approach was found to be limited by the absence of temporal information and statistical stationarity of the observed fluctuations. The time-resolved lidar measurements in this case study allow a more thorough analysis to be developed in this section.

By making use of the CAS technique, *Moustaoui* [1995] found agreement between the occurrence of higher ozone amounts from ozonesonde profiles at Arctic stations and the presence of polar vortex air over the observation station. However, the impact of vortex air in changing the observed vertical structure of ozone and the possible interplay between the presence of large tongues of vortex air enhancing ozone response to atmospheric waves present was not examined. A CAS study provided by Dr Roger Atkinson was used, in conjunction with the temporal and vertical ozone structure observed with the DIAL system, to investigate specifically the occurrence of large-scale lamination which may have driven mesoscale ozone structures present in the lidar vertical profiles.

Danielsen et al. [1991] analyzed ER-2 aircraft temperature and tracer measurements to investigate the different scales of variability and the possible mechanisms responsible for the observed tracer distributions. The role of an inertia-gravity wave in driving tracer transport was suggested by a hodograph analysis of wind measurements from a vertical segment of the aircraft flight path [*Chan et al.,*1991; *Danielsen et al.,*1991]. This interpretation has since been refuted on the grounds that a large-scale analysis reproduces the major features of the ozone distribution without recourse to a wave-based explanation and also because *Danielsen et al.* [1991] overestimated the wave-induced displacements [*Newman and Schoeberl,*1995]. However, the hodograph displayed by *Chan et al.* [1991] certainly indicates an elliptically polarized wave feature.

The following sections present a full analysis of dynamical activity during the case study. The mesoscale dynamical structure in the vertical is well described by the RD lidar profiles, which are analyzed using a hodograph analysis and Stokes parameters.

5.4.1 Long–period fluctuations

Successive zonal and meridional velocity profiles from RD lidar (Figure 5.3) indicate a wave-like feature most strongly defined below 20 km. A consistent downward phase (upward energy) progression is discernible throughout the 6.5 hr observation period. The vertical wavelength of this wave is estimated as 2.3 km from the vertical separation of peaks in the wind lidar profiles.

From Figure 5.3 it is possible to estimate a vertical phase propagation speed from the distance of ~1.5 km moved in 6.5 hr by successive peaks in the wind profiles. Thus,

$$c_{z\mathrm{obs}} = \frac{\text{displacement}}{\text{time}} = \frac{-1.5\ \text{km}}{6.5 \times 3600\ \text{s}} \approx -0.06\ \text{m s}^{-1}. \tag{5.6}$$

From this calculation of vertical phase speed, the observed wave frequency ω_{obs} was then calculated by rearranging (2.49) as

$$\omega_{\mathrm{obs}} = m c_{z\mathrm{obs}} = \frac{2\pi}{\lambda_z} c_{z\mathrm{obs}} \sim 0.00016\ \text{rad s}^{-1}. \tag{5.7}$$

This value of observed frequency corresponds to an observed wave period of 10.6 hr.

In Figure 5.9 the long-term averages of zonal and meridional wind velocities, as displayed in Figure 5.5, were detrended by fitting a cubic polynomial to extract fluctuations on timescales greater than the 6.5 hour observation period. A bandpass filter was then applied to extract variation on vertical scales between 1-10 km. The sensitivity of gravity wave variances to the exact form of detrending applied was examined by *Vincent et al.* [1996] where a cubic polynomial was applied uniformly.

Figure 5.10 displays a hodograph analysis of the detrended zonal and meridional velocity perturbations, as discussed in Appendix C. The hodograph indicates mostly clockwise rotation of the velocity fluctuations with height and a well-defined 'gravity-wave' ellipse, which suggests that this feature is a long-period inertia-gravity wave. The individual hodographs for four consecutive 30 min average wind measurements are displayed in Figure 5.11 and confirm the persistence of the wave event, as was suggested by the phase progression evident in Figure 5.3.

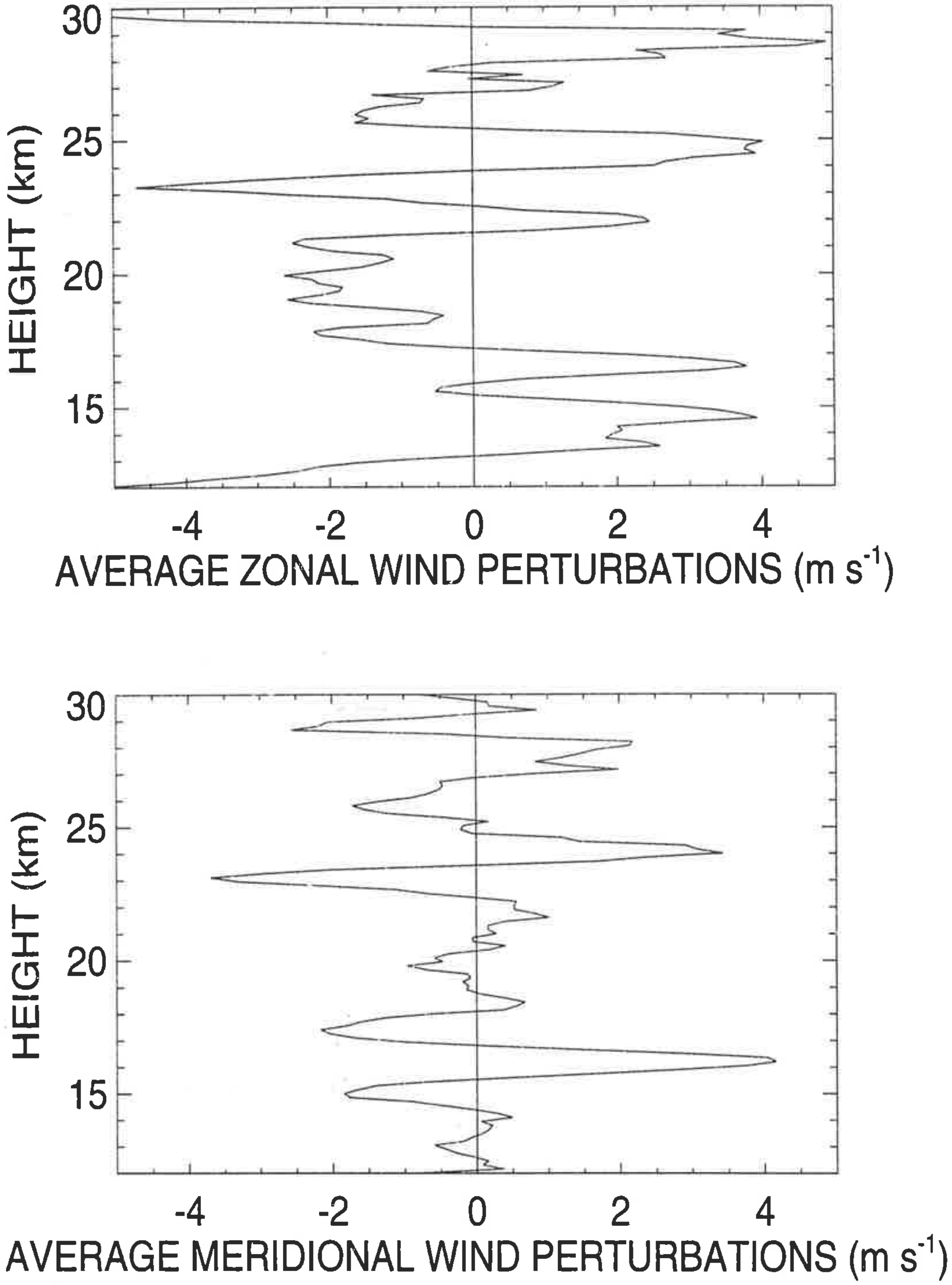

Figure 5.9: Detrended 6.5 hr average zonal and meridional wind velocities.

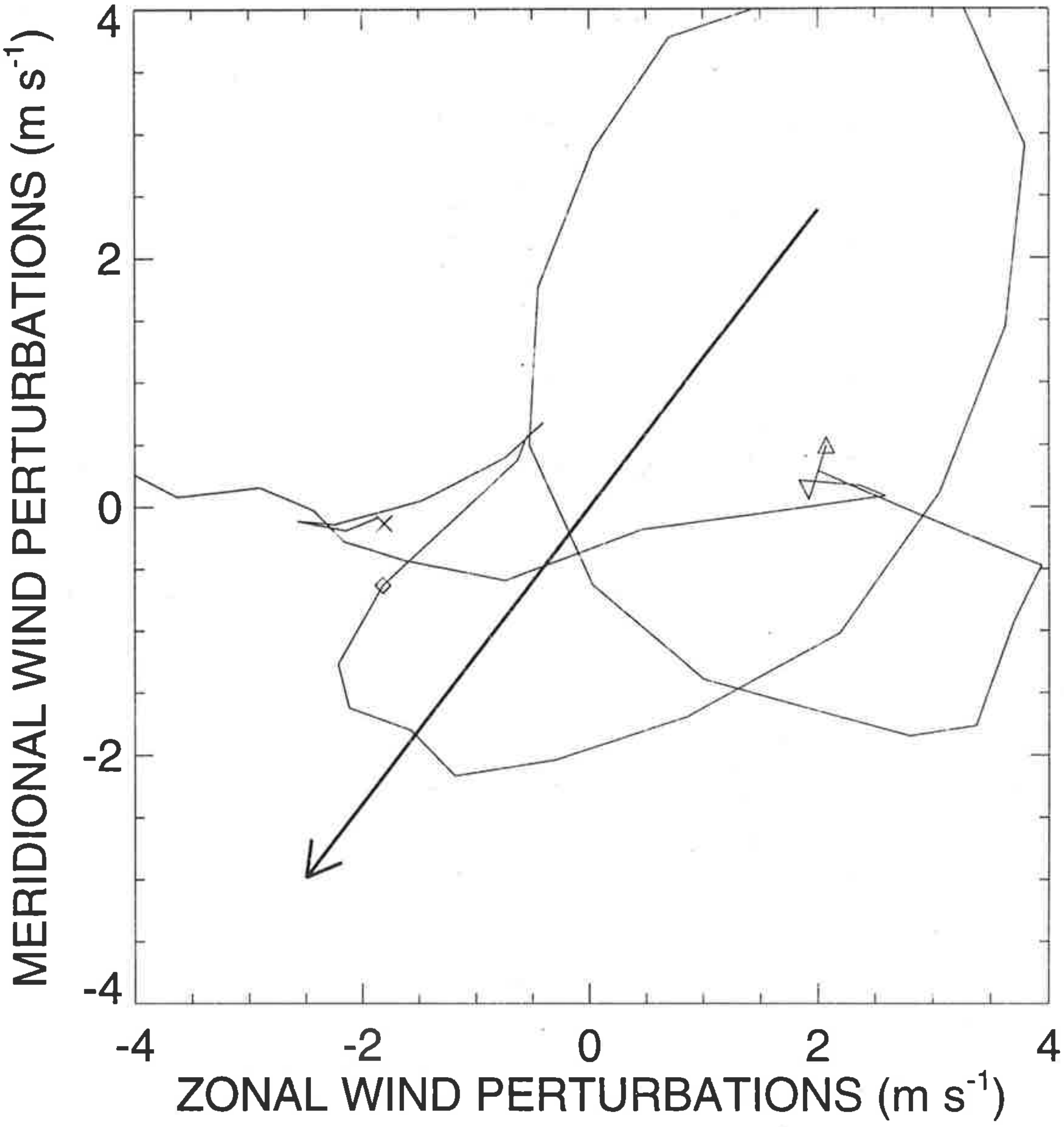

Figure 5.10: Hodograph between 12-20 km of 6.5 hr average zonal and meridional wind fluctuations smoothed over 600 m. The bold line indicates the major axis of the gravity-wave ellipse as determined from a Stokes parameter analysis. The triangle marks the 14 km level, the diamond marks 18 km, and the cross indicates the upper height limit (20 km).

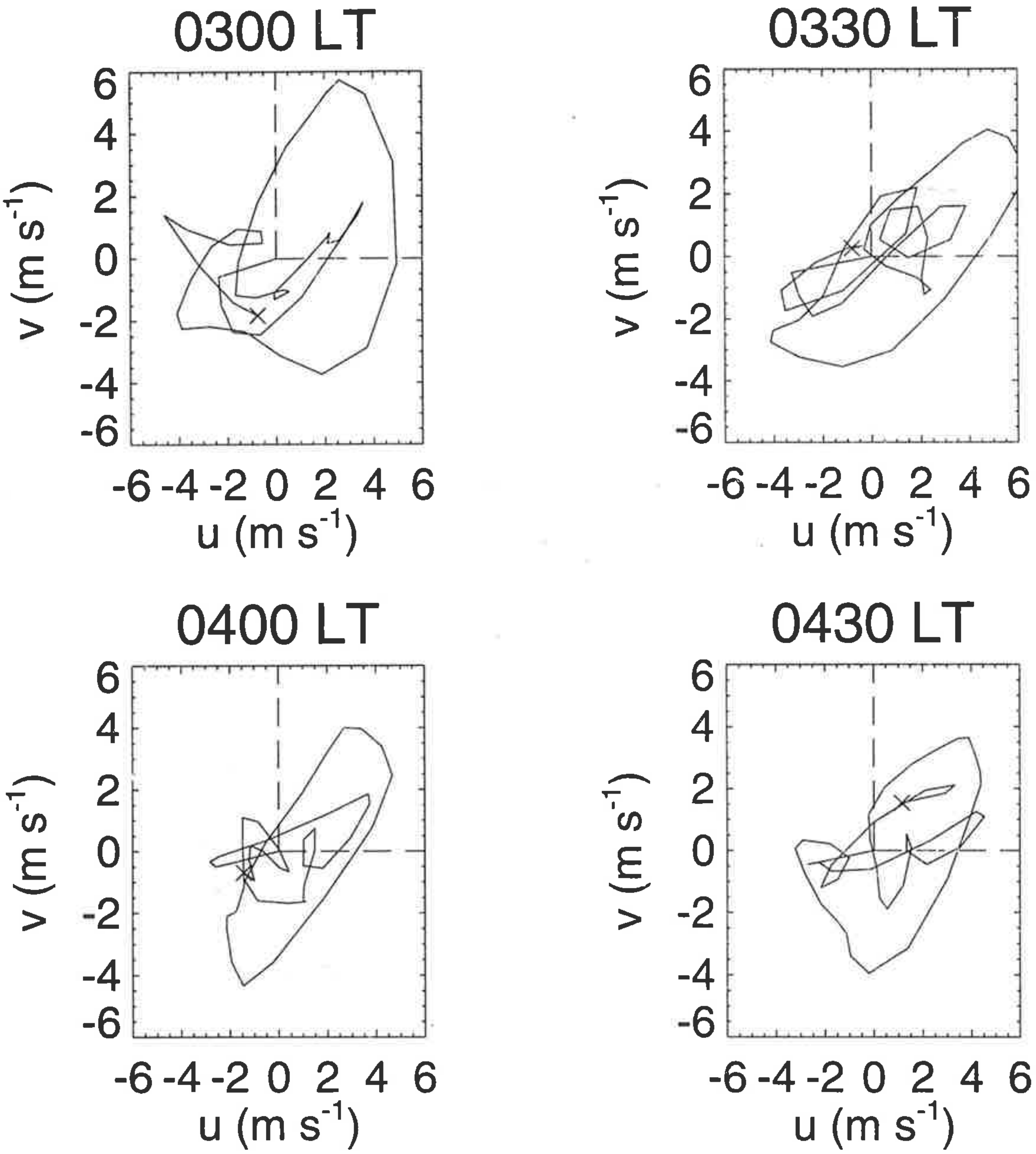

Figure 5.11: Hodographs of individual profiles of zonal and meridional velocity fluctuations smoothed over 600 m. Labels indicate the starting time of the 30 min observation intervals. The cross marks the upper height limit of 20 km.

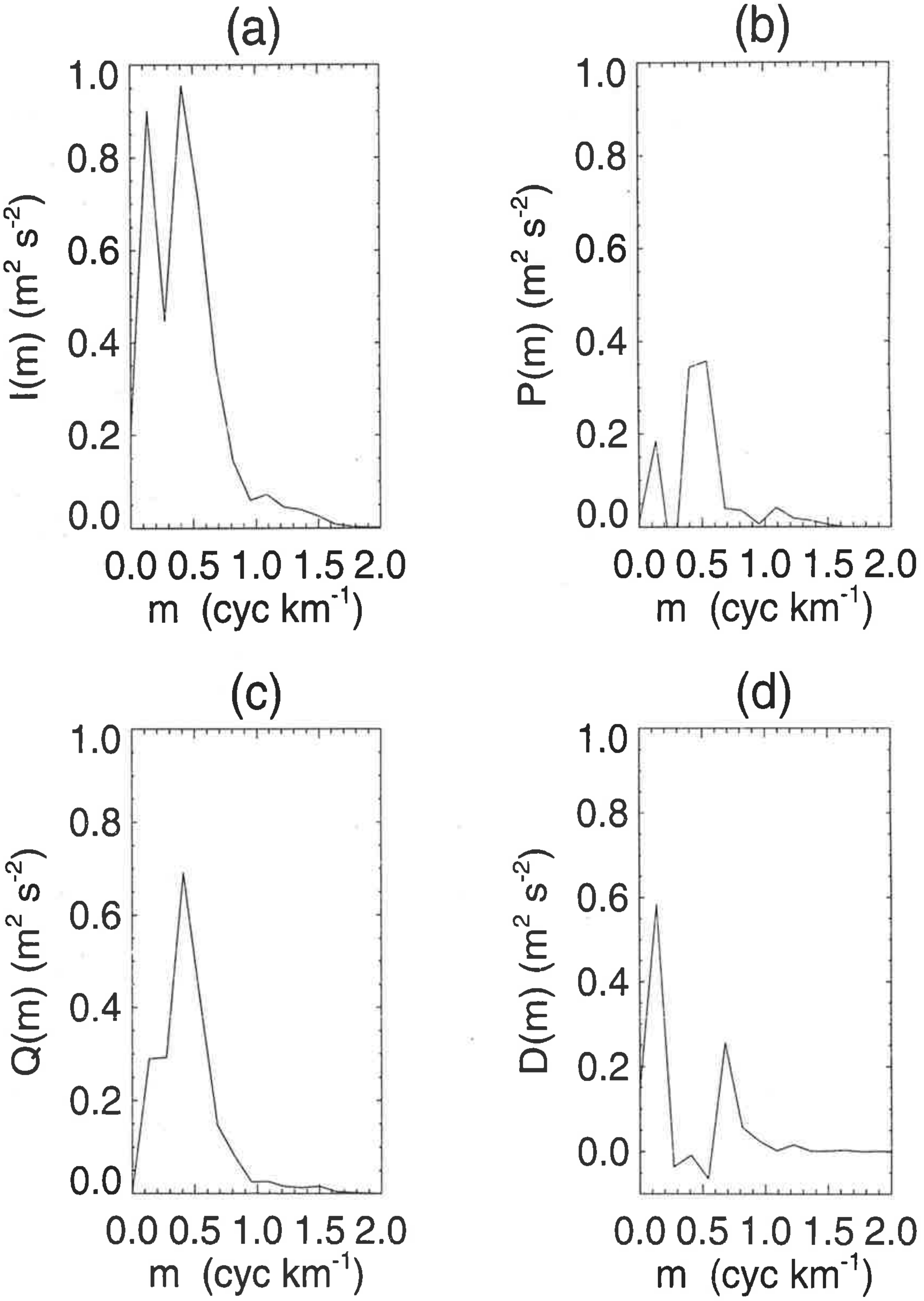

Figure 5.12: Averaged spectral Stokes parameters calculated from RD lidar zonal and meridional velocity fluctuations [see Appendix C].

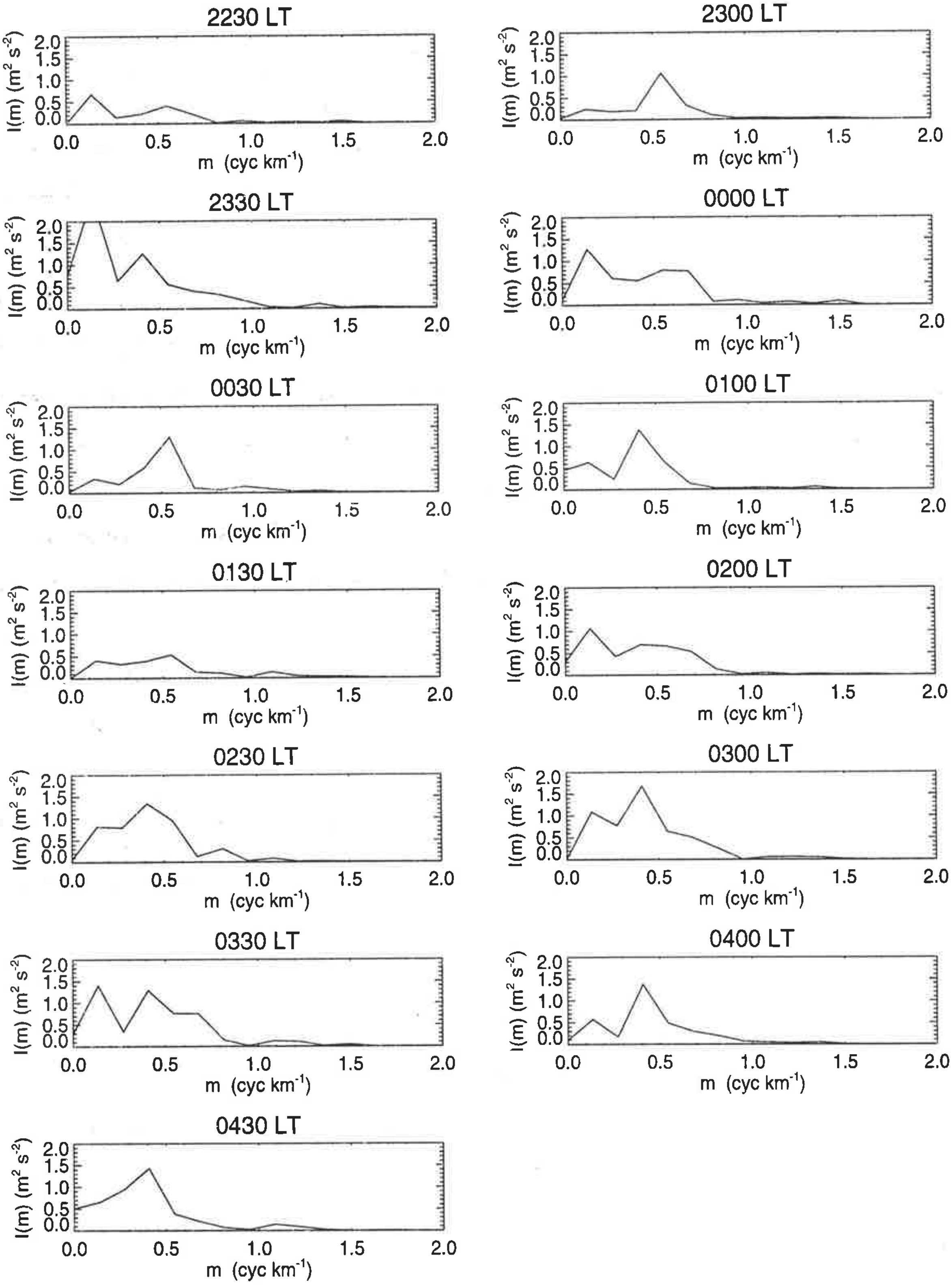

Figure 5.13: Stokes parameter I(m) calculated for successive lidar zonal and meridional velocity profiles.

Wave Parameter	Estimated Value	Information Source
Vertical wavelength	2.3 km	profiles and Stokes
Observed vertical phase speed	-0.06 m s^{-1}	profiles
Observed frequency	$1.6f$ ~0.00016 rad s^{-1}	profiles
Intrinsic frequency	$2.2f$ ~0.00022 rad s^{-1}	Stokes
Zonal wavelength	~360 km	dispersion relation
Total horizontal wavelength	~230 km	dispersion relation

Table 5.2: Inertia-gravity wave parameters for the OHP case study.

A spectral Stokes parameter analysis was performed by calculating the Stokes parameters [see Appendix C; *Eckermann and Vincent*,1989; *Eckermann*,1996] as functions of vertical wavenumber for each profile. An example of a time-resolved sequence of the Stokes parameter $I(m)$ is shown in Figure 5.13. From the averaged Stokes parameters (Figure 5.12) the degree of polarization of the average hodograph was calculated to be approximately 66%, the axial ratio was 2.2, and the axial rotation angle was 50°. This indicates that the intrinsic wave frequency was $\approx 2.2f$ or 0.00022 rad s^{-1} at the latitude of 44°N.

Through the dispersion relation (2.43) the value of the total horizontal wavenumber of the observed long period wave was calculated as

$$K_{TOT} = \frac{m\hat{\omega}}{N}\sqrt{1-\left(\frac{f^2}{\hat{\omega}^2}\right)} = 0.027 \text{ rad km}^{-1}. \quad (5.8)$$

The zonal wavenumber k was then calculated as a projection of K_{TOT} onto the zonal axis direction through,

$$k = K_{TOT}\cos 50^\circ = 0.017 \text{ rad km}^{-1}. \quad (5.9)$$

Hence, the estimated zonal wavelength of the inertia-gravity wave was 360 km. The inertia-gravity wave parameters that were derived from these data are summarized in Table 5.2.

The long-period wave feature evident in the nightly-averaged profiles of horizontal velocities can be thought of as a quasi-time-invariant background structure which acts as a local background for shorter-period fluctuations. In general, the concept of a quasi-time-invariant background ozone structure is supported by ozone trend measurements [*e.g. Lacoste*,1994].

How might the presence of the inertia-gravity wave affect the measured ozone? The 6.5 hr mean winds and gravity wave parameters are used to calculate the ozone response. Theoretical results in terms of mixing ratio are here applied to ozone concentrations as they are directly measured by the DIAL ozone lidar. Relative mixing ratio values have also been calculated using a Raman channel of the ozone lidar but are subject to errors in both ozone and density measurements and are not presented here. The relative density profiles indicate maximum fluctuations of 1-2% which justifies the approximation that relative mixing ratio is equal to relative concentration for this case study.

From the continuity equation, the relative ozone concentration perturbation $\frac{O_3'}{\bar{O}_3}$ is

$$\frac{O_3'(z,t)}{\bar{O}_3(z)} \approx \left(\frac{-\zeta'(z,t)}{\bar{O}_3(z)}\right)\left(\frac{d\bar{O}_3(z)}{dz} + \frac{\bar{O}_3(z)}{\gamma H}\right), \tag{5.10}$$

where $\zeta'(z,t)$ is the vertical displacement perturbation ($\int w'(z,t)dt$) and $\bar{O}_3(z)$ is the mean ozone concentration, as justified above.

For an inertia-gravity wave the vertical displacement is related to the total horizontal wind velocity perturbation through

$$\zeta'(z,t) \approx \frac{iU'(z,t)}{N}\left(\frac{\sqrt{\hat{\omega}^2 - f^2}}{\hat{\omega}}\right). \tag{5.11}$$

Figure 5.14 shows the measured and calculated response of ozone to the inertia-gravity wave with parameters determined from the horizontal wind measurements. A major concern is the estimation of the $\bar{O}_3(z)$ that is 'seen' by this long-period wave. Here, a low-pass filtered ozone profile (10 km) has been used. The lamina at 18 km is associated with ozone features estimated from the wind profile (Figure 5.14). The relative magnitudes of the measured and calculated ozone perturbations in Figure 5.14 suggest that inertia-gravity waves may drive a small but important component of the observed mesoscale ozone fluctuations.

5.4.2 Spectral analysis of short–period fluctuations

The ozone concentration and horizontal wind velocity data sets were analyzed in the previous section to identify longer-period features. The nightly-averaged ozone profiles

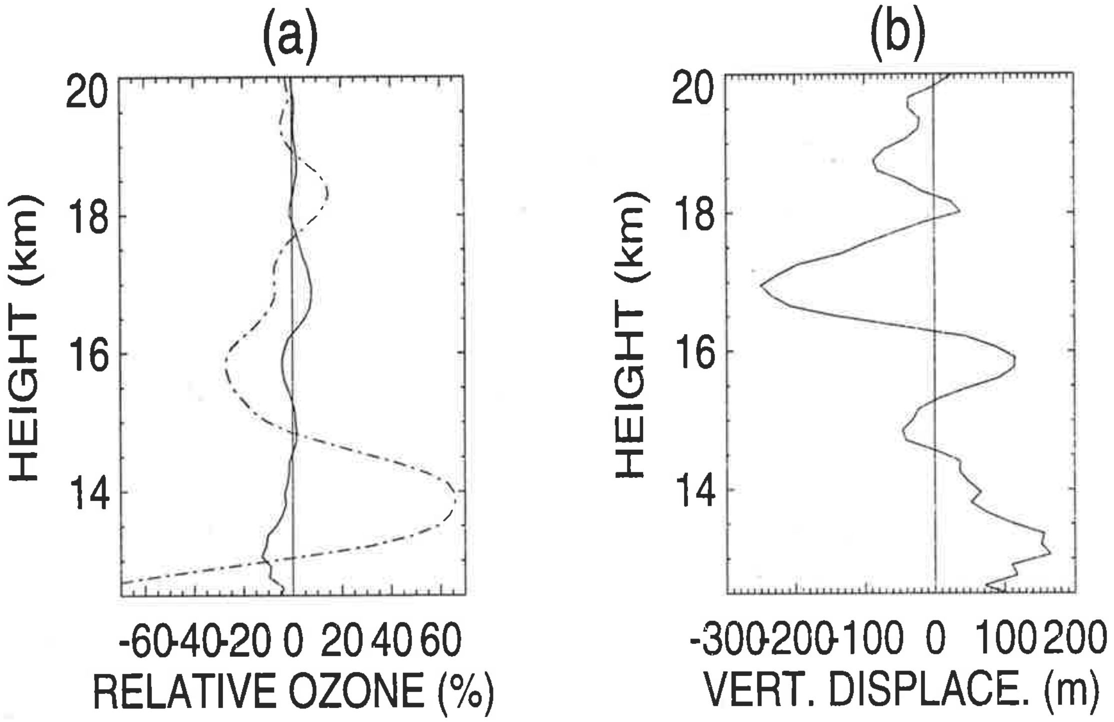

Figure 5.14: Measured relative perturbation of ozone concentration as determined by subtracting a cubic polynomial mean profile is shown with a dotted-dashed curve in panel (a). A calculated response from the IGW using (5.10) and (5.11) is shown with the solid curve in panels (a) and (b), respectively.

(Figure 5.4) indicated persistent features with vertical scales of ~2-3 km which may bias a gravity wave spectral analysis. In this section the shorter-period fluctuations present in tracer profile perturbations will be investigated through the calculation of mesoscale vertical wavenumber power spectra.

Mesoscale fluctuations with timescales shorter than the observation period are to be separated from longer period variations using the mean–perturbation approach described in Chapter 2. The mean profile in this study was determined using two common processes applied in atmospheric data analysis — a polynomial fit, and a time-based average. The average background profile of ozone concentration $< O_3(z,t) >$ and zonal velocity $< u(z,t) >$ were subtracted from each of the individual time-resolved profiles to obtain the perturbation quantities

$$O_3'(z,t) = O_3(z,t) - < O_3(z,t) >, \tag{5.12}$$

$$u'(z,t) = u(z,t) - < u(z,t) > . \tag{5.13}$$

In contrast, it is very common in gravity wave spectral studies, particularly those using sonde data, to calculate the perturbation quantities by extracting a polynomial fit or bandpass filtered mean profile $\bar{O_3}(z)$ [*Teitelbaum et al.*,1994; *Allen and Vincent*,1995; Chapter 4].

$$O_3'(z,t) = O_3(z,t) - \bar{O_3}(z), \tag{5.14}$$

and similarly for wind components and/or temperature.

The OHP data set provides an opportunity to investigate the implications of applying a time-averaged background as opposed to a statistical fit. Figure 5.15(a) compares power spectra of relative ozone concentration calculated by extracting the 6.5 hr average ozone profile $< O_3(z,t) >$ (dashed-dotted line) and by extracting a low-pass filtered background profile $\bar{O_3}(z)$ (solid line).

Gage and Nastrom [1986] obtained a predicted spectral shape for conservative tracer perturbations which depends on the spectra of wind fluctuations and the background ozone vertical gradient. This spectral prediction is overplotted as the dashed line in Figure 5.15(a). *Gage and Nastrom* [1986] suggested a relation between the observed spectra of vertical displacements and those of conservative atmospheric tracers. Their analysis was based on a quasi-horizontal two-dimensional turbulence interpretation of atmospheric motions, where vertical transport results from gradual movement of parcels along sloping quasi-horizontal isentropic surfaces [*e.g.* *Gage*,1979]. This interpretation has been largely superceded by a gravity wave-based approach.

However, the predicted relationships between spectra of tracers and of potential temperature, for example, are a product of the polarization relations [Chapter 2] for monochromatic wave motions and are hence independent of the exact physical mechanism assumed responsible for the observed spectra. The relationship between spectra of mixing ratio perturbations $F_q(m)$ and vertical displacement perturbations $F_{\zeta'}(m)$ is [*Gage*,1979],

$$F_q(m) = \left(\frac{d\bar{q}}{dz}\right)^2 F_{\zeta'}(m). \tag{5.15}$$

As an extension of the expressions presented in *Gage and Nastrom* [1986], their results will here be adapted in a manner analagous to *Fritts and VanZandt* [1993] whereby $F(m)$ is obtained from the two-dimensional spectrum $H(m,\omega)$ by integration over an assumed frequency spectrum proportional to ω^{-p} [Chapter 2]. Using this process the predicted relationship between q' and u' is

$$< q' >= \frac{p}{N}\left(\frac{d\bar{q}}{dz}\right) < u' > . \tag{5.16}$$

Figure 5.15(b) displays the power spectrum of zonal wind fluctuations (solid line) and the predicted $\propto \frac{N^2}{m^3}$ slope calculated with $N \approx 0.02$ rad s^{-1} (dashed line). The magnitude and slope of Figure 5.15(b) are consistent with previous stratospheric analyses [*e.g. Tsuda et al.*,1989].

5.4.3 Discussion of the separability of gravity wave spectra

As mentioned in Chapter 2, the question of the separability of the spatial and temporal gravity wave spectra remains an important area of investigation. Lidar measurements, with their high temporal and spatial resolution, are able to provide key insights into both vertical wavenumber $F(m)$ and frequency $G(\omega)$ spectra as well as the two-dimensional gravity wave $H(m,\omega)$ spectrum.

Gardner [1996*a*] made use of measurements from the Starfire Optical Range to argue that the gravity wave spectrum is nonseparable. In contrast, *Hecht et al.* [1996a] interpreted 2D spectra from airglow imaging observations as supporting evidence for separability of the gravity wave spectrum.

In a qualitative sense, the results presented in this case study of DIAL ozone and RD lidar data from OHP are consistent with separability of $H(m,\omega)$. The presence of an inertia-gravity wave, with period ~10 hr and vertical wavelength 2.3 km, simultaneously with shorter period variations with similar vertical scales, as suggested by the profiles (Figure 5.3), is an indication of the presence of a two-dimensional spectrum where a specific m component does not correspond to a narrow band of preferred ω values.

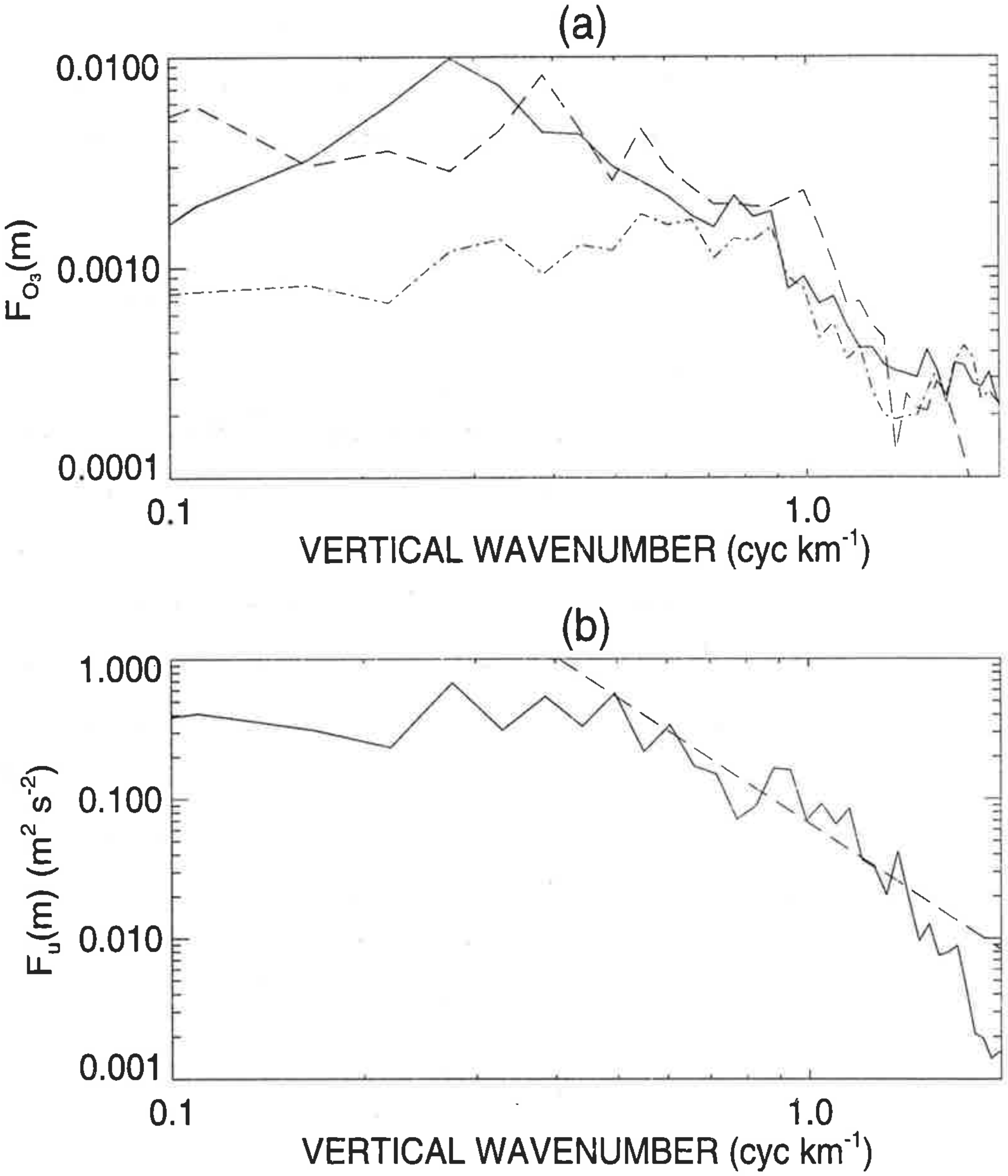

Figure 5.15: (a) Power spectra of relative ozone concentration from *Gage and Nastrom* [1986] model prediction (dashed line), spectrum calculated by extracting the 6.5 hr average ozone profile (dashed-dotted line) and by extracting a low-pass filtered background profile (solid line). (b) Power spectrum of zonal wind fluctuations (solid line) with predicted saturated spectral slope (dashed line).

It is clear that at locations where both internal and inertia-gravity waves are prevalent, either forced by meteorological or orographic effects, there may exist strong wave components with similar vertical scales but widely differing temporal scales. Hence this case study provides supporting evidence toward the findings of *Hecht et al.* [1996a]. Further case studies, particularly using lidar techniques, which examine the form of the two-dimensional gravity wave spectrum could clarify this important issue.

5.5 Chapter Summary

DIAL ozone lidar and RD lidar measurements from OHP have provided a new and improved framework for observing and interpreting mesoscale fluctuations in the stratosphere. The information on time-evolution of the ozone vertical profile available from DIAL measurements was used to infer a minimum continuous lifetime of two ozone laminae of 6.5 hr. It was possible to estimate a minimum lifetime of 14 hr for a major lamina event by using the sequence of lidar measurements in conjunction with measurements of ozone concentration from an ozonesonde released 7 hr after the final lidar measurement. Reliable information on the timescales and evolution of stratospheric ozone laminae has previously not been available through direct measurements.

The high resolution wind measurements obtained using the RD lidar provided a detailed picture of the mesoscale dynamic structure during the case study. A 6.5 hr sequence of vertical profiles of horizontal velocity structure revealed a downward propagating long-period inertia-gravity wave feature with vertical wavelength 2.3 km and observed vertical phase speed -0.06 m s^{-1}, which was most obviously present below ~20 km. Values of intrinsic wave frequency of 0.00022 rad s^{-1} and zonal wavelength of 360 km were estimated from the wind velocity fluctuations using a Stokes parameter analysis and the gravity wave dispersion relation.

The response of the ozone field to this inertia-gravity wave was estimated. The inertia-gravity wave alone, acting on the smooth background ozone profile, was found to produce fluctuations in phase agreement with those observed, particularly above ~16 km. However, the magnitudes of these fluctuations were a factor of at least 2-5 times smaller than those observed at lamina heights.

The role of large-scale isentropic transport in driving observed fluctuations was suggested from a preliminary CAS calculation for the lidar observation period which indicated the presence of a large-scale intrusion of polar air over OHP at approximately 14 km, in agreement with the height at which an important laminar feature was identified in the DIAL ozone lidar profiles [Roger Atkinson, private communication]. It is suggested that the presence of such a pre-existing large-scale filamentary feature may affect the local ozone response to gravity waves. This aspect will be approached from a modeling perspective in Chapter 6.

The quasi-time-invariant structure of zonal velocity and ozone concentration was removed in order to calculate the vertical wavenumber power spectra of relative ozone perturbations and zonal velocity perturbations for vertical scales of 1-10 km. The vertical wavenumber power spectra of zonal wind perturbations agreed in slope and magnitude with previous spectra determined from observations of stratospheric winds. The power spectra of ozone concentration fluctuations were compared with the predictions of *Gage and Nastrom* [1986] and found to be in agreement for vertical wavelengths in the range studied.

The dependence of power spectra of relative ozone fluctuations on the process of removal of a background layer shape was investigated. A vertical wavenumber power spectrum of relative ozone fluctuations calculated by fitting a smooth polynomial background profile was compared with a spectrum obtained by removing a time-averaged background profile. It was noted that the total ozone variance was much reduced in the latter case, and that the form of the power spectrum was significantly altered for smaller wavenumbers. It is suggested that the time-resolved DIAL ozone concentration measurements provide an excellent framework for the calculation of tracer power spectra which allows the separation of processes with similar vertical scales but different temporal scales.

This work has drawn extensively on both lidar processing considerations and analysis procedures similar to those used in the identification of monochromatic wave parameters and also determination of spectral properties from Na lidar data [Chapter 3; Appendix A; GV87; SG91]. The issue of the sensitivity of the gravity wave spectral magnitudes and spectral slopes to the definition of a mean profile has been further addressed here with the motivation of trying to understand the anomalous tracer spectra slopes and forms determined by *Bacmeister et al.* [1996].

In conclusion, the case study presented in this chapter has provided a wealth of detailed new information relating to the mesoscale structure of stratospheric ozone. A many-layered picture of ozone structure was suggested by the observations. Large-scale quasi-horizontal transport of ozone on isentropic surfaces was responsible for an initial laminated ozone structure. In addition, a long-period inertia-gravity wave was identified in horizontal velocity observations resulting in a further steepening of the vertical gradients of ozone. Hence, increased local background ozone gradients were experienced by short-period gravity waves leading to a convincing possible explanation for the larger variability observed in ozone than is suggested by temperature measurements alone [*Ehhalt et al.,*1983; *Bacmeister et al.,*1996; Chapter 4].

Chapter 6

Mesoscale Transport Modeling

We know little, but that we must hold to what is difficult ... that something is difficult must be a reason the more for us to do it.

Rainer Maria Rilke

6.1 Introduction

Mesoscale transport modeling aims to both reproduce observations and predict subsequent motions of trace quantities in the atmosphere on vertical scales of ~0.1-10 km, horizontal scales of 1-1000 km, and timescales of ~10 min to ~1 day. Mesoscale modeling studies provide a useful tool with which to examine the complex processes observed in high resolution observations of stratospheric tracer structure. A Lagrangian transport model, where individual parcels are initialized and followed as they undergo velocity-induced displacements, is a very convenient theoretical concept whereby tracer mixing ratios, potential temperature, and potential vorticity, which are conserved during Lagrangian transport, can be used to label parcels directly.

This chapter introduces a two-dimensional Lagrangian mesoscale parcel advection model. This modeling study was carried out in collaboration with Dr S. D. Eckermann from Computational Physics Inc., Fairfax, Virginia, and Dr J. T. Bacmeister from Naval Research Laboratory, Washington, D.C., and forms part of a continuing project

[*Eckermann, Gibson-Wilde, and Bacmeister*, manuscript in preparation]. Segments of Section 6.7 were presented at the *First SPARC General Assembly, Melbourne, Australia, December 1996* as the poster "Parcel Advection Model of Stratospheric Tracer Fluctuations Due to Gravity Waves" by D. E. Gibson-Wilde, S. D. Eckermann, and J. T. Bacmeister.

Section 6.2 presents an overview of key observational evidence of mesoscale tracer structure, particularly stratospheric ozone and potential temperature, which will be the primary focus of the chapter. Measurements from sonde, lidar, and stratospheric aircraft techniques are summarized. In Section 6.3, previous approaches to mesoscale modeling which are relevant to the interpretation of vertical profile observations are reviewed, bringing together concepts from Chapters 3-5. The discussion commences with three related models: a number density transport model, a linearized analytical model, and an extended analytical model including non-linear terms. These modeling approaches have been used previously to explore gravity-wave phenomena in the ozone layer and in ionospheric layers [*Dudis and Reber*,1976; *Chiu and Ching*,1978], and in the mesospheric sodium layer [GS85; Chapter 3].

In order to investigate the complex mesoscale ozone variability suggested by stratospheric measurements, Section 6.4 overviews a model which simulates the advection of air parcels by gravity waves [*Eckermann, Gibson-Wilde, and Bacmeister*, manuscript in preparation]. The model is based on the conservation of potential temperature and the ozone mixing ratio in air parcels advected by gravity wave motions [Chapter 2]. In Section 6.5, the predictions of the Lagrangian parcel advection scheme are compared with those of the existing analytical models. The different physical assumptions invoked in the analytical models lead to differing results in regions where strong tracer gradients are present; such as ozone lamination events. The parcel advection model then forms the basis of a simulation in Section 6.6 of gravity-wave-induced fluctuations of ozone abundances within representative stratospheric environments.

A model-based investigation in Section 6.7 addresses the effects of tracer structures produced by large-scale quasi-horizontal transport, specifically ozone laminae, on the mesoscale ozone response. The form of vertical wavenumber power spectra of stratospheric tracer quantities $F_q(m)$ under different large-scale conditions is then examined.

Section 6.8 examines a modeled inertia-gravity wave (IGW) which was based on the observational case study from OHP presented in Chapter 5 [see also Appendix B]. From a numerical modeling perspective on the case study data, the ozone response calculation of Section 5.4.1 will be extended and the modeled modulation of the laminar structure by long-period fluctuations will be compared with observations.

6.2 Stratospheric Tracer Variability

Specific results relating to stratospheric tracer variability gathered from the ozone observational studies of Chapters 4 and 5, as well as previous observational campaigns, are surveyed here. Based on these observational sources, a modeled atmospheric framework is developed in Section 6.6 from which gravity wave parcel advection is explored in Sections 6.7 and 6.8.

Analysis of ozonesonde vertical profiles of ozone mixing ratio and potential temperature from a southern hemisphere mid-latitude location were presented in Chapter 4. These data indicated mesoscale ozone variability in the stratosphere of 5-20% superimposed on quasi-stationary mean ozone vertical profiles. The corresponding potential temperature variations maximized at ~2% over the same height range. Studies of tracer variance and the related EDH calculated from long-term averages of northern hemisphere observations [*Ehhalt et al.*,1983], suggested a similar result of very large mesoscale ozone variances with important seasonal variation.

A recent preliminary study by *Ogino et al.* [1997] investigated the latitudinal variation (60°S-43°N) of the correlation between potential temperature and ozone fluctuations using data from a sequence of ship-launched ozonesondes from November-December 1987-1990. Strong correlations were calculated in the stratosphere at equatorial latitudes (15°S-15°N), whereas weak correlations were obtained from the mid-latitude sonde flights. This result suggests the importance of strong mean meridional ozone mixing ratio gradients at mid-latitudes in producing ozone variability which is not correlated with temperature variability (see Figure 1.2(b)).

Time-resolved vertical profiles of ozone concentration obtained using the DIAL technique, as presented in Chapter 5, permitted the calculation of vertical wavenumber power spectra of ozone and horizontal velocity fluctuations. The vertical wavenumber power spectrum calculated from relative ozone concentration perturbations was found to have a spectral shape which was consistent with that calculated from the horizontal velocity spectrum through a relationship suggested by *Gage and Nastrom* [1986].

Aircraft measurements, such as the Global Atmospheric Sampling Program (GASP) [*Gage and Nastrom,*1986] and numerous campaigns using the NASA ER-2 aircraft [*e.g. Bacmeister et al.,*1996], have provided a statistically reliable means of calculating mesoscale spectra of stratospheric tracers. These measurements are limited by the sporadic nature of the aircraft-based experiments and can provide only horizontal wavenumber spectra. The variation in large-scale tracer structure from flight to flight, as well as that along flight paths, must be considered as an important source of variation in the calculated tracer spectra. The effect of differing large-scale horizontal structure as traversed by an aircraft can be anticipated based on the model results in Section 6.7.

Recent analysis by *Bacmeister et al.* [1996] showed that stratospheric wind velocity and potential temperature variability were consistent with an interpretation in terms of a spectrum of gravity waves. However, tracer spectra such as those of ozone and nitrous oxide number densities were inconsistent with the predictions of a simple linear gravity wave theory. *Bacmeister et al.* [1996] suggested that the perturbations may still be influenced by gravity waves, but that a more general theory was needed to explore the effects of large-scale structure and horizontal inhomogeneity of tracer profiles on the wave-induced response.

Large-scale Lagrangian transport calculations, such as the contour advection with surgery (CAS) technique [*Waugh and Plumb,*1994], provide a useful framework within which to examine the dynamical transport of tracers. The CAS technique has been used extensively, in association with assimilated meteorological data, to deduce the evolution of tracer structures, particularly in the region of the polar vortex. These models can reproduce many features in the tracer measurements made with the ER-2 aircraft during polar stratospheric missions [*e.g. Tuck,*1989; *Newman and Schoeberl,*1995], as well as satellite observations of large-scale ozone structure [*e.g. Manney* *et al.*,1995b].

Large-scale quasi-horizontal advection is implicated in ozone variations since ozone has been observed to vary strongly across isentropic surfaces compared with potential temperature [*e.g. Danielsen et al.*,1991; Figure 4.9]. An estimation of large-scale mean meridional ozone gradients was obtained in Chapter 4 from quasi-meridional flight paths of the ER-2 aircraft combined with vertically resolved mesoscale perturbations calculated from quasi-simultaneous sonde measurements. This process yielded estimated mean meridional ozone mixing ratio gradients of <0.005 ppmv km^{-1} (Figure 4.11) calculated over mid-latitude–polar meridional trajectories of length 100-800 km. These calculated gradients were found to be less than required to explain the observed fluctuations in ozonesonde vertical profiles in terms of gravity wave motions in a majority of cases. However, the limitations inherent in such an approach were highlighted, and further it is clear that no present observations are suitable for a full observational characterization of the vertical and horizontal mesoscale variability of ozone or other stratospheric tracers. Several major issues remain unresolved or incompletely determined with the data sources presently available; for instance, the relative importance of large-scale and mesoscale dynamical processes in the production of observed tracer variability remains a controversial issue. The parcel advection modeling approach developed in this chapter provides a useful framework for the exploration of these issues.

6.3 Analytical Models

The analytical models of gravity wave effects on tracer vertical profiles, as presented by *Chiu and Ching* [1978] and *Gardner and Shelton* [1985]], relate perturbations in mixing ratio of a conservative or quasi-conservative tracer present in a well-defined layer directly to relative atmospheric density perturbations through (2.26). *Chiu and Ching* [1978] discussed the problem of calculating the linear gravity wave response of a horizontally stratified constituent. They applied their analysis to the examination of the observed variability of the stratospheric ozone layer and ionospheric layers. *Gardner and Shelton* [1985] extended the approach of *Chiu and Ching* [1978] by investigating

Gaussian vertical profiles and obtaining expressions for second-order non-linear tracer response terms [Chapter 3; Appendix A]. An inverse procedure derived from this approach has been used extensively to obtain relative density fluctuations from sodium number density fluctuations measured using the Na lidar technique [Appendix A; *Senft and Gardner*,1991].

The major advantage of such an analytical approach is the capability of relating tracer fluctuations to atmospheric density fluctuations dependent only on the tracer's vertical distribution. Hence its frequent use in the interpretation of ground-based vertical profile observations, such as lidar and sonde data, where no information on horizontal distribution is available [discussed in Chapters 3-5; Appendix A]. The assumptions applied uniformly in the three models discussed in this section are: horizontal homogeneity of the mean constituent structure, and background layer temporal stationarity.

The following sections draw heavily upon the work of *Chiu and Ching* [1978] as well as *Dudis and Reber* [1976] and *Gardner and Shelton* [1985]. A major difference between the theoretical development presented here and that of these original authors is the primarily Lagrangian view-point which is followed initially, and from which the parcel advection approach is developed in Section 6.4.

6.3.1 Number density transport

Mixing ratio, a conserved quantity, is not measured directly by all measurement techniques.[1] Hence it is necessary to examine the transport of the measured quantity, number density or concentration n [see Table 2.1]. Number density is not a conserved quantity under Lagrangian transport since it is dependent on compressional effects experienced by the parcel as it is transported. The transport of number density must therefore be evaluated subject to the constraint of conservation of mixing ratio (2.21) [*e.g. Lindzen and Goody*,1965],

---

[1] Ozonesondes provide mixing ratio measurements. DIAL ozone lidars measure number densities from which mixing ratios can be calculated indirectly (see Section 5.2.2). The Na lidar technique measures directly Na number density [GS85; Chapter 3].

$$\frac{dq}{dt} = 0 \Rightarrow \frac{d}{dt}\left(\frac{n}{\rho}\right) = 0. \tag{6.1}$$

Evaluating the derivative in (6.1) using the quotient rule, and assuming an initial parcel located at (y, z, t) which is transported from the mean $(\bar{n}(y,z,t),\ \bar{\rho}(y,z,t))$ distribution over a time t' yields,

$$n(y+\eta', z+\zeta', t') = \int_0^{t'} \frac{\bar{n}(y,z,t)}{\bar{\rho}(y,z,t)} \frac{d\rho(y,z,t)}{dt} dt \ |^{z\to z+\zeta',\ y\to y+\eta'} . \tag{6.2}$$

Here $(\eta'(y,z,t), \zeta'(y,z,t))$ are the meridional and vertical displacements induced by a gravity wave although (6.2) is not derived for a specific form of the displacements.

From (6.2), which satisfies the physical constraint of conservation of mixing ratio in Lagrangian transport, it is possible to calculate a wave-perturbed number density profile as a function of latitude, height, and time. However (6.2) is a non-local expression in the sense that $n(y+\eta', z+\zeta', t)$ cannot be calculated directly in closed form from a known initial $\bar{n}(y,z,t)$ distribution. For this reason, it is appropriate first to search for a local closed-form expression, and hence linearization is suggested.

In the approach of *Gardner and Shelton* [1985], which was developed specifically for the analysis of ground-based tracer number density vertical profiles, the variation of density perturbations with height was neglected implicitly. It was assumed that a parcel undergoes transport between the heights $z \to (z+\zeta')$ without meridional motion $(\eta' = 0)$, and with its number density corrected subject to the relative density variations at the height z only. Equation (6.2) then simplifies to,

$$n(z+\zeta', t) = \bar{n}(z)\frac{\rho(z+\zeta', t)}{\bar{\rho}(z)}. \tag{6.3}$$

Equation (6.3) is equivalent to (40) in *Gardner and Shelton* [1985] and does not satisfy the constraint of conservation of mixing ratio for generalized atmospheric density variations. A correct theoretical development of number density transport which satisfies the constraints inherent in Lagrangian transport is provided by the Lagrangian parcel advection model in Section 6.4.

6.3.2 Linear analytical model

The evaluation of the Lagrangian-based expression (6.3) from a data set consisting of vertically sampled profiles is not straightforward. Using a McLaurin series expansion of (6.3) *Gardner and Shelton* [1985] derived

$$\frac{n'}{\bar{n}} \approx \frac{-1}{(\gamma-1)}\left(1+\frac{\gamma H}{\bar{n}}\bar{n}_z\right)\frac{\rho'}{\bar{\rho}}, \tag{6.4}$$

which is a linearized analytical local[2] relationship (see also Section 3.3) derived by retaining the full compressible gravity wave equations.

The linearized analytical model (6.4) has several major disadvantages. The first disadvantage is that a vertical derivative of the mean tracer number density profile is required. The values of derivatives calculated from discretely sampled data are sensitive to the measuring instrument's sampling frequency, as well as to any smoothing applied to the data. An example of this limitation was discussed in Chapter 5 where a vertical profile was fitted for a profile from the OHP data set.

The second disadvantage is that (6.4) is linked directly to number density fluctuations and the $\bar{n}_z(z)$ profile, which has a vertical variation different from that of the equivalent quantity expressed in mixing ratio terms. This means that the tracer fluctuations calculated from the $\bar{n}_z(z)$ profile will have a different form from those which include the conservation of mixing ratio in the presence of atmospheric density variation. The different properties of number density and mixing ratio representations are developed further in Section 6.5. This difficulty is particularly important in terms of the inverse procedure of calculating atmospheric density perturbations, and hence power spectra, from Na lidar measurements [Chapter 3; *Senft and Gardner*,1991].

6.3.3 Non-linear tracer response

The previous segment presented the first-order or linear response of number density variations to the atmospheric density perturbations which were obtained as an approximation to (6.1). This linearization is valid for atmospheric density perturbations less than ~10% [*Gardner and Shelton*,1985] and regions of the atmosphere with smoothly

---

[2] Number density of a parcel at (z, t_2) is calculated dependent only on data available at (z, t_1).

varying mean tracer vertical gradients. In order to develop a more generally valid approach, although still limited to vertical variations, higher order terms in $\frac{\rho'}{\bar{\rho}}$ in the McLaurin expansion were derived by *Gardner and Shelton* [1985],

$$\frac{n'}{\bar{n}}_{NL} = \frac{-1}{(\gamma-1)^2}\left(1 + \frac{3\gamma H}{2\bar{n}}\frac{d\bar{n}}{dz} + \frac{\gamma^2 H^2}{2\bar{n}}\right)\left(\frac{\rho'}{\bar{\rho}}\right)^2 . \tag{6.5}$$

Equation (6.5) represents an additional term to the linear analytical model which results from retaining the second order, non-linear terms in the McLaurin expansion. It was noted in Appendix A (Figure 12) that the magnitudes of the second-order non-linear terms given by (6.5) maximized at ~0.5%.

6.4 Lagrangian Parcel Advection Model

In this section a fully Lagrangian transport approach is described, followed by the development of a localized parcel advection model. A Lagrangian approach to transport modeling is not dependent on the calculation of vertical (and/or horizontal) derivatives from discretely sampled data, as was attempted in Chapter 4. The number density perturbations calculated at a given time depend only on the integrated change in density experienced by parcels over the elapsed time. It is this integrated density change which gives an exact measure of parcel advection, independent of the background layer gradient.

The fundamental concept of the conservation of tracer mixing ratio during Lagrangian parcel advection is illustrated in Figure 6.1. In order to explore the variation of tracer number density during such transport, a density-based constructed quantity is introduced, analagous to potential temperature, known as *potential density*, which is conserved under Lagrangian transport. Potential density is defined as [*Eckermann, Gibson-Wilde, and Bacmeister*, manuscript in preparation]

$$D(z) = \rho(z)\left(\frac{p_0}{p(z)}\right)^{\frac{1}{\gamma}} . \tag{6.6}$$

The exact Lagrangian expressions for the conservation of q and D are simply

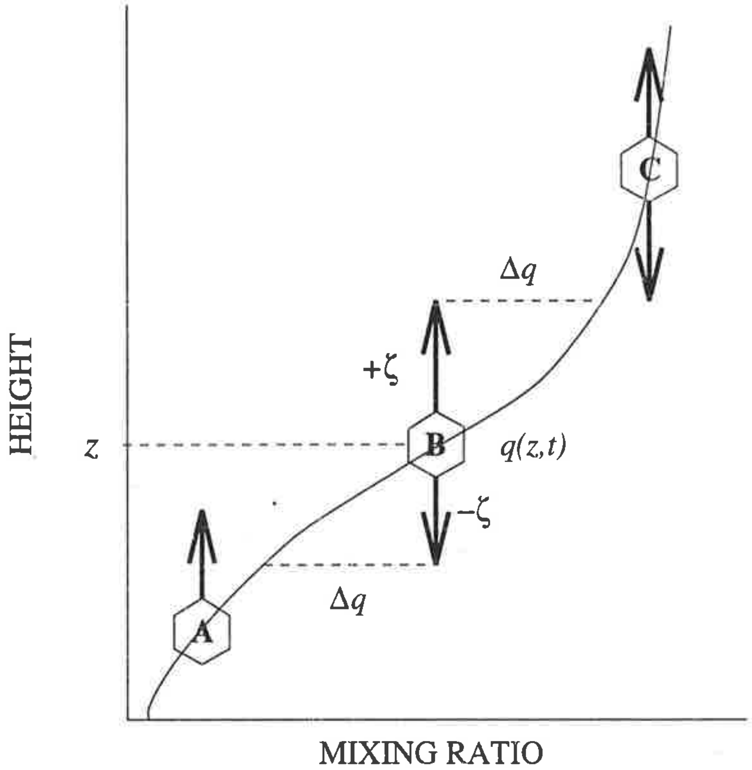

Figure 6.1: Schematic diagram of Lagrangian parcel advection process illustrating parcel displacements in the vertical direction only. Parcels A, B, and C are defined on the initial $q(z,t)$ profile and are transported while conserving their tracer mixing ratio q.

$$q(y+\eta', z+\zeta', t') = q(y,z,t), \tag{6.7}$$

and

$$D(y+\eta', z+\zeta', t') = D(y,z,t). \tag{6.8}$$

(6.7) and (6.8) are the basis for an exact Lagrangian transport calculation which must be re-gridded to determine the distribution of atmospheric variables at (y,z,t') from the known initial conditions at the position (y,z,t).

Figure 6.2 illustrates the process of transporting parcels from the initial regular, gridded distribution through the defined vertical and meridional gravity-wave-induced displacements.

The evaluation of the above approach is a process in which there is no direct relationship between $q(y,z,t)$ and $q(y,z,t')$, which parallels the non-local, non-analytical

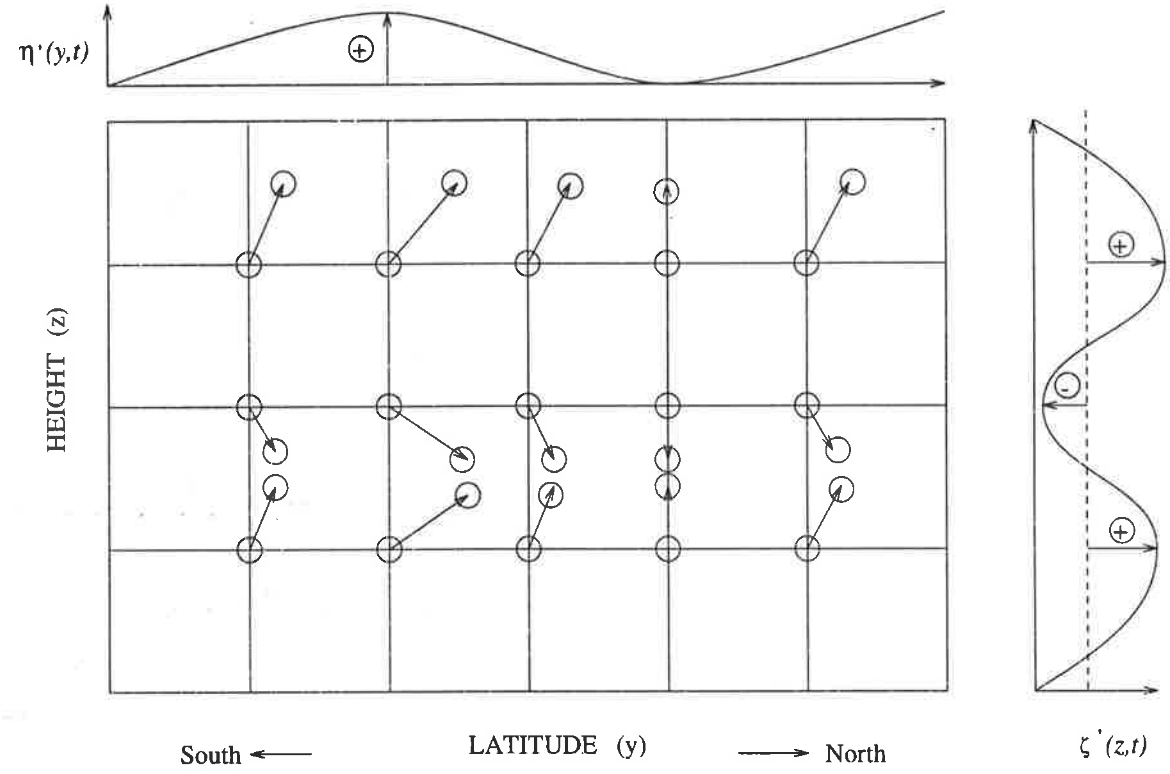

Figure 6.2: Schematic diagram of two-dimensional parcel advection.

problem with (6.2). Hence it is useful to search for a closed-form expression, analagous to the analytical models which were discussed previously, which retains the exact conservation relations inherent in the purely Lagrangian approach, but is suitable for application to gridded number density data sets. Such a model was suggested by the desire to avoid the approximations implicit in *Gardner and Shelton* [1985] while retaining the ease of calculation of the analytical models.

In the parcel advection theory approach, it is first noted that the atmospheric density variation for a parcel transported between heights $z \rightarrow z + \zeta'$ is

$$\rho(z+\zeta',t) = \bar{\rho}(z)\exp(\frac{-\zeta'}{H_\rho}), \tag{6.9}$$

from which the the number density variation can be expressed as

$$n(z+\zeta',t') = \bar{n}(z,t)\frac{\rho(z+\zeta')}{\bar{\rho}(z)} = \bar{n}(z,t)\exp(\frac{-\zeta'}{\gamma H}). \tag{6.10}$$

(6.10) is a closed-form parcel advection expression which forms the basis for the parcel advection modeling carried out in the remainder of this chapter. The two-dimensional parcel advection model was initialized with a mean atmospheric temperature, pressure, density, zonal and meridional velocity, and tracer number density gridded distribution. Air parcels were then transported by gravity-wave-induced meridional and vertical vector displacements $\zeta'(z,t)$ to new locations (z',t') according to (6.10). In the parcel advection model a two-dimensional spline interpolation was applied to perform the regridding to obtain $n(z,t')$.

6.5 Model Comparison and Summary

The previous sections have introduced four specific model equations used to relate atmospheric density variations and tracer number density variations. These equations are listed here:

- Number density transport (6.3)
- Linear analytical model (6.4)
- Second-order non-linear model (6.4) and (6.5)
- Lagrangian parcel advection (6.10)

Number density fluctuations in the linear model (6.4) are in phase with the atmospheric density variations for $\bar{n}_z(z) > 0$ (see also Section 4.3). Chapter 3 discussed the implications of this phase reversal on the calculated vertical wavenumber spectra of Na lidar observations.

For a Gaussian mean number density layer defined as

$$\bar{n}(z) = n_0 \exp\left(\frac{-(z-z_n)^2}{\sigma^2}\right), \tag{6.11}$$

the mean vertical gradient is given by

$$\bar{n}_z(z) = -2\frac{(z-z_n)}{\sigma^2}\bar{n}(z), \tag{6.12}$$

and (6.4) becomes [*Gardner and Shelton*,1985]

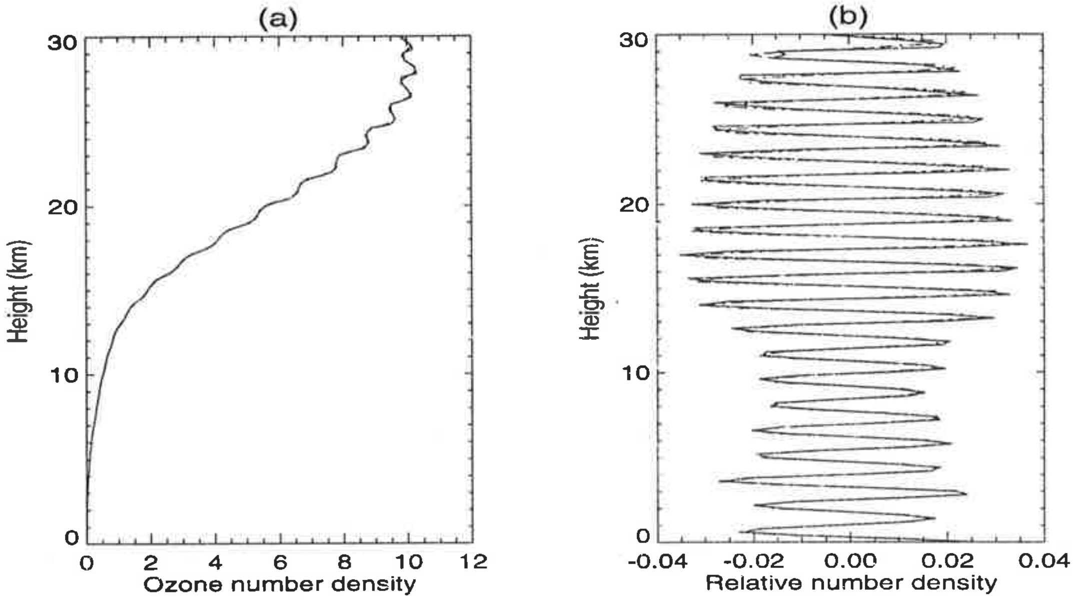

Figure 6.3: Comparison of parcel advection model (solid line) and linear analytical model (dashed-dotted line) for a mean Gaussian ozone number density profile. Note that the two curves overlap in most cases as is expected for this simple test case.

$$\frac{n'}{\bar{n}} \approx \frac{-1}{(\gamma - 1)} \left(1 - \frac{2\gamma H_\rho (z - z_n)}{\sigma^2} \right) \frac{\rho'}{\bar{\rho}}. \tag{6.13}$$

The relative number density fluctuations at the layer peak are then

$$\frac{n'}{\bar{n}} \approx \frac{-1}{(\gamma - 1)} \frac{\rho'}{\bar{\rho}}. \tag{6.14}$$

In contrast, for the parcel advection model (6.10) there is not necessarily an approximately symmetric or anti-symmetric peak structure or an anti-node at the peak. It is the height structure of the vertical displacements which controls the vertical structure of the number density perturbations. The relative number density variations are related to the relative mixing ratio variations through

$$r_n = r_q + r_\rho. \tag{6.15}$$

Figure 6.3 displays number density profiles and relative number density perturbations calculated using the parcel advection model (6.10) and the linear analytical model (6.4) for a model Gaussian mean vertical ozone number density profile. These are included to illustrate the agreement of these two modeling approaches for this straightforward case.

It is also important to note that a monochromatic sinusoidal fluctuation in the tracer models examined here will result in reversible transport, since the mean profiles are assumed stationary. Transport produced by a spectrum of interacting waves will not satisfy reversibility in the most general cases as a consequence of Stokes drift [*e.g. Walterscheid and Hocking,*1991] and/or wave saturation. The Lagrangian modeling approach discussed here lends itself to a detailed transport study including non-stationarity and complex vertical structure since the integrated parcel displacements are exact measures of transport.

The response of tracers to gravity wave motions in the presence of lamination, and hence potentially steep vertical gradients, will be the subject of detailed modeling investigations in Sections 6.7 and 6.8.

6.6 Stratospheric Modeling Studies

6.6.1 Modeled mean stratospheric distributions

Mean distributions of stratospheric tracers and thermodynamical variables were initialized over a height range of 0-30 km and a latitude range of 35°N-55°N. This height region was chosen as it comprises the dynamically controlled region of the stratospheric ozone layer. The latitude region investigated here reflects the mid-latitude analyses presented in Chapters 4 and 5; most particularly the northern hemispheric observations in Chapter 5 which are to be drawn upon specifically in Section 6.8.

A mesoscale grid resolution of 200 m in height and of 0.5° (~56 km) in latitude was chosen as a standard for the model results presented in this thesis. The chosen height resolution highlights mesoscale features resolved typically by sonde vertical profiles and lidars [*e.g.* Chapters 4 and 5], while remaining computationally inexpensive. Similarly the model meridional resolution retains wave motions with meridional scales larger than ~100 km. Meridional transport will not be investigated within the scope of this thesis, however it is anticipated that an improved meridional resolution will be included at a later stage to address specific meridional transport issues.

Zonal mean motions were assumed (Section 2.1.3.2) since this work initiates a meridionally and vertically resolved mesoscale modeling study. This limitation to a two-dimensional study is partially justified by the very important meridional variations of dynamical and tracer structure observed in mid-latitude regions (*e.g.* Figure 4.9) and the approximately zonally symmetric state of the atmosphere at many times of the year [*e.g. Andrews et al.,*1987]. Throughout modeling studies presented in this chapter, zero mean vertical winds are also assumed.

6.6.1.1 Simple models of stratospheric ozone, horizontal velocity, and temperature structure

A simplified background atmosphere model was used primarily for model evaluations and comparisons in Section 6.7. The model comprised zero mean zonal and meridional velocities, a constant temperature gradient of -1 K km^{-1}, and constant ozone mixing ratio gradient of 0.3 ppmv km^{-1}.

In light of the calculated mid-latitude mean vertical ozone profiles from Chapters 4 and 5, it was determined that a Gaussian layer provided a suitable modeled form for a generalized background ozone profile (see Figures 4.3 and 5.4). A Gaussian mean vertical ozone profile with a centroid height of 25 km, a layer half-width of 5 km, and a maximum ozone mixing ratio of 4 ppmv was defined as a simple, physically realistic, model representation of the mean ozone vertical distribution (Figure 6.4). Since the analytical models are dependent on mean vertical ozone gradients, specifically of number density, Figure 6.5 displays the mean ozone number density and mass mixing ratio and their vertical gradients (see also discussion in Section 6.5).

The southern hemisphere mean seasonal ozone profiles presented in Chapter 4 (Figure 4.3), indicate that such a stationary long-term mean profile is observed most commonly in autumn and spring. The variability of ozone profiles in southern hemisphere winter suggests non-stationarity of the mean profile over timescales of days and hence significant variations in total column abundances.

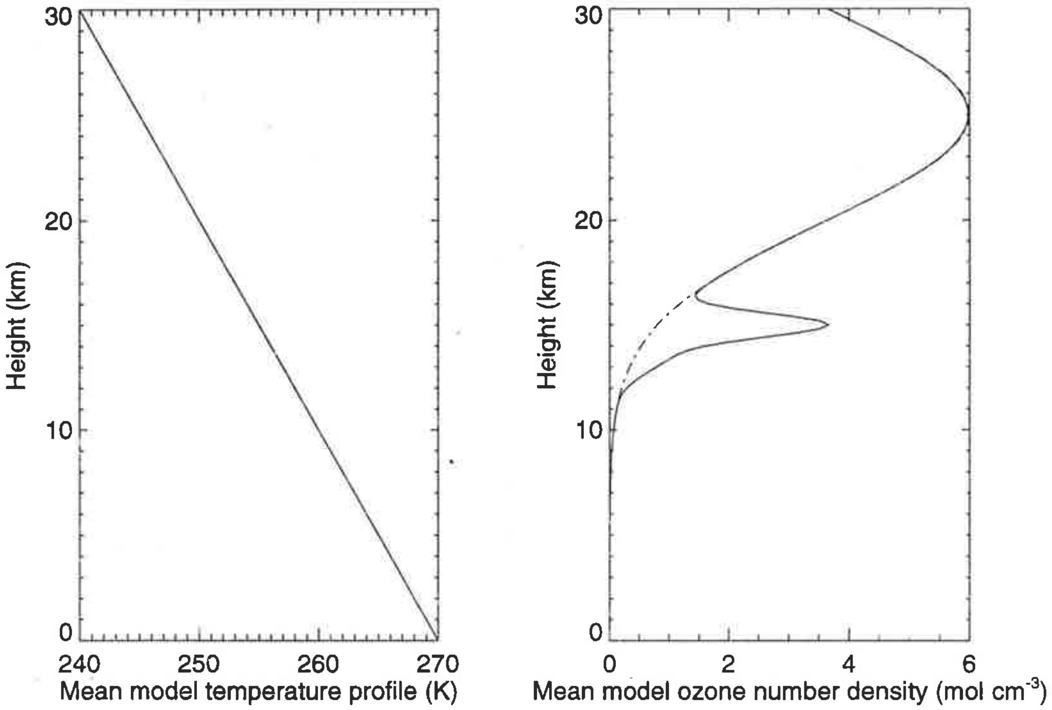

Figure 6.4: Mean linear model temperature profile (left panel) and Gaussian model mean ozone profile (right panel) with an ozone lamina present (bold line) and without a lamina present (dashed-dotted line).

6.6.1.2 Large-scale mean atmospheric model

The Committee for Space Research (COSPAR) International Reference Atmosphere [*COSPAR*,1986] large-scale model, was used here as a basis for middle atmosphere measurements of temperature, and zonal and meridional velocities. The *COSPAR* [1986] data are available at a latitude resolution of 10° and a height resolution of 3.5 km, with latitude coverage 80°S-80°N and height coverage 0-122.5 km. These large-scale gridded data were interpolated onto the higher-resolution model grid described above in order to initialize the mesoscale two-dimensional grid of vertical and meridional velocities and temperature. A zonal mean ozone mixing ratio distribution was inferred from *Andrews et al.* [1987]. Figure 6.6 displays the latitude-height contours of zonal mean zonal wind, mean zonal temperature, and ozone mixing ratio for January (northern hemisphere winter).

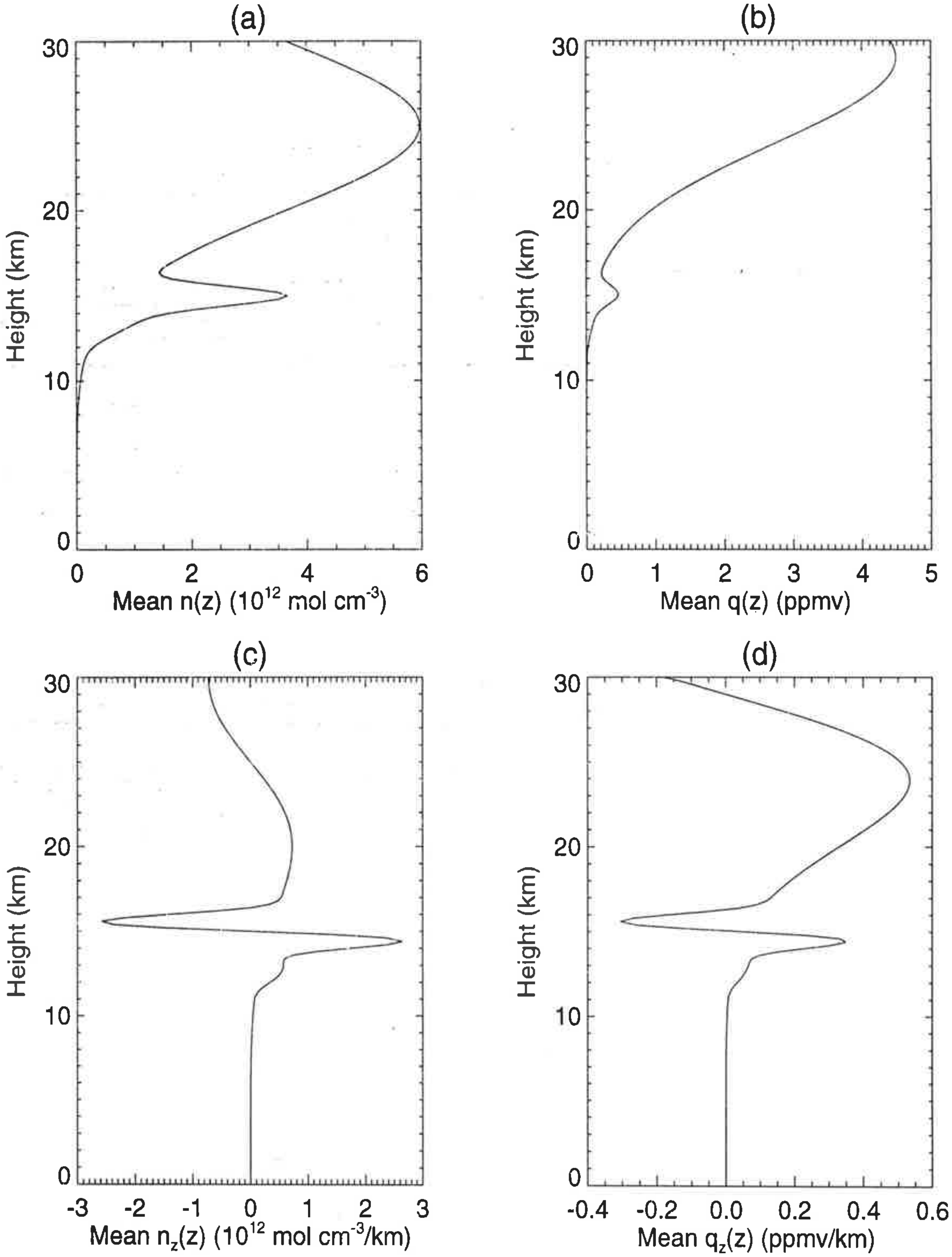

Figure 6.5: Modeled vertical profiles of (a) mean ozone number density, (b) mean ozone volume mixing ratio, (c) mean vertical gradient of ozone number density, and (d) mean vertical gradient of ozone volume mixing ratio.

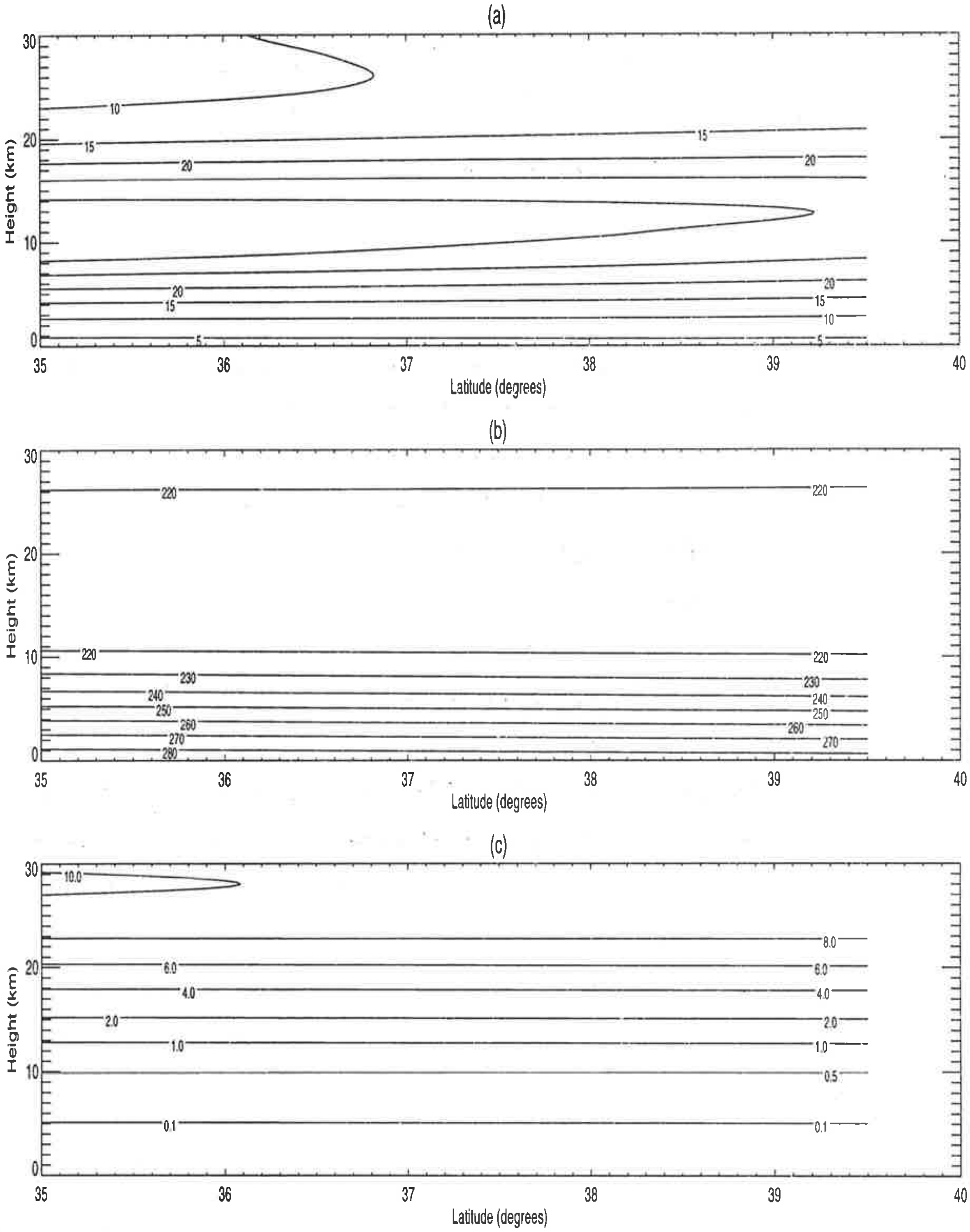

Figure 6.6: Latitude-height contours of background zonal mean zonal wind (m s^{-1}), temperature (K), and ozone mixing ratio (ppmv).

Wave parameter	Symbol	Inertia-gravity
Intrinsic frequency	$\hat{\omega}$	0.00022 rad s^{-1}
Vertical wavelength	λ_z	~1-3 km
Horizontal wavelength	λ_h	1-1000 km
Relative density at 20 km	A_{20}	0.1-1.0%
Atmospheric density scale height	H_ρ	7 km

Table 6.1: Wave parameters of IGWs simulated in this study.

6.6.2 Monochromatic gravity wave model

A monochromatic gravity wave was chosen as a straightforward starting point in this modeling study of mesoscale ozone variations. Typical vertical wavelengths of gravity-wave motions in the stratosphere, determined primarily from radiosonde velocity measurements, are ~2 km [*e.g. Tsuda et al.,*1989]. Gravity wave fluctuations are to be simulated in this chapter specifically to represent wave motions in the stratosphere in a similar vein to the mesospheric monochromatic wave study discussed in Chapter 3 [see also Appendix A]. The form of monochromatic wave used in the modeling study was (2.31). Wave parameters input to the wave model are summarized in Table 6.1, along with ranges of values which were explored for the stratosphere.

The initial fluctuations in temperature and constituent abundances were set to zero, representing the idea that parcels are positioned initially on the mean profile. A $\tanh(t/100)$ dependence was included to simulate the 'ramping' up of the modeled gravity wave amplitudes from the initial condition.

The model was tested for non-critical amplitudes, representing the restriction that no convective instabilities were generated. This restriction implies that the vertical wave displacements must be constrained by

$$\zeta' < \frac{\lambda_z}{2\pi}. \qquad (6.16)$$

6.6.3 Ozone lamina model

Observational evidence of the horizontal structure of ozone filaments or laminae has been provided at low resolution by satellite data, such as the Upper Atmosphere Research Satellite Microwave Limb Sounder [*e.g. Manney et al.,*1995b] and sporadically at high resolution by ER-2 aircraft data [*e.g. Danielsen et al.,*1991; *Newman and Schoeberl,*1995]. Estimations of the horizontal extent of filaments from these observations, as well as large-scale modeling methods are ~100-1000 km [*Orsolini et al.,*1995]: however the typical horizontal resolution of satellites is O(100 km). Some indication of the transport processes responsible for the formation of ozone laminae has been provided by large-scale modeling techniques [*e.g. Orsolini et al.,*1995].

High resolution observations of the vertical structure of laminae have been obtained primarily from ozonesonde measurements of vertical ozone profiles [*Dobson,*1973; *Reid and Vaughan,*1991], and more recently from ozone lidar observations [Chapter 5; *Gibson-Wilde et al.,*1997]. Study of a database of ozonesonde profiles has suggested that laminae occur predominantly at altitudes of 12-18 km and that the most commonly occurring heights of laminae are 14-15 km, typically $\bar{\theta}$ ≈400 K [*Reid et al.,*1993]. These authors found magnitudes of laminae were 40-70 nbars and the most commonly occurring vertical extent of laminae was 1.5-2 km.

Some examples of ozone laminae, observed in the southern hemisphere at Macquarie Island (54.5°S, 159.0°E), and in the northern hemisphere at OHP (44°N, 6°E), were presented in Chapters 4 and 5, respectively (Figures 4.6 and 5.4). The profusion of available northern hemisphere mid- and polar latitude ozonesonde observations, as opposed to tropical and southern hemisphere observations, led to the modeling effort presented here emphasizing these regions.

In light of these observational studies, a simple mean ozone vertical profile was used here which consists of a Gaussian layer of half-width 5 km, centroid at 25 km, and peak ozone concentration 6×10^{12} molecules cm^{-3}. A typical ozone lamina was modeled as a Gaussian layer of half-width σ_L=0.3 km, vertical extent ~2 km, centroid magnitude twice the background concentration, and positioned at a height of ~15 km (Figure 6.7(a)). The transition between the modeled background profile and the lamina was smoothed using a running mean to ensure a smooth vertical ozone gradient. The horizontal variations in laminar structure have not been explored fully in the initial modeling study. It should be noted that the simple lamina model developed here is not applicable in the polar vortex edge region, where airborne ozone lidar data presented by *Reid et al.* [1993] have indicated very significant meridional gradients in

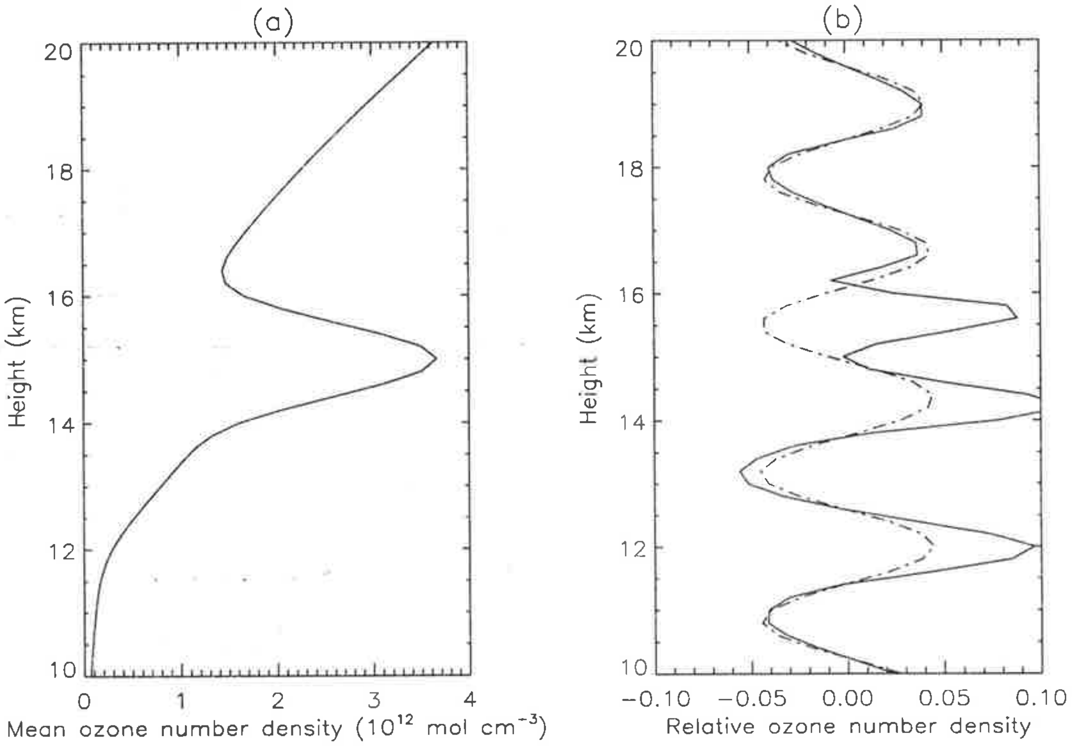

Figure 6.7: (a) Simple model of laminated mean ozone profile, and (b) relative ozone number density perturbations with (solid line) and without (dashed-dotted line) lamina present as simulated by parcel advection model using the IGW in Table 6.1.

the laminae.

6.7 Gravity Wave Response in Laminated Ozone Environments

The Lagrangian parcel advection model [*Eckermann, Gibson-Wilde, and Bacmeister*, manuscript in preparation], including a modeled background ozone structure, a modeled monochromatic gravity wave fluctuation, and the ozone lamina model as described in previous sections, is here applied to the investigation of the response of gravity waves in a layered ozone environment with lamination present. Figure 6.8 summarizes the major elements of the parcel advection model. This chapter specifically concerns stratospheric ozone applications, and hence ozone lamination, however the ideas are clearly suited to other investigations, such as the mesospheric SSL events [Chapter 3].

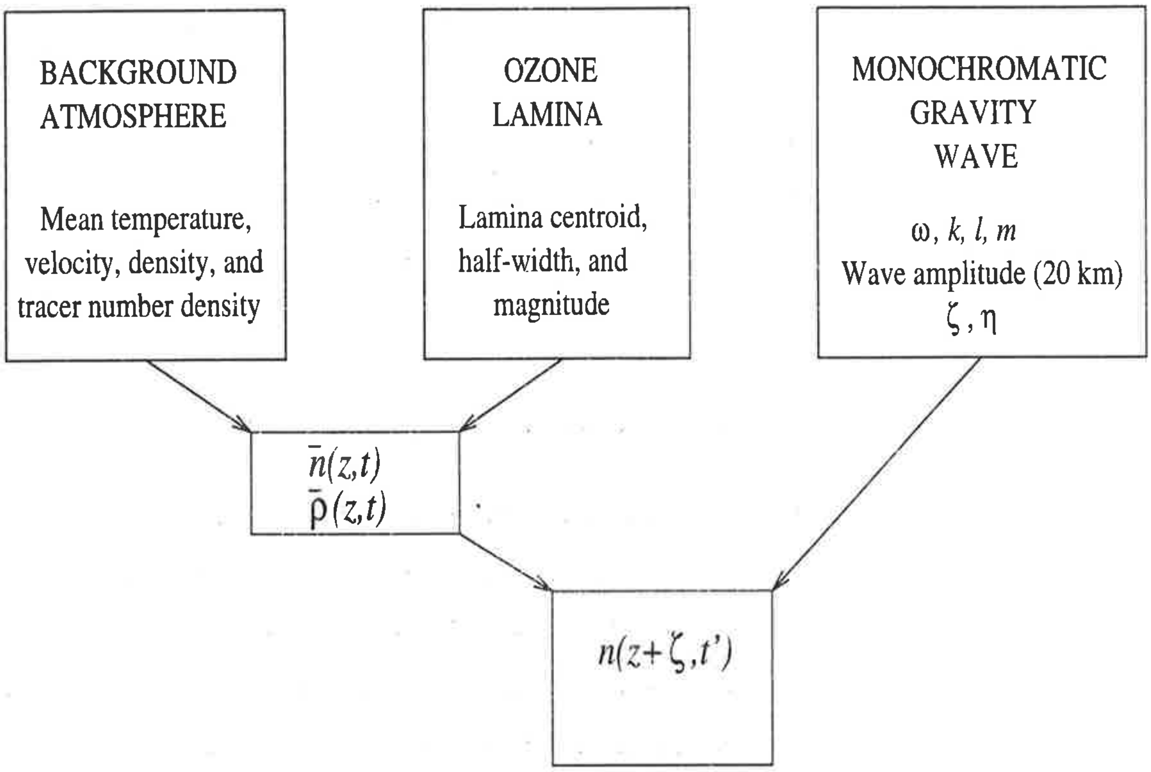

Figure 6.8: Schematic diagram of a model implementation of the Lagrangian parcel advection concept.

In this section, an internal gravity wave is simulated, representive of a short-period wave motion in the stratosphere. The vertical (and horizontal) scales of laminar structures present will have an important impact on the gravity wave response. Two effects were observed in the modeling studies and are described here as *modulation* and *superposition*. These were explored by making use of the same lamina structure, as described in Section 6.6.3, responding to different vertical wavelengths. The modulation effect is described below in preparation for the re-examination of the OHP case study carried out in Section 6.8.

6.7.1 Modulation of laminar structure by gravity waves

The term *modulation* in the present context refers to the response of ozone number density perturbations to gravity wave motions of a similar vertical scale to the modeled laminar feature, *i.e.* $\lambda_z \approx \sigma_L$. This process results in an interaction between two fluctuations of similar vertical scale — analagous to the constructive or destructive interference between two wave motions.

This study was chosen specifically to investigate the interaction between a background laminated structure and an IGW. Figure 6.7(b) displays the relative ozone number density perturbations $r_{O_3}(z)$ calculated in the presence and the absence of an ozone lamina. It is clear that the laminated structure is responsible for an increase in maximum $r_{O_3}(z)$ from ~4% to ~10%.

6.7.2 Effect of lamination on tracer spectra

This section investigates the effect of the presence of a laminated tracer structure on the spectral characteristics of the calculated vertical wavenumber power spectra. The parcel advection model was directed specifically to evaluate the suggestion of *Bacmeister et al.* [1996] that the vertical gradients in tracer distributions induced by large-scale quasi-isentropic advection processes may enhance the tracer response to smaller-scale wave motions, particularly gravity waves.

This exploration of tracer spectra is restricted to the highly simplified case of monochromatic wave variations. A vertical wavenumber power spectrum of relative ozone number density perturbations was calculated from the model-generated profiles (Figure 6.7(b)) in the presence of and in the absence of ozone lamination. Figure 6.9 indicates that the magnitude of the power spectrum is larger by approximately a factor of 10 over a range of vertical wavenumber values of approximately 0.1-1.0 cyc km^{-1}. This result has clear implications for the associated ozone variance, and hence provides supporting evidence for the role of large-scale structures in the enhancement of mesoscale tracer spectra as proposed by *Bacmeister et al.* [1996].

6.8 A Re-examination of the OHP Case Study

The DIAL ozone concentration measurements and RD lidar velocity measurements analyzed in Chapter 5 provide a very suitable observational basis from which to construct a model simulation. The case study from OHP is re-examined by initializing the parcel advection model with the average background ozone and temperature profiles, and a simplified horizontal velocity structure based on those observed at OHP. This

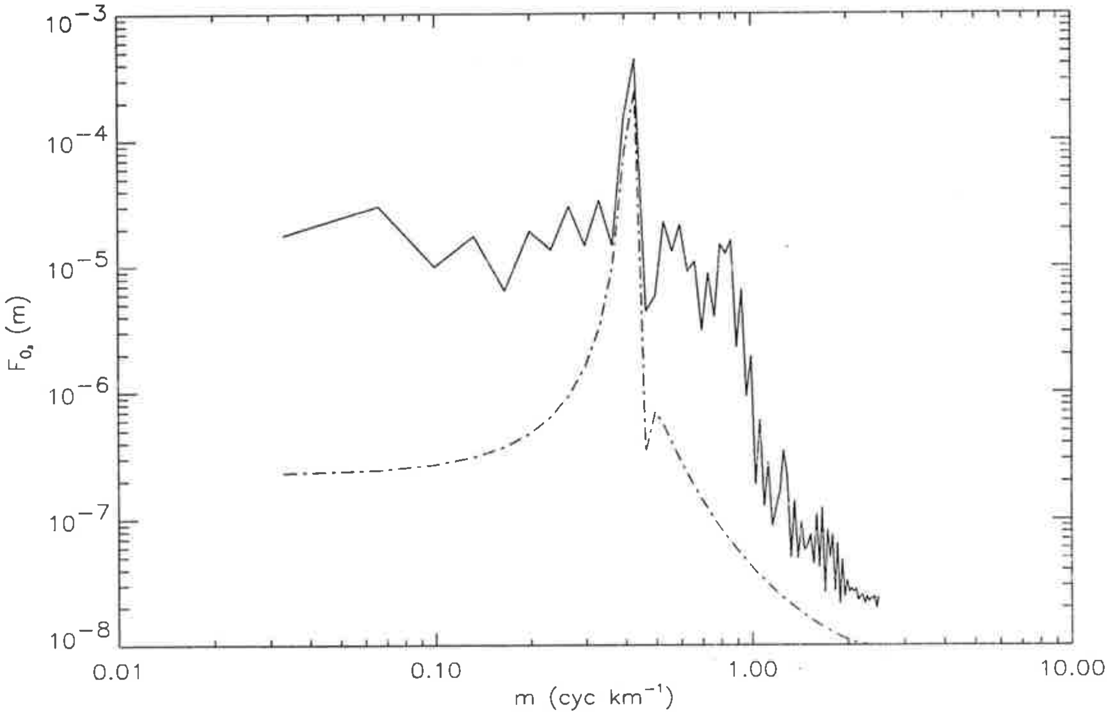

Figure 6.9: Vertical wavenumber spectra of relative ozone number density calculated with (solid line) and without (dashed-dotted line) the presence of the modeled laminar feature for OHP-like conditions.

situation extends the simple model study of Section 6.7 with the aim of exploring some of the features observed in the OHP case study through a model-based simulation.

The specific form of lamination observed during the night of 23-24 October 1995, consisting of two laminae at approximately 14 km and 18 km, and the ozonesonde measured mean temperature profile were used to describe a mean atmospheric structure (Figure 6.10) into which a gravity wave perturbation was introduced. This approach contains the underlying assumption that the 6.5 hr average DIAL ozone profile provides an accurate picture of the mean ozone concentration, assumed to be due to large-scale quasi-horizontal isentropic advection processes, and experienced as a stationary background structure by wave motions. This assumption is certainly valid for wave motions with timescales significantly less than 6.5 hr, where the discussion in Section 6.7 is applicable for the OHP data set (see also Section 5.4.2).

The IGW detected in the RD lidar data, with an observed period close to the inertial period, is certainly of a timescale longer than 6.5 hr, and hence it must be

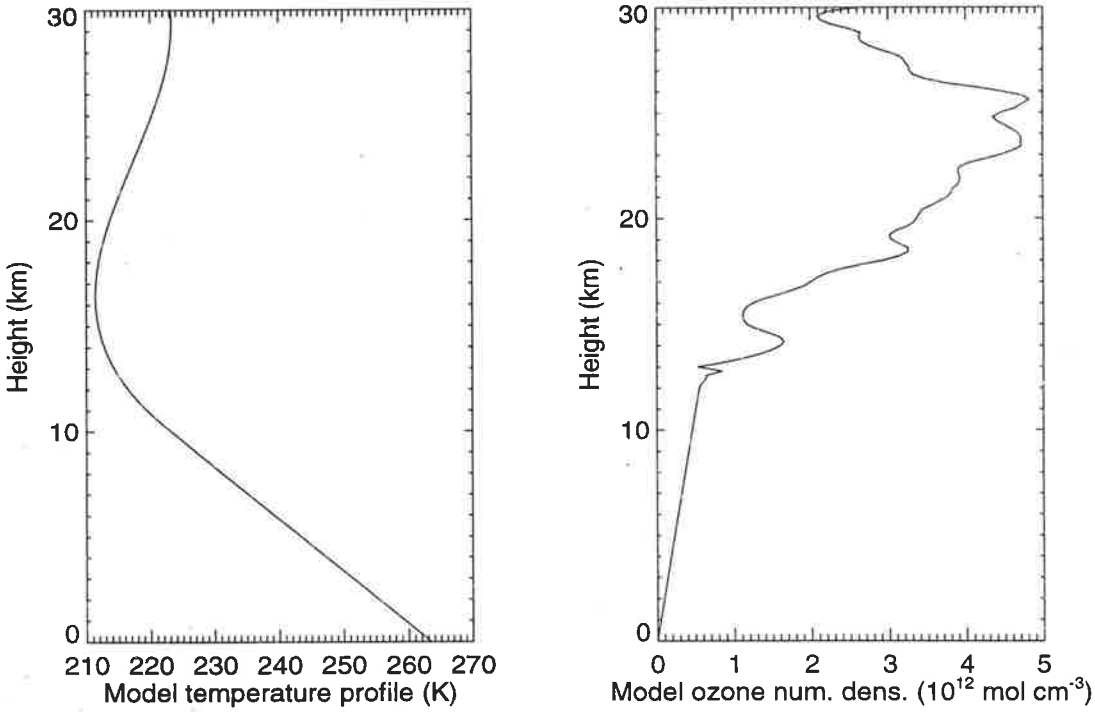

Figure 6.10: Mean model temperature profile (left panel) and mean ozone profile (right panel) based on the OHP case study presented in Chapter 5.

assumed that the average profile from the lidar observations may still contain some elements of bias due to incomplete removal of long-period wave motions. However, Figure 5.7 indicates that the laminar formation at 14 km exhibits strong stationarity over the 14 hr between the first lidar observation (2230 LT on 23 October 1995) and the ozonesonde flight (1200 LT on 24 October 1995), suggesting that the time-averaged background profile reproduces the vertical profile due to the large-scale long timescale processes.

The aim of such an investigation was to explore further the wave-induced ozone structure from the case study by drawing on the dynamical information available from the RD lidar measurements. In particular, as was noted in Chapter 5, the height structure of features in the ozone concentration measurements was not observed to propagate vertically as would have been expected if the IGW detected in wind measurements alone was responsible for driving the observed fluctuations (see Figures 5.1 and 5.3). In fact, the laminated structure at 14 km was observed to evolve in shape during the 6.5 hr while remaining centred at approximately the same height (Figure

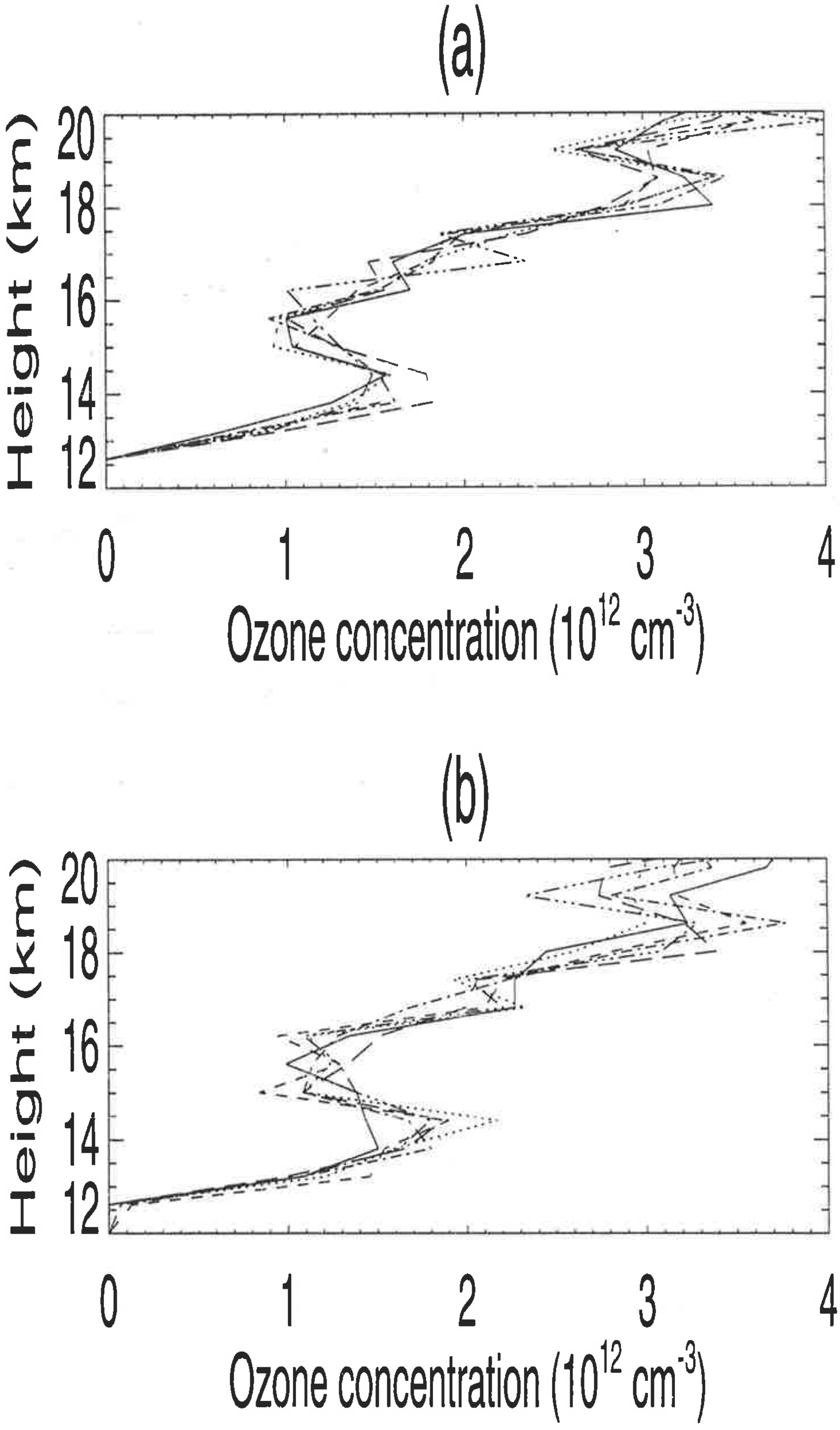

Figure 6.11: (a) Overplotted sequential DIAL ozone concentration profiles from OHP at local times 2230 (solid line), 2300 (dotted line), 2330 (dashed line), 0000 (dashed-dotted line), 0030 (dashed-three dotted line), and 0100 (long dashed line). (b) As for (a) at 0130 (solid line), 0200 (dotted line), 0230 (dashed line), 0300 (dashed-dotted line), 0330 (dashed-three dotted line), and 0400 (long dashed line) [see also Chapter 5].

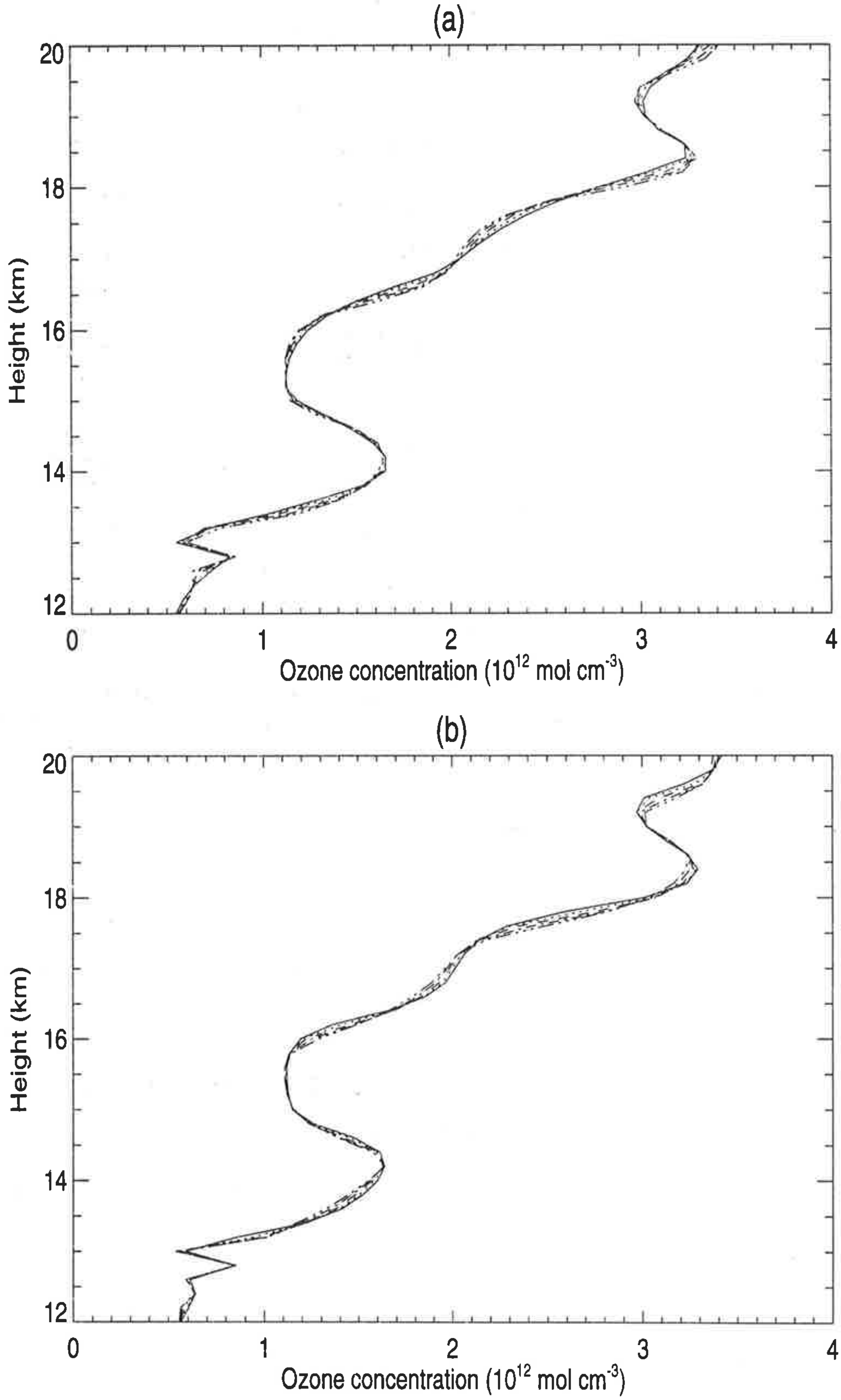

Figure 6.12: Overplotted sequential modeled ozone concentration profiles based on the mean ozone concentration profile calculated for the OHP case study. Panels (a) and (b) present two sequences, each of 5 profiles, with time resolution 30 min.

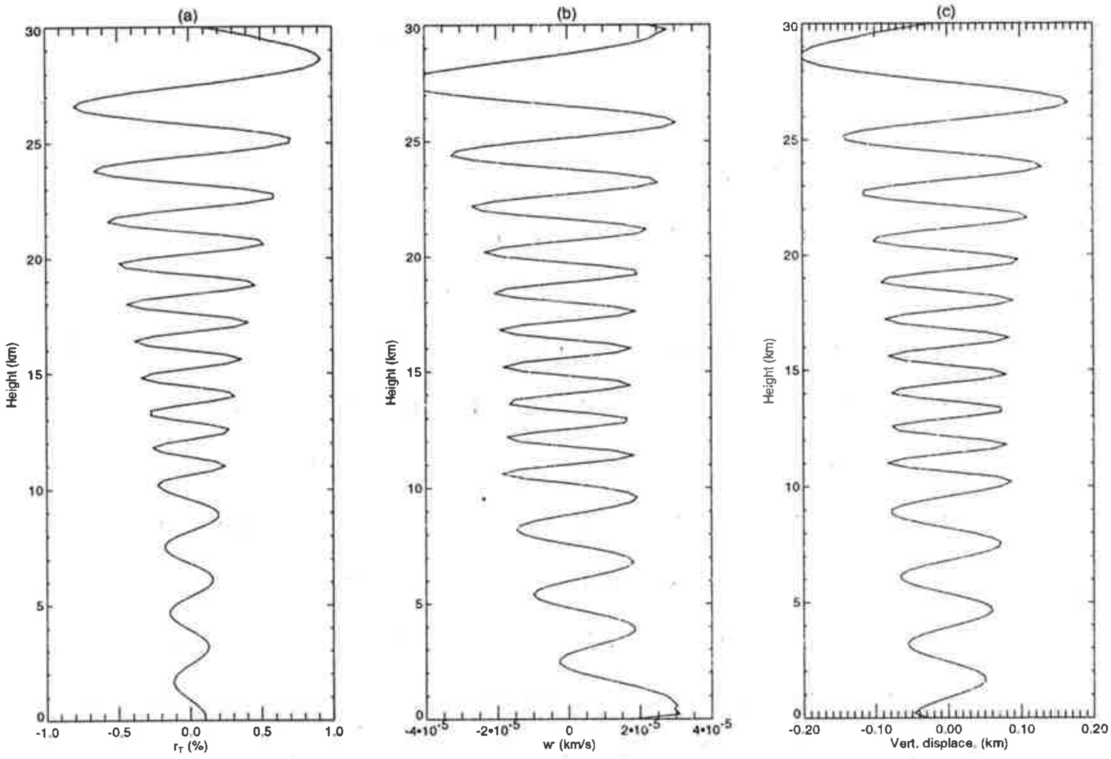

Figure 6.13: Model generated (a) relative temperature perturbations, (b) vertical velocity perturbations, and (c) vertical displacements calculated for the OHP case study modelization. Note the variation in vertical wavelength due to the tropopausal temperature structure.

6.11). This laminar evolution is consistent with the modulation effect described in Section 6.7.1 where the simple pre-existing model lamina was perturbed by a gravity wave of similar vertical scale.

The IGW was initially examined from the standpoint of a single monochromatic wave component present in a complex vertical ozone structure consisting of the dual lamination events at 14 km and 18 km, in addition to the mean temperature profile (Figure 6.10). Figure 6.13 illustrates gravity-wave-induced perturbations of the relative temperature, vertical velocity, and vertical displacements.

The results of the modeling study can be visualized succinctly in Figure 6.12. It is clear from the comparison of Figures 6.11 and 6.12 that there is modulation of the lamina induced by the interaction between the IGW and the initial laminated structure.

6.9 Chapter Summary

This chapter has modeled an exact picture of the mesoscale transport of tracer parcels which is applicable in any predefined mean stratospheric tracer configuration and dynamical conditions. For this preliminary study, mesoscale fluctuations driven by a monochromatic gravity wave were incident on a simplified background tracer field.

A recently developed parcel advection model was used to investigate monochromatic gravity wave effects in several highly simplified model stratospheric environments. The parcel advection model was used to investigate the impact of ozone laminae, produced by large-scale quasi-horizontal advection, on the vertical wavenumber spectra of relative ozone fluctuations. Observational studies had suggested that the interpretation of the variability of stratospheric tracer spectra required knowledge of both the large-scale structure of the tracer and the mesoscale fluctuations present. Such information was able to be incorporated into the parcel advection model. It was clear from this initial modeling study that the presence of a modeled laminar event, representative of those produced by large-scale quasi-horizontal advection, resulted in significant enhancement of the calculated mesoscale spectral magnitudes.

The parcel advection model has been used in this chapter to investigate specific situations and problems. The complexity of variations in mean winds, temperature, and mixing ratio structures was not able to be investigated fully within the scope of this thesis. However the vertical variation of tracer mixing ratio was investigated in some depth. Section 7.5 discusses extensions and future applications which are envisaged as a result of the initial study presented here.

Chapter 7

Summary and Conclusions

There are Always ... Possibilities

Spock

This work has explored atmospheric gravity wave effects on layered atmospheric constituents. The specific area of atmospheric gravity wave study was initiated since previous studies had provided controversial results relating to the dynamical interpretation of mesoscale tracer measurements, even in regions where tracers were anticipated to be quasi-conservative.

A primary theme was to explore observational evidence of atmospheric constituents, along with the corresponding dynamical variables, and set out to interpret the interactions taking place. This interpretation was undertaken using modeling and simulation approaches. In this way the response of constituents to gravity waves was investigated. This chapter overviews the main themes of the thesis. The reader is referred to the individual chapter summaries for further discussion of specific chapters.

Two important atmospheric trace constituents were emphasized: neutral sodium in the mesopause region, and ozone in the stratosphere. Both of these constituents were examined from a primarily dynamical stand-point with a view to the interpretation of mesoscale observations; either pre-existing, as was the case for mesospheric sodium, or as presented in this thesis, as was the case for stratospheric ozone. From observational and modeling perspectives on the mesoscale dynamical processes affecting stratospheric ozone, it has been possible to obtain an improved understanding of gravity-wave-induced ozone variability in the stratosphere.

The thesis was structured as a progressive, chronological study, following the development of the ideas and processes required in the modeling and analysis of atmospheric tracers. The major themes of the thesis are listed below; then the corresponding results and related future work are discussed in the following sections.

- Gravity wave modeling
- Lidar processing techniques
- Stratospheric ozone observations
- Ozone lamination

7.1 Gravity Wave Modeling

The topic of mesoscale gravity wave modeling permeated the thesis with a range of modeling approaches having been explored. Gravity wave modeling of mesospheric sodium was undertaken first as a 'test case' due to its primarily vertical variation and slow chemical timescales which were ideal for a dynamical study. Chapter 3 represented a preparatory study in two important respects: an introduction to the processing techniques used to extract gravity wave information from high-resolution lidar data, and a study of a more straightforward tracer than ozone from a dynamical viewpoint. From this preparatory simulation study it was possible to test important aspects of lidar data processing techniques, and to evaluate their reliability in detecting and characterizing gravity wave motions.

The effect of atmospheric gravity waves on constituents was approached in a very simple sense in Chapters 3-5 by focussing on the investigation of gravity-wave-induced vertical advection, as predicted by an analytical model. Such a simplified model had formed the basis of the majority of previous mesoscale modeling studies, which were further examined from a theoretical view-point in Chapter 6. The development of a new technique for the modeling of mesoscale constituent variations was motivated by the limitations inherent in the analytical models. The implementation of a fully non-local Lagrangian calculation of mixing ratio transport was discussed first; before a closed-form Lagrangian parcel advection model was introduced. The parcel advection model has the advantage of being conceptually simple and computationally efficient, and is suited to the investigation of gravity wave effects in a range of atmospheric conditions and constituents.

The parcel advection model was applied to the investigation of monochromatic gravity wave effects in the stratospheric ozone distribution. In particular the presence of ozone laminae was simulated, based on a range of previous observations, as well as those presented here in Chapters 4 and 5. A major result of this modeling study was the important enhancement of gravity-wave-induced fluctuations of ozone, and hence tracer variance, produced by the response of a gravity wave to the strong vertical gradients associated with the ozone lamina. This effect was pronounced in the mesoscale vertical wavenumber power spectrum calculated from the modeled fluctuations of relative ozone perturbations.

The presence of inertia-gravity wave features in the stratosphere was also a strong theme. A well-defined inertia-gravity wave signature was identified in RD lidar velocity profiles analyzed in Chapter 5. This time-resolved observation of ozone laminae, observed simultaneously with a well-defined inertia-gravity wave feature in horizontal velocity measurements, enabled a model-based estimation of the role of the inertia-gravity wave in the production of the observed ozone variability. From this study it was determined that the IGW alone contributed to relative ozone fluctuations of ~10% IGW features were further investigated using the parcel advection simulation in Chapter 6.

7.2 Lidar Processing Techniques

In light of the lidar-based discussions in Chapters 3 and 5, the data processing techniques applied in the analysis of lidar data were also an underlying theme. A fundamental requirement in such processing was the removal of a mean constituent distribution in order to extract gravity wave variability — the mean–perturbation approach. It was found in Chapter 3, from a simulation of time- and height-resolved Na lidar profiles, that a background layer calculated from a time average of a ~2 hr sequence of sodium number density profiles did not extract the modeled mean vertical distribution correctly.

This incorrect extraction was found to influence the spectral slope of the calculated vertical wavenumber power spectra towards flatter large-wavenumber slopes. Long-period wave components were identified through this simulation as being responsible for the residual variations in the extracted mean profile [Appendix A]. A similar effect was examined for the experimental study in Chapter 5, where stratospheric DIAL ozone lidar measurements were subjected to two forms of removal of a background layer profile; a time-averaged profile (6.5 hr) and a cubic polynomial fit. The simulation and observational studies both indicated the advantages of time-resolved, continuous constituent observations over a longer period, such as those available from lidar techniques, in determination of a mean tracer distribution, and hence the extraction of mesoscale variations.

7.3 Stratospheric Ozone Observations

The observations presented here provided a more complete picture of mesoscale ozone variability in several respects. The scarcity of stratospheric observational techniques providing high resolution measurements suitable for mesoscale studies of tracers and dynamics necessitated the bringing together of data from measurement techniques with different capabilities. The novel approach of combining information from different instruments in both cases examined in this thesis proved insightful in the interpretation of ozone observations; quasi-simultaneous ozonesonde, radiosonde, and ER-2 aircraft data in Chapter 4, and simultaneous DIAL ozone and RD lidar data in Chapter 5.

The relative importance of horizontal and vertical motions in the mesoscale transport of ozone was examined in Chapter 4. Previous studies had emphasized either the large-scale transport on quasi-horizontal isentropic surfaces [*Newman and Schoeberl*,1995], or the vertical advection of air parcels by mesoscale motions, specifically internal gravity waves [*Teitelbaum et al.*,1994], as the predominant means of driving the important mesoscale variability observed in ozone measurements. Through the use of estimated large-scale mean meridional ozone mixing ratio gradients calculated from ER-2 aircraft data, it was possible to identify situations where predominantly gravity wave effects were responsible for the observed variability, as well as situations where predominantly large-scale motions were occurring.

The dual DIAL ozone and RD lidar measurements discussed in Chapter 5 provided a most valuable means of evaluating the relative contributions of motions of different scales, and transporting air parcels in different directions, in the transport of stratospheric ozone. The major advantage of the lidar techniques for such an investigation over the sonde-based study undertaken in Chapter 4, was the time-resolved vertical profiles of both ozone and horizontal velocities. These profiles allowed both the identification of long-lived dynamical and constituent features, and the characterization of the mesoscale variability.

7.4 Ozone Lamination

The lamination of stratospheric ozone was a strong theme in Chapters 4-6. The vast majority of previous studies of ozone laminae have focussed on observations from northern hemisphere locations due to the sparseness of southern hemispheric data sources. To address this imbalance, examples of ozone laminae observed at the southern hemisphere mid-latitude location of Macquarie Island, Australia, during the 1994 ASHOE campaign were presented in Chapter 4. The Macquarie Island study indicated the occurrence of laminar features in many of the ozonesonde profiles measured between April and November. It was noted that many features of the observed ozone variability agreed with those observed at the northern hemisphere mid-latitude location of

Hohenpeissenberg, Germany, as presented by *Ehhalt et al.* [1983].

The case study from the northern hemisphere mid-latitude location of OHP, France, presented in Chapter 5, brought to light the first time-resolved measurement of ozone lamination. In fact, the observation period exhibited two ozone laminae with estimated lifetimes of 14 hr. This newly available constituent information, combined with simultaneously measured dynamical variables, provided a case study of the time evolution of ozone laminae. Following these observational studies, Chapter 6 made use of a modeling approach to simulate the effects of atmospheric gravity waves in a laminated tracer environment.

7.5 Further Work

It was clear in both Chapters 4 and 5 that knowledge of the large-scale horizontal structure of ozone is vital in the determination of the contributions of mean and gravity-wave-induced motions to the observed mesoscale ozone variability. The estimation of vertically resolved mean horizontal tracer gradients from adjunct CAS calculations is envisaged as a collaborative project to be undertaken in 1997 [Roger Atkinson, private communication].

Further international collaborations are planned with the aim of coordinating high resolution vertical measurements of stratospheric tracers from lidar and sondes, and high resolution horizontal information from the ER-2 aircraft [Stephen Eckermann, private communication]. A further campaign of ozonesonde observations at Macquarie Island, Australia, is scheduled for 1997.

Substantial further studies are envisaged as extensions of the Lagrangian modeling concepts pursued in Chapter 6. Extra applications and ideas arise naturally from the work presented. The generalized parcel advection model, which was applied to stratospheric ozone, is highly relevant in the study of a range of atmospheric constituents such as chemically stable ozone-destroying chemicals, water vapour, aerosols, pollutants, mesospheric metals, and ionospheric phenomena. The inclusion of chemistry and radiation terms, and parameterization of diffusive as well as advective effects are worthwhile extensions of the modeling approach. The monochromatic wave studies performed can be extended to investigate the effects of a superposition of gravity waves, analagous to the spectral gravity wave studies undertaken for mesospheric neutral sodium in Chapter 3.

The modeled interaction between inertia-gravity wave motions and laminar structures investigated the role of gravity-wave-induced vertical displacements in modulating pre-existing ozone laminae. This was investigated as a possible explanation for the time-varying structure of a lamina observed in vertical profile measurements at OHP. However a more realistic investigation of the interaction between large-scale and mesoscale constituent structure will require an extension to the full meridional (and potentially zonal) capability of the model.

The future modeling of constituent fluxes is anticipated as a fascinating extension of the present parcel advection model capability. It is envisaged that aspects of tracer transport such as irreversible mixing and the interaction between features due to large-scale transport and gravity waves, as commenced in Sections 6.7 and 6.8, may be studied within a variety of atmospheric regions and environments. The full breadth of these topics proved beyond the scope of this thesis, but leads into exciting future research possibilities.

The great thing is to last and get your work done
and see and hear and learn and understand;
and write when there is something that you know;
and not before; and not too damned much after.
Let those who want to save the world if you can get to see it clear and as a whole.
Then any part you make will represent the whole if it's made truly.
The thing to do is work and learn to make it.
No. It is not enough of a book, but still there were a few things to be said.
There were a few practical things to be said.

From the Epilogue to *Death in the Afternoon* by Ernest Hemingway.

Appendix A

Simulation of Lidar Measurements of Gravity Waves in the Mesosphere

This is a reproduction of a paper by D. E. Gibson-Wilde, I. M. Reid, S. D. Eckermann, and R. A. Vincent published in the *Journal of Geophysical Research*, Vol. 101, 9509–9525, 1996.

JOURNAL OF GEOPHYSICAL RESEARCH, VOL. 101, NO. D5, PAGES 9509–9522, APRIL 27, 1996

Simulation of lidar measurements of gravity waves in the mesosphere

D. E. Gibson-Wilde, I. M. Reid, S. D. Eckermann,[1] and R. A. Vincent
Department of Physics and Mathematical Physics,
University of Adelaide, Adelaide, Australia

Abstract. Lidar measurements of mesospheric gravity wave characteristics are simulated using a simple numerical model. Simple theory is used to superimpose gravity wave fluctuations upon typical background densities and sodium abundances in the height range 80-100 km, which we then assume are perfectly observed by a Rayleigh and Na lidar, respectively. These lidar "data" are then analyzed for their gravity wave content using the standard reduction and analysis methods which are routinely applied to these data sets. Our goal is to assess whether this analysis of lidar data faithfully recovers the underlying wave field. In both quasi-monochromatic and spectral wave studies, the height range over which Na number density can be measured and the shape of the background Na profile impose a limit on the gravity wave information which can be extracted from Na lidar data. The limitations due to background layer shape do not exist for Rayleigh lidar measurements. The simulations reveal that quasi-monochromatic gravity waves with vertical wavelengths larger than approximately 10 km may not be reliably retrieved from Na lidar data. It is also shown that there are limitations on the accurate extraction of spectral parameters from Na lidar data due to the limited vertical extent of the mesospheric Na layer.

Introduction

The measurement and interpretation of atmospheric internal gravity wave (gw) characteristics in the middle atmosphere is a challenging problem. Early work concentrated on the identification and characterization of quasi-monochromatic waves [e.g., *Cot and Barat*, 1986; *Reid*, 1986; *Yamamoto et al.*, 1987; *Gardner and Voelz*, 1987, hereinafter referred to as GV87]. Most recent work has concentrated on both temporal and spatial spectral studies of gw activity, with the observational record consisting of data from rockets [e.g., *Wu and Widdel*, 1991; *Thrane et al.*, 1994], balloons [e.g., *Allen and Vincent*, 1995], aircraft [e.g., *Bacmeister et al.*, 1995], radars [e.g., *Murayama et al.*, 1992; *Sato and Yamada*, 1994], airglow imagers [e.g., *Hecht et al.*, 1994] and lidars [e.g., *Shibata et al.*, 1986; *Wilson et al.*, 1991b; *Whiteway and Carswell*, 1994].

The temporal and spatial resolution of lidar measurements makes them especially useful for studies of atmospheric gw activity. Here we concentrate on the analysis and interpretation of lidar observations, with occasional reference to other techniques, most particularly radar wind measurements.

Rayleigh lidar measurements of atmospheric density and temperature are typically possible in the 25- to 80-km height region. Sodium (Na) lidar measurements of neutral sodium density are possible in the 80- to 100-km height region. The atmospheric density variations measured using a Rayleigh lidar are superimposed on the exponentially decreasing background atmospheric density profile. In contrast, the Na layer is essentially Gaussian in shape with a typical maximum number density of about 5000 cm^{-3} at 90 km. Chemical modeling and observational studies indicate that the layer takes the form of a skewed Gaussian with a steeper number density gradient on the lower edge of the layer than on the upper edge [e.g., *Thomas et al.*, 1983; *Senft and Gardner*, 1991, hereinafter referred to as SG91; *Cox et al.*, 1993; *Helmer and Plane*, 1993].

The Gaussian shape of the Na layer has important consequences when attempting to describe the structure in Na lidar profiles in terms of gw dynamics. Equations for the linear response of a constituent to a single gw were developed by *Chiu and Ching* [1978]. *Shelton et al.* [1980] considered the Na layer linear response to a gw and *Gardner and Shelton* [1985] developed important nonlinear terms in the Na layer response.

Recent improvements in lidar technology have led to high-resolution Na layer measurements and observational testing of the aforementioned models. The most

---

[1] Now at Computational Physics, Inc., Fairfax, Virginia, and E. O. Hulburt Center for Space Research, Naval Research Laboratory, Washington, D. C.

Paper number 95JD03578.
0148-0227/96/95JD-03578$05.00

active group in this area has been researchers at the University of Illinois, Urbana (40°N, 88°W) [e.g., GV87; *Kwon et al.*, 1990; SG91; *Beatty et al.*, 1992; *Gardner et al.*, 1993a; *Senft et al.*, 1993]. Their work includes studies both of quasi-monochromatic gw parameters and of temporal and spatial atmospheric density spectra derived from Na layer number densities as measured with a Na lidar. Their lidar determinations of gw wavelengths and periods showed distinctive groupings [e.g., GV87]. SG91 reported agreement among spectral parameters determined from Na lidar data and the predictions of spectral models [e.g., *Weinstock*, 1990]. Accumulated lidar data led to the development of a "diffusive filtering" theory of gw spectra which could better account for their observations [*Gardner*, 1994; *Lintelmann and Gardner*, 1994].

Rayleigh lidar studies from 30 to 80 km were used by *Chanin and Hauchecorne* [1981] to obtain density and temperature profiles over southern France, while *Wilson et al.* [1991a,b] used Rayleigh lidar measurements to characterize gw perturbations of atmospheric density. *Meriwether et al.* [1994] made use of a high-power Rayleigh lidar located at Dayton, Ohio (40°N, 84°W), a similar latitude to the Urbana, Illinois, Na lidar site. A number of purely stratospheric studies have been performed with lower-power Rayleigh lidar systems.

In this paper we consider computer simulations of lidar remote sensing of the upper middle atmosphere. The simulations provide a means of comparing the sensitivity and selectivity of different gw measurements and analysis techniques.

Lidar investigations of gw are characterized by two limiting cases. These are the identification and investigation of quasi-monochromatic waves and, at the other limit, the investigation of gw spectra. Both approaches have been used extensively and here we will consider both cases for both Na and Rayleigh lidar.

In this paper the theory of gw perturbations of atmospheric density for both quasi-monochromatic waves and a spectrum of waves is developed. This theory is applied to obtain simulated Rayleigh lidarlike observations. The response of the Na layer to gw in atmospheric density is derived and Na lidar measurements are simulated. The GV87 and SG91 techniques are used to extract gw monochromatic and spectral parameters, respectively.

Atmospheric Gravity Wave Model

Synthesis of Superposition of Gravity Waves

We simulate density perturbations produced by a linear superposition of gw, each with intrinsic frequency (ω_i) and vertical wavenumber (m_i), as follows:

$$r_a(z,t) = \frac{\rho'_a(z,t)}{\bar{\rho}_a(z)} = e^{\frac{z}{2H_\rho}} \sum_i A_i \cos(\omega_i t - m_i z + \varphi_i), \tag{1}$$

where $r_a(z,t)$ is the relative atmospheric density perturbation, $\rho'_a(z,t)$ is the atmospheric density perturbation, $\bar{\rho}_a(z)$ is the background atmospheric density profile, A_i is the peak relative-density amplitude of the ith gw at $z{=}0$, z is the height above the Earth's surface, H_ρ is the density scale height (assumed constant), t is the time of the observation, and φ_i is the random phase associated with the ith gw. In our simulations the phases φ_i have been set to zero.

This expression (1) assumes an exponential decrease in density with height of the form

$$\bar{\rho}_a(z) = \bar{\rho}_0 e^{\frac{-z}{H_\rho}}, \tag{2}$$

where $\bar{\rho}_0$ is the surface atmospheric density value.

The effect of wave dissipation can be simulated by including a variable wave-amplitude growth factor (the β term in GV87 and *Beatty and Gardner* [1990, hereinafter referred to as BG90]). Significant wave dissipation is expected to occur at mesospheric heights. However, for simplicity, dissipation has not been considered in this study.

Equation (1) is valid only when there is no variation in the background wind or temperature with height and assumes that the waves do not mutually interact, so that ω_i and m_i remain constant for each wave i. The "quasi-monochromatic" profiles generated using (1) provide the simplest test case for the method. More realistic profiles were generated using a spectral approach, described below.

Spectral Studies of Gravity Waves

Both atmospheric density vertical wavenumber spectra ($F_a(m)$) and frequency spectra ($G_a(\omega)$) have been derived from lidar data. The major feature common to all estimates of $F_a(m)$ from these and other data sources is the large wavenumber power law decay of the form

$$F_a(m) \propto m^{-q}, \tag{3}$$

for m significantly greater than the characteristic vertical wavenumber m_* and with $q \approx 3$; m_* is believed to be less than 0.067 cycle km^{-1} (vertical wavelength $\lambda_z \geq 15$ km) in the mesosphere [e.g., *Murayama et al.*, 1992]. A number of theories concerning the experimentally observed powerlaw decay have been developed for $F_a(m)$ [e.g., *Dewan and Good*, 1986; *Smith et al.*, 1987; *Weinstock*, 1990; *Hines*, 1991; *Gardner*, 1994; *Zhu*, 1994].

The simulations used in this work are based on the modified Desaubies spectrum in which $F_a(m)$ is given by [e.g., *Fritts and VanZandt*, 1993]

$$F_a(m) = E_0 \frac{\mu^s}{1 + \mu^{(s+q)}}, \tag{4}$$

where E_0 is a normalization factor, $\mu = m/m_*$, and the spectral indices s and q are equal to 1 and 3, respectively, in the model.

SG91 obtained measured values of the large-m power spectral index q of between 2.2 and 3.6 from Na lidar observations at Urbana, Illinois. Using Na lidar data from Antarctica, *Collins et al.* [1994] obtained an average value for q of 2.4, somewhat smaller than the average midlatitude value of near 3. *Meriwether et al.* [1994] obtained q values between 1.5 and 2.5 from Rayleigh lidar observations at a similar location to SG91. Spectral slopes can be strongly influenced by the signal processing techniques. *Meriwether et al.* [1994] comment that their values of q may be smaller than expected for this reason. *Mitchell et al.* [1990] have illustrated the variation in Rayleigh lidar power spectra caused by using different processing techniques on the same data set. *Lefrère and Sidi* [1990] and *Gardner et al.* [1993b] showed that a high-frequency cutoff can also reduce measured q values. *Eckermann* [1995] has argued that some observed spectral variations from $q = 3$ are real and arise from the refractive effects of larger-scale wind systems, while *Zhu* [1994] attributes $q < 3$ to the influence of radiative damping.

The value of the small wavenumber spectral index s can only be determined from measurements obtained over a large vertical range. Since Na lidar data are limited to the height range of the Na layer (about 20-25 km), the minimum resolvable vertical wavenumber is 0.04-0.05 cycle km^{-1}. This is very close to m_* anticipated at mesospheric heights, and so s cannot be measured.

The height range of Rayleigh lidar observations is controlled only by the power of the lidar (i.e., the uppermost height, as determined by the signal-to-noise ratio) and the vertical density profile of the atmosphere. Hence the small wavenumber segment of $F_a(m)$ may be measured with sufficiently powerful Rayleigh lidars which cover a larger height range than Na lidar. The measurements performed by *Meriwether et al.* [1994] over a height range of 50 km effectively halve the minimum resolvable vertical wavenumber from Na lidar observations.

The magnitudes of $F_a(m)$ obtained from the radar and Na lidar techniques have been compared with spectral models. *Murayama et al.* [1992] found good agreement among the magnitudes of spectra obtained from MU radar, rocketsonde, and radiosonde observations in the height range 5-90 km and the predicted magnitudes from *Dewan and Good* [1986]. SG91 compared results from the Na lidar technique with the model of *Weinstock* [1990] and obtained close agreement. However, the magnitudes of the *Dewan and Good* [1986] model are approximately one third those of the *Weinstock* [1990] model. Hence the spectral magnitudes resulting from Na lidar are approximately a factor of 3 larger than those obtained using radar techniques.

Recently *Zhu* [1994] found that the *Weinstock* [1990] result was overestimated by a factor of 4. This brings the predictions of *Dewan and Good* [1986] and *Weinstock* [1990] into much closer agreement. Hence the spectra obtained from Na lidar data are significantly larger in large-m spectral density than any of the suggested models of the vertical wavenumber spectrum. Spectral densities typical of lidar measurements have been assumed in this study to obtain Na profiles similar to experimental measurements.

Experimental studies of the frequency spectrum of atmospheric density variations ($G_a(\omega)$) suggest that it also follows a power law decay of the form [e.g., *Fritts and VanZandt*, 1993].

$$G_a(\omega) \propto \omega^{-p}. \quad (5)$$

Values for the spectral parameter p obtained by SG91 were between 1.28 and 2.45. A value of $p = 2$ has been used in our simulations.

In generating height-time density perturbations governed by representative spectra such as these, we follow *Fritts and VanZandt* [1993] and assume a separable two-dimensional spectral model of the form

$$H_a(m, \omega) \propto F_a(m) G_a(\omega). \quad (6)$$

Relative density perturbations were synthesized from this spectrum (appropriately normalized) by applying an inverse FFT. To simulate variations among individual measurements taken on different nights and in different locations, random phases were assigned to each wavenumber and frequency component. Exponential growth of wave amplitude with height was imposed by dividing the synthesized Na profiles by an exponential of the form shown in (2).

Background Na Layer Model for Na Lidar Measurements

Chemical studies suggest that the background atmospheric Na layer can be modeled as a skewed Gaussian [*Thomas et al.*, 1983; *Helmer and Plane*, 1993]. Since the periods of gw at mesospheric heights are short compared to the timescales of chemical processes affecting the Na layer, production and loss processes which might affect the wave dynamics can be ignored. SG91 calculate an approximate background Na layer by fitting a smooth Gaussian function to time-averaged Na lidar profiles.

Since the spectra calculated from Na lidar measurements are sensitive to the extraction of the background Na layer, the function used to fit the mean profile is important. In this work both smooth and skewed Gaussian background Na layers were used, in order to determine whether a standard Gaussian fitting procedure effectively removes the background layer and isolates the gw signal.

The form of the skewed Gaussian chosen for this work is the sum of a smooth Gaussian layer and a quadratic term. The background Na number density profile ($\bar{n}_{\mathrm{Na}}(z)$) is given by

$$\bar{n}_{\mathrm{Na}}(z) = a_0 \exp\left(\frac{-(z - a_1)^2}{2a_2}\right) + a_3 + a_4 z + a_5 z^2. \quad (7)$$

The coefficients a_j ($j = 1, .., 5$) used here were determined by a least squares fit to the profile of *Thomas et al.* [1983] where the model Na layer has a peak height (a_1) of $\approx$ 91 km and a half-power half width (a_2) of $\approx$ 4 km. The profile has a steeper slope on the lower edge of the layer, in agreement with chemical models [e.g., *Thomas et al.*, 1983; *Helmer and Plane*, 1993]. This profile agrees closely with the Gaussian fit to long-term average Na profiles obtained by SG91.

Gardner and Shelton [1985] and SG91 fit a smooth Gaussian to define their background Na layer. The figures included in this paper were obtained using a smooth Gaussian background Na layer to permit a consistent comparison with SG91. The smooth background Na layer that we used is shown in Figure 1. A skewed background Na layer was also investigated. It was found that the background layer shape did not greatly influence the results.

Model of the Na Layer Response to Gravity Waves

Relative Na density perturbations ($r_{\mathrm{Na}}(z,t)$) are calculated from $r_a(z,t)$ using the expression [e.g., *Gardner and Shelton*, 1985],

$$r_{\mathrm{Na}}(z,t) = \frac{-r_a(z,t)}{\gamma - 1}\left(1 + \gamma H_\rho \frac{\bar{n}_{\mathrm{Na}_z}(z)}{\bar{n}_{\mathrm{Na}}(z)}\right), \qquad (8)$$

where $\bar{n}_{\mathrm{Na}_z}(z)$ is the vertical derivative of the background Na profile and γ is the ratio of specific heats (≈ 1.4). A brief summary of the way in which (8) relates to formulae derived in other studies of wave-induced tracer fluctuations is given in the Appendix. For a smooth Gaussian layer, *Gardner and Shelton* [1985] obtained an expression for the layer response at the peak which is due to nonlinear effects (that is, linear solutions predict no response at the layer peak). *Gardner and Shelton* [1985] argue that the nonlinearities become important at heights where the ratio of the second vertical derivative of $\bar{n}_{\mathrm{Na}}(z)$ to the background value $\bar{n}_{\mathrm{Na}}(z)$ is large, which occurs in the vicinity of the layer peak.

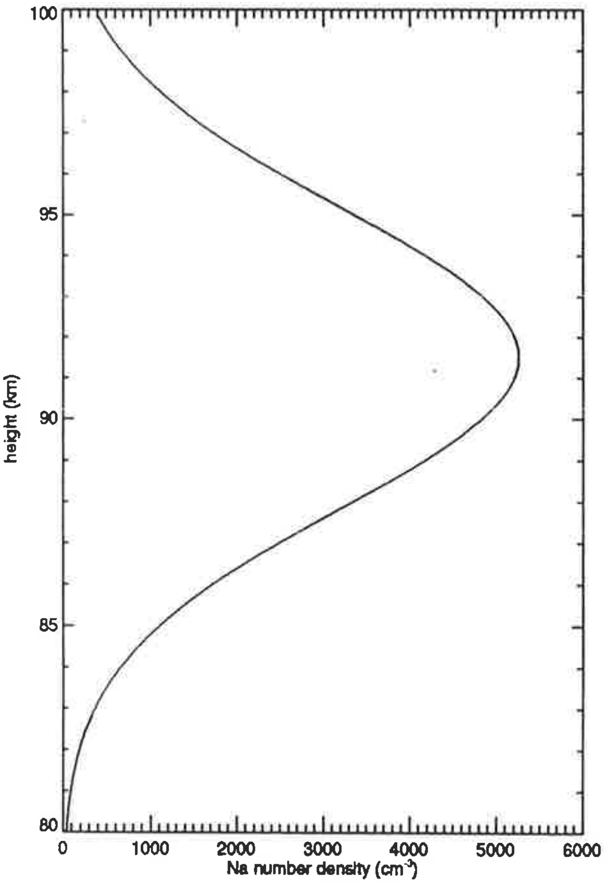

Figure 1. Background Na layer in form of Gaussian.

SG91 apply linear gw theory to interpret the small-scale variability in their Na lidar data, since relative Na density perturbations come directly from the experimental data and the nonlinear terms make a negligible contribution to the relative Na density. For simplicity, the nonlinear terms have been neglected for the quasi-monochromatic simulations but are retained in the spectral simulations described in section 3.

The absolute Na density profiles ($n_{\mathrm{Na}}(z,t)$) were calculated from $r_{\mathrm{Na}}(z,t)$ using

$$n_{\mathrm{Na}}(z,t) = \bar{n}_{\mathrm{Na}}(z) + n'_{\mathrm{Na}}(z,t), \qquad (9)$$

where

$$n'_{\mathrm{Na}}(z,t) = r_{\mathrm{Na}}(z,t).\bar{n}_{\mathrm{Na}}(z). \qquad (10)$$

For physically real Na number densities, $n_{\mathrm{Na}}(z,t)$ must obviously be greater than or equal to zero. At the upper and lower edges of the Na layer the simulation may yield unphysical Na densities since the vertical gradient of the layer is large at these heights, and so our linear method of simulating perturbations can become inaccurate. When this occurs, the value of the perturbation $n'_{\mathrm{Na}}(z,t)$ may become larger than and of opposite sign to the background Na number density, which then yields a negative total number density. Synthesized profiles which yielded such unphysical values were rejected from the analysis.

Relative and absolute Na density perturbations were calculated from the relative atmospheric density perturbations using (8) and (9) in both quasi-monochromatic and spectral simulations of the wave field. Typical values of root-mean-square (RMS) density perturbations obtained by *Beatty and Gardner* [1990] from Na lidar observations are 2-8%. *Collins et al.* [1994] obtained average RMS density perturbations from Antarctic observations of $\sim$ 6%. SG91 obtained RMS density perturbations at Urbana between 3 and 11% with an average of 5.6%. In this study we have chosen values within this range.

Results of simulation

Quasi-Monochromatic Gravity Waves

Gravity wave perturbations of the Na layer were simulated using (1), (8), and (9) for a gw with λ_z= 2 km, ω=0.0008 cycle km^{-1}, and RMS relative density amplitude of 3%. The height resolution of the simulated data was 37.5 m and profiles are displayed in Figure 2 at 1-min intervals to simulate high-resolution Na lidar data: Figure 2a shows relative atmospheric density

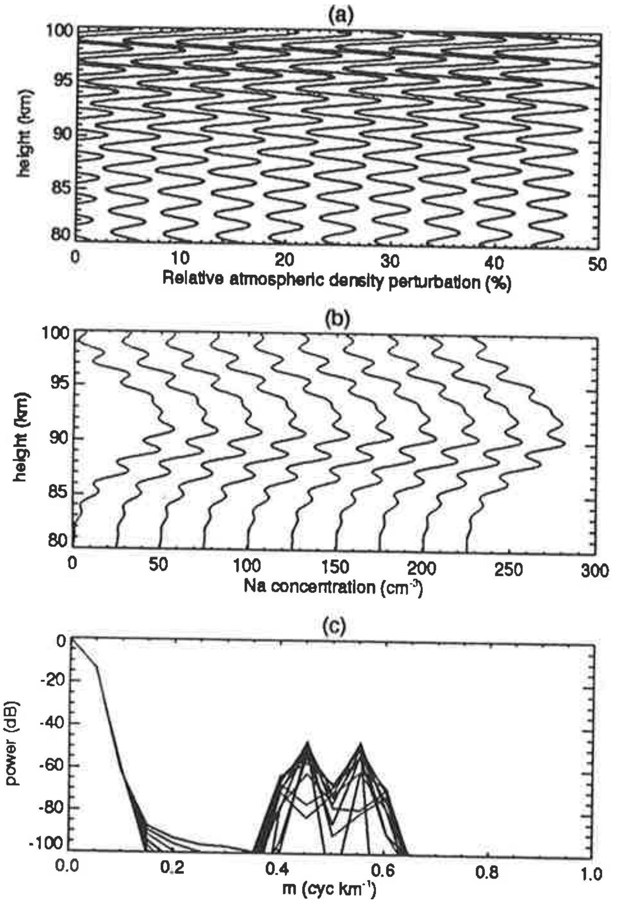

Figure 2. Time variation of (a) relative atmospheric density perturbations (%), (b) Na number density, and (c) power spectra of successive perturbed Na layers at 1-min intervals.

profiles and Figure 2b shows Na number density profiles. The profiles of $n_{\mathrm{Na}}(z,t)$ obtained using the above method resemble experimental Na lidar profiles [e.g., GV87; BG90]. The GV87 analysis technique was used to extract the vertical wavelength λ_z and observed vertical phase speed $c_{z\mathrm{obs}}$ from these lidar "data."

In the GV87 technique both the Na profiles and their vertical wavenumber spectrum are inspected to identify any quasi-monochromatic gravity waves that might be present. The value of λ_z is determined from the position of the characteristic "notch" that bisects two equal peaks, as shown in Figure 2c. The value of $c_{z\mathrm{obs}}$ is determined by inspection of the motion of successive peaks in the filtered Na lidar profiles in Figure 2b. The observed period is calculated using $T_{\mathrm{obs}} = \frac{\lambda_z}{c_{z\mathrm{obs}}}$ [GV87].

A GV87 analysis can be applied to the simulated profiles and vertical wavenumber spectrum in Figure 2. The λ_z and downward vertical phase progression (representing upward energy propagation) are clearly visible in the successive Na density profiles in Figure 2b. The characteristic "notched" gw signature, which results from the phase change of oscillations either side of the Na layer peak, is clearly seen in the vertical wavenumber spectrum in 2c [e.g., GV87].

The minimum $c_{z\mathrm{obs}}$ detectable from 10 (20) min of Na lidar observations is 0.06 (0.03) m s^{-1} (corresponding to $T_{\mathrm{obs}} \sim 9$ (18) hours for λ_z=2 km), assuming a sufficiently long wave coherence time. In this simulation all waves are effectively infinite wave trains and hence only the length of the observation period controls the detectability of the wave motions. For experimental Na lidar measurements the minimum detectable phase speed is controlled by the lidar height–time resolution and the coherence time of the gw. Gravity waves with small λ_z have relatively short coherence times and may not be present in more than a couple of profiles [e.g., BG90].

The determination of $c_{z\mathrm{obs}}$ from Na lidar profiles is a difficult process. It requires the selection of data sets which display wavelike variations with downward phase progression [GV87]. There is some ambiguity in interpreting phase propagation direction from successive profiles; waves with large downward propagation speeds may be mistaken as slow moving upward propagating waves and hence ignored by GV87. *Lintelmann and Gardner* [1994] have shown that when background wind variations are included, Doppler shifting may reverse the observed phase progression of waves with small λ_z.

Na lidar observations at Urbana, Illinois, and at other sites were made on a campaign basis with the lidar pointing vertically at a height resolution of 37.5 m and time resolution of 1-10 min [e.g., GV87; BG90]. Data typically contain significant variability, with signals about 10-20 dB above the photon noise floor, which is ~40–60 dB below the signal peak [BG90].

To resolve $T_{\mathrm{obs}} \sim 720$ min, as displayed by *Reid* [1986] and GV87, it would be necessary to combine several profiles over more than 20 min in order to unambiguously track the vertical phase motion in the profiles. Thus the GV87 method may not be able to accurately determine T_{obs} as large as 720 min unless observation periods longer than 20 min are used.

Figure 3 compares the simulated Na vertical wavenumber spectrum for waves with λ_z of 10, 12, and 15 km. Each wave has an intrinsic frequency of 0.0008 cycle s^{-1} and RMS relative density amplitude of 3%. The value of λ_z of 15 km is the stated limit of the GV87 technique [GV87].

The extraction of λ_z from such a spectrum requires clear identification of the spectral notch. However, in Figure 3 the spectral signal of the background Na layer and the notch due to the gw effects interfere, so that no clear notch is visible in the vertical wavenumber spectrum. All three spectra are distorted to produce a notch at a vertical wavelength of 10 km.

By simulating a number of monochromatic gw in the Na layer with different parameters and applying the GV87 technique to the generated profiles, it was determined that the processing limits for the GV87 technique were approximately as follows: Vertical wavelength, 1-10 km; observed period, 20 to 720 min or less. These limits assume a minimum observation time of 20 min and a cutoff vertical wavelength of 1 km.

The upper limit on λ_z results from identifying this parameter from the vertical profiles of Na density which are significant only over the region 80-100 km (Figure 3). Outside this region the lidar measurements appear

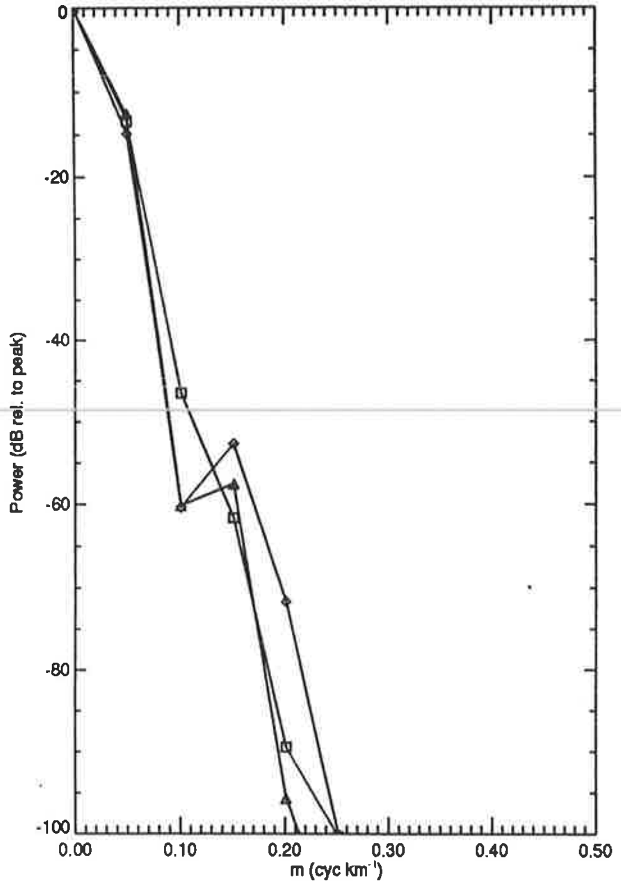

Figure 3. Power spectra of Na lidarlike observations of single waves with vertical wavenumbers 0.1 cycle km^{-1} (diamond), 0.083 cycle km^{-1} (triangle), and 0.067 cycle km^{-1} (square).

to be too noisy to give any gw information (see BG90, Figure 1). The lower limit on λ_z depends on the cutoff wavelength imposed in the filtering of the lidar profiles [BG90]. Values between 1 and 2 km were used as cutoff values by GV87 depending on the photon noise floor and the amplitude of the gw perturbations. SG91 applied a cutoff vertical wavelength of 1.5 km to Na lidar data.

Apart from the physical limit imposed by the Brunt-Väisälä frequency, it is important to consider the limitations in measuring frequencies from inspection of a sequence of 10–20 Na profiles. The lower limit on the observed period is imposed by GV87. Given a sampling time of 10 min, as used by GV87 and BG90, a perturbation must be observable for more than 20 min before it can be identified as a gw [*Voelz and Gardner,* 1986; GV87].

The above restrictions indicate that the GV87 process would not be capable of detecting gravity waves with λ_z outside the above limits. This means that the comparison of radar and lidar results in the work of *Reid* [1988] is less surprising since the radar results for which $\lambda_z \gtrsim 10$ km would not have been identified using the Na lidar technique or may even be falsely interpreted as a $\lambda_z \sim 10$ km wave (see Figure 3).

To detect large λ_z waves, the background profile could be removed. However, as has been explored in the case of a spectrum of waves in Na lidar data, the extracted gw perturbations are sensitive to the process of removing a background.

Gravity Wave Interference in Na Lidar Data

Simulations were conducted to quantify the smallest separation between the vertical wavenumbers of two gw which still enabled the parameters of both waves to be correctly identified from lidar profiles using the GV87 technique. To determine the minimum separation, it was assumed that the notch depth in the gw signature was deep enough to be visible ($\geq$ 2 dB less than the peaks of the signature).

In Figure 4 a gw with vertical wavenumber of 0.2 cycle-km^{-1} (λ_z=5 km), frequency 0.0008 cycle s^{-1}, and RMS relative density amplitude 3% was used as a reference in the power spectrum. An additional gw of equal amplitude and frequency but different vertical wavenumber was included with the reference wave in a two-wave simulation. Vertical wavenumbers of 0.25 and 0.3 cycle km^{-1} were used for the extra wave in separate simulations.

Initially, both gw could not be identified in the vertical wavenumber spectrum since their notched spec-

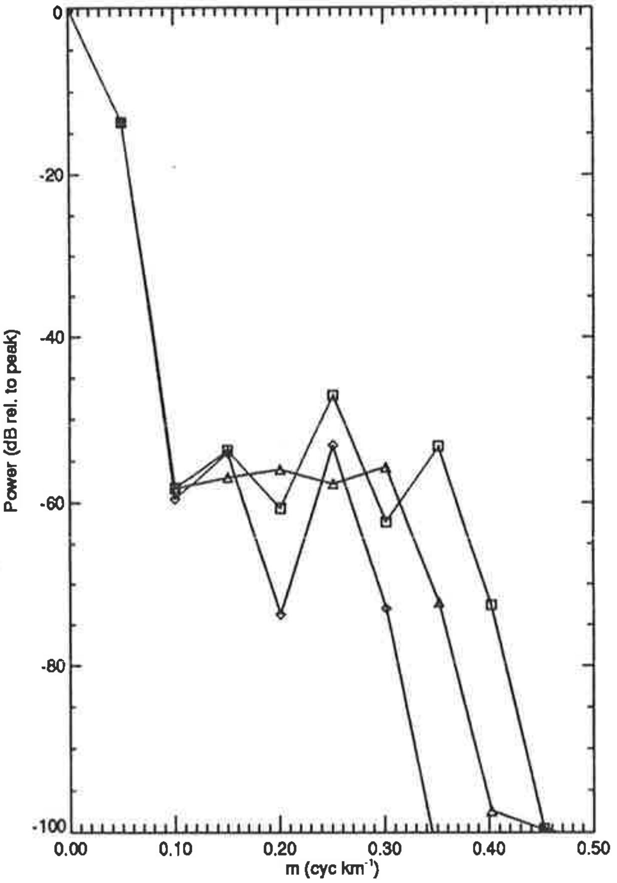

Figure 4. Power spectra of Na lidarlike observations of gw combinations: single wave with vertical wavenumber 0.2 cycle km^{-1} (diamond), two waves of wavenumber 0.2 and 0.25 cycle km^{-1} (triangle), and two waves of wavenumber 0.2 and 0.3 cycle km^{-1} (square).

tral signatures overlapped and mutually interfered. The wavenumber separation was gradually increased until two separate notched peaks could be identified in the power spectrum. The identification of two separate gw is dependent on the vertical wavenumber resolution (0.05 cycle km^{-1} in this case). The minimum requirement for the waves to be resolved is for the vertical wavenumber difference to be $\geq$ 0.1 cycle km^{-1}. For values between 0.05 and 0.1 cycle km^{-1} the waves will interfere to produce a single wide notch in the vertical wavenumber spectrum which simplifies to a quasi-monochromatic-like notch for a wavenumber difference of less than 0.05 cycle km^{-1}.

By zero padding the simulated Na profiles, it is possible to increase the resolution in the vertical wavenumber spectrum. However, unless the data are windowed rather than box filtered, extra variations are introduced in the spectrum due only to the response of the box filter. The GV87 technique also provides a method of obtaining the gw amplitude (A_i) and amplitude growth factor with height (β) from the vertical wavenumber spectrum. These values are calculated from the notch depth and notch width, respectively [GV87]. Zero padding was also found to interfere with the notch depth in the vertical wavenumber spectrum and hence affected the GV87 determination of the gw amplitude.

This simulation emphasizes that the extraction of quasi-monochromatic parameters from Na lidar data must be approached carefully. A spurious quasi-monochromatic-like notched gw signature can be produced through the interaction of two or more gravity waves. The effect of a spectrum of gravity waves is considered in the next section.

Simulation of a Spectrum of Gravity Waves

A model spectrum $H_a(m,\omega)$ with spectral indices s=1, q=3, and p=2 and m_*=0.067 cycle km^{-1} (λ_{z*}= 15 km) was adopted, and randomly phased density fluctuations were generated from it.

The value of the turbulent diffusion coefficient η used in the calculation of the maximum allowed wavenumber [e.g., *Hines*, 1960; *Pitteway and Hines*, 1963; *Fukao et al.*, 1985; *Marks and Eckermann*, 1995] has a significant effect on the vertical scales of perturbations visible in the relative atmospheric density profiles. Turbulent diffusion coefficients up to 150 $\mathrm{m}^2\ \mathrm{s}^{-1}$ with an average of 28 $\mathrm{m}^2\ \mathrm{s}^{-1}$ were estimated at Arecibo [BG90]. At Urbana the average was 37 $\mathrm{m}^2\ \mathrm{s}^{-1}$ [GV87].

A typical value of η of 30 $\mathrm{m}^2\ \mathrm{s}^{-1}$ was used to determine the maximum allowed wavenumber for each frequency component in the simulated data. Values of 3 and 300 $\mathrm{m}^2\ \mathrm{s}^{-1}$ were also used and resulted in density profiles with more and less small-scale variability, respectively, as expected.

An inverse FFT was performed to obtain time-height profiles of relative atmospheric density perturbations. An example of a set of atmospheric density profiles is shown in Figure 5.

In this study, the synthesized fluctuations were then scaled in amplitude vertically so that the relative atmospheric density perturbations (r_a) were approximately 4% at 80 km and 8% at 100 km, compatible with the BG90 and SG91 results. The atmospheric density variance, although variable due to the random phases chosen, varied approximately from 10 to 40 $(\%)^2$ between different simulated data sets, in agreement with experimental values [e.g., SG91].

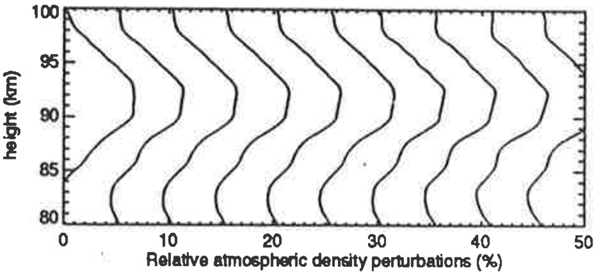

Figure 5. Simulated atmospheric relative density perturbations at 1-min intervals assuming a spectrum of waves in the atmosphere.

Extraction of Spectral Parameters from Simulated Lidar Data

Given a set of simulated Rayleigh or Na lidar profiles, is it possible to extract the generating spectral parameters? Do the extracted values agree with the input values?

Simulated data were filtered as described by SG91 for CEDAR Na lidar measurements and relative atmospheric density perturbations were calculated. A cutoff wavenumber (m_c) of 0.67 cycle km^{-1} (λ_z=1.5 km) was applied in the calculation of $G_a(\omega)$ and a cutoff frequency (ω_c) of 0.0017 cycle s^{-1} (T_{obs}=10 min) in the calculation of $F_a(m)$ [SG91]. This filtering technique approximately matches the limits imposed by turbulent diffusivity $\eta = 30\ \mathrm{m}^2\ \mathrm{s}^{-1}$.

Comparison of the density variance of the unfiltered and filtered profiles showed that negligible variance is removed from the spectrum by the filtering, as argued by *Senft et al.* [1993]. For smaller diffusion coefficients the SG91 filtering may remove a more significant amount of variance from the spectrum.

Simulated observation periods of 2 hours, consisting of 120 profiles at 1-min intervals, were then used to obtain $F_a(m)$ and $G_a(\omega)$ directly from the Na lidarlike data.

Figure 6 compares the input and extracted background (bg) Na layers. In general, it was found that the input and extracted bg layers differed due to the process of obtaining the extracted bg Na layer from an average of Na profiles. Unresolved long-period waves in the spectrum were included in the average Na bg layer which tended to bias the estimated bg layer.

Figure 7 shows the difference between the input and extracted Na layers as a function of height. This difference is particularly important at the upper edge of the layer, above about 95 km, where it causes maximum errors of approximately 500 cm^{-3} in the extracted relative Na density perturbations.

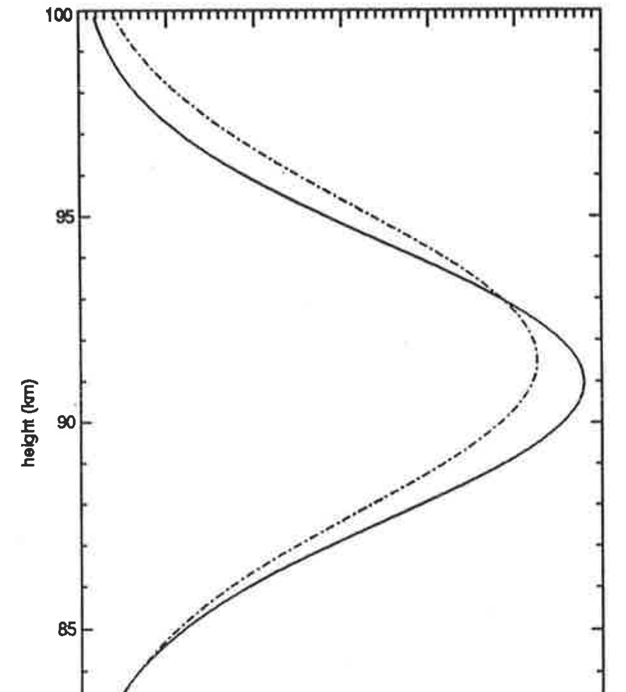

Figure 6. Input Gaussian (dashed-dotted) and average background Na number density profile (solid line) over a 2-hour observation period.

Figure 8 compares the input and extracted relative Na density perturbations. Because of the difference between the input and the extracted bg Na layers the extracted relative Na density perturbations are increased at the edges of the layer. This effect leads to incorrect values of spectral magnitudes when $F_a(m)$ is computed.

The effect of the nonlinear terms on the extracted bg Na layers and spectral parameters was investigated. It was noted that when nonlinear terms were included in the simulation, the disparity between input and extracted bg layers and spectra did not improve.

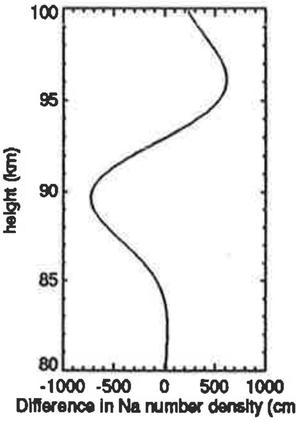

Figure 7. Difference between input and extracted average background Na number density profiles over a 2-hour observation period.

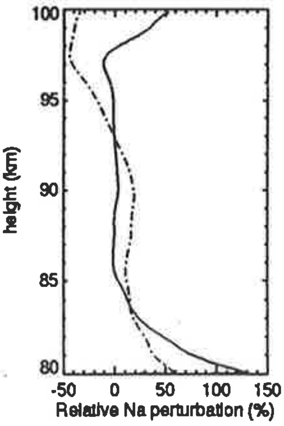

Figure 8. Input (dashed-dotted) and extracted (solid line) relative Na perturbations.

The use of random phases in the synthesis of the wave field means that significant variations occur from profile to profile. By examining multiple plots produced with different random phases, it is possible to investigate the sensitivity of the extracted parameters to slight variations in the phases of the wavenumber-frequency spectrum.

Figure 9 shows the input and extracted spectra of $F_a(m)$. The input spectra differ from the smooth curve due to incompletely resolved low-frequency waves in the spectrum. In Figure 9 the extracted spectral index q appears to be smaller than the input value and values of the characteristic vertical wavenumber are not reliably extracted by the method. The power law slope of $G_a(\omega)$ shows less variation among simulations and agrees reasonably well with the input value, as shown in Figure 10.

The results presented in Figures 9 and 10 show a case where the input and extracted spectra are in reasonable agreement. As discussed in the next section, the agreement was frequently less pronounced.

The extracted value of m_* is obtained using the expression from SG91

$$m_* = \left(\frac{\Pi m^q F_a(m)}{2\pi < r_a^2 >} \right)^{\frac{1}{q-1}}, \qquad (11)$$

where $< \bar{r}_a^2 >$ is the total variance and Π is a proportionality factor which depends on q and s.

To obtain a value of m_* from the Na lidar data, SG91 assume that $s = 2$, although s cannot be determined from Na lidar data for reasons discussed above. With this assumption the variance associated with the small wavenumber region of $F_a(m)$ becomes small relative to the total wave variance. SG91 then assume that the wave variance calculated from the Na lidar observations in the saturated wave spectrum is equal to the total variance.

Using the expression for Π given by SG91, we obtain

$$s = 1: \quad \Pi = 0.785; \qquad (12)$$

$$s = 2: \quad \Pi = 0.661. \tag{13}$$

For $F_a(m)$ with m_*=0.067 cycle km^{-1}, the small wavenumber variance as a proportion of the total variance is 0.35. Hence the value of m_* expected due to setting $s = 2$ and assuming that the large wavenumber variance is equal to the total variance is approximately 10% larger than the value with $s = 1$.

Since the simulated density spectrum assumed $s = 1$ and a known value of m_*, it can be used to test the determination of m_*. The values of m_* calculated directly from the input (Rayleigh lidarlike) spectrum using (11) are displayed in Figure 11 along with the values calculated from the extracted (Na lidarlike) spectra. The comparison is complicated by variation in the spectral index q extracted from the Na profiles which leads to uncertainty in the exponent of (11).

Comparison of Rayleigh Lidarlike and Na Lidarlike Techniques

The main difference between the Rayleigh and the Na lidar observations of gw is that for the latter technique the response to gw is complicated by the dependence on the background vertical (and possibly horizontal) Na number density gradient. The filtering applied to data acquired by each lidar technique may also be different; however, in this study the same filtering is applied to both types of lidar data.

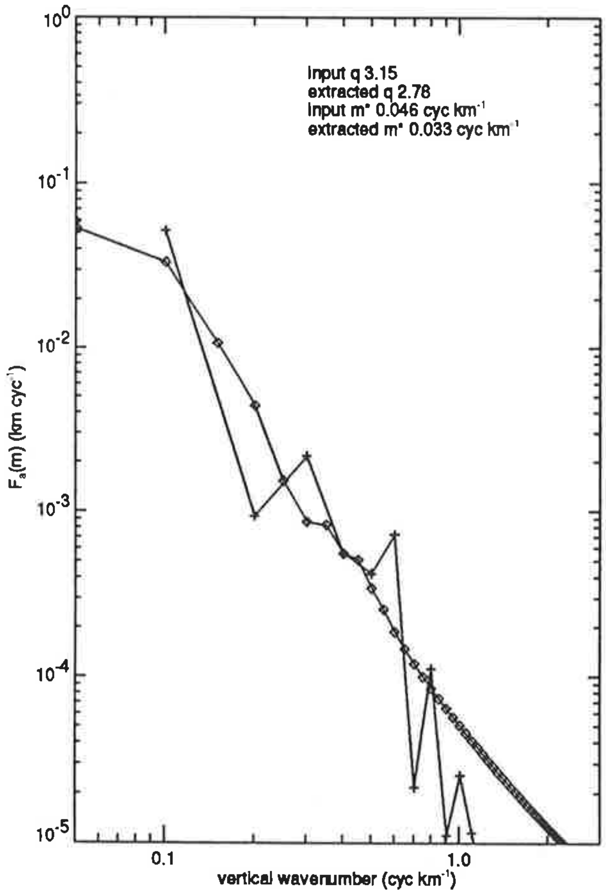

Figure 9. Input (plus) and extracted (diamond) $F_a(m)$.

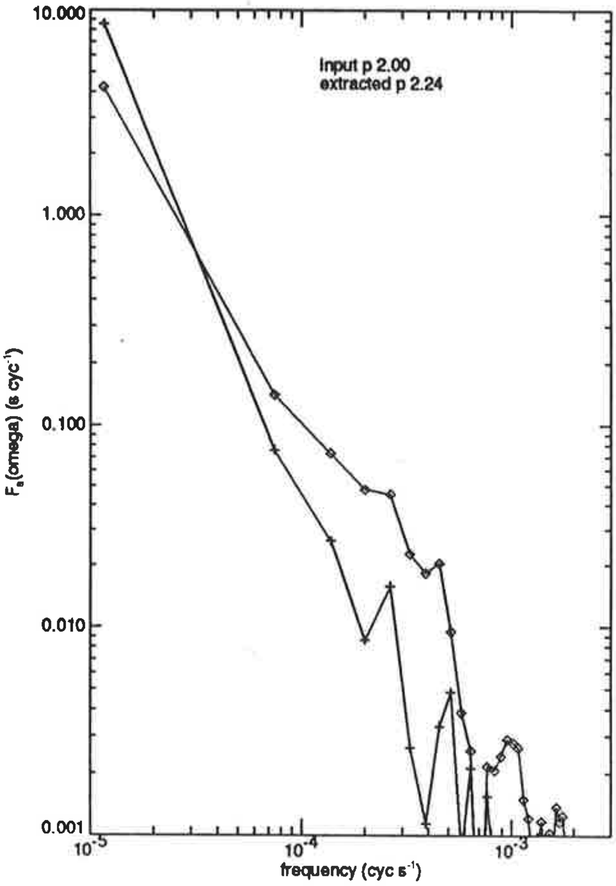

Figure 10. Input (plus) and extracted (diamond) $G_a(\omega)$.

Practical difficulties exist in obtaining Rayleigh lidar measurements in the region covered by Na lidar. By simulating idealized Rayleigh lidar observations at mesopause heights, it is possible to compare the spectra that would be observed by a Rayleigh lidar directly measuring density variations in the atmosphere and a Na lidar obtaining density spectra indirectly using the SG91 processing technique. The histograms in Figure 11 represent such comparisons.

A simulation consisting of 150 2-hour observation periods, each with superposed, randomly phased waves, was carried out. The input parameters were calculated from a spectrum of waves perturbing the background density profile, which represents a Rayleigh lidarlike observed spectrum [e.g., *Wilson et al.*, 1991a]. Na lidarlike profiles were synthesized from the density variations as before, and these profiles were used to generate the extracted spectral slopes and characteristic wavenumbers.

Figures 11a and 11b show the value of q calculated from the input Rayleigh lidarlike $F_a(m)$ and that extracted from Na lidarlike data, respectively. The Rayleigh lidarlike q varies between approximately 1.9 and 2.8 with an average of 2.6, whereas the average Na lidarlike q is 2.2.

The characteristic wavenumber extracted from Na lidarlike data is less than 0.05 cycle km^{-1} for all data sets with an average of 0.02 cycle km^{-1}. This represents a characteristic wavelength of more than 20 km.

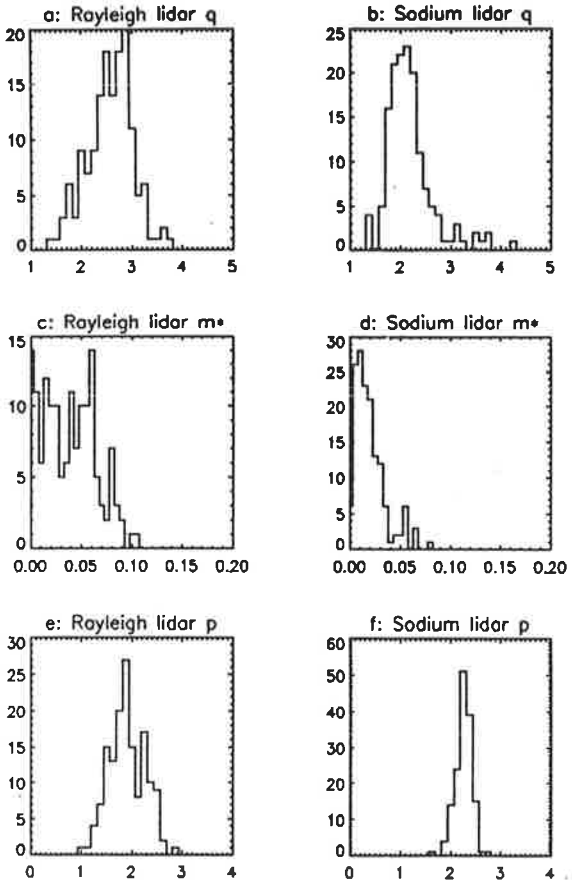

Figure 11. Histograms of input and extracted spectral parameters from 150 simulations of 2-hour observations of Na lidarlike data sets. (a) Input q. (b) Extracted q. (c) Input m_*. (d) Extracted m_*. (e) Input p. (f) Extracted p. Generated with q=3, m_*=0.067 cycle km^{-1} and p=2.

The underestimation of m_* is displayed in Figures 11c and 11d.

The Rayleigh lidarlike m_* are distributed around the generating value of 0.067 cycle km^{-1}. The spectral parameters from the Rayleigh lidarlike data show considerable variation. Hence the Rayleigh lidarlike data also overestimates m_* in the mesosphere in some cases.

Figures 11e and 11f compare the input and extracted values of p of approximately 2.0 and 2.3, respectively. In general, $G_a(\omega)$ was found to be extracted more reliably than $F_a(m)$ in the simulations.

The accurate extraction of $G_a(\omega)$ is understandable since the background profile $\bar{n}_{\mathrm{Na}}(z)$ is explicitly a function of height and not time. Hence an average over a set of successive profiles with associated random phases is expected to provide a reasonable mean and perturbation signal for the time variation at a given height. The background profile for the simulated variations is exactly stationary in time. Stationarity of both time and height variations of experimental profiles is an assumption required for the validity of the SG91 analysis technique. *Eckermann* [1990] has shown that nonstationarity of mesoscale variations affects the calculated spectral shapes and indices of vertical wavenumber spectra.

Discussion and Conclusions

Both monochromatic and spectral gw perturbations in atmospheric density and Na density have been modeled numerically. Simulated lidar profiles were generated which are representative of experimental measurements using Na and Rayleigh lidars in the height range 80-100 km.

The determination of quasi-monochromatic wave parameters from Na lidar measurements using the GV87 technique has been investigated. The technique has been applied to simulated Na lidar data with known wave parameters and energy distribution. It has been shown that only waves with wavelengths between about 1 and 10 km and observed periods from 20 min to less than 720 min can be reliably resolved using the GV87 technique.

Wavenumber and frequency spectral forms typically found at mesospheric heights were used to simulate the effect of a spectrum of gravity waves on Na density, as measured by a Na lidar. The SG91 analysis technique was then applied to the simulated data. The retrieved spectral parameters were compared with the generating parameters as a measure of the performance of the analysis technique. It was shown in this simulation that (1) the extracted background profile typically included longer-period gravity waves and hence the vertical wavenumber spectrum was incorrectly extracted; (2) the characteristic wavelength in the mesosphere was generally overestimated in the simulations investigated; (3) spectral parameters and magnitudes of the extracted frequency spectrum agreed reasonably well with generating values.

The SG91 processing method assumes a smooth Gaussian background Na layer shape, whereas chemical studies have suggested a skewed Gaussian shape. SG91 fitted a Gaussian to the time-averaged layer shape from successive Na profiles. It was shown in this simulation, however, that an averaged Na profile did not reproduce the true background structure over the 2-hour observational intervals used by SG91. To extract a more accurate background profile, longer-period waves and tidal components should be identified and filtered from the time-averaged layer shape.

Even with a powerful Na lidar it is not possible to resolve λ_z larger than the limit imposed by the vertical extent of the Na layer. This leads to unavoidable difficulties in determining m_* in the mesopause region using Na lidar data.

Background wind and temperature variations as well as photochemical effects have been ignored in the simulation. The simulated data therefore contains significantly simpler wave variations than in the real atmosphere. The techniques used to extract gw information from Na lidar data assume a constant temperature gradient, zero mean wind, and linear response of gravity waves in the Na layer. Hence the simulation is a simplified test of the experimental processing techniques.

No tidal effects were included in the model. Tides may be important for observations over several hours since the tide effectively lifts and drops the Na layer [e.g., *Batista et al.*, 1985]. This may increase the rate of photochemical destruction of Na, since at lower levels, Na oxidation is more likely to occur. Unless this increased loss rate was balanced by increased meteoric input or Na transport into the region by background winds, a net loss of Na would result. Averaging over longer timescales would then result in misleading spectra due to photochemical effects causing nonstationarity of the background Na layer.

Helmer and Plane [1993] showed that photochemical effects may cause variations in Na number density at the lower edge of the Na layer within timescales of lidar observations. They also obtained a large seasonal variation in background Na layer shape between June and January.

Appendix

Many researchers have investigated the response of atmospheric constituents to wave perturbations. This appendix compares the approaches used in modeling waves in ozone [e.g., *Zhu and Holton*, 1986] and sodium concentrations [e.g., *Gardner and Shelton*, 1985]. The different physical assumptions applied in the two approaches are discussed and their implications are presented.

Several papers have modeled wave perturbations in ozone concentrations. *Lindzen and Goody* [1965] used a linear model, which included basic ozone photochemistry and radiative effects, to investigate wave perturbations in ozone and temperature. *Zhu and Holton* [1986] used the equations developed by *Lindzen and Goody* [1965] to investigate the influence of photochemistry and solar radiation on the properties of gravity waves in the stratosphere. *Randel* [1990] and *Ziemke and Stanford* [1994] modeled Kelvin wave perturbations in total ozone and extracted Kelvin wave signatures from satellite total ozone data.

The starting point for all models of waves in constituent distributions is the continuity equation,

$$\frac{\partial r_i}{\partial t} + \nabla \cdot (r_i \bar{v}) = P_i. \qquad \text{(A1)}$$

Here r_i is the density of the constituent, $\bar{v}$ is the background wind speed and P_i is the net production rate of the constituent.

For stratospheric ozone, P_i is controlled by photochemical and radiative effects. For gravity waves in the Na layer the continuity equation can be simplified due to the assumption that photochemical terms are dominated by dynamical terms on gw timescales. Hence the continuity equation becomes

$$\frac{\partial r_i}{\partial t} + \nabla \cdot (r_i \bar{v}) = 0. \qquad \text{(A2)}$$

Expanding the second term on the left-hand side of (A2) gives

$$\frac{\partial r_i}{\partial t} + r_i \nabla \cdot \bar{v} + \nabla r_i \cdot \bar{v} = 0, \qquad \text{(A3)}$$

or

$$\frac{dr_i}{dt} + r_i \nabla \cdot \bar{v} + w' \bar{r}_{iz} = 0, \qquad \text{(A4)}$$

where $\frac{dr_i}{dt}$ is the Lagrangian derivative.

At this point it is possible to make the assumption that the atmosphere is approximately an incompressible fluid, in which case the continuity equation simplifies to

$$\frac{dr_i}{dt} + w' \bar{r}_{iz} = 0. \qquad \text{(A5)}$$

Assuming a wave solution of the form

$$r_i \propto e^{\frac{z}{2H_\rho}} \exp(i(\hat{\omega} t - kx - mz)), \qquad \text{(A6)}$$

the polarization relation between the perturbations in constituent concentration and vertical wind speed is

$$r_i = i w' \bar{r}_z / \hat{\omega}. \qquad \text{(A7)}$$

Converting to a polarization relation between the constituent density and atmospheric density perturbations and writing in a similar form to (8) results in

$$\mid r_i \mid = \frac{-r_a(z,t)}{\gamma - 1} \left(\gamma H_\rho \frac{\bar{\rho}_{i_z}(z)}{\bar{\rho}_i(z)} \right). \qquad \text{(A8)}$$

Equations (A5), (A6), and (A8) are equivalent to the ozone model equations used by *Lindzen and Goody* [1965], *Zhu and Holton* [1986], *Randel* [1990], and *Ziemke and Stanford* [1994] without the photochemistry terms included. How do these equations relate to the Na model used by *Gardner and Shelton* [1985]?

For a compressible atmosphere the approximation used to obtain (A5) is not valid. *Gardner and Shelton* [1985] and SG91 obtain a solution to (A4) by using a wave solution of the form

$$\rho_{\mathrm{Na}}(z,t) = e^{-\chi} \rho_0 (z - \xi), \qquad \text{(A9)}$$

where χ represents variation in wave amplitude due to wind divergence and ξ represents transport by the vertical wind perturbation.

It is possible to determine the relative size of the wind divergence terms in comparison with the terms due to transport by the vertical wind. It is clear that the relative importance of the different terms is dependent on the choice of background Na layer shape. However, if a Gaussian background layer, with standard deviation σ_o and centroid z_o, is assumed, then the three terms are

$$r_{\mathrm{Na}}(z,t) = \frac{-1}{\gamma - 1} \left(1 - \gamma H_\rho \frac{(z - z_o)}{\sigma_o^2} + \mathrm{NL} \right) r_a(z,t). \qquad \text{(A10)}$$

Figure 12 shows a typical plot of the value of the three terms in (A10). The first term on the right-hand side of (A10) depends only on the height variation of atmospheric density perturbations and only appears in models which do not assume an incompressible atmosphere. The second term is a linear relation between

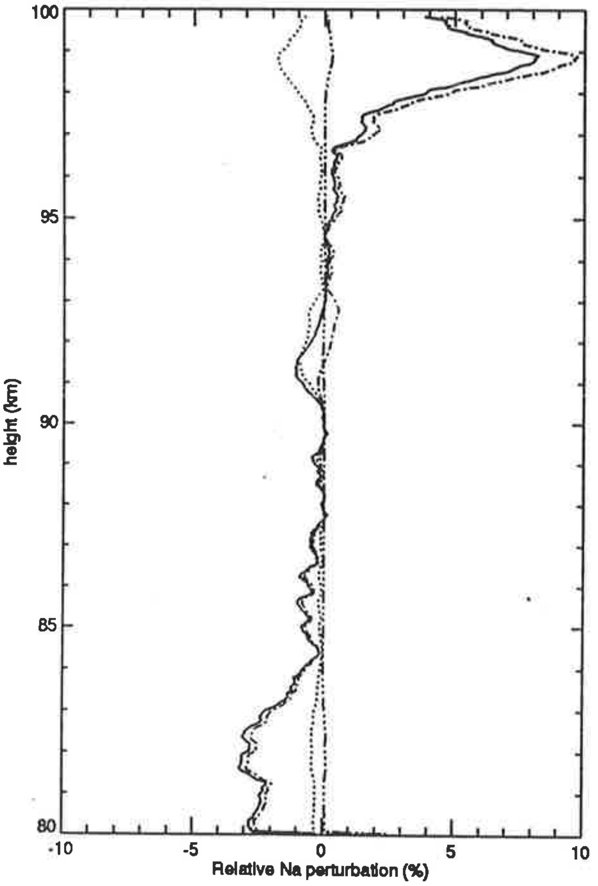

Figure 12. Comparison of magnitude of constant (dotted), linear (dashed-dotted) and nonlinear (dashed-dotted-dotted-dotted) contribution to the total Na perturbations (solid line).

Na and atmospheric density perturbations and has its maximum value in regions away from the peak of the Na layer. The nonlinear term NL, as discussed by *Gardner and Shelton* [1985], is most significant in the vicinity of the peak of the layer.

Hence the difference between the *Lindzen and Goody* [1965] approach and that used by *Gardner and Shelton* [1985] is not related to specifically considering Na in the modeling. It originates in the assumed form of the wave perturbation in background density. This in turn results from the assumption that the amplitude of the wave perturbation does not vary due to the divergence of the wind field.

Acknowledgments. The authors wish to thank U.-P. Hoppe, R. L. Collins, and one anonymous reviewer for useful comments. This research is supported by Australian Research Council grants and DGW is supported by an Australian Postgraduate Award.

References

Allen, S. J., and R. A. Vincent, Gravity-wave activity in the lower atmosphere: Seasonal and latitudinal variations, *J. Geophys. Res.*, *100*, 1327–1350, 1995.

Bacmeister, J. D., S. D. Eckermann, P. A. Newman, L. Lait, K. R. Chan, M. Loewenstein, M. H. Profitt, and B. L. Gary, Stratospheric horizontal waenumber spectra of winds, potential temperature and atmospheric tracers observed by high-altitude aircraft, *J. Geophys. Res.*, in press, 1995.

Batista, P. P., B. R. Clemesha, D. M. Simonich, and V. W. Kirchhoff, Tidal oscillations in the atmospheric sodium layer, *J. Geophys. Res.*, *90*, 3881–3888, 1985.

Beatty, T. J., and C. S. Gardner, Lidar observations of gravity waves and their spectra near the mesopause and stratopause at Arecibo, *Tech. Rep. EOSL 90-002*, Dep. of Electr. and Comput. Eng., Univ. of Ill. at Urbana-Champaign, Urbana, 1990.

Beatty, T. J., C. A. Hostetler, and C. S. Gardner, Lidar observations of gravity waves and their spectra near the mesopause and stratopause at Arecibo, *J. Atmos. Sci.*, *49*(6), 477–496, 1992.

Chanin, M-L., and A. Hauchecorne, Lidar observation of gravity and tidal waves in the stratosphere and mesosphere, *J. Geophys. Res.*, *86*(C10), 9715–9721, 1981.

Chiu, Y. T., and B. K. Ching, The response of atmospheric and lower ionospheric layer structures to gravity waves, *Geophys. Res. Lett.*, *5*, 539–542, 1978.

Collins, R. L., A. Nomura, and C. S. Gardner, Gravity waves in the upper mesosphere over Antarctica: Lidar observations at the South Pole and Syowa, *J. Geophys. Res.*, *99*, 5475–5485, 1994.

Cot, C., and J. Barat, Wave–turbulence interaction in the stratosphere, *J. Geophys. Res.*, *91*, 2749–2756, 1986.

Cox, R. M., J. M. C. Plane, and J. S. A. Green, A modelling investigation of sudden sodium layers, *Geophys. Res. Lett.*, *2*, 2841–2844, 1993.

Dewan, E. M., and R. E. Good, Saturation and the "universal" spectrum for vertical profiles of horizontal scalar winds in the atmosphere, *J. Geophys. Res.*, *91*, 2742–2748, 1986.

Eckermann, S. D., Effects of nonstationarity on spectral analysis of mesoscale motions in the atmosphere, *J. Geophys. Res.*, *95*, 16,685–16,703, 1990.

Eckermann, S. D., Effect of background winds on vertical wavenumber spectra of atmospheric gravity waves, *J. Geophys. Res.*, *100*, 14,097–14,112, 1995.

Fritts, D. C., and T. E. VanZandt, Spectral estimates of gravity wave energy and momentum fluxes, I, energy dissipation, acceleration, and constraints, *J. Atmos. Sci.*, *50*, 3685–3694, 1993.

Fukao, S., Y. Maekawa, T. Sato, and S. Kato, Fine structure in mesospheric wind fluctuations observed by the Arecibo UHF Doppler radar, *J. Geophys. Res.*, *90*, 7547–7556, 1985.

Gardner, C. S., Diffusive filtering theory of gravity wave spectra in the atmosphere, *J. Geophys. Res.*, *99*, 20,601–20,622, 1994.

Gardner, C. S., and J. D. Shelton, Density response of neutral atmospheric layers to gravity wave perturbations, *J. Geophys. Res.*, *90*, 1745–1754, 1985.

Gardner, C. S., and D. G. Voelz, Lidar studies of the nighttime sodium layer over Urbana, Illinois, 2, Gravity waves, *J. Geophys. Res.*, *92*, 4673–4694, 1987.

Gardner, C. S., C. A. Hostetler, and S. J. Franke, Gravity wave models for the horizontal wave number spectra of atmospheric velocity and density fluctuations, *J. Geophys. Res.*, *98*, 1035–1049, 1993a.

Gardner, C. S., C. A. Hostetler, and S. Lintelmann, Influence of the mean wind field on the separability of atmospheric perturbation spectra, *J. Geophys. Res.*, *98*, 8859–8872, 1993b.

Hecht, J. H., R. L. Walterscheid, and M. N. Ross, First measurements of the two–dimensional horizontal wave number spectrum from ccd images of the nightglow, *J. Geophys. Res.*, *99*, 11,449–11,460, 1994.

Helmer, M., and J. M. C. Plane, A study of the reaction Na O_2+O $\rightarrow$ NaO + O_2: Implications for the chemistry of sodium in the upper atmosphere, *J. Geophys. Res.*, *98*, 23,207–23,222, 1993.

Hines, C. O., Internal atmospheric gravity waves at ionospheric heights, *Can. J. Phys.*, *38*, 1441–1481, 1960.

Hines, C. O., The saturation of gravity waves in the middle atmosphere, II, Development of Doppler-spread theory, *J. Atmos. Sci.*, *48*(11), 1360–1379, 1991.

Kwon, K. H., D. C. Senft, and C. S. Gardner, Airborne sodium lidar observations of horizontal and vertical wave number spectra of mesopause density and wind perturbations, *J. Geophys. Res.*, *95*, 13,723–13,736, 1990.

Lefrère, J., and C. Sidi, Distortion of gravity wave spectra measured from ground–based stations, *Geophys. Res. Lett.*, *17*, 1581–1584, 1990.

Lindzen, R., and R. Goody, Radiative and photochemical processes in mesospheric dynamics, 1, Models for radiative and photochemical processes, *J. Atmos. Sci.*, *22*, 341–348, 1965.

Lintelmann, S. A., and C. S. Gardner, Observation and interpretation of spectra of atmospheric gravity wave perturbations with upward and downward phase progression, *J. Geophys. Res.*, *99*, 16,959–16,971, 1994.

Marks, C. J., and S. D. Eckermann, A three–dimensional nonhydrostatic ray–tracing model for gravity waves: Formulation and preliminary results for the middle atmosphere, *J. Atmos. Sci.*, *52*, 1959–1984, 1995.

Meriwether, J. W., P. D. Dao, R. T. McNutt, W. Klemetti, W. Moskowitz, and G. Davidson, Rayleigh lidar observations of mesosphere temperature structure, *J. Geophys. Res.*, *99*, 16,973–16,987, 1994.

Mitchell, N. J., L. Thomas, and A. K. P. Marsh, Lidar studies of stratospheric gravity waves: A comparison of analysis techniques, *Ann. Geophys.*, *8*, 705–712, 1990.

Murayama, Y., T. Tsuda, M. Yamamoto, T. Nakamura, T. Sato, S. Kato, and S. Fukao, Dominant vertical scales of gravity waves in the middle atmosphere observed with the MU radar and rocketsondes, *J. Atmos. Terr. Phys.*, *54*, 339–346, 1992.

Pitteway, M. L. V., and C. O. Hines, The viscous damping of atmospheric gravity waves, *Can. J. Phys.*, *41*, 1935–1948, 1963.

Randel, W. J., Kelvin–wave–induced trace constituent oscillations in the equatorial stratosphere, *J. Geophys. Res.*, *95*, 18,641–18,652, 1990.

Reid, I. M., Gravity wave motions in the upper middle atmosphere (60-110 km), *J. Atmos. Terr. Phys.*, *48*(11–12), 1057–1072, 1986.

Reid, I. M., MF Doppler and spaced antenna radar measurements of upper middle atmosphere winds, *J. Atmos. Terr. Phys.*, *50*(2), 117–134, 1988.

Sato, K., and M. Yamada, Vertical structure of atmospheric gravity waves revealed by the wavelet analysis, *J. Geophys. Res.*, *99*, 20,623–20,631, 1994.

Senft, D. C., and C. S. Gardner, Seasonal variability of gravity wave activity and spectra in the mesopause region at Urbana, *J. Geophys. Res.*, *96*, 17,229–17,264, 1991.

Senft, D. C., C. A. Hostetler, and C. S. Gardner, Characteristics of gravity wave activity and spectra in the upper stratosphere and upper mesosphere at Arecibo during early April 1989, *J. Atmos. Terr. Phys.*, *55*, 425–439, 1993.

Shelton, J. D., C. S. Gardner, and C. F. Sechrist Jr., Density response of the mesospheric sodium layer to gravity wave perturbations, *Geophys. Res. Lett.*, *7*, 1069–1072, 1980.

Shibata, T., T. Fukuda, and M. Maeda, Density fluctuations in the middle atmosphere over Fukuoka observed by an XeF Rayleigh lidar, *Geophys. Res. Lett.*, *13*, 1121–1124, 1986.

Smith, S. A., D. C. Fritts, and T. E. VanZandt, Evidence for a saturated spectrum of atmospheric gravity waves, *J. Atmos. Sci.*, *44*, 1404–1410, 1987.

Thomas, L., M. C. Isherwood, and M. R. Bowman, A theoretical study of the height distribution of sodium in the mesosphere, *J. Atmos. Terr. Phys.*, *45*(8/9), 587–594, 1983.

Thrane, E. V., T. Blix, U.-P. Hoppe, F.-J. Lübken, W. Hillert, G. Lehmacher, and D. C. Fritts, A study of small-scale waves and turbulence in the mesosphere using simultaneous *in situ* observations of neutral gas and plasma fluctuations, *J. Atmos. Terr. Phys.*, *56*, 1797–1808, 1994.

Voelz, D. G., and C. S. Gardner, Theoretical and lidar studies of the seasonal and nocturnal variations of the mesospheric sodium layer at Urbana, Illinois, *Tech. Rep. EOSL 86-006*, Dep. of Electr. and Comput. Eng., Univ. of Ill. at Urbana-Champaign, Urbana, 1986.

Weinstock, J., Saturated and unsaturated spectra of gravity waves and scale dependent diffusion, *J. Atmos. Sci.*, *47*, 2211–2225, 1990.

Whiteway, J. A., and A. I. Carswell, Rayleigh lidar observations of thermal structure and gravity wave activity in the high Arctic during a stratospheric warming, *J. Atmos. Sci.*, *51*(21), 3122–3136, 1994.

Wilson, R., M. L. Chanin, and A. Hauchecorne, Gravity waves in the middle atmosphere observed by Rayleigh lidar, 1, Case studies, *J. Geophys. Res.*, *96*, 5153–5167, 1991a.

Wilson, R., M. L. Chanin, and A. Hauchecorne, Gravity waves in the middle atmosphere observed by Rayleigh lidar, 2, Climatology, *J. Geophys. Res.*, *96*, 5169–5183, 1991b.

Wu, Y.-F., and H.-U. Widdel, Further study of a saturated gravity wave spectrum in the mesosphere, *J. Geophys. Res.*, *96*, 9263–9272, 1991.

Yamamoto, M., T. Tsuda, S. Kato, T. Sato, and S. Fukao, A saturated inertia gravity wave in the mesosphere observed by the middle and upper atmosphere radar, *J. Geophys. Res.*, *92*, 11,993–11,999, 1987.

Zhu, X., A new theory of the saturated gravity wave spectrum for the middle atmosphere, *J. Atmos. Sci.*, *51*(24), 3615–3626, 1994.

Zhu, X., and J. R. Holton, Photochemical damping of inertio-gravity waves, *J. Atmos. Sci.*, *43*(22), 2578–2584, 1986.

Ziemke, J. R., and J. L. Stanford, Kelvin waves in total column ozone, *Geophys. Res. Lett.*, *21*(2), 105–108, 1994.

D. E. Gibson-Wilde, I. M. Reid, and R. A. Vincent, Department of Physics and Mathematical Physics, University of Adelaide, S. A. 5005, Adelaide, Australia. (e-mail: dgibson@physics.adelaide.edu.au; ireid@physics.adelaide.edu.au; rvincent@physics.adelaide.edu.au)

S. D. Eckermann, Computational Physics, Inc., Suite #600, 2750 Prosperity Ave., Fairfax, VA 22031, and E. O. Hulburt Center for Space Research, Naval Research Laboratory, Washington, D. C. 20375. (e-mail: eckerman@ismap5.nrl.navy.mil)

(Received December 7, 1994; revised September 13, 1995; accepted October 18, 1995.)

Appendix B

Dual Lidar Observations of Mesoscale Fluctuations of Ozone and Horizontal Winds

This is a preprint of a paper by D. E. Gibson-Wilde, R. A. Vincent, C. Souprayen, S. Godin, A. Hertzog, and S. D. Eckermann submitted for publication in *Geophysical Research Letters*, to appear in 1997.

Dual Lidar Observations of Mesoscale Fluctuations of Ozone and Horizontal Winds

D. E. Gibson-Wilde and R. A. Vincent
Department of Physics and Mathematical Physics,

University of Adelaide, S.A. 5005, Australia

C. Souprayen, S. Godin, and A. Hertzog
Service d'Aeronomie, CNRS, France

S. D. Eckermann[1]
Computational Physics, Inc., Fairfax, Virginia

Short title: MESOSCALE OZONE FLUCTUATIONS

Abstract.

A case study is presented of 6.5 h of simultaneous colocated stratospheric DIfferential Absorption Lidar (DIAL) measurements of ozone concentration and Rayleigh-Mie Doppler (RD) lidar measurements of horizontal wind velocity from the Observatoire de Haute Provence (OHP), France (44°N,6°E). The lidar observations provide both temporal and vertical information on mesoscale dynamics and ozone variability. This data set permits a more detailed study of mesoscale ozone fluctuations than has been possible previously using other measurement techniques.

Introduction

Stratospheric ozone abundances exhibit appreciable mesoscale variability. Perturbations with vertical scales ~1–5 km are observed routinely in ozonesonde data [*Ehhalt et al.,* 1983; *Hofmann et al.,* 1989; *Reid and Vaughan,* 1991; *Teitelbaum et al.,* 1994], while in situ measurements from stratospheric aircraft show variability over a broad range of horizontal scales [*Gage and Nastrom,* 1986; *Danielsen et al.,* 1991; *Bacmeister et al.,* 1996]. Since ozone in the lower stratosphere (below ~25 km) is photochemically inactive on timescales up to 5 days (in the absence of heterogeneous processing), then such variability must in general have a dynamical origin. Observed ozone fluctuations have been attributed primarily either to gravity-wave advection or to larger-scale transport effects.

Gravity-wave-induced vertical advection was first suggested as a possible cause of ozone perturbations by *Chiu and Ching* [1978]. Aircraft observations during the Stratosphere–Troposphere Exchange Project (STEP) revealed inertia gravity waves (IGWs) [*Chan et al.,* 1991] and seemingly related perturbations of ozone and other constituents [*Wilson et al.,* 1991]. *Danielsen et al.* [1991] argued that the vertical and horizontal displacements of these IGWs produced the observed ozone perturbations, and that irreversible constituent transport resulted as these waves dissipated. Similar arguments were advanced by *Teitelbaum et al.* [1994] to explain fluctuations in selected ozonesonde profiles.

Conversely, *Ehhalt et al.* [1983] found that long-term variances of ozone perturbations inferred from ozonesonde releases at Hohenpeissenberg (47°N, 11°E) were significantly larger than those expected on the basis of wave-induced potential temperature fluctuations alone, indicating that gravity wave vertical advection cannot explain all of the structure. Later analysis of variability in a large base of ozonesonde data from middle to high northern latitudes by *Reid et al.* [1993] identified the largest perturbations (so-called "laminae") with differential transport across the polar vortex edge. High-resolution parcel advection models of this transport have succeeded in simulating laminated vertical ozone profiles which are similar to those observed [e.g., *Orsolini et al.,* 1995]. Indeed, *Newman and Schoeberl* [1995] recently used such a model to argue that quasi-horizontal flow in and out of the polar vortex could explain those laminar ozone structures observed in STEP data which *Danielsen et al.* [1991] had previously attributed to IGW motions. Recent analysis of a large amount of airborne stratospheric ozone data by *Bacmeister et al.* [1996] concluded that neither IGWs nor large-scale advection alone could explain the mean mesoscale variability evident in these data, and that both effects may combine and interact to produce the observed variability.

Clearly, then, both processes can and do produce mesoscale ozone variability. In practice, however, it can be difficult to differentiate between the effects of either process in a given data set, since the data often lack the horizontal, vertical, and temporal resolution required to characterize fully both the dynamical fields and the ozone distribution. Thus, improved observations are needed which avoid some of these shortcomings.

To this end, *Reid et al.* [1994] recently combined MST radar observations of stratospheric velocities with nearby ozonesonde measurements to deduce that the IGW observed in the velocity data could not explain the observed lamination in the ozonesonde profile. *Langford et al.* [1996] combined radiosonde data (used to characterize IGWs in the troposphere) with DIAL measurements of tropospheric ozone to conclude that gravity waves made important contributions to their observed tropospheric ozone concentrations. In both of these studies, only one data set had high time-height resolution, while the other had good height resolution but poor time resolution. Here, we report on an experiment in which two colocated lidar instruments were used to acquire simultaneous stratospheric velocity and ozone data which both had high vertical and temporal resolution. We use these velocity data to identify and characterize an

IGW in the stratosphere and to predict its effect on ozone profiles, then compare these predictions with the contemporaneous ozone data to infer the processes responsible for the structure in the ozone data.

Observations

The observations used in this case study were obtained at OHP between 2230 LT on 23 October and 0500 LT on 24 October, 1995. The DIAL ozone lidar and RD lidar, located approximately 10 m apart within the same building, were run simultaneously during the observation period. Table 1 summarizes the operational specifics of both lidar systems. The OHP RD lidar and DIAL ozone systems have been described by *Garnier and Chanin* [1992] and *Lacoste et al.* [1992], respectively. Measurements of lower stratospheric (12-30 km) ozone concentration are provided by the DIAL system and zonal and meridional wind velocities are provided by the RD lidar.

Lidar data processing may involve both temporal and spatial averaging of the received signal. For this study, emphasis was placed on obtaining simultaneous profiles of wind velocities and ozone concentration which had the same time resolution. A common time resolution of 30 min was chosen as a compromise between the statistical reliability of the DIAL ozone measurement and the need to obtain profiles with significant mesoscale variability.

Figure 1 presents the sequence of DIAL ozone concentration profiles in two consecutive plots. The estimated error in measurement is 10% in the height range 12-20 km. The RD zonal and meridional velocity profiles in Figure 2 are displayed at a height resolution of 150 m, obtained from regridding using spline interpolation from the initial 115 m resolution, for compatibility with the DIAL profiles. A height-independent bias in RD lidar zonal wind measurements was corrected by comparing with velocity measurements from a radiosonde released from Nimes, 100 km west of OHP, at 2300 LT on 23 October, 1995. The RD velocity data are acquired typically with a time resolution of 5 min so that the 30 min profiles presented here have an estimated error of less than 5% between 12-20 km.

Figure 3 displays the average profile of ozone concentration calculated over the 6.5 hour observation period. The error associated with this average profile is ~2 % in the height range 12-20 km. The small-scale features evident in this average profile must result from dynamical activity on timescales greater than approximately 7 hours.

Ozone Laminae

The two local maxima in ozone concentration in Figure 3 at approximately 14 km and 18 km are examples of ozone laminae. They were identified as such using the definition of *Reid and Vaughan* [1991] which requires large positive or negative ozone concentrations which are limited to a layer less than 2.5 km in vertical extent. A major lamina occurs at ~14 km and a minor lamina also occurs at ~18 km. *Reid and Vaughan* [1991] found that a majority of laminae in mid-latitude, northern hemispheric ozonesonde data were within the height range 12-18 km.

The two laminae remain well-defined throughout the observation period, as is evident in the sequence of ozone concentration profiles (Figure 1). The 6.5 h mean lidar ozone concentration profile was compared with an ozone concentration profile from an ozonesonde launched from OHP at 1200 LT on 24 October 1995, 7 hours after the final lidar profile (not shown here). The ozonesonde profile confirmed the lidar observation of the lamina at 14 km. The secondary lamina at 18 km was reduced in magnitude by the time of the ozonesonde flight, suggesting a shorter time or horizontal scale mechanism was responsible for this feature.

From the lidar observations alone, the estimated minimum lifetime for the two laminae was 6.5 h. A minimum lifetime of 14 h was estimated for the lamina at 14 km based on the occurrence in both the lidar and ozonesonde ozone concentration profiles. The duration of the 14 km lamina suggests that it was generated by large-scale processes. Initial indications from synoptic-scale isentropic parcel advection calculations suggest that a filamentary structure was present at approximately 14 km over OHP [*Roger Atkinson*, private communication].

Long–period Fluctuations

Successive vertical profiles of zonal and meridional velocities from the RD lidar (Figure 2) indicate a wave-like feature below 20 km with downward phase (upward energy) propagation which persists throughout the 6.5 h observation period. A hodograph analysis (Figure 4) shows mostly clockwise rotation of the velocity fluctuations with height and a well-defined velocity ellipse, which suggests that this feature is a long-period upward-propagating inertia gravity wave (IGW). IGW parameters were derived from these data using a Stokes parameter analysis [e.g. *Eckermann and Vincent,* 1989] and are presented in Table 2. The values of observed and intrinsic wave frequency were used to determine that the horizontal propagation direction of the IGW was towards the south-west.

The 6.5 h mean winds and IGW parameters were used to calculate the ozone response using the approach of *Chiu and Ching* [1978]. Theoretical results in terms of relative mixing ratio are here applied to the relative ozone concentration as measured directly by the DIAL technique. From the continuity equation, the relative ozone perturbation $\frac{O_3'}{\bar{O}_3}$ driven by gravity-wave vertical advection alone is [after *Chiu and Ching,* 1978],

$$\frac{O_3'(z,t)}{\bar{O}_3(z)} \approx \left(\frac{-\zeta'}{\bar{O}_3(z)}\right)\left(\frac{d\bar{O}_3(z)}{dz} + \frac{\bar{O}_3(z)}{\gamma H}\right), \tag{1}$$

where

$$\zeta' \approx \frac{iU'(z,t)}{N}\left(\frac{\sqrt{\hat{\omega}^2 - f^2}}{\hat{\omega}}\right) \tag{2}$$

is the vertical displacement of a parcel by the IGW, $U'(z,t)$ is the total horizontal wind velocity perturbation, $\bar{O_3}(z)$ is the mean ozone concentration, assumed time-invariant, H is the density scale height, γ is the ratio of specific heats (~ 1.4), and $\frac{d\bar{O_3}(z)}{dz}$ is the mean vertical concentration gradient. Based on ozonesonde temperature data, the value of the Brunt-Väisälä frequency, N, was 0.02 rad/s in the lower stratosphere. $\bar{O_3}(z)$ was estimated by a low-pass filtered cubic polynomial fit which neglects the probable vertical ozone structure due to large-scale processes.

Horizontal IGW displacements have been neglected in (1) because the lidar data do not provide any information on mean horizontal gradients in $\bar{O_3}(z)$. Thus, in (1) we have implicitly assumed that they are negligible. Other synoptic-scale data and/or analyses may be able to provide this information, whereupon (1) can be generalized to consider both horizontal and vertical gradient and displacement terms [e.g., *Danielsen et al.,* 1991; *Teitelbaum et al.,* 1994].

Figure 5a shows the measured $\frac{O_3'(z,t)}{\bar{O_3}(z)}$ about the cubic polynomial-fitted profile, as well as the expected perturbation produced by the IGW in Figure 4, calculated by first converting $U'(z,t)$ to a $\zeta'(z,t)$ oscillation using (2) (see Figure 5b), then using this to calculate $\frac{O_3'(z,t)}{\bar{O_3}(z)}$ using (1). The relative magnitudes of the measured and calculated ozone perturbations in Figure 5a suggest that the IGW alone may drive a maximum contribution of ~ 5 % relative ozone fluctuations, except in the height region below $\sim$ 14.5 km where the inverse dependence on $\bar{O_3}(z)$ in Equation (1) leads to calculated relative ozone fluctuations of up to 10 %. The estimation of $\bar{O_3}(z)$ used in calculation of the ozone response to the IGW is a vital factor. The smooth $\bar{O_3}(z)$ profile probably underestimates the vertical gradients on which the IGW parcel displacements act. Hence, the calculation presented in Figure 5a was based on a minimum $\frac{d\bar{O_3}(z)}{dz}$ estimate which is only relevant in the absence of large-scale processes.

The lamina at 14 km is not strongly associated with ozone features estimated from the horizontal wind perturbation profile, however there is some indication of phase agreement in the region of 18 km (Figure 5). It must be concluded that IGW alone, without some filamentation present due to large-scale horizontal ozone structure, cannot be responsible for the magnitude of lamination observed in this case study. In the presence of lamination, background ozone gradients of 2-5 times mean values may be observed. Thus the data seem to indicate that the laminae observed here result from synoptic-scale advection processes, and that IGW-induced displacements induce secondary distortions of these preexisting laminae.

Conclusions

DIAL ozone measurements and RD lidar wind velocity measurements from OHP were used to examine mesoscale structure in the stratosphere. The time evolution of the ozone profile available from lidar measurements was used to infer a minimum continuous lifetime of two ozone laminae of 6.5 h. One of the ozone laminae persisted in measurements carried out over 14 h apart.

The dual lidar measurement technique described here permits a more thorough study of mesoscale dynamics and tracer variability than has been previously possible using data from infrequent aircraft or sonde flights. The RD lidar data showed conclusively that an upward-propagating IGW was present below 20 km, with a vertical wavelength of 2.3 km and an observed vertical phase speed ~ 0.06 ms^{-1}. The response of ozone to this long-period wave feature was estimated. The magnitudes of ozone fluctuations driven by the long-period wave feature are not sufficient to explain fully the observed ozone laminae.

It is suggested that the observed ozone structure during this case study is a result of large-scale lamination due to horizontal advection in coexistence with a long-period IGW. These two processes contribute to long-lived vertical gradients in ozone concentration which drive an enhanced ozone response to short-period wave motions. Analysis and modeling continue to try to understand these features further.

Acknowledgments.

We wish to thank the staff at OHP and Dr Roger Atkinson of the Bureau of Meteorology Research Centre, Melbourne, for useful comments. DGW acknowledges support from the University of Adelaide to visit CNRS.

References

Bacmeister, J. T., S. D. Eckermann, P. A. Newman, L. Lait, K. R. Chan, M. Loewenstein, M. H. Profitt, and B. L. Gary, Stratospheric horizontal wavenumber spectra of winds, potential temperature and atmospheric tracers observed by high-altitude aircraft, *J. Geophys. Res.*, *101*, 9441–9470, 1996.

Chan, K. R., S. G. Scott, S. W. Bowen, S. E. Gaines, E. F. Danielsen, and L. Pfister, Horizontal wind fluctuations in the stratosphere by internal waves of short vertical wavelength, *J. Geophys. Res.*, *96*, 17,425–17,432, 1991.

Chiu, Y. T., and B. K. Ching, The response of atmospheric and lower ionospheric layer structures to gravity waves, *Geophys. Res. Lett.*, *5*, 539–542, 1978.

Danielsen, E. F., R. S. Hipskind, W. L. Starr, J. F. Vedder, S. E. Gaines, D. Kley, and K. K. Kelly, Irreversible transport in the stratosphere by internal waves of short vertical wavelength, *J. Geophys. Res.*, *96*, 17,433–17,452, 1991.

Eckermann, S. D., and R. A. Vincent, Falling sphere observations of anisotropic gravity wave motions in the upper stratosphere over Australia, *Pure and Appl. Geophys.*, *130*, 509–532, 1989.

Ehhalt, D. G., E. P. Roth, and U. Schmidt, On the temporal variance of stratospheric gas concentrations, *J. Atmos. Chem.*, *1*, 27–51, 1983.

Gage, K. S., and G. D. Nastrom, Spectrum of atmospheric vertical displacements and spectrum of conservative scalar passive additives due to quasi–horizontal atmospheric motions, *J. Geophys. Res.*, *91*, 13,211–13,216, 1986.

Garnier, A., and M. L. Chanin, Description of a Doppler Rayleigh LIDAR for measuring winds in the middle atmosphere, *App. Phys. B*, *55*, 35–40, 1992.

Hofmann, D. J., J. W. Harder, J. M. Rosen, J. V. Hereford, and J. R. Carpenter, Ozone profile measurements at McMurdo Station, Antarctica, during the spring of 1987, *J. Geophys. Res.*, *94*, 16,527–16,536, 1989.

Lacoste, A. M., S. Godin, and G. Megie, Lidar measurements and Umkehr observations of the ozone vertical distribution at the Observatoire de Haute Provence, *J. Atmos. Terr. Phys.*, *54*, 571–580, 1992.

Langford, A. O., M. H. Proffitt, T. E. VanZandt, and J.-F. Lamarque, Modulation of tropospheric ozone by gravity waves, Part 1: Observations and analysis of linear effects, *J. Geophys. Res.*, , in press, 1996.

Newman, P. A., and M. R. Schoeberl, A reinterpretation of the data from the NASA Stratosphere–Troposphere Exchange Project, *Geophys. Res. Lett.*, *22*, 2501–2504, 1995.

Orsolini, Y., P. Simon, and D. Cariolle, Filamentation and layering of an idealized tracer by observed winds in the lower stratosphere, *Geophys. Res. Lett.*, *22*, 839–842, 1995.

Reid, S. J., and G. Vaughan, Lamination in ozone profiles in the lower stratosphere, *Q. J. R. Meteorol. Soc.*, *117*, 825–844, 1991.

Reid, S. J., G. Vaughan, and E. Kyro, Occurrence of ozone laminae near the boundary of the stratospheric polar vortex, *J. Geophys. Res.*, *98*, 8883–8890, 1993.

Reid, S. J., G. Vaughan, N. J. Mitchell, I. T. Prichard, H. J. Smit, T. S. Jorgensen, C. Varotsos, and H. de Backer, Distribution of ozone laminae during EASOE and the possible influence of inertia–gravity waves, *Geophys. Res. Lett.*, *21*, 1479–1482, 1994.

Teitelbaum, H., J. Ovarlez, H. Kelder, and F. Lott, Some observations of gravity–wave–induced structure in ozone and water vapour during EASOE, *Geophys. Res. Lett.*, *21*, 1483–1486, 1994.

Wilson, J. C., W. T. Lai, and S. D. Smith, Measurements of condensation nuclei above the jet stream: Evidence for cross jet transport by waves and new particle formation at high altitudes, *J. Geophys. Res.*, *96*, 17,415–17,423, 1991.

Dorothy Gibson-Wilde and Robert Vincent, Department of Physics and Mathematical Physics, University of Adelaide, S.A. 5005, Australia. (e-mail: dgibson@physics.adelaide.edu.au)

Claude Souprayen, Sophie Godin, and Albert Hertzog, Service d'Aeronomie, CNRS, France.

Stephen Eckermann, Computational Physics, Inc., Fairfax, Virginia

Received ______________________

---

[1] E. O. Hulburt Center for Space Research, Naval Research Laboratory, Washington, D.C. 20375

Table 1. DIAL ozone and RD lidar capabilities at OHP.

	Ozone DIAL	RD lidar
Beam direction	vertical	vertical + 40 N/E
Wavelengths	λ absorbed=308 nm λ reference=355 nm	λ=532 nm
PRF	50 Hz	30 Hz
Height resolution	600 m	115 m
Time resolution	30 min	30 min
Height range	12 - 30 km	12 - 45 km
Major error sources	water vapour aerosol contamination	aerosol contamination

Table 2. IGW parameters derived from successive RD lidar profiles and Stokes parameter analysis.

Wave Parameter	Estimated Value
Vertical wavelength	2.3 km
Observed vertical phase speed	-0.06 m/s
Observed frequency	1.6f $\sim$ 0.00016 rad/s
Intrinsic frequency	2.2f $\sim$ 0.00022 rad/s
Horizontal wavelength	360 km

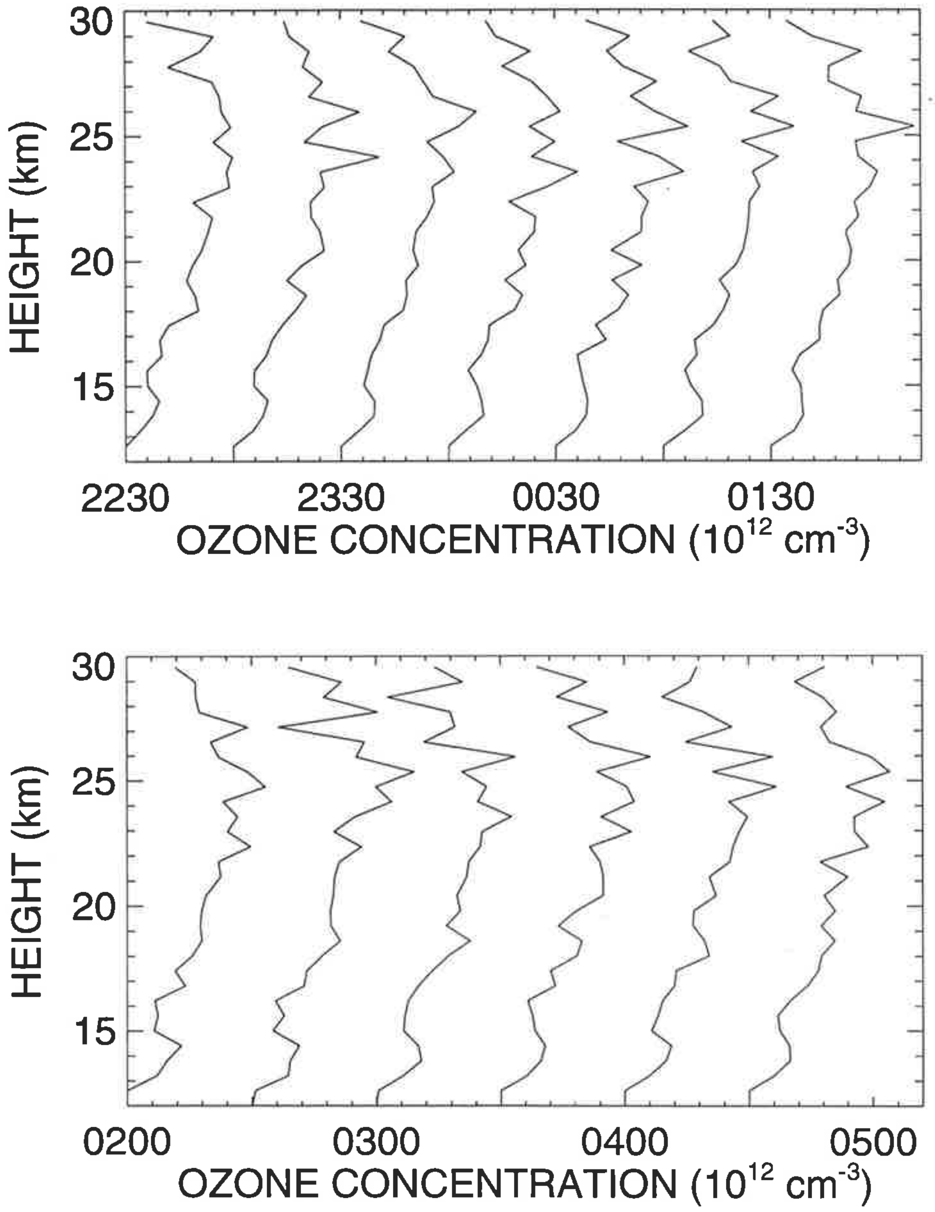

Figure 1. Sequence of DIAL ozone concentration profiles from 2230 LT on 23 October, 1995 to 0500 LT on 24 October, 1995. The zero point of each profile is labeled with the starting time of its 30 min observational integration. Successive profiles are separated by 5×10^{12}cm^{-3}.

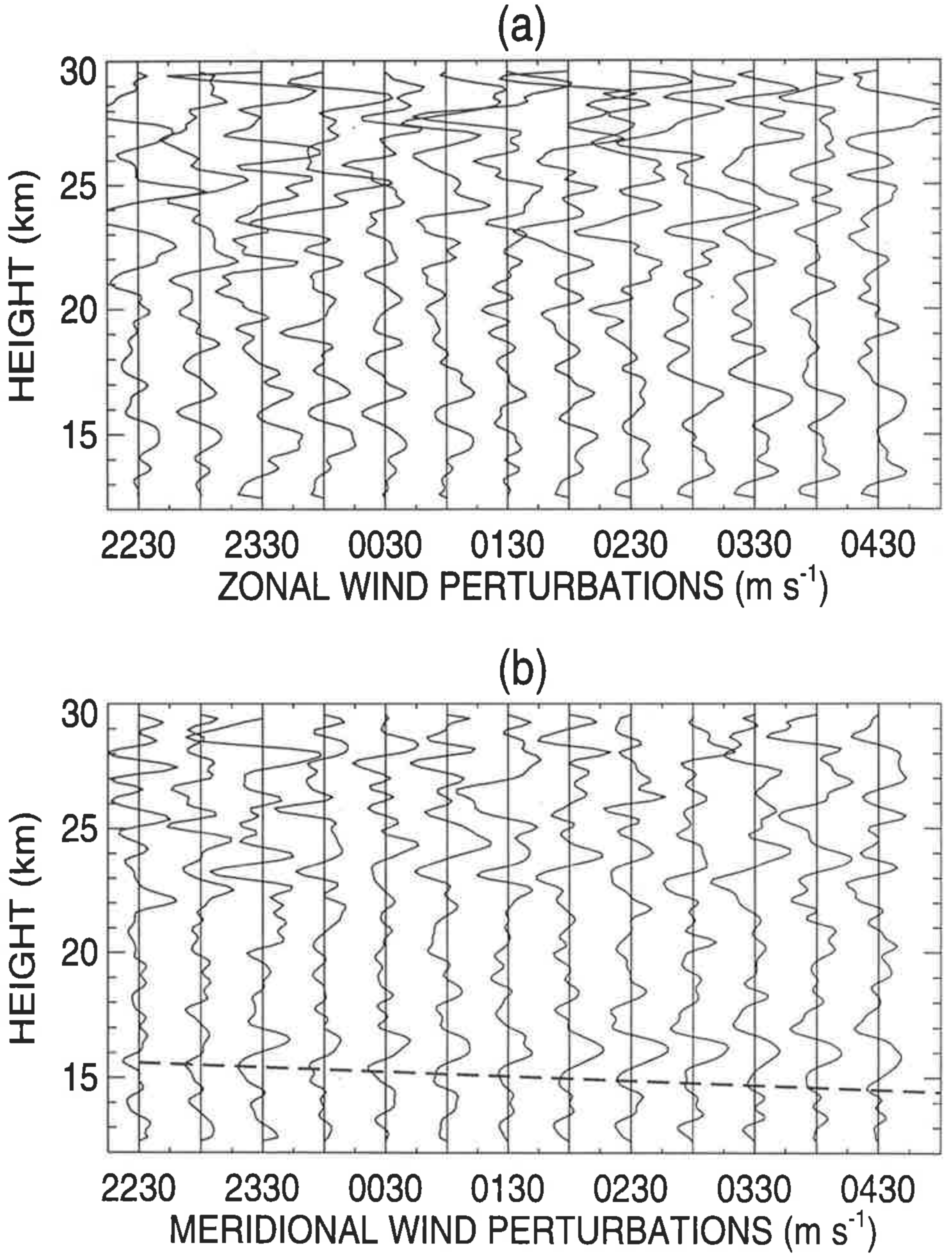

Figure 2. Rayleigh Doppler wind lidar profiles from 2230 LT on 23 October, 1995 to 0500 LT on 24 October, 1995. The zero point of each profile is labeled with the starting time of its 30 min observational integration. Successive profiles are offset by 10 m/s.

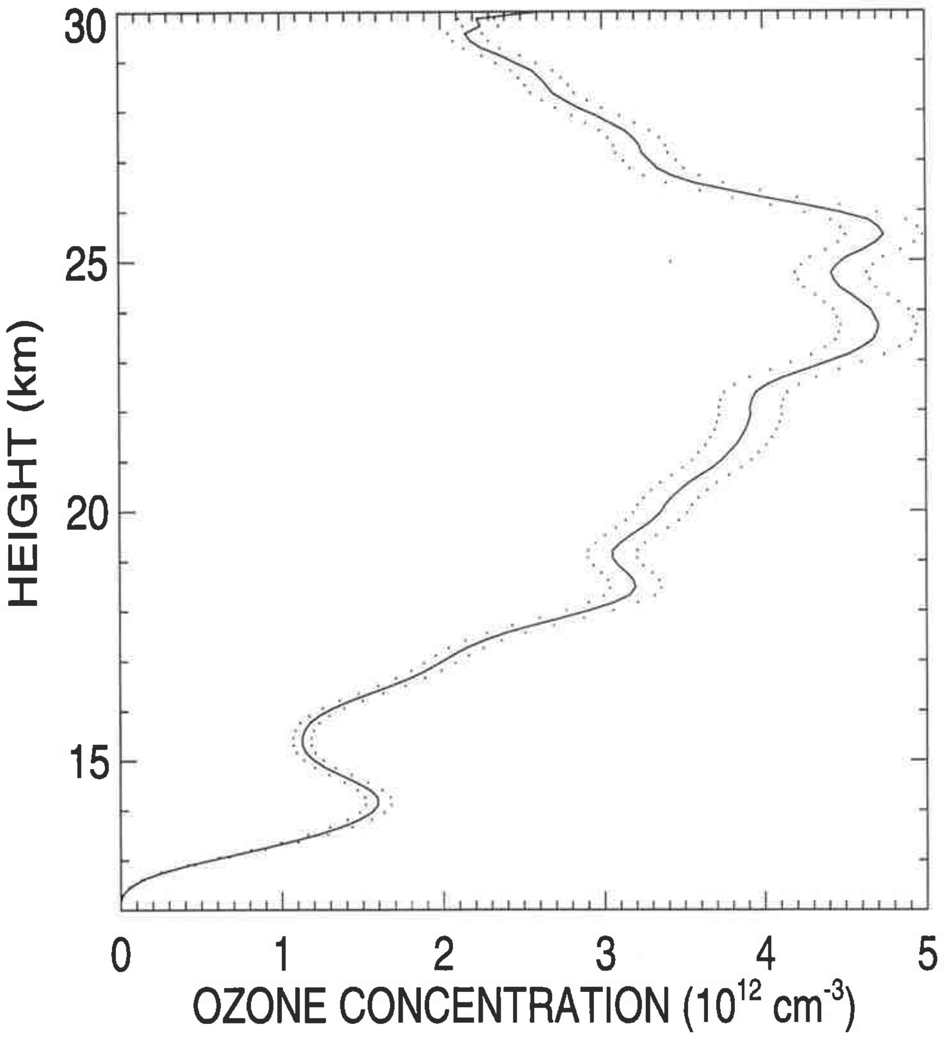

Figure 3. Average vertical profile of ozone concentration. A 5% error estimate is indicated by the dotted line.

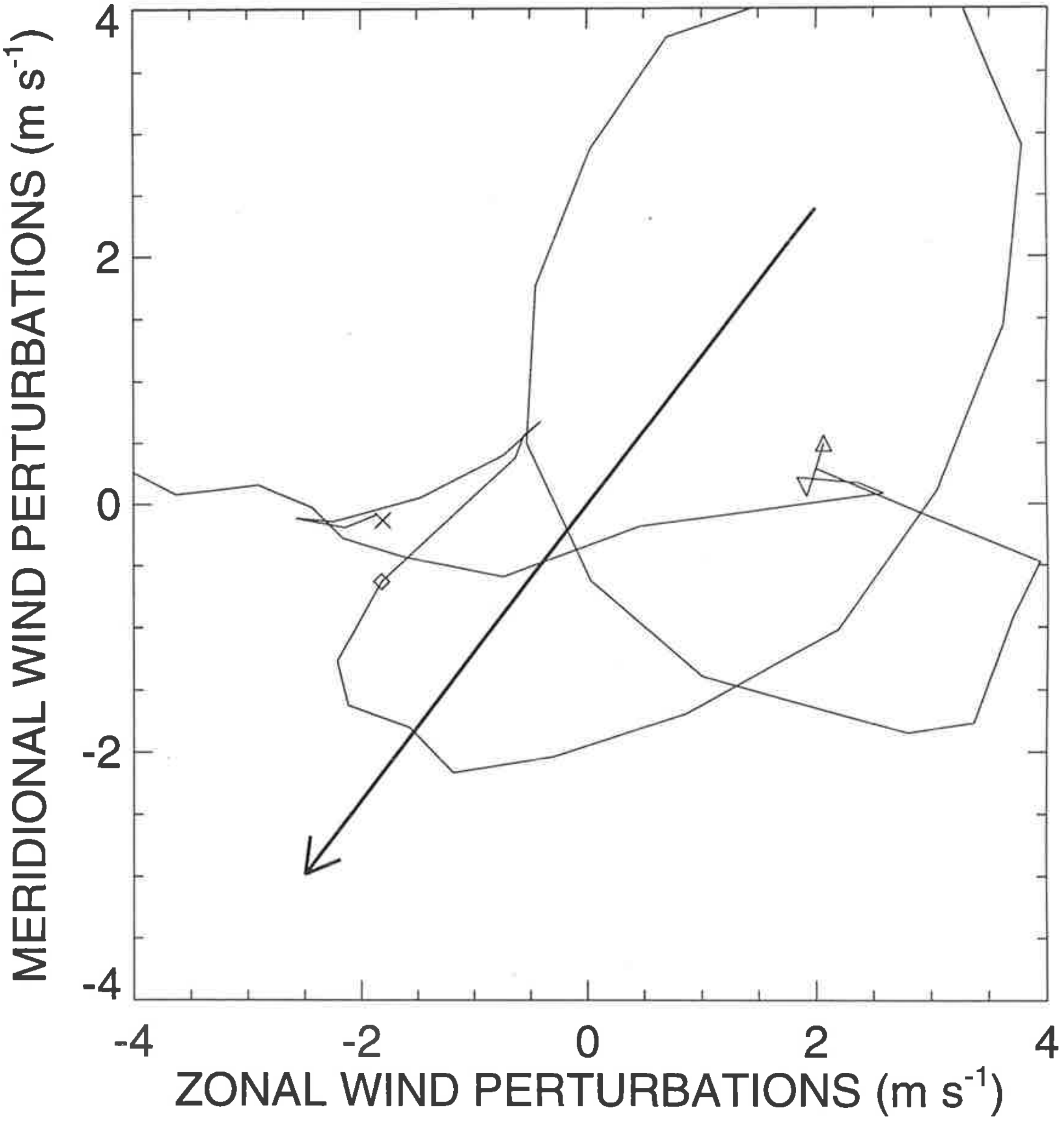

Figure 4. Hodograph between 12-20 km of 6.5 hr average zonal and meridional wind fluctuations smoothed over 600 m. The bold line indicates the major axis of the gravity-wave ellipse as determined from a Stokes parameter analysis. The triangle marks the 14 km level, the diamond marks 18 km, and the cross indicates the upper height limit (20 km).

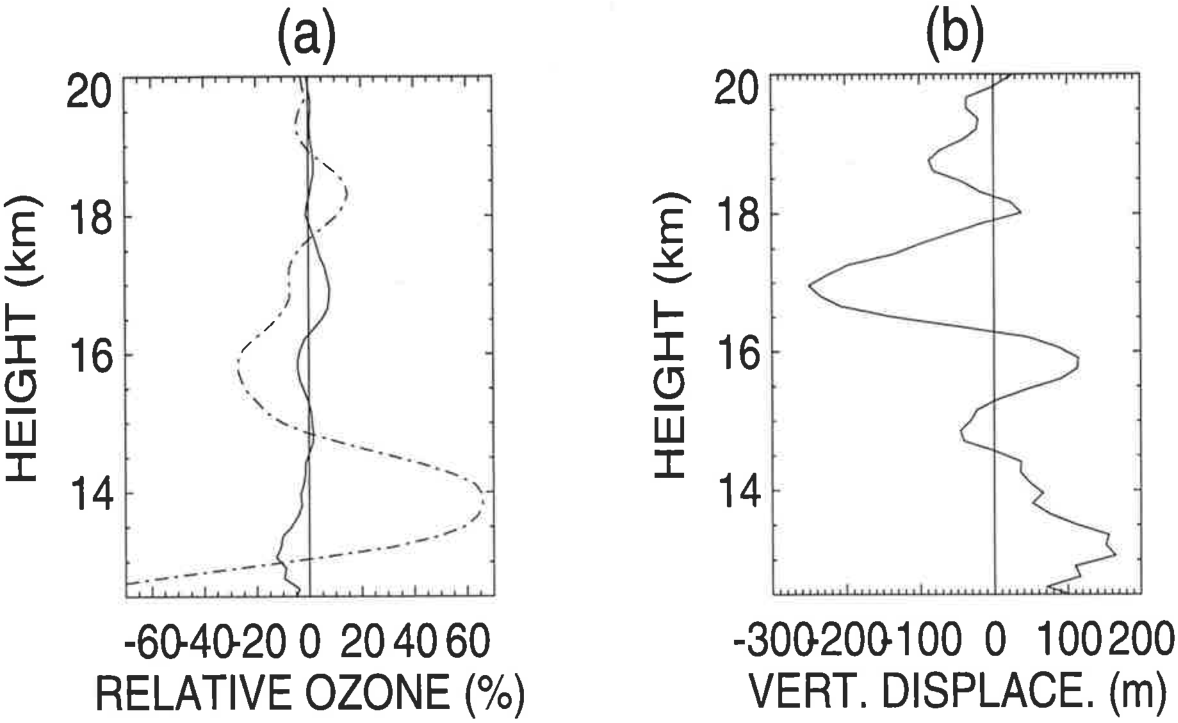

Figure 5. Measured relative perturbation of ozone concentration as determined by subtracting a cubic polynomial mean profile is shown with a dotted-dashed curve in panel (a). A calculated response from the IGW in Figure 4 using (1) and (2) is shown with the solid curve in panels (a) and (b), respectively.

Appendix C

Hodograph analysis and Stokes parameters

A hodograph analysis of atmospheric wind velocities consists of plotting the detrended zonal velocities $u'(z)$ against the detrended meridional velocities $v'(z)$. The hodograph traces out the tip of the vector ($u'(z)$,$v'(z)$) and hence represents a plan view of the horizontal velocity variation. An idealized hodograph, due to a single monochromatic gravity wave component, takes the form of a conic section. The most common form is an elliptically polarized hodograph as illustrated in Figure C.1. Chapter 5 presented examples of an average hodograph (Figure 5.10), as well as a time-resolved sequence of hodographs (Figure 5.11).

From a hodograph it is possible to calculate the so-called Stokes parameters. The Stokes parameter method is one of several techniques developed to estimate properties of gravity wave perturbations in wind velocity [*Eckermann*,1996]. These parameters derive from optical theory [*e.g. Jenkins and White*,1966] and were originally used in the analysis of the direction of polarization of light.

The parameters are defined as [*Eckermann and Vincent*,1989; *Eckermann*,1996]:

$$I(m) = < U_R(m)^2 > + < U_I(m)^2 > + < V_R(m)^2 > + < V_I(m)^2 > \tag{C.1}$$

$$D(m) = < U_R(m)^2 > + < U_I(m)^2 > - < V_R(m)^2 > - < V_I(m)^2 > \tag{C.2}$$

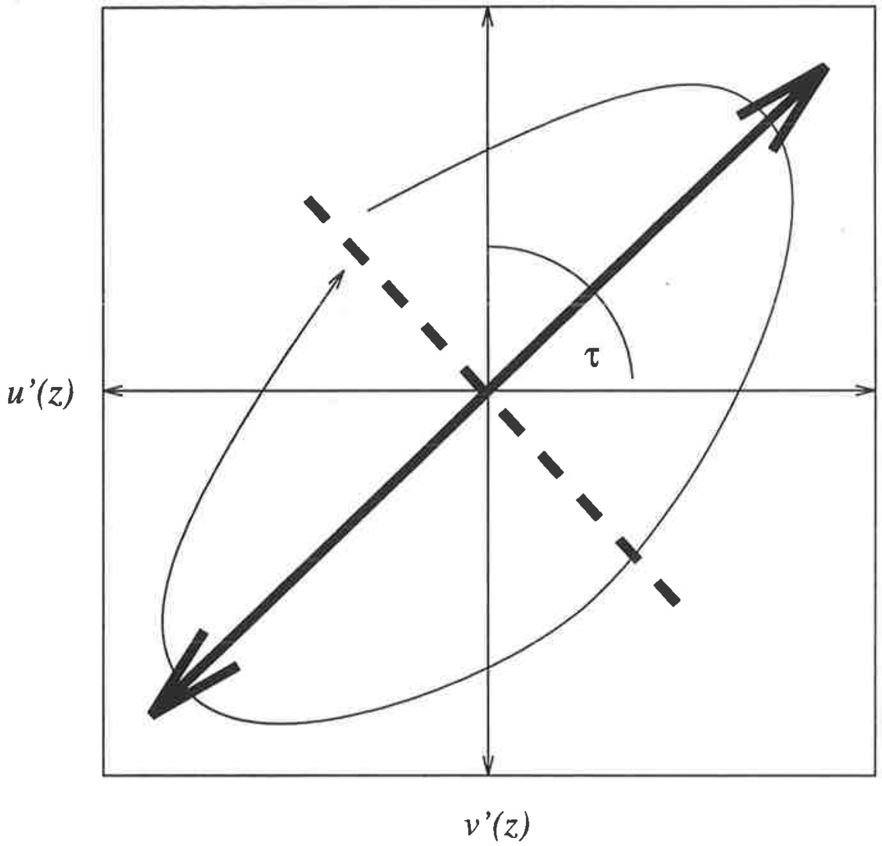

Figure C.1: Schematic diagram of an idealized hodograph signature.

$$P(m) = 2(< U_R(m)V_R(m) > + < U_I(m)V_I(m) > \tag{C.3}$$

$$Q(m) = 2(< U_R(m)V_I(m) > - < U_I(m)V_R(m) > \tag{C.4}$$

where $U_R(m) + iU_I(m)$ and $V_R(m) + iV_I(m)$ are the FFTs of $u'(z)$ and $v'(z)$, respectively, and the angle brackets denote a time average.

The gravity wave properties calculated from the Stokes parameters are as follows:

$$\text{Phase difference} \quad \delta = \arctan\left(\frac{Q(m)}{P(m)}\right), \tag{C.5}$$

$$\text{Ellipse major axis orientation} \quad \tau = \arctan\left(\frac{P(m)}{D(m)}\right), \tag{C.6}$$

$$\text{Degree of polarization} \quad d = \frac{\sqrt{D(m)^2 + P(m)^2 + Q(m)^2}}{I(m)}, \tag{C.7}$$

$$\text{Gravity wave ellipse axial ratio} \quad \mathrm{AR} = \frac{\hat{\omega}}{f} = \cot\ \xi, \tag{C.8}$$

where

$$\xi = \frac{1}{2}\arcsin\left(\frac{Q(m)}{dI(m)}\right). \tag{C.9}$$

Appendix D

Further ER-2/sonde Comparisons

This appendix is included as an extension to Section 4.4. For each flight date, plots are displayed of potential temperature–ozone surfaces (upper panel) and of estimated meridional ozone mixing ratio gradients (lower panel).

For the plots of potential temperature–ozone surfaces, the dashed line indicates the ozonesonde measurement and the dotted region indicates the ER-2 values measured in the vicinity of Macquarie Island. The crosses indicate the values of (θ,O_3) at the estimated positions of the ER-2 aircraft's closest approach to Macquarie Island.

For the plots of estimated meridional ozone mixing ratio gradients, the bold line indicates the value of meridional ozone mixing ratio gradient calculated from sonde data. Symbols represent gradients calculated over different ER-2 aircraft horizontal flight path lengths: cross - 800 km, square - 400 km, triangle - 200 km, diamond - 100 km.

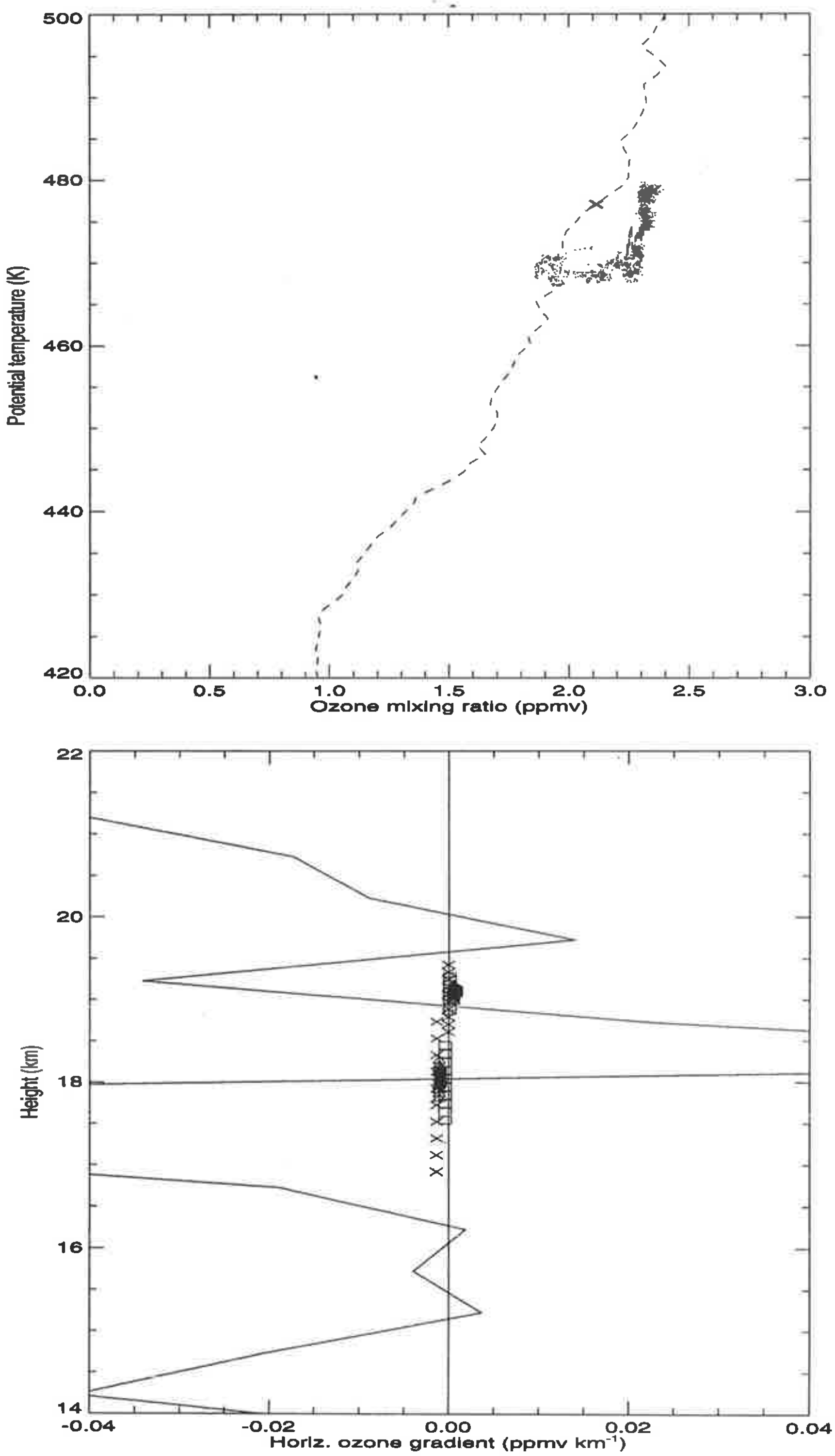

Figure D.1: 13 April 1994.

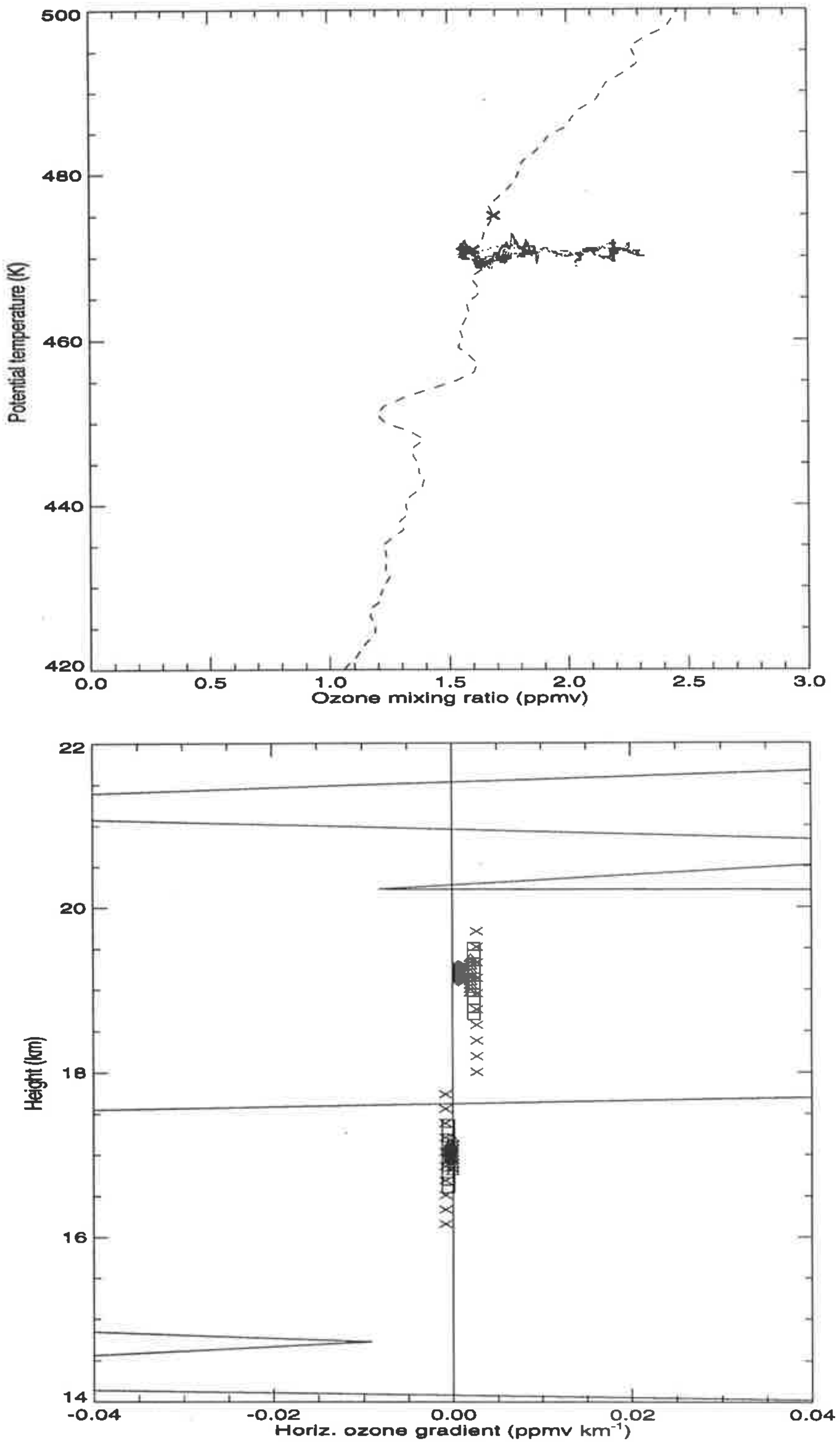

Figure D.2: 24 May 1994.

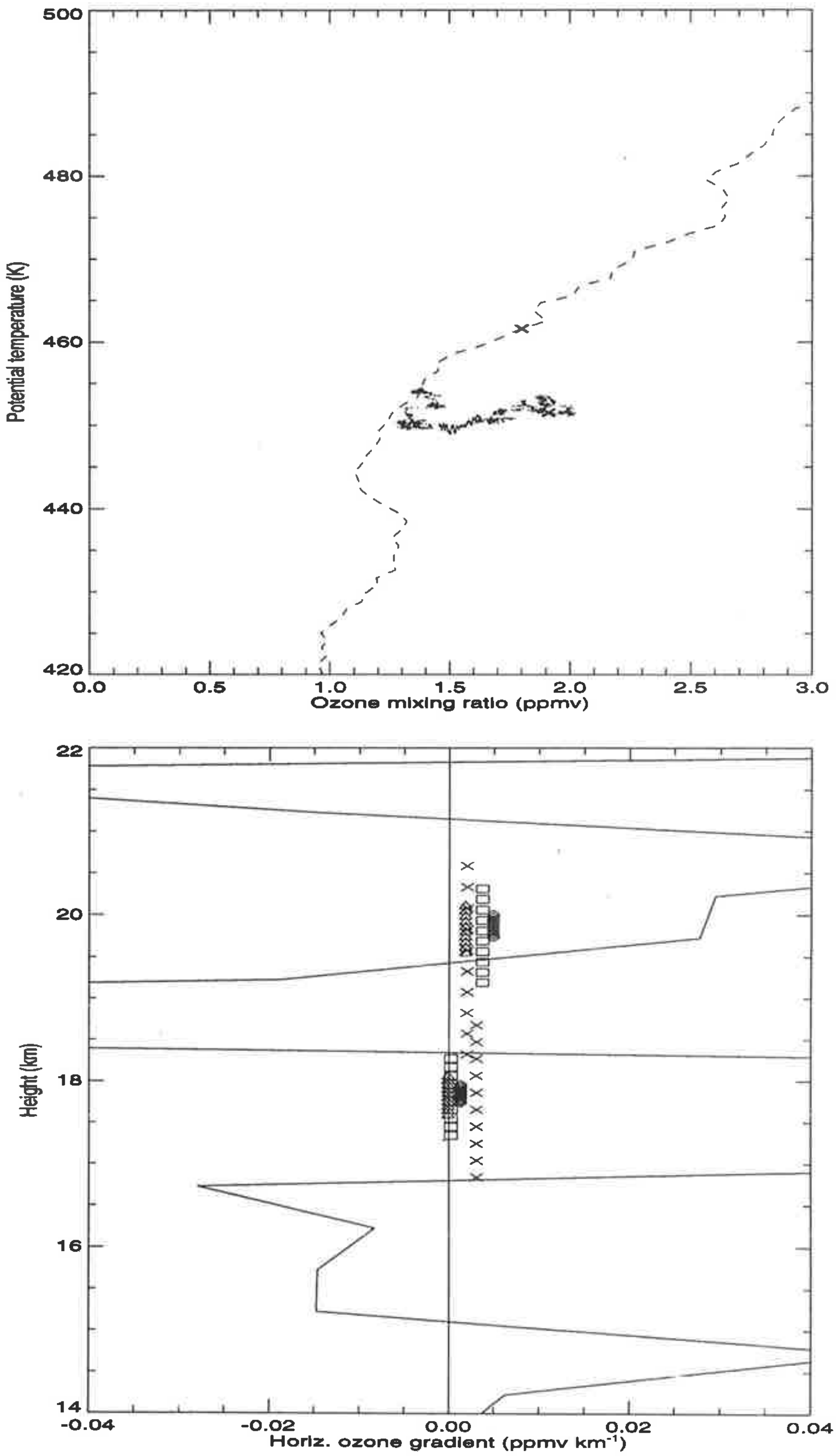

Figure D.3: 3 June 1994.

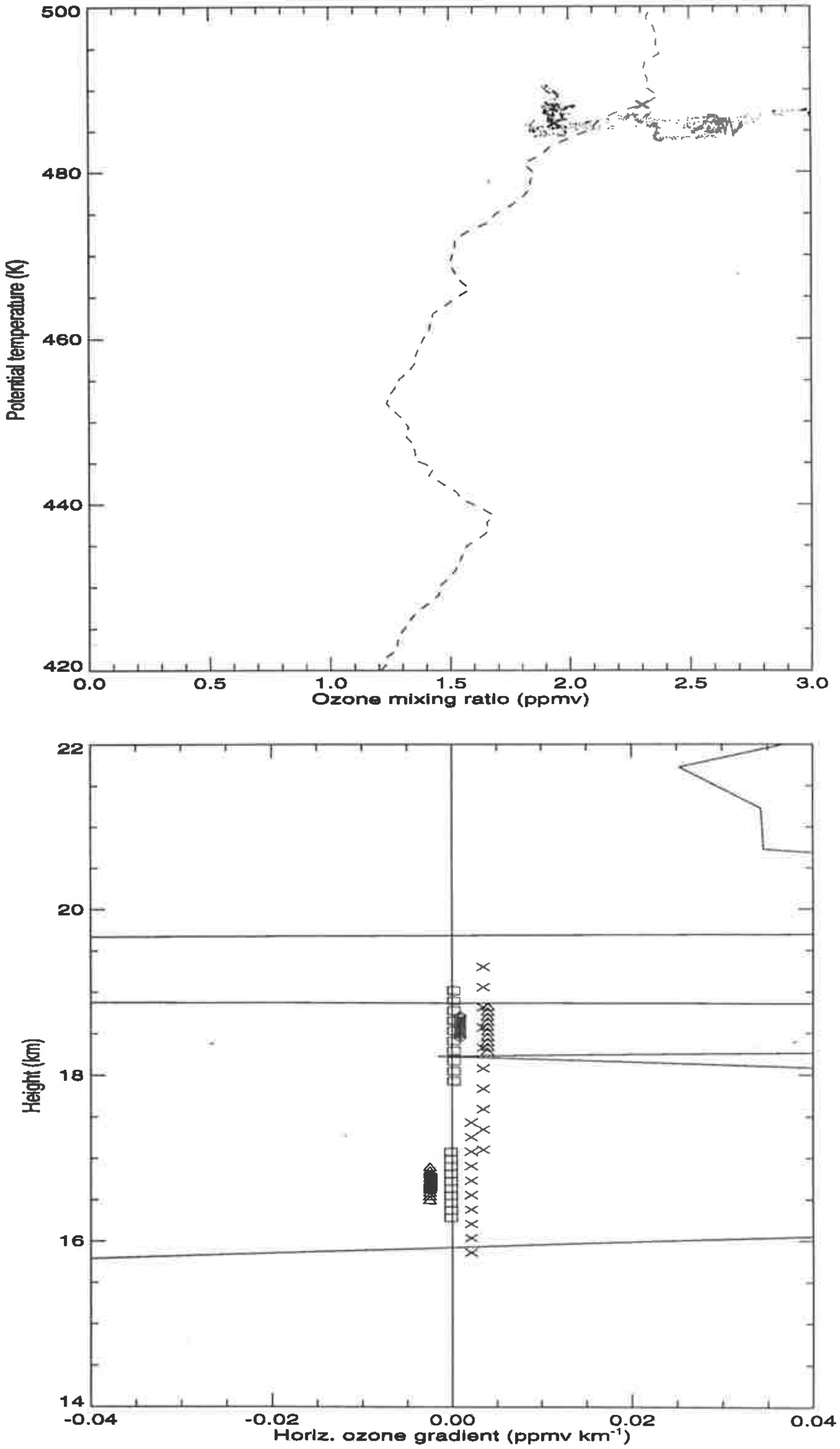

Figure D.4: 10 October 1994.

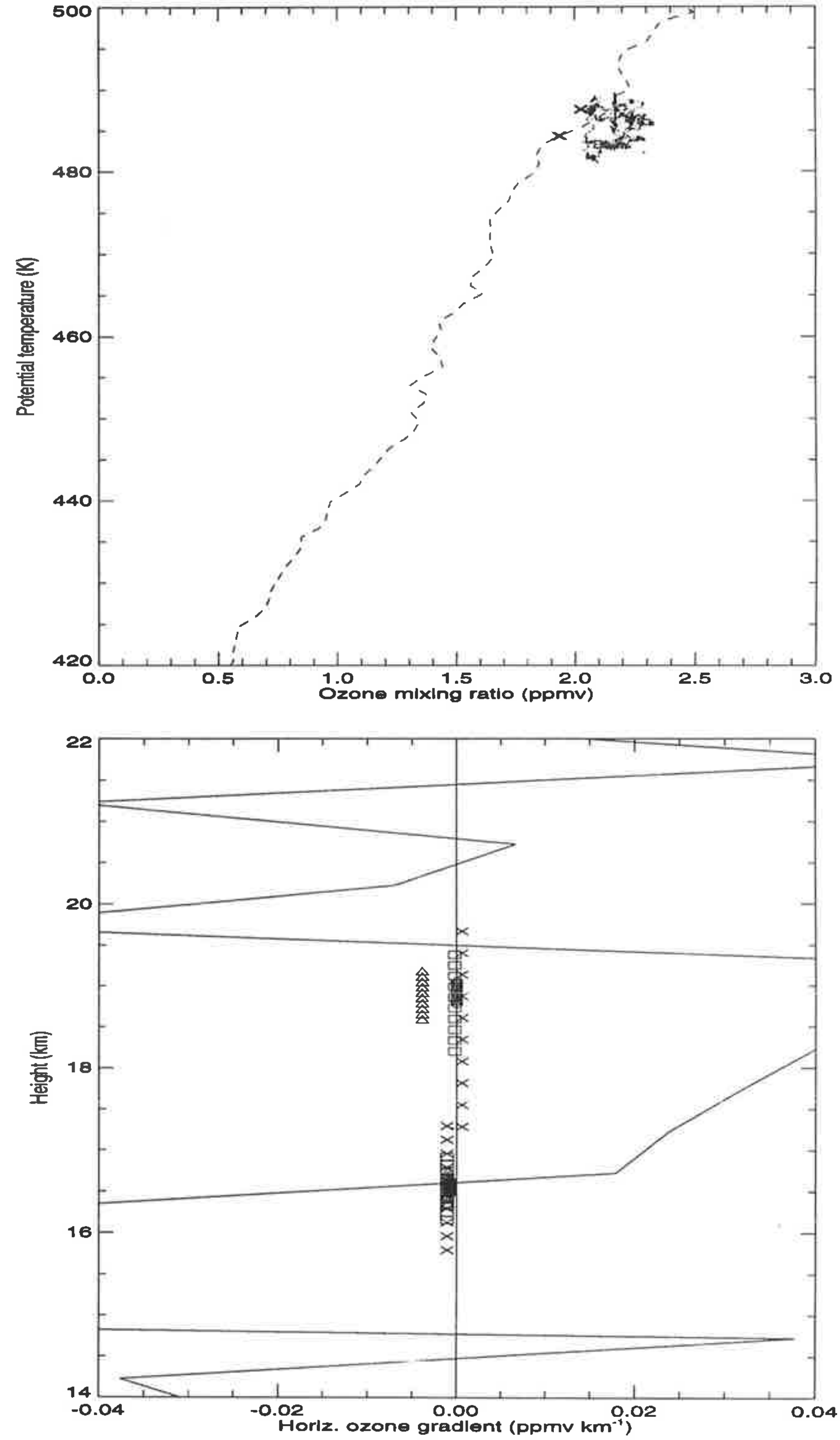

Figure D.5: 13 October 1994.

References

Alexander, M. J., Holton, J. R. and Durran, D. R. (1995), 'The gravity wave response above deep convection in a squall line simulation', *J. Atmos. Sci.* **52**, 2212–2226.

Allen, S. J. (1996), Gravity wave motions in the troposphere and lower stratosphere, PhD thesis, University of Adelaide, Adel., Australia.

Allen, S. J. and Vincent, R. A. (1995), 'Gravity–wave activity in the lower atmosphere: Seasonal and latitudinal variations', *J. Geophys. Res.* **100**, 1327–1350.

Andrews, D. G., Holton, J. R. and Leovy, C. B. (1987), *Middle Atmosphere Dynamics*, Academic Press, Orlando, Florida.

Bacmeister, J. T. and Eckermann, S. D. (1997), 'Mesoscale cooling rates and temperature fluctuations in the stratosphere induced by a spectrum of gravity waves', *J. Geophys. Res.* . in press.

Bacmeister, J. T., Eckermann, S. D., Newman, P. A., Lait, L., Chan, K. R., Loewenstein, M., Profitt, M. H. and Gary, B. L. (1996), 'Stratospheric horizontal wavenumber spectra of winds, potential temperature and atmospheric tracers observed by high–altitude aircraft', *J. Geophys. Res.* **101**, 9441–9470.

Bacmeister, J. T. and Schoeberl, M. R. (1989), 'Breakdown of vertically propagating two-dimensional gravity waves forced by orography', *J. Atmos. Sci.* **46**, 2109–2134.

Bacmeister, J. T., Schoeberl, M. R., Lait, L. R., Newman, P. A. and Gary, B. (1990), 'ER-2 mountain wave encounter over Antarctica: Evidence for blocking', *Geophys. Res. Lett.* **17**, 81–84.

Batista, P. P., Clemesha, B. R., Batista, I. S. and Simonich, D. M. (1989), 'Characteristics of the sporadic sodium layers observed at 23°S', *J. Geophys. Res.* **94**, 15,349–15,358.

Beatty, T. J., Collins, R. L., Gardner, C. S., Hostetler, C. A., Sechrist, C. F. and Tepley, C. C. (1989), 'Simultaneous radar and lidar observations of sporadic E and Na layers at Arecibo', *Geophys. Res. Lett.* **16**, 1019–1022.

Beatty, T. J. and Gardner, C. S. (1990), Lidar observations of gravity waves and their spectra near the mesopause and stratopause at Arecibo, Technical Report EOSL

90-002, Dep. of Electr. and Comput. Eng., Univ. of Ill. at Urbana-Champaign, Urbana.

Beatty, T. J., Hostetler, C. A. and Gardner, C. S. (1992), 'Lidar observations of gravity waves and their spectra near the mesopause and stratopause at Arecibo', *J. Atmos. Sci.* **49**, 477–496.

Blake, D. and Lindzen, R. S. (1973), 'Effect of photochemical models on calculated equilibria and cooling rates in the stratosphere', *Monthly Weather Review* **101**, 783–802.

Blamont, J. E. and de Jager, C. (1962), 'Upper atmospheric turbulence determined by means of rockets', *J. Geophys. Res.* **67**, 3113–3119.

Blix, T. A., Thrane, E. V., Fritts, D. C., von Zahn, U., Lübken, F. J. L., Hillert, W., Blood, S. P., Mitchell, J. D., Kokin, G. A. and Pakhomov, S. V. (1990), 'Small-scale structure observed *in-situ* during MAC/EPSILON', *J. Atmos. Terr. Phys.* **52**, 835–854.

Brasseur, G. and Solomon, S. (1984), *Aeronomy of the middle atmosphere*, D. Reidel Publishing Company.

Cervera, M. A. and Reid, I. M. (1995), 'Comparison of simultaneous wind measurements using colocated VHF meteor radar and MF spaced antenna radar systems', *Radio Science* **30**, 1245–1261.

Chan, K. R., Scott, S. G., Bowen, S. W., Gaines, S. E., Danielsen, E. F. and Pfister, L. (1991), 'Horizontal wind fluctuations in the stratosphere by internal waves of short vertical wavelength', *J. Geophys. Res.* **96**, 17,425–17,432.

Chanin, M.-L., Garnier, A., Hauchecorne, A. and Porteneuve, J. (1989), 'A Doppler lidar for measuring winds in the middle atmosphere', *Geophys. Res. Lett.* **16**, 1273–1276.

Chanin, M.-L. and Hauchecorne, A. (1981), 'Lidar observation of gravity and tidal waves in the stratosphere and mesosphere', *J. Geophys. Res.* **86**, 9715–9721.

Chanin, M.-L. and Hauchecorne, A. (1987), Lidar sounding of the structure and dynamics of the middle atmosphere: A review of recent results relevant to transport processes, *in* G. Visconti and R. Garcia, eds, 'Transport Processes in the Middle Atmosphere', Reidel, Dordrecht, pp. 459–477.

Chapman, S. (1930), 'A theory of upper atmospheric ozone', *Mem. Roy. Meteor. Soc.* **3**, 103.

Chiu, Y. T. and Ching, B. K. (1978), 'The response of atmospheric and lower ionospheric layer structures to gravity waves', *Geophys. Res. Lett.* **5**, 539–542.

Clancy, R. T. and Rusch, D. W. (1990), 'Solar Mesosphere Explorer temperature climatology of the mesosphere as compared to the CIRA model', *Adv. Space Res.* **10**, 187–206.

Clemesha, B. R., Batista, P. P. and Simonich, D. M. (1996), 'Formation of sporadic sodium layers', *J. Geophys. Res.* **101**, 19,701–19,706.

Clemesha, B. R., Kirchhoff, V. W. J. H., Simonich, D. M. and Takahashi, H. (1978), 'Evidence of an extraterrestrial source for the mesospheric sodium layer', *Geophys. Res. Lett.* **5**, 873–876.

Clemesha, B. R., Kirchhoff, V. W. J. H., Simonich, D. M., Takahashi, H. and Batista, P. P. (1980), 'Spaced lidar and nightglow observations of an atmospheric sodium enhancement', *J. Geophys. Res.* **85**, 3480–3489.

Collins, R. L., Nomura, A. and Gardner, C. S. (1994), 'Gravity waves in the upper mesosphere over Antarctica: Lidar observations at the South Pole and Syowa', *J. Geophys. Res.* **99**, 5475–5485.

Collins, R. L., Tao, X. and Gardner, C. S. (1996), 'Gravity wave activity in the upper mesosphere over Urbana, Illinois: Lidar observations and analysis of gravity wave propagation models', *J. Atmos. Terr. Phys.* **58**, 1905–1926.

COSPAR (1986), *Cospar international reference atmosphere: 1986. Part II: Middle atmosphere models*, Pergamon Press.

Cot, C. and Barat, J. (1986), 'Wave–turbulence interaction in the stratosphere', *J. Geophys. Res.* **91**, 2749–2756.

Cox, R. M., Plane, J. M. C. and Green, J. S. A. (1993), 'A modelling investigation of sudden sodium layers', *Geophys. Res. Lett.* **2**, 2841–2844.

Craig, R. A. (1950), 'The observations and photochemistry of atmospheric ozone and their meteorological significance', *Meteorological Monographs* **1**(2), 2–41.

Danielsen, E. F., Hipskind, R. S., Starr, W. L., Vedder, J. F., Gaines, S. E., Kley, D. and Kelly, K. K. (1991), 'Irreversible transport in the stratosphere by internal waves of short vertical wavelength', *J. Geophys. Res.* **96**, 17,433–17,452.

Desaubies, Y. J. F. (1976), 'Analytical representation of internal wave spectra', *J. Phys. Oceanogr.* **11**, 541–556.

Dewan, E. M. and Good, R. E. (1986), 'Saturation and the "universal" spectrum for vertical profiles of horizontal scalar winds in the atmosphere', *J. Geophys. Res.* **91**, 2742–2748.

Dobson, G. M. (1930), 'Observations of the amount of ozone in the earth's atmosphere and its relation to other geophysical conditions, Part IV', *Proc. Roy. Soc. Lond. A* **129**, 411–433.

Dobson, G. M. (1973), 'The laminated structure of ozone in the atmosphere', *Q. J. R. Meteorol. Soc.* **99**, 599–607.

Donovan, D. P., Bird, J. C., Whiteway, J. A., Duck, T. J., Pal, S. R. and Carswell, A. I. (1995), 'Lidar observations of stratospheric ozone and aerosol above the Canadian high arctic during the 1994-95 winter', *Geophys. Res. Lett.* **22**, 3489–3492.

Dudis, J. J. and Reber, C. A. (1976), 'Composition effects in thermospheric gravity waves', *Geophys. Res. Lett.* **3**, 727–730.

Eckermann, S. D. (1995), 'Effect of background winds on vertical wavenumber spectra of atmospheric gravity waves', *J. Geophys. Res.* **100**, 14,097–14,112.

Eckermann, S. D. (1996), 'Hodographic analysis of gravity waves: Relationships among Stokes parameters, rotary spectra, and cross-spectral analysis', *J. Geophys. Res.* **101**, 19,169–19,174.

Eckermann, S. D., Hirota, I. and Hocking, W. K. (1995), 'Gravity wave and equatorial wave morphology of the stratosphere derived from long-term rocket soundings', *Q. J. R. Meteorol. Soc.* **121**, 149–186.

Eckermann, S. D. and Hocking, W. K. (1989), 'Effect of superposition on measurements of atmospheric gravity waves: A cautionary note and some reinterpretations', *J. Geophys. Res.* **94**, 6333–6339.

Eckermann, S. D. and Marks, C. J. (1996), 'An idealized ray model of gravity wave–tidal interactions', *J. Geophys. Res.* **101**, 21,195–21,212.

Eckermann, S. D. and Vincent, R. A. (1989), 'Falling sphere observations of anisotropic gravity wave motions in the upper stratosphere over Australia', *Pure and Appl. Geophys.* **130**, 509–532.

Ehhalt, D. G., Roth, E. P. and Schmidt, U. (1983), 'On the temporal variance of stratospheric gas concentrations', *J. Atmos. Chem.* **1**, 27–51.

Farman, J. C., Gardiner, B. G. and Shanklin, J. D. (1985), 'Large losses of total ozone in Antarctica reveal seasonal ClO_x/NO_x interaction', *Nature* **315**, 207–210.

Forbes, J. M. and Vial, F. (1989), 'Monthly simulations of the solar semi-diurnal tide in the mesosphere and lower thermosphere', *J. Atmos. Terr. Phys.* **51**, 649–661.

Fritts, D. C. and Isler, J. R. (1992), 'First observations of mesospheric dynamics with a partial reflection radar in Hawaii (22° N, 160° W)', *Geophys. Res. Lett.* **19**, 409–412.

Fritts, D. C., Isler, J. R., Thomas, G. E. and Andreassen, O. (1993), 'Wave breaking signatures in noctilucent clouds', *Geophys. Res. Lett.* **20**, 2039–2042.

Fritts, D. C. and Lu, W. (1993), 'Spectral estimates of gravity wave energy and momentum fluxes. Part II: parameterization of wave forcing and variability', *J. Atmos. Sci.* **50**, 3695–3713.

Fritts, D. C. and Luo, Z. (1995), 'Dynamical and radiative forcing of the summer mesopause circulation and thermal structure 1. Mean solstice conditions', *J. Geophys. Res.* **100**, 3119–3128.

Fritts, D. C. and VanZandt, T. E. (1993), 'Spectral estimates of gravity wave energy and momentum fluxes, I, energy dissipation, acceleration, and constraints', *J. Atmos. Sci.* **50**, 3685–3694.

Fritts, D. C. and Vincent, R. A. (1987), 'Mesospheric momentum flux studies at Adelaide, Australia: Observations and a gravity wave–tidal interaction model', *J. Atmos. Sci.* **44**, 605–619.

Fukao, S., Maekawa, Y., Sato, T. and Kato, S. (1985), 'Fine structure in mesospheric wind fluctuations observed by the Arecibo UHF Doppler radar', *J. Geophys. Res.* **90**, 7547–7556.

Gage, K. S. (1979), 'Evidence for a $k^{5/3}$ power law inertial range in mesoscale two-dimensional turbulence', *J. Atmos. Sci.* **36**, 1950–1954.

Gage, K. S. and Nastrom, G. D. (1986), 'Spectrum of atmospheric vertical displacements and spectrum of conservative scalar passive additives due to quasi-horizontal atmospheric motions', *J. Geophys. Res.* **91**, 13,211–13,216.

Garcia, R. R. and Solomon, S. (1985), 'The effect of breaking gravity waves on the dynamics and chemical composition of the mesosphere and lower thermosphere', *J. Geophys. Res.* **90**, 3850–3868.

Garcia, R. R. and Solomon, S. (1987), 'A possible relationship between interannual variability in Antarctic ozone and the quasi-biennial oscillation', *Geophys. Res. Lett.* **14**, 848–851.

Gardner, C. S. (1994), 'Diffusive filtering theory of gravity wave spectra in the atmosphere', *J. Geophys. Res.* **99**, 20,601–20,622.

Gardner, C. S. (1996*a*), Gravity wave processes and their parameterisation in Global Climate Models: A NATO Advanced Research Workshop, Santa Fe, USA, *in* K. Hamilton, ed., 'SPARC newsletter, July 1996', SPARC, p. 19.

Gardner, C. S. (1996*b*), 'Testing theories of atmospheric gravity wave saturation and dissipation', *J. Atmos. Terr. Phys.* **58**, 1575–1589.

Gardner, C. S., Kane, T. J., Senft, D. C., Qian, J. and Papen, G. C. (1993), 'Simultaneous observations of sporadic E, Na, Fe, and Ca+ layers at Urbana, Illinois: Three case studies', *J. Geophys. Res.* **98**, 16,865–16,873.

Gardner, C. S. and Shelton, J. D. (1985), 'Density response of neutral atmospheric layers to gravity wave perturbations', *J. Geophys. Res.* **90**, 1745–1754.

Gardner, C. S., Tao, X. and Papen, G. C. (1995), 'Observations of strong wind shears and temperature enhancements during several sporadic Na events above Haleakala', *Geophys. Res. Lett.* **22**, 2809–2812.

Gardner, C. S. and Voelz, D. G. (1987), 'Lidar studies of the nighttime sodium layer over Urbana, Illinois, 2, Gravity waves', *J. Geophys. Res.* **92**, 4673–4694.

Garnier, A. and Chanin, M. L. (1992), 'Description of a Doppler Rayleigh LIDAR for measuring winds in the middle atmosphere', *App. Phys. B* **55**, 35–40.

Gavrilov, N. M. and Shved, G. M. (1982), 'Study of internal gravity waves in the lower thermosphere from observations of the nocturnal sky airglow [O1] 5577 A in Ashkhabad', *Ann. Geophys.* **38**, 789–803.

Gibson-Wilde, D. E., Reid, I. M., Eckermann, S. D. and Vincent, R. A. (1996), 'Simulation of lidar measurements of gravity waves in the mesosphere', *J. Geophys. Res.* **101**, 9509–9525.

Gibson-Wilde, D. E., Vincent, R. A., Souprayen, C., Godin, S., Hertzog, A. and Eckermann, S. D. (1997), 'Dual lidar observations of mesoscale fluctuations of ozone and horizontal winds', *Geophys. Res. Lett.* . in press.

Godin, S. (1984), Etude experimentale par teledetection laser et modelisation de la distribution verticale d'ozone dans la haute stratosphere, PhD thesis, Université Pierre et Marie Curie, France.

Gossard, E. E. and Hooke, W. H. (1975), *Waves in the atmosphere*, Elsevier scientific publishing company.

Götz, F. W., Meetham, A. R. and Dobson, G. M. (1934), 'The vertical distribution of ozone in the atmosphere', *Proc. Roy. Soc. Lond. A* **145**, 416–446.

Granier, C., Jegou, J. P. and Megie, G. (1985), 'Resonant lidar detection of Ca and Ca+ in the upper atmosphere', *Geophys. Res. Lett.* **12**, 655–658.

Griffiths, M. and Reeder, M. J. (1996), 'Stratospheric inertia-gravity waves generated in a numerical model of frontogenesis Part II. Wave sources and generation mechanisms', *Q. J. R. Meteorol. Soc.* **122**, 1175–1195.

Guest, F. M., Reeder, M. J., Karoly, D. J. and Marks, C. J. (1996), Analyses of stratospheric gravity waves over Macquarie Island, *in* 'Proceedings of the 1st SPARC General Assembly', SPARC, Cooperative Centre for Southern Hemisphere Meteorology. in press.

Hagan, M. E., Forbes, J. M. and Vial, F. (1995), 'On modeling migrating solar tides', *Geophys. Res. Lett.* **22**, 893–896.

Hamilton, K. (1991), 'Climatological statistics of stratospheric inertia-gravity waves deduced from historical rocketsonde wind and temperature data', *J. Geophys. Res.* **96**, 20,831–20,839.

Hansen, G. and von Zahn, U. (1990), 'Sudden sodium layers in polar latitudes', *J. Atmos. Terr. Phys.* **52**, 585–608.

Harris, T. J. (1994), 'A long–term study of the quasi–two–day wave in the middle atmosphere', *J. Atmos. Terr. Phys.* **56**, 569–580.

Hartmann, D. L. and Garcia, R. R. (1979), 'A mechanistic model of ozone transport by planetary waves in the stratosphere', *J. Atmos. Sci.* **36**, 350–364.

Hecht, J. H., Ramsay-Howat, S. K. and Walterscheid, R. L. (1996a), 'Results from airglow observations duing ALOHA-93', *EOS, Transactions* **77**, 101.

Hecht, J. H., Walterscheid, R. L., Fritts, D. C., Isler, J. R., Senft, D. C., Gardner, C. S. and Franke, S. J. (1996b), 'Wave breaking signatures in OH airglow an sodium densities and temperatures, Part I: Airglow imaging, Na lidar, and MF radar observations', *J. Geophys. Res.* **101**. in press.

Hecht, J. H., Walterscheid, R. L. and Ross, M. N. (1994), 'First measurements of the two–dimensional horizontal wave number spectrum from CCD images of the nightglow', *J. Geophys. Res.* **99**, 11,449–11,460.

Helmer, M. and Plane, J. M. C. (1993), 'A study of the reaction Na O_2+O → NaO + O_2: Implications for the chemistry of sodium in the upper atmosphere', *J. Geophys. Res.* **98**, 23,207–23,222.

Hess, P. G. and O'Sullivan, D. (1995), 'A three-dimensional modeling study of the extratropical quasi-biennial oscillation in ozone', *J. Atmos. Sci.* **52**, 1539–1554.

Hines, C. O. (1960), 'Internal atmospheric gravity waves at ionospheric heights', *Can. J. Phys.* **38**, 1441–1481.

Hines, C. O. (1991*a*), 'The saturation of gravity waves in the middle atmosphere, I, Critique of linear-instability theory', *J. Atmos. Sci.* **48**, 1348–1359.

Hines, C. O. (1991*b*), 'The saturation of gravity waves in the middle atmosphere, II, Development of Doppler-spread theory', *J. Atmos. Sci.* **48**, 1360–1379.

Hines, C. O. (1993), 'Pseudosaturation of gravity waves in the middle atmosphere: an interpretation of certain lidar observations', *J. Atmos. Terr. Phys.* **55**, 441–445.

Hines, C. O. (1995), 'Comments on 'Observations of low-frequency inertia-gravity waves in the lower stratosphere over Arecibo', *J. Atmos. Sci.* **52**, 607–610.

Hines, C. O. (1997a), 'Doppler-spread parameterization of gravity-wave momentum deposition in the middle atmosphere. part 1: basic formulation', *J. Atmos. Terr. Phys.* **59**, 371–386.

Hines, C. O. (1997b), 'Doppler-spread parameterization of gravity-wave momentum deposition in the middle atmosphere. part 2: broad and quasi monochromatic spectra, and implementation', *J. Atmos. Terr. Phys.* **59**, 387–400.

Hines, C. O. and Tarasick, D. W. (1987), 'On the detection and utilization of gravity waves in airglow studies', *P. S. S.* **35**, 851–866.

Hocking, W. K. (1987), 'Radar studies of small scale structure in the upper middle atmosphere and lower ionosphere', *Adv. Space Res.* **7**(10), 327–338.

Hofmann, D. J., Harder, J. W., Rosen, J. M., Hereford, J. V. and Carpenter, J. R. (1989), 'Ozone profile measurements at McMurdo Station, Antarctica, during the spring of 1987', *J. Geophys. Res.* **94**, 16,527–16,536.

Hofmann, D. J., Oltmans, S. J., Johnson, B. J., Lathrop, J. A., Harris, J. M. and Vomel, H. (1995), 'Recovery of ozone in the lower stratosphere at the south pole during the spring of 1994', *Geophys. Res. Lett.* **18**, 2493–2496.

Holton, J. R. (1979), *An Introduction to Dynamic Meteorology*, 2nd edn, Academic Press, New York.

Holton, J. R. (1982), 'The role of gravity wave induced drag and diffusion in the momentum budget of the mesosphere', *J. Atmos. Sci.* **39**, 791–799.

Holton, J. R. (1983), 'The influence of gravity wave breaking on the general circulation of the middle atmosphere', *J. Atmos. Sci.* **40**, 2497–2507.

Holton, J. R. (1987), The production of temporal variability in trace constituent concentrations, *in* G. Visconti and R. Garcia, eds, 'Transport Processes in the Middle Atmosphere', Reidel, Dordrecht, chapter 3, pp. 313–326.

Jenkins, F. A. and White, H. E. (1966), *Fundamentals of Optics*, 3rd edn, McGraw-Hill, New York.

Jensen, E. J. and Thomas, G. E. (1994), 'Numerical simulations of the effects of gravity waves on noctilucent clouds', *J. Geophys. Res.* **99**, 3421–3430.

Johnson, B. J., Deshler, T. and Thompson, R. A. (1992), 'Vertical profiles of ozone at McMurdo Station, Antarctica; Spring 1991', *Geophys. Res. Lett.* **19**, 1105–1108.

Juramy, P., Chanin, M. L., Megie, G., Toulinov, G. F. and Doudoladov, Y. P. (1981), 'Lidar sounding of the mesospheric sodium layer at high latitudes', *J. Atmos. Terr. Phys.* **43**, 209–215.

Kane, T. J., Hostetler, C. A. and Gardner, C. S. (1991), 'Horizontal and vertical structure of the major sporadic sodium layer events observed during ALOHA-90', *Geophys. Res. Lett.* **18**, 1365–1368.

Kirkwood, S. and Collis, P. N. (1989), 'Gravity wave generation of simultaneous auroral sporadic-E layers and sudden neutral sodium layers', *J. Atmos. Terr. Phys.* **51**, 259–269.

Komhyr, W. D. (1969), 'Electrochemical concentration cells for gas analysis', *Ann. Geophys.* **25**, 203–210.

Lacoste, A.-M. (1994), Observations de l'ozone dans la stratosphere: validation et mise en place d'une base de donnees obtenues par sondage laser, PhD thesis, Université Pierre et Marie Curie, France.

Langford, A. O., Proffitt, M. H., VanZandt, T. E. and Lamarque, J.-F. (1996), 'Modulation of tropospheric ozone by gravity waves, Part 1: Observations and analysis of linear effects', *J. Geophys. Res.* . in press.

Leovy, C. B., Sun, C. R., Hitchman, M. H., Remsberg, E. E., Russell, J. M., Gordley, L. L., Gille, J. C. and Lyjak, L. V. (1983), 'Transport of ozone in the middle stratosphere: Evidence for planetary wave breaking', *J. Atmos. Sci.* **42**, 230–244.

Lilly, D. K. and Lester, P. F. (1974), 'Waves and turbulence in the stratosphere', *J. Atmos. Sci.* **31**, 800–812.

Lindzen, R. and Goody, R. (1965), 'Radiative and photochemical processes in mesospheric dynamics, 1, Models for radiative and photochemical processes', *J. Atmos. Sci.* **22**, 341–348.

Lindzen, R. S. (1981), 'Turbulence and stress owing to gravity wave and tidal breakdown', *J. Geophys. Res.* **86**, 9707–9714.

Lintelmann, S. A. and Gardner, C. S. (1994), 'Observation and interpretation of spectra of atmospheric gravity wave perturbations with upward and downward phase progression', *J. Geophys. Res.* **99**, 16,959–16,971.

London, J. and Liu, S. C. (1992), 'Long-term tropospheric and lower stratospheric ozone variations from ozonesonde observations', *J. Atmos. Terr. Phys.* **54**, 599–626.

Lu, W. and Fritts, D. C. (1993), 'Spectral estimates of gravity wave energy and momentum fluxes. Part III: Gravity wave–tidal interactions', *J. Atmos. Sci.* **50**, 3714–3727.

Manney, G. L., Zurek, R. W., Froidevaux, L., Waters, J. W., O'Neill, A. and Swinbank, R. (1995b), 'Lagrangian transport calculations using UARS data. Part II: Ozone', *J. Atmos. Sci.* **52**, 3069–3081.

Manney, G. L., Zurek, R. W., Lahoz, W. A., Harwood, R. S., Gille, J. C., Kumer, F. B., Mergenthaler, J. L., Roche, A. E., O'Neill, A., Swinbank, R. and Waters, J. W. (1995a), 'Lagrangian transport calculations using UARS data. Part I: Passive tracers', *J. Atmos. Sci.* **52**, 3049–3068.

Manson, A. H. (1990), 'Gravity wave horizontal and vertical wavelengths: An update of measurements in the mesopause region (~80–100 km)', *J. Atmos. Sci.* **47**, 2765–2773.

Marks, C. J. and Eckermann, S. D. (1995), 'A three–dimensional nonhydrostatic ray–tracing model for gravity waves: Formulation and preliminary results for the middle atmosphere', *J. Atmos. Sci.* **52**, 1959–1984.

McCormick, M. P., Zawodny, J. M., Veiga, R. E., Larsen, J. C. and Lang, P. H. (1989), 'An overview of SAGE I and II ozone measurements', *P. S. S.* **37**, 1567–1586.

McDermid, I. S. (1993), 'A 4-year climatology of stratospheric ozone from lidar measurements at Table Mountain, 34.4° N', *J. Geophys. Res.* **98**, 10,509–10,515.

McDermid, I. S., Godin, S. M., Wang, P. and McCormick, M. P. (1990), 'Comparison of stratospheric ozone profiles and their seasonal variations as measured by lidar and stratospheric aerosol and gas experiment during 1988', *J. Geophys. Res.* **98**, 5605–5612.

Meek, C. E., Reid, I. M. and Manson, A. H. (1985), 'Observations of mesospheric wind velocities - 2. Cross sections of power spectral density for 48–8 hours, 8–1 hour and 1 hour to 10 min over 60–110 km for 1981', *Radio Science* **20**, 1383–1402.

Meilinger, S. K., Koop, T., Luo, B. P., Huthwelker, T., Carslaw, K. S., Krieger, U., Crutzen, P. J. and Peter, T. (1995), 'Size–dependent stratospheric droplet composition in lee wave temperature fluctuations and their potential role in PSC freezing', *Geophys. Res. Lett.* **22**, 3031–3034.

Meriwether, J. W., Dao, P. D., McNutt, R. T., Klemetti, W., Moskowitz, W. and Davidson, G. (1994), 'Rayleigh lidar observations of mesosphere temperature structure', *J. Geophys. Res.* **99**, 16,973–16,987.

Mitchell, N. J., McDonald, A. J., Reid, S. J. and Price, J. D. (1996), 'Observations of gravity waves in the upper and lower stratosphere by lidar and ozonesondes', *Ann. Geophys.* **14**, 309–314.

Mitchell, N. J., Thomas, L. and Marsh, A. K. P. (1990), 'Lidar studies of stratospheric gravity waves: A comparison of analysis techniques', *Ann. Geophys.* **8**, 705–712.

Molina, M. J. and Rowland, F. S. (1974), 'Stratospheric sink for chlorofluoromethanes: Chlorine atom-catalyzed destruction of ozone', *Nature* **249**, 810–812.

Moustaoui, M. (1995), Influence des ondes et de la structure du vortex polaire sur les fluctuations du profil vertical de l'ozone stratospherique, PhD thesis, Laboratoire de Météorologie Dynamique du CNRS, Ecole Polytechnique, France.

Murayama, Y., Tsuda, T., Yamamoto, M., Nakamura, T., Sato, T., Kato, S. and Fukao, S. (1992), 'Dominant vertical scales of gravity waves in the middle atmosphere observed with the MU radar and rocketsondes', *J. Atmos. Terr. Phys.* **54**, 339–346.

Murphy, D. M. and Gary, B. L. (1995), 'Mesoscale temperature fluctuations and polar stratospheric clouds', *J. Atmos. Sci.* **52**, 1753–1760.

National Research Council (U.S.) (1982), Causes and effects of stratospheric ozone reduction, an update, Technical report, Committee on Chemistry and Physics of Ozone Depletion, Washington, D.C.: National Academy Press.

Newman, P. A. and Schoeberl, M. R. (1995), 'A reinterpretation of the data from the NASA Stratosphere–Troposphere Exchange Project', *Geophys. Res. Lett.* **22**, 2501–2504.

Norton, W. A. (1994), 'Breaking Rossby waves in a model stratosphere diagnosed by a vortex-following coordinate system and a technique for advecting material contours', *J. Atmos. Sci.* **51**, 654–673.

Ogino, S., Yamanaka, M. D., Kaneto, S., Yamanouchi, T. and Fukao, S. (1997), 'Meridional distribution of short-vertical-scale fluctuations in the lower stratosphere revealed by cross-equatorial ozonesonde observations at Shirase', *Proc. NIPR Symp. Polar Meteorol. Glaciol.* . in press.

Orsolini, Y., Simon, P. and Cariolle, D. (1995), 'Filamentation and layering of an idealized tracer by observed winds in the lower stratosphere', *Geophys. Res. Lett.* **22**, 839–842.

O'Sullivan, D. and Dunkerton, T. J. (1995), 'Generation of inertia-gravity waves in a simulated life cycle of baroclinic instability', *J. Atmos. Sci.* **52**, 3695–3716.

Pfister, L., Chan, K. R., Bui, T. P., Bowen, S., Legg, M., Gary, B., Kelly, K., Proffitt, M. and Starr, W. (1993), 'Gravity waves generated by a tropical cyclone during the STEP tropical field program: A case study', *J. Geophys. Res.* **98**, 8611–8638.

Qian, J., Gu, Y. Y., Papen, G. C. and Gardner, C. S. (1995), 'Horizontal wavenumber spectra of density and temperature perturbations in the mesosphere measured during the 4 August flight of ANLC-93', *Geophys. Res. Lett.* **22**, 2865–2868.

Rajasekhar, B. and Plane, J. M. C. (1993), 'An *ab initio* study of dissociative electron attachment to $NaNCO_3$ and $NaCO_3$ and the role of these reactions in the formation of sudden sodium layers', *Geophys. Res. Lett.* **20**, 21–24.

Randall, C. E., Rusch, D. W., Bevilacqua, R. M., Lumpe, J., Ainsworth, T. L., Debrestian, D., Fromm, M., Krigman, S. S., Hornstein, J. S., Shettle, E. P., Olivero, J. J. and Clancy, R. T. (1995), 'Preliminary results from POAM II: Stratospheric ozone at high northern latitudes', *Geophys. Res. Lett.* **22**, 2733–2736.

Randel, W. J. (1990), 'Kelvin–wave–induced trace constituent oscillations in the equatorial stratosphere', *J. Geophys. Res.* **95**, 18,641–18,652.

Reid, I. M. (1986), 'Gravity wave motions in the upper middle atmosphere (60-110 km)', *J. Atmos. Terr. Phys.* **48**, 1057–1072.

Reid, S. J. and Vaughan, G. (1991), 'Lamination in ozone profiles in the lower stratosphere', *Q. J. R. Meteorol. Soc.* **117**, 825–844.

Reid, S. J., Vaughan, G. and Kyro, E. (1993), 'Occurrence of ozone laminae near the boundary of the stratospheric polar vortex', *J. Geophys. Res.* **98**, 8883–8890.

Röth, E. P. and Ehhalt, D. H. (1987), Seasonal variation in the variance of stratospheric ozone and potential temperature over Hohenpeissenberg, F.R.G., *in* G. Visconti and R. Garcia, eds, 'Transport Processes in the Middle Atmosphere', Reidel, Dordrecht, pp. 137–152.

Rowlett, J. R., Gardner, C. S., Richter, E. S. and Sechrist, C. F. (1978), 'Lidar observations of wavelike structure in the atmospheric sodium layer', *Geophys. Res. Lett.* **8**, 683–686.

Sato, K. and Yamada, M. (1994), 'Vertical structure of atmospheric gravity waves revealed by the wavelet analysis', *J. Geophys. Res.* **99**, 20,623–20,631.

Schmidlin, F. J. (1992), 'First observation of mesopause temperatures lower than 100 K', *Geophys. Res. Lett.* **19**, 1643–1646.

Sears, F. W. and Salinger, G. L., eds (1975), *Thermodynamics, Kinetic Theory, and Statistical Thermodynamics*, 3rd edn, Addison–Wesley, Reading, MA.

Senft, D. C., Collins, R. L. and Gardner, C. S. (1989), 'Mid-latitude lidar observations of large sporadic sodium layers', *Geophys. Res. Lett.* **16**, 715–718.

Senft, D. C. and Gardner, C. S. (1991), 'Seasonal variability of gravity wave activity and spectra in the mesopause region at Urbana', *J. Geophys. Res.* **96**, 17,229–17,264.

She, C. Y., Yu, J. R., Krueger, D. A., Roble, R., Keckhut, P., Hauchecorne, A. and Chanin, M. L. (1995), 'Vertical structure of the mid-latitude temperature from stratosphere to mesopause', *Geophys. Res. Lett.* **22**, 377–380.

Shibata, T., Fukuda, T. and Maeda, M. (1986), 'Density fluctuations in the middle atmosphere over Fukuoka observed by an XeF Rayleigh lidar', *Geophys. Res. Lett.* **13**, 1121–1124.

Slipher, V. M. (1929), 'Emissions in the spectrum of the light of the night sky', *Publ. Astron. Soc. Pac.* **41**, 262.

Smith, S. A., Fritts, D. C. and VanZandt, T. E. (1987), 'Evidence for a saturated spectrum of atmospheric gravity waves', *J. Atmos. Sci.* **44**, 1404–1410.

Sun, C. R. and Leovy, C. B. (1990), 'Ozone variability in the equatorial middle atmosphere', *J. Geophys. Res.* **95**, 13,829–13,849.

Swider, W. (1992), 'Sodium chemistry: a brief review and two new mechanisms for sudden sodium layers', *P. S. S.* **40**, 247–253.

Tarrago, A. and Chanin, M.-L. (1982), 'Interpretation in terms of gravity waves of structures observed at the mesopause level by photogrammetry and lidar', *P. S. S.* **30**, 611–616.

Teitelbaum, H., Ovarlez, J., Kelder, H. and Lott, F. (1994), 'Some observations of gravity–wave–induced structure in ozone and water vapour during EASOE', *Geophys. Res. Lett.* **21**, 1483–1486.

Thomas, L., Isherwood, M. C. and Bowman, M. R. (1983), 'A theoretical study of the height distribution of sodium in the mesosphere', *J. Atmos. Terr. Phys.* **45**, 587–594.

Thompson, R. O. R. Y. (1978), 'Observation of inertial waves in the stratosphere', *Q. J. R. Meteorol. Soc.* **104**, 691–698.

Thrane, E. V., Blix, T., Hoppe, U.-P., Lübken, F.-J., Hillert, W., Lehmacher, G. and Fritts, D. C. (1994), 'A study of small-scale waves and turbulence in the mesosphere using simultaneous *in situ* observations of neutral gas and plasma fluctuations', *J. Atmos. Terr. Phys.* **56**, 1797–1808.

Thunis, P. and Bornstein, R. (1996), 'Hierarchy of mesoscale flow assumptions and equations', *J. Atmos. Sci.* **53**, 380–397.

Tie, X. X. and Brasseur, G. (1995), 'The response of stratospheric ozone to volcanic eruptions: Sensitivity to atmospheric chlorine loading', *Geophys. Res. Lett.* **22**, 3035–3038.

Tsuda, T., Inoue, T., Fritts, D. C., VanZandt, T. E., Kato, S., Sato, T. and Fukao, S. (1989), 'MST radar observations of a saturated gravity wave spectrum', *J. Atmos. Sci.* **46**, 2440–2447.

Tsuda, T., Murayama, Y., Yamamoto, M., Kato, S. and Fukao, S. (1990), 'Seasonal variation of the momentum flux in the mesosphere observed with the MU radar', *Geophys. Res. Lett.* **17**, 725–728.

Tsuda, T., VanZandt, T. E., Mizumoto, M., Kato, S. and Fukao, S. (1991), 'Spectral analysis of temperature and Brunt-Vaisala frequency fluctuations observed by radiosondes', *J. Geophys. Res.* **96**, 17,265–17,278.

Tuck, A. F. (1989), 'Synoptic and chemical evolution of the Antarctic vortex in late winter and early spring, 1987', *J. Geophys. Res.* **94**, 11,687–11,737.

U.S. Standard Atmosphere (1976), U.S.A. Committee on Extension to the Standard Atmosphere, Technical report, U.S. Government Printing Office, Washington.

VanZandt, T. E. (1982), 'A universal spectrum of buoyancy waves in the atmosphere', *Geophys. Res. Lett.* **9**, 575–578.

Vincent, R. A. (1994), 'Gravity-wave motions in the mesosphere and lower thermosphere observed at Mawson, Antarctica', *J. Atmos. Terr. Phys.* **56**, 593–602.

Vincent, R. A., Allen, S. J. and Eckermann, S. D. (1996), Gravity wave parameters in the lower stratosphere, *in* K. Hamilton, ed., 'Gravity wave processes and their parameterization in global climate models', Springer-Verlag. in press.

Vincent, R. A. and Fritts, D. C. (1987), 'A climatology of gravity wave motions in the mesosphere at Adelaide, Australia', *J. Atmos. Sci.* **44**, 748–760.

Vincent, R. A. and Lesicar, D. (1991), 'Dynamics of the equatorial mesosphere: First results with a new generation partial reflection radar', *Geophys. Res. Lett.* **18**, 825–828.

Vincent, R. A. and Reid, I. M. (1983), 'HF Doppler measurements of mesospheric gravity wave momentum fluxes', *J. Atmos. Sci.* **40**, 1321–1333.

Vincent, R. A., Tsuda, T. and Kato, S. (1988), 'A comparative study of mesospheric solar tides observed at Adelaide and Kyoto', *J. Geophys. Res.* **93**(D3), 699–708.

Voelz, D. G. and Gardner, C. S. (1986), Theoretical and lidar studies of the seasonal and nocturnal variations of the mesospheric sodium layer at Urbana, Illinois, Technical Report EOSL 86-006, Dep. of Electr. and Comput. Eng., Univ. of Ill. at Urbana-Champaign, Urbana.

von Zahn, U. and Hansen, G. (1988), 'Sudden neutral sodium layers: A strong link to sporadic E layers', *J. Atmos. Terr. Phys.* **50**, 93–104.

von Zahn, U., von der Gathen, P. and Hansen, G. (1987), 'Forced release of sodium from upper atmospheric dust particles', *Geophys. Res. Lett.* **14**, 76–79.

Walterscheid, R. L. and Hocking, W. K. (1991), 'Stokes diffusion by atmospheric internal gravity waves', *J. Atmos. Sci.* **48**, 2213–2230.

Waugh, D. W. and Plumb, R. A. (1994), 'Contour advection with surgery: A technique for investigating finescale structure in tracer transport', *J. Atmos. Sci.* **51**, 530–540.

Wayne, R. P. (1988), *Principles and Applications of Photochemistry*, Oxford University Press, Oxford.

Weinstock, J. (1978), 'Theory of the interaction of gravity waves with o_2 airglow', *J. Geophys. Res.* **83**, 5175–5185.

Weinstock, J. (1990), 'Saturated and unsaturated spectra of gravity waves and scale dependent diffusion', *J. Atmos. Sci.* **47**, 2211–2225.

Whiteway, J. A. and Carswell, A. I. (1994), 'Rayleigh lidar observations of thermal structure and gravity wave activity in the high Arctic during a stratospheric warming', *J. Atmos. Sci.* **51**, 3122–3136.

Wilson, R., Chanin, M. L. and Hauchecorne, A. (1991), 'Gravity waves in the middle atmosphere observed by Rayleigh lidar, 2, Climatology', *J. Geophys. Res.* **96**, 5169–5183.

WMO (1994), Scientific assessment of ozone depletion, Technical Report 37, World Meteorological Organization, Global Ozone Research and Monitoring Project, Geneva, Switzerland.

Wu, Y.-F. and Widdel, H.-U. (1991), 'Further study of a saturated gravity wave spectrum in the mesosphere', *J. Geophys. Res.* **96**, 9263–9272.

Yamamoto, M., Tsuda, T., Kato, S., Sato, T. and Fukao, S. (1987), 'A saturated inertia gravity wave in the mesosphere observed by the middle and upper atmosphere radar', *J. Geophys. Res.* **92**, 11,993–11,999.

Zhu, X. (1994), 'A new theory of the saturated gravity wave spectrum for the middle atmosphere', *J. Atmos. Sci.* **51**, 3615–3626.

Zhu, X. and Holton, J. R. (1986), 'Photochemical damping of inertio-gravity waves', *J. Atmos. Sci.* **43**, 2578–2584.

Ziemke, J. R. and Stanford, J. L. (1994), 'Kelvin waves in total column ozone', *Geophys. Res. Lett.* **21**(2), 105–108.